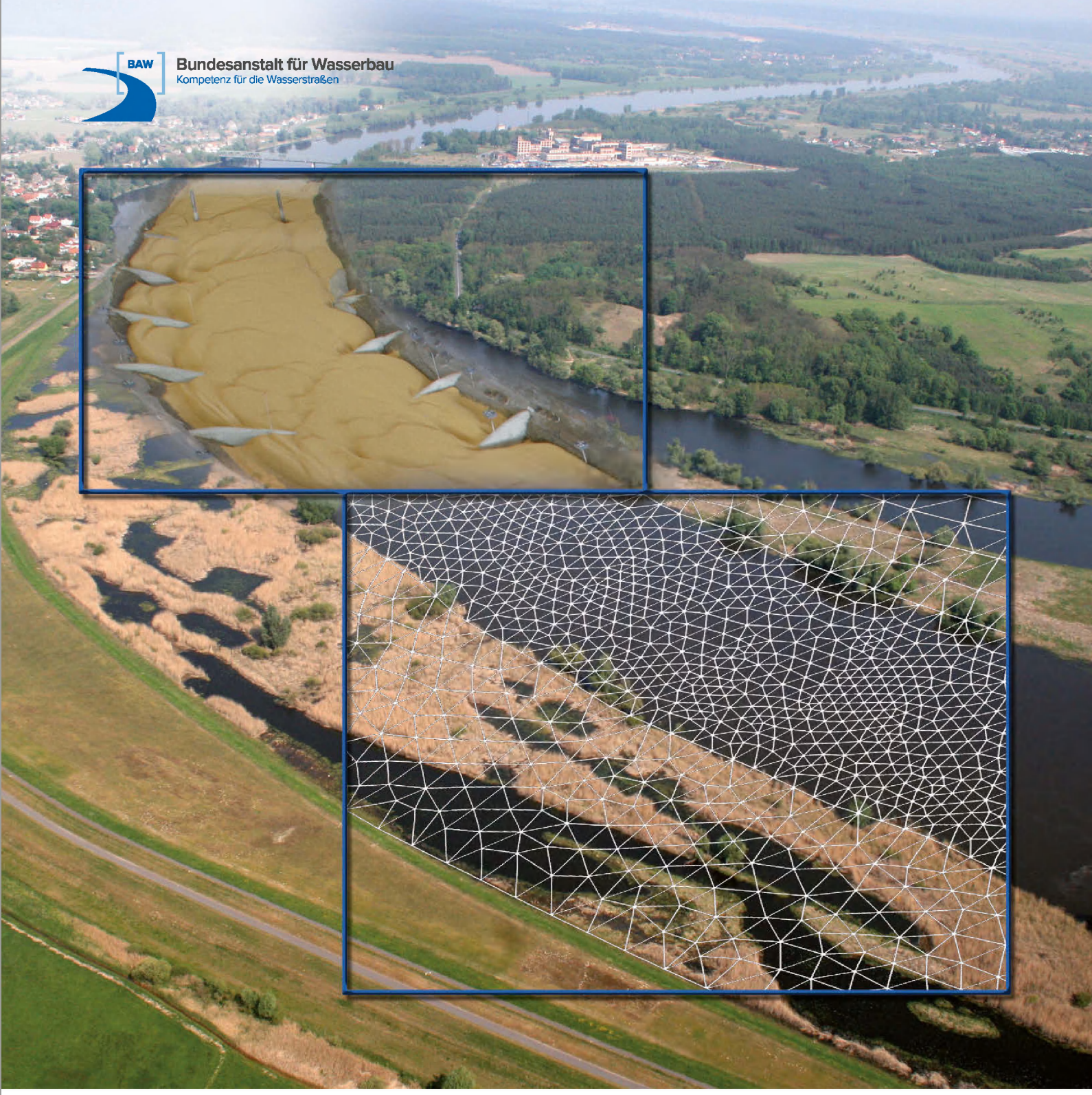

XXth TELEMAC-MASCARET User Conference 2013

Rebekka Kopmann · Annalena Goll
Editors

XXth TELEMAC-MASCARET User Conference

Karlsruhe, Germany
October 16–18, 2013

TUC 2013

Editors

Rebekka KOPMANN
Federal Waterways Engineering and Research Institute, Germany

Annalena GOLL
Federal Waterways Engineering and Research Institute, Germany

Proceedings of the

XXth TELEMAC-MASCARET User Conference
October 16–18, 2013

Organised by

Bundesanstalt für Wasserbau
Kussmaulstr. 17
76187 Karlsruhe
Germany
www.baw.de

Edited by

Rebekka Kopmann
Annalena Goll

Published by: Bundesanstalt für Wasserbau
Federal Waterways Engineering and Research Institute
e-mail:info@baw.de
www.baw.de

ISBN 978-3-939230-07-6

Printed in Germany

Table of Contents

3 Sediment Transport

4 Water Quality

Bundesanstalt für Wasserbau
Kompetenz für die Wasserstraßen

Foreword to the XXth TELEMAC-MASCARET User Conference

Dear participants,

BAW is proud to present the proceedings of the XXth TELEMAC-MASCARET User Conference. As the service provider for Germany's federal waterways, numerical modelling is one of the main tools for engineering tasks in BAW.

Beginning to apply and develop TELEMAC in the last century, it is now a standard for 2D modelling of waterways at BAW. Today sediment transport modelling, high resolution grids, increasing sizes of modelling areas, long-term prognoses and massively parallel computing define our challenges here. Collaboration in the TELEMAC-MASCARET Consortium and many productive co-operations with universities guarantee continuous progress and new developments to face the diverse and complex tasks.

20 years of user conferences stand for 20 years of fruitful interaction between developers and users and active networking among the users themselves. They also represent tradition, which is one significant component of the TELEMAC-MASCARET programming family. Evolution is another element, apparent at the annual conference when the latest developments are presented. A wonderful example for this is the yearly presentation of an even better advection scheme by Jean-Michel Hervouet. As always I am looking forward to that presentation and the enhancement of the calculation due to the new, amazing scheme.

On behalf of BAW and of the TELEMAC-MASCARET Consortium, I would like to thank all authors and participants for the exciting contributions to the TELEMAC-MASCARET User Conference. The numerous articles clearly demonstrate that the TELEMAC-MASCARET software is an excellent tool for research and application.

Rebekka Kopmann
Chair of Local Organising Committee

Bundesanstalt für Wasserbau
Kußmaulstr. 17
76187 Karlsruhe
Germany

Organisation

International Scientific Committee

Rebekka Kopmann	BAW
Thomas Brudy-Zippelius	BAW
Jacek Jankowski	BAW
Jean-Michel Hervouet	EDF R&D and Saint-Venant Laboratory
Damien Violeau	EDF R&D and Saint-Venant Laboratory
Emile Razafindrakoto	EDF R&D
Michel Benoit	EDF R&D and Saint-Venant Laboratory
Nicole Goutal	EDF R&D and Saint-Venant Laboratory
Pablo Tassi	EDF R&D and Saint-Venant Laboratory
Christophe Coulet	Artelia
Olivier Bertrand	Artelia
Sébastien Bourban	HR Wallingford
Catherine Villaret	HR Wallingford
Alan Cooper	HR Wallingford
Michiel Knaapen	HR Wallingford
Noémie Durand	HR Wallingford
François Hissel	CETMEF
Patrick Chassé	CETMEF
David Emerson	STFC Daresbury Laboratory
Charles Moulinec	STFC Daresbury Laboratory

Local Organising Committee

Rebekka Kopmann
Annalena Goll
Simone Knobloch
Thomas Brudy-Zippelius

TELEMAC-MASCARET Core Group

Artelia
www.arteliagroup.com

Bundesanstalt für Wasserbau
(Federal Waterways Engineering and Research Institute)
www.baw.de

CETMEF – centre d'études techniques maritimes et fluviales
www.cetmef.developpement-durable.gouv.fr/

EDF – Electricité de France
National Hydraulic and Environment Laboratory (LNHE)
research.edf.com

HR Wallingford
www.hrwallingford.com/

Science & Technology Facilities Council
Daresbury Laboratory
http://www.stfc.ac.uk/

TUC 2013, 16-18/10/2013, Karlsruhe - Kopmann, Goll (eds.) - © 2013 Bundesanstalt für Wasserbau ISBN 978-3-939230-07-6

The weak form of the method of characteristics, an amazing advection scheme

J.-M. Hervouet
Laboratoire National d'Hydraulique et Environnement (LNHE)
Electricité de France
6 Quai Watier, 78400 Chatou FRANCE
j-m.hervouet@edf.fr

***Abstract*— The weak form of the method of characteristics is described. The principle is given and the technical problems exposed. Results on the rotating cone test show the amazing quality of this scheme, but the method suffers from a number of implementation problems. It can however advantageously be used in some specific situations.**

I. INTRODUCTION

The weak form of the method of characteristics is used for solving advection, or even advection-diffusion equations with source terms. It couples the classical method of characteristics, as already used in TELEMAC, and a finite element formulation. Though invented at LNHE in the eighties (see [1]), this technique was not developed in Europe but is now widely known in the US as ELLAM (Eulerian Lagrangian Localized Adjoint Method, see [2]). Though still relying on linear elements this method surprisingly yields extraordinary results in terms of phase error and amplification, but suffers from a number of implementation problems. It can however advantageously be used in some specific situations. The principle of the method is briefly recalled hereafter, and the application to TELEMAC is tried.

II. PRINCIPLE

The method is explained here in the context of Navier-Stokes equations, with a pure advection in the conservative form:

$$\frac{\partial f}{\partial t} + \mathrm{div}(f\vec{u}) = 0 \tag{1}$$

Where f is the advected function and $\vec{u}$ the advection field. With the classical method of characteristics (now called "strong" characteristics), a solution would consist of tracing back the characteristics (backwards trajectories but with fixed advection field), and interpolate the value of f at time t^n for every point i in the mesh (the result is denoted $\widetilde{f}_i$), and to eventually write: $f_i^{n+1} = \widetilde{f}_i$. However the strong characteristics solve the non-conservative equation, their advantage is that they are monotonous, as the interpolation (if linear, this would not be the case with higher orders) cannot give under- or overshoots, and a drawback is that they are not mass conservative. They are unconditionally stable. The basic idea of the weak form of characteristics is to apply a variational Galerkin formulation of the equation, not only in space:

$$\int_\Omega \left(\frac{\partial f}{\partial t} + \mathrm{div}(f\vec{u}) \right) \Psi_i \, d\Omega = 0 \tag{2}$$

but also in time!

$$\int_{t^n}^{t^{n+1}} \left(\int_\Omega \left(\frac{\partial f}{\partial t} + \mathrm{div}(f\vec{u}) \right) \Psi_i \, d\Omega \right) dt = 0 \tag{3}$$

Ψ_i is a linear test function, defined for all degrees of freedom in the mesh, with property $\sum_{i=1}^{np} \Psi_i = 1$, np being the total number of nodes in the mesh. We then apply two integrations by part, on one hand:

$$\int_{t^n}^{t^{n+1}} \left(\int_\Omega \frac{\partial f}{\partial t} \Psi_i \, d\Omega \right) dt = \left[\int_\Omega f \Psi_i \, d\Omega \right]_{t^n}^{t^{n+1}} - \int_{t^n}^{t^{n+1}} \left(\int_\Omega \frac{\partial \Psi_i}{\partial t} f \, d\Omega \right) dt \tag{4}$$

and on the other hand the divergence term with the Stokes theorem. Commuting the integrals in space and time is possible if Ω is independent from time, it finally gives:

$$\int_\Omega f^{n+1}\Psi_i^{n+1}\,d\Omega - \int_\Omega f^n\Psi_i^n\,d\Omega + \int_{t^n}^{t^{n+1}}\left(\int_\Gamma \Psi_i\ f\vec{u}.\vec{n}\,d\Gamma\right)dt - \int_{t^n}^{t^{n+1}}\left(\int_\Omega f\left(\frac{\partial\Psi_i}{\partial t}+\vec{u}\ .\overrightarrow{grad}(\Psi_i)\right)d\Omega\right)dt = 0 \quad (5)$$

The Ψ_i have been indexed with time when necessary, for reasons that will now appear clearly. It seems that things are more complicated with this new equation, but the tremendous idea in the method is to remark that we have in the second line the term $\frac{\partial\Psi_i}{\partial t}+\vec{u}\ .\overrightarrow{grad}(\Psi_i)$, which looks like a non conservative advection equation of the test functions. This term would be 0 if the test functions were advected, and it is what will be done! Note that we started from a conservative advection equation on f and arrive at a non conservative equation of the test functions. On the contrary a non conservative advection equation of f would lead to a conservative equation of the test functions.

So now we admit that the test functions are advected in a non conservative form, so that $\frac{\partial\Psi_i}{\partial t}+\vec{u}\ .\overrightarrow{grad}(\Psi_i)=0$, and we are left with:

$$\int_\Omega f^{n+1}\Psi_i^{n+1}\,d\Omega = \int_\Omega f^n\Psi_i^n\,d\Omega - \int_{t^n}^{t^{n+1}}\int_\Gamma \Psi_i\ f\vec{u}.\vec{n}\,d\Gamma\,dt \quad (6)$$

If we sum on all points in the mesh, we have:

$$\int_\Omega f^{n+1}\,d\Omega = \int_\Omega f^n\,d\Omega - \int_{t^n}^{t^{n+1}}\left(\int_\Gamma f\vec{u}.\vec{n}\,d\Gamma\right)dt \quad (7)$$

which is a mass conservation proof stating that the increase of mass in the domain is only due to the flux at the boundaries between t^n and t^{n+1}, $\vec{n}$ being a vector pointing outward the domain. Can we solve (6)? The left-hand side is $\sum_{j=1}^{np} f_j^{n+1}\int_\Omega \Psi_j^{n+1}\Psi_i^{n+1}d\Omega$. If we choose a backward advection of test functions, Ψ_i^{n+1} will be the classical test functions of our mesh and $\int_\Omega \Psi_j^{n+1}\Psi_i^{n+1}d\Omega$ will be the classical mass matrix M. We shall eventually have to solve a linear system: $M\ F^{n+1} = RHS$, where:

$$RHS = \int_\Omega f^n\Psi_i^n\,d\Omega - \int_{t^n}^{t^{n+1}}\left(\int_\Gamma \Psi_i\ f\vec{u}.\vec{n}\,d\Gamma\right)dt \quad (8)$$

In this right-hand side Ψ_i^n will be the same test function advected backward, thus at time t^n and this is a new concept. We can imagine for example a set of test functions based on the feet of all characteristics, the feet being the nodes of an advected mesh (with the assumption that triangles remain correctly oriented triangles during advection, which is not guaranted). The property $\sum_{i=1}^{np}\Psi_i^n = 1$ must be preserved if we want to keep our proof of mass conservation. Actually the term $\int_\Omega f^n\Psi_i^n\,d\Omega$ only requires the knowledge of Ψ_i^n, not the full trajectory. As function f_i^n is known on the real mesh (not the backward advected one), we have to write: $f^n = \sum_{j=1}^{np} f_j^n\Psi_i^{n+1}$, and term $\int_\Omega f^n\Psi_i^n\,d\Omega$ is thus:

$$\int_\Omega f^n\Psi_i^n\,d\Omega = \sum_{j=1}^{np} f_j^n\int_\Omega \Psi_j^{n+1}\Psi_i^n\,d\Omega \quad (9)$$

This is where we find the main technical difficulty: the test functions Ψ_j^{n+1} and Ψ_i^n are based on meshes that are different. To have a unique polynomial definition of both we must decompose the domain into a number of areas, every area belonging to a unique triangle of the original mesh and a unique triangle of the advected mesh. Such areas may be triangles, quadrilaterals, pentagons, or even hexagons. A general solution of this problem, based on the theory of distributions, has been proposed in 1986 (see [3]). However it could be sensitive to truncation errors, the final exact formula using the Heavyside function (denoted *H*). As a matter of fact terms like *H(ax+by+c)* may give randomly 0 or 1, depending on truncation errors, if *ax+by+c* is close to 0. Research in this direction would include finding a formula insensitive to truncation errors and a fast way to decompose the mesh into areas with unique polynomial definition of Ψ_j^{n+1} and Ψ_i^n.

Actually, for a practical use, the integral of (9) is computed with Gauss points. The Gauss points (a given constant number for every triangle, namely 1, 3, 4 or 6 were tested) are defined on the original mesh and advected backwards. The idea has been published in [4]. However, whatever the number of Gauss points (see [5] for numerical values and positions of Gauss points of various elements), this is an approximation because it will be used to integrate a function that is only piece-wise polynomial. Though it eventually gives a very simple procedure, the use of Gauss points is here conceptually complex and needs explanations. The first idea is to decompose the term $\int_\Omega f^n\Psi_i^n\,d\Omega$ into the integral over all the triangles surrounding point *i* in the backward advected mesh. On such triangles Ψ_i^n has a unique polynomial (in fact linear) definition, but f^n is only piece-

wise linear, because it is defined on the original mesh. Then on a triangle T we can write:

$$\int_T f^n \, \Psi_i^n \, dT = \sum_{g=1}^{ngauss} w_g \, f_g^n \, \Psi_i^n(g) \tag{10}$$

Where: *ngauss* is the number of Gauss points, w_g is the weight of Gauss points, and f_g^n is the value of f^n at the position of the Gauss point. $\Psi_i^n(g)$ is the value of the test function at the position of the Gauss point. $\sum_{g=1}^{ngauss} w_g$ is the area of the triangle. The Gauss weights, because they are proportional to the area of the triangle, are liable to change with time. However, the definition of a divergence free velocity field ensures that the areas of triangles will not change (unless we have errors in the discretisation). For this reason, but only in a context where $div(\vec{u}) = 0$, the Gauss weights are taken in the mesh at time t^{n+1}. Note that if the velocity field is not divergence free, e.g. if the local space is expanding, $\int_\Omega \Psi_i \, d\Omega$ would grow with time, then f would be locally reduced to keep mass conservation according to its conservative equation. To sum up, in the sum $\sum_{g=1}^{ngauss} w_g \, f_g^n \, \Psi_i^n(g)$ the weights w_g can be taken in the mesh at time t^{n+1}, it is also the case of $\Psi_i^n(g)$ because Ψ_i is advected in a non conservative form, which keeps its height unchanged. Now what is f_g^n ? This is where we use the strong form of the method of characteristics: the backward characteristics will be built for all the Gauss points, and f_g^n will be the value of f^n at the foot the Gauss point characteristic. Now what will happen if a backward characteristic goes out of the domain? It can only do this through a liquid boundary which is an entrance of the domain, hence were we have the boundary conditions of f and we can take it for the value of f_g^n. In other terms the Gauss points exiting the domain will provide the term $\int_{t^n}^{t^{n+1}} \left(\int_\Gamma \Psi_i \, f\vec{u}.\vec{n} \, d\Gamma \right) dt$. Using the technique of Gauss points, the whole method will result in solving the system:

$$\left(M \, F^{n+1} \right)_i = \sum_{g=1}^{ng} w_g \, f_g^n \, \Psi_i^n(g) \tag{11}$$

where ng represents all Gauss points involved in the computation of the terms:

$$\int_\Omega f^n \Psi_i^n \, d\Omega + \int_{t^n}^{t^{n+1}} \left(\int_\Gamma \Psi_i \, f\vec{u}.\vec{n} \, d\Gamma \right) dt \tag{12}$$

The procedure thus consists of choosing a number of Gauss points per triangle (the larger the better because it will never be an exact integration), of computing their characteristic and interpolating the advected function at their foot. With this the right-hand side of the linear system is easily built, and this system is easily inverted (with an iterative solver), because its matrix is a mass matrix. The procedure is mass conservative (in a divergence-free velocity field context), but we can check it only if we are able to find out what is $\int_{t^n}^{t^{n+1}} \left(\int_\Gamma \Psi_i \, f\vec{u}.\vec{n} \, d\Gamma \right) dt$ in the right-hand side, which is not obvious as the Gauss points procedure computes simultaneously both terms of (12).

III. A FIRST TEST CASE

This first test case is done in the context of a divergence free rotating velocity field. It was also used in [6] (where a figure showing the velocities is given). It consists of the advection of a tracer in a solid rotation velocity field. Namely the computational domain is a square between abscissae 0 and 20.1 m and between ordinates 0 and 20.1 m. The mesh is composed of squares of side 0.3 m split into two triangles. The velocity field has the two components $u(x,y)=10.05-y$ and $v(x,y)=x-10.05$, and the initial tracer value is between 0 and 1, of the form: $T(x,y) = e^{-\left[(x-15)^2+(y-10.05)^2\right]/2}$.

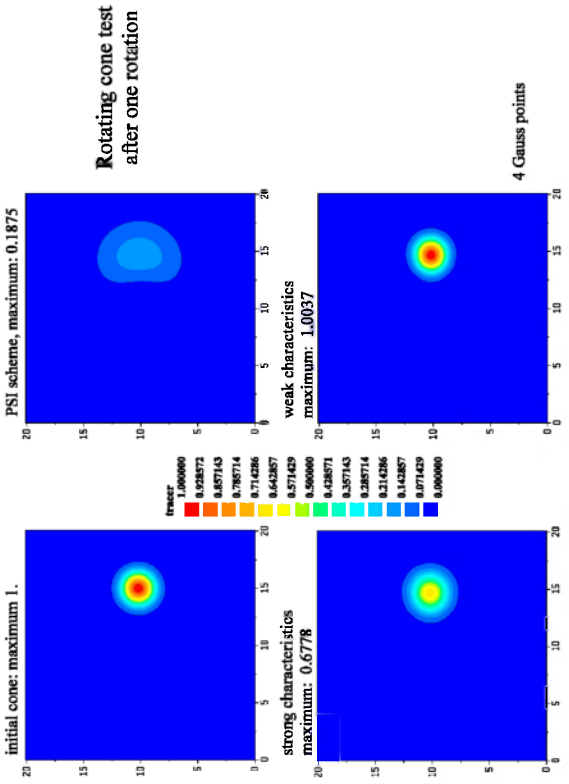

Figure 1. The rotating cone test with various advection schemes

The principle of the test is to simulate one rotation of the tracer around the center of the square. With an ideal solver, there should be no variation of the tracer after one rotation. We do here one rotation in 32 iterations, with a time step of 0.196349541 s (actually the conditions chosen in Reference 3, which show that the method is insensitive to the Courant number).

The original maximum height of the cone is 1. After one rotation the tracer maximum is given in Table I and the shape of the cone is shown on Figure 1.

TABLE I. ROTATING CONE TEST

Advection scheme	Height of cone after 1 rotation
explicit PSI scheme	0.1875
"strong" characteristics	0.6778
"weak" characteristics	0.996929 (6 Gauss points)

In this case the Courant number is at most 7 if we consider sides of triangles as the mesh size. The cone after 1 rotation is virtually unchanged. Now you understand why this method is worth looking at, even if it has technical drawbacks! Note that with a more physically recommended Courant number of 1 the cone height after one rotation is 0.9545, which shows that the method is less diffusive for large Courant numbers (even one rotation in 1 step would work!). The reason for the excellent quality of the method is certainly the inversion of the mass matrix, which prevents artificial diffusion. If we lump the matrix, so that it becomes a diagonal with positive terms, monotonicity is thus ensured, but the height after one rotation becomes 0.5013, which is less than the strong form (but compared to the strong form of characteristics it would be however a way to improve mass conservation, with a result better than the distributive schemes).

Increasing the number of Gauss points is rapidly useless, as shown in Table II, though the six-point case eventually shows that the overshoot is due to the quadrature.

TABLE II. INFLUENCE OF THE NUMBER OF GAUSS POINTS

Number of Gauss points	Maximum of cone	Minimum of cone
1	0.840168	$-2.77\ 10^{-6}$
3	1.004790	$-3.28\ 10^{-5}$
4	1.003720	$-5.31\ 10^{-5}$
6	0.996929	$-1.39\ 10^{-5}$

IV. NOW THE DRAWBACKS

A test case with a tracer, e.g. a tracer added in the bridge piers test case, shows the drawbacks of the loss of monotonicity. In this case a tracer at value 1 is entered on 3 points in the entrance, whereas on other points it is set to 0. We compare the results after 80 s of simulation. The strong form of characteristics is monotonous, but the highest value of the tracer at the exit is only 0.398. The weak form has values at the exit greater than 0.9, but strong undershoots and overshoots (range of values from -0.31 to 1.22). Lumping the mass matrix saves monotonicity, but in this case numerical diffusion is worse than the strong form. A partial lumping can give intermediate results.

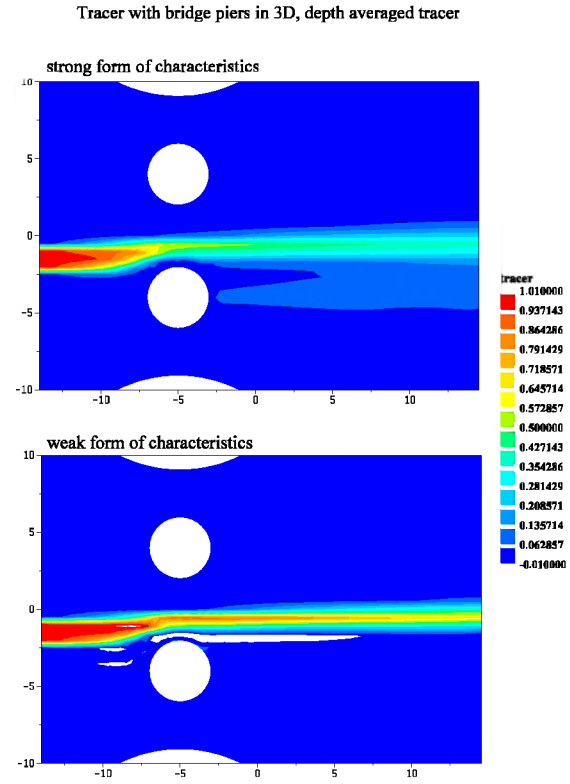

Figure 2. von Karman eddies with strong or weak characteristics used for advection of velocities

If we use the weak form in a context where monotonicity is not so important, e.g. for the velocities, we find a dramatic improvement, like on Figure 2, showing the von Karman eddies behind the bridge piers.

The advantages and drawbacks of the method are thus:

Advantages:

- very little phase error
- very little damping

Drawbacks:

- an approximation with Gauss points for computing an integral (mass conservation only approximated)
- a mass matrix to invert, with subsequent undershoots and overshoots in the solution (no monotonicity)

Except the loss of monotonicity, the inversion of the mass matrix is not really a problem, because in reality it is not done. Actually the following fractional step after advection, which is diffusion, requires $M\ F^{n+1}$, not F^{n+1}.

V. WEAK FORM IN THE CONTEXT OF SHALLOW WATER EQUATIONS

In a depth-integrated context, the correct conservative equation reads: $\frac{\partial(hf)}{\partial t} + \mathrm{div}(hf\vec{u}) = 0$, which can be interpreted as (1) with the variable hf. If we do this, the derivation leads to the equation:

$$\int_\Omega h^{n+1} f^{n+1} \Psi_i^{n+1} \, d\Omega = \int_\Omega h^n f^n \Psi_i^n \, d\Omega - \int_{t^n}^{t^{n+1}} \left(\int_\Gamma \Psi_i \, hf \, \vec{u}.\vec{n} \, d\Gamma \right) dt \tag{13}$$

Strictly speaking, the left-hand side term is:

$$\int_\Omega h^{n+1} f^{n+1} \Psi_i^{n+1} \, d\Omega = \sum_{j=1}^{np} f_j^{n+1} \int_\Omega h^{n+1} \Psi_j^{n+1} \Psi_i^{n+1} \, d\Omega \tag{14}$$

which is $M(h^{n+1})F^{n+1}$, where $M(h^{n+1})$ is a kind of mass matrix with an extra term h^{n+1}. A Gauss points approach would lead to solve the system:

$$\left(M(h^{n+1}) \, F^{n+1} \right)_i = \sum_{g=1}^{ng} w_g \, h_g^n \, f_g^n \, \Psi_i^n(g) \tag{15}$$

Where h_g^n are the depths interpolated at the feet of characteristics. The problem is that the velocity field is no longer divergence free, so the Gauss weights evolve along the pathlines. The case f constant shows in fact that we must have:

$$\int_\Omega h^{n+1} \Psi_i^{n+1} \, d\Omega = \sum_{g=1}^{ng} w_g \, h_g^n \, \Psi_i^n(g) \tag{16}$$

which gives us, assuming w_g taken at time t^{n+1}, a correction factor leading to the equation:

$$\left(M(h^{n+1}) \, F^{n+1} \right)_i = \int_\Omega h^{n+1} \Psi_i^{n+1} \, d\Omega \, \frac{\sum_{g=1}^{ng} w_g \, h_g^n \, f_g^n \, \Psi_i^n(g)}{\sum_{g=1}^{ng} w_g \, h_g^n \, \Psi_i^n(g)} \tag{17}$$

with a simplified lumped form:

$$f_i^{n+1} = \frac{\sum_{g=1}^{ng} w_g \, h_g^n \, f_g^n \, \Psi_i^n(g)}{\sum_{g=1}^{ng} w_g \, h_g^n \, \Psi_i^n(g)} \tag{18}$$

where a division by 0 would only occur if the numerator is also 0.

This depth-integrated form of weak advection has also been tested on the bridge piers case, but it brings very little difference, which is normal because the variations of depth in this case are small.

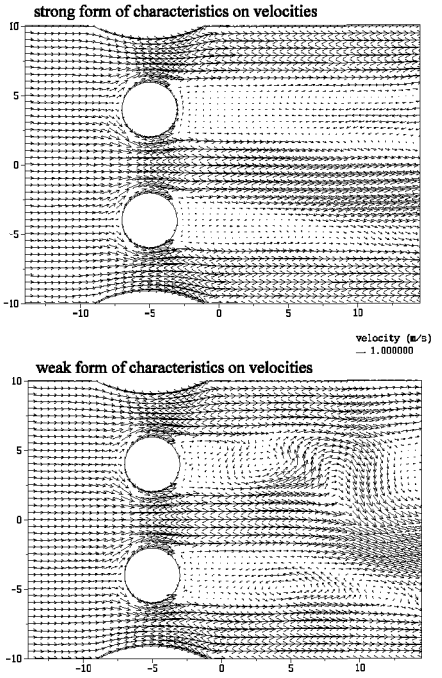

Figure 3. Bridge piers case with a tracer, showing undershoots of weak form of characteristics

VI. WEAK FORM IN 3D

3D is a priori simpler than 2D, and the theory can be readily applied. In the context of the sigma-mesh transformation of TELEMAC-3D, the computation of the characteristics pathlines can be done in the transformed mesh, thus taking into account the relocalization. Then when the feet of characteristics are known, we can apply the weak form in the real mesh. With prisms and for second order in the computation of the integral, 6 points per element are necessary. Figure 3 shows the results obtained on the bridge piers test case in 3D. The depth-averaged tracer is plotted. The initial value of the tracer is 0 and the value of 1 is given at 3 points of the entrance, without specified unit. Again we see undershoots, but less than in 2D. The difference with 2D is not explained, though it may be due to the depth-averaging process that filters oscillations. For a final "mass" (actually

integral over the whole domain) of tracer of about 109, the loss with the strong form is 48.38 or 44%, the loss with the weak form is 0.308 or 0.28%, a big improvement, the remaining error of 0.28% being due to the aforementioned Gauss quadrature. The computer time is 6'54" with the strong form, 9'34" with the weak form (i.e. an extra cost of 39%, but this is so far without any optimization of the weak form).

VII. FORWARD CHARACTERISTICS

A proposed alternative to the choice of backward characteristics is to do forward characteristics. The interpolation at the foot of the characteristic is then replaced by a projection. Basically the Gauss points take a mass at time t^n and carry it further, on arrival in an element the mass is shared between the points in the element with respect to the isoparametric coordinates, and this yields the right-hand side. The integral is computed exactly, but even with a full lumping of the mass matrix the monotonicity is not ensured, because the divergence free character of the velocity may be altered by the approximated computation of the characteristics, namely if the characteristics carry too many or too few Gauss points to an element. We can use this technique in the context of settling velocity in 3D. The forward characteristics are well adapted: while an infinite time step would lead backward characteristics to the free surface where concentrations are virtually 0, forward characteristics would go to the bottom and the Gauss points would release all the mass on the bottom. The loss of monotonicity may not be a problem, as high concentrations will trigger a deposition. Actually the problem is in reality 1-dimensional. The procedure is very simple:

1) take the mass at Gauss points, or even mesh points (with proper weights).

2) move the masses downward, locating the new position in a vertical segment.

3) projecting the mass on the two points of the segment, i.e. sharing the mass between the two points of the vertical segment. This is new, due to forward characteristics.

4) final division by the volumes around points (integral of test functions) to get concentrations. Here inverting a mass-matrix can also be envisaged, but with loss of monotonicity.

VIII. CONCLUSION

The weak form of the method of characteristics shows amazingly good results but is plagued a remaining technical problem of quadrature, which spoils mass conservation, and by the lack of monotonicity. It can however already be used for the advection of velocities because in this case mass conservation and monotonicity are of a lesser importance while artificial diffusion may be hindering, e.g. to get von Karman eddies. In a forward mode, the treatment of settling velocity for suspended sediment is possible without any drawback. The amazing performances on the rotating cone test indicate that, for other advection schemes, there is still a large room for improvement.

REFERENCES

[1] J.-P. Benque, G. Labadie, and J. Ronat, “Une méthode d’éléments finis pour la résolution des équations de Navier-Stokes couplées à une équation thermique” Proceedings of 4th International Symposium on finite element methods for fluid mechanics problems. Tokyo, Japan, July 1982.

[2] T. F. Russell and M.A. Celia, “An overview of research on Eulerian-LAgrangian localized adjoint methods (ELLAM)”. Advances in Water Resources 25. 2002. Pp. 1215-1231

[3] J.-M. Hervouet, “Application of the method of characteristics in their weak formulation to solving two-dimensional advection equations on mesh grids”, Chapter 6 of book “Computational techniques for fluid flow”. Editors C. Taylor, J.A. Johnson, W.R. Smith, Pineridge Press Swansea, UK. 1892, pp.149–185.

[4] Y. Hasbani, E. Livne and M. Bercovier, “Finite elements and characteristics applied to advection-diffusion equations” in Computers and fluids, vol. 11, 1983, pp. 71–83.

[5] G. Dhatt and G. Touzot, “Une présentation de la méthode des éléments finis” 2nd edition. Maloine S.A. Editor. Paris. 1984. 543 pp.

[6] J.-M. Hervouet and C.-T. Pham, “Telemac version 5.7, release notes. Telemac-2D and Telemac-3D” 2007. Available on Website www.opentelemac.org.

TUC 2013, 16-18/10/2013, Karlsruhe - Kopmann, Goll (eds.) - © 2013 Bundesanstalt für Wasserbau ISBN 978-3-939230-07-6

Application and validation of TELEMAC-3D: Case study of flow in Delft U-shaped channel

S. Sinha, D. Borchardt
Helmholtz Centre for Environmental Research-UFZ
Aquatic Ecosystem Analysis and Management Bruckstrasse 3a, 39114 Magdeburg
sumit.sinha@ufz.de

***Abstract*—The multi-fold increase in the available computational resources has led to frequent application of three-dimensional models in the field of environmental hydraulics. These models are routinely based on the numerical solution of three-dimensional Reynolds Average Navier–Stokes equations with or without hydrostatic pressure assumption and usually incorporating Boussinesq approximation. Examples of such commonly available three-dimensional models are, e.g. Princeton Ocean Model (POM), Delft3D, Finite Volume Coastal Ocean Model (FVCOM), Environmental Fluid Dynamics Code (EFDC), MIKE3D and TELEMAC-3D. Although based on the same governing equations, the aforementioned models differ in the numerical technique employed for the solution of the non-linear governing equations. As the number of three-dimensional models increases, there has been an enhanced emphasis on the verification and validation of three-dimensional models (see e.g. Wang et al. (2009)). In this research work systematic application and validation of TELEMAC-3D is carried out for the famous benchmark case of Delft U-shaped channel flow (Figure 1). Measured velocity data along the flow direction, at a number of sections, is freely available at http://www.ncche.olemiss.edu/publishing/. We conducted a comparison between measured and modelled data, including a grid-sensitivity test. Finally, differences between using the hydrostatic and non-hydrostatic version of TELEMAC-3D are compared and discussed.**

I. INTRODUCTION

Significant increase in the computing capacity of desktop as well as cluster computers has made the application of numerical models more and more common. In the field of environmental hydraulics, one dimensional (1D) models based on either integral or differential form of St. Venant's equations are used frequently. HEC-RAS developed by US Army Corp of Engineers, Brunner (2010), is an example of one of the most popular models for conducting hydrodynamic simulation of rivers.

Although the popularity and usefulness of 1D models cannot be ignored, it is a well-known fact that they are based on simplifying assumptions and consequently suffers from some inherent limitation. 1D models are only able to provide information in a section-averaged manner without giving any information about the variation of flow characteristics in transverse and vertical direction. The next level of accuracy in the area of physics based numerical models for flow simulation is obtained by using two dimensional (2D) models. 2D models are based on depth-averaged form of the three dimensional Navier-Stokes equations. 2D models based on different methodologies utilize finite-difference, finite-volume or finite-element technique for the numerical solution of the 2D St. Venant's equations. Some examples are Alcrudo (2004), Kramer & Stelling (2008) and Hervouet (2007) among numerous others.

Although 2D models have been successfully applied to numerous river engineering problems, it is important to reiterate that depth-averaged models do not provide any insights in the vertical direction. For example in the case of curved channels in natural rivers and streams there are distinctive characteristics that are completely three dimensional (3D) in nature and cannot be simulated with a depth-averaged model. In the case of curved channels surface superelevations are observed and flow near the free surface is towards the concave banks and near the bed in the opposite direction. This flow pattern sets up a secondary current which is again usually not captured by the depth-averaged model. Secondary currents cause a unique morphological evolution of the channel cross-section and have a significant bearing on the bank migration of the meandering rivers. There has been increased interest in recent years in numerical simulation of flow through curved channels. In order to capture the physics of flow in a curved channel 3D models are needed. These models are based on the numerical solution of the Navier-Stokes equations again via finite difference, finite volume or finite element methodology. 3D numerical models usually are based on assumption of hydrostatic pressure in the vertical direction. In this research a finite element based 3D model TELEMAC-3D is used for flow simulation in the curved channel. Both a hydrostatic and non-hydrostatic version of TELEMAC-3D is used for the aforementioned simulation.

This research paper is organized as follows; section II describes the experimental setup and model used. In section III simulation results from both the hydrostatic and non-hydrostatic version of the model are presented along with the result from a mesh sensitivity test. Finally the summary and conclusion are provided in section IV.

II. Experimental Setup & Model Used

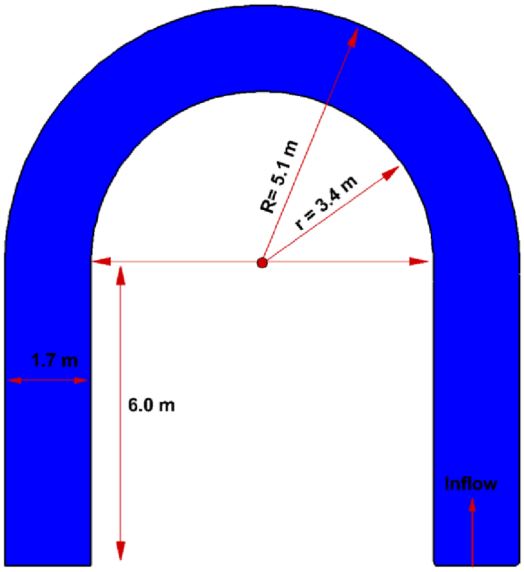

Figure 1. Delft U-shaped flume

A. U-shaped Flume

The configuration of the physical model simulated as a part of this research is shown in Fig.1. This test case is based on the laboratory experiment of De Vriend (1979). The conditions for the simulated flow are presented in Table I. The circular portion of the channel starts at y = 6 m from the origin, which is located at the left hand bottom corner of the channel. An inflow discharge of 0.189 m^3/s is prescribed at the entrance (Fig. 1) and a constant water elevation of 0.18 m is maintained at the other end.

TABLE I. Boundary conditions for flow in U-shaped channel

Bed slope So	Dis. Q(m3/s)	Depth (m)	Width (m)	Len. (m)	Inner rad. (m)	Outer rad. (m)
0.00	0.189	0.18	1.7	25.35	3.4	5.1

B. Model used

In order to examine the evolving flow structure and changing water surface elevation in the U-shaped channel, TELEMAC-3D was used for conducting a series of numerical simulations. TELEMAC-3D solves the 3D Navier-Stokes (NS) equations via a fractional step algorithm, Hervouet (2007). When using TELEMAC-3D, the user is free to choose the hydrostatic or non-hydrostatic version of the code. One of the major advantages of the fractional step algorithm implemented in TELEMAC-3D, is that the most suitable numerical operator can be used for different terms of the NS equations. For example the advective term in the NS equations is resolved using the method of characteristics. The advected velocity field along with diffusion and various source terms in the momentum equations is then used for obtaining further intermediate velocity fields. The third and the final step consists of resolving water depth from the vertical integration of continuity equation, using the intermediate velocity field obtained in the previous step, and including only the pressure term of the momentum equations (TELEMAC-Modelling System 2007). The simulation results presented in this research effort are based on both the hydrostatic and non-hydrostatic version of TELEMAC-3D model. Furthermore a grid sensitivity exercise for both versions of the model is conducted.

III. Simulation Results & Model Parameters

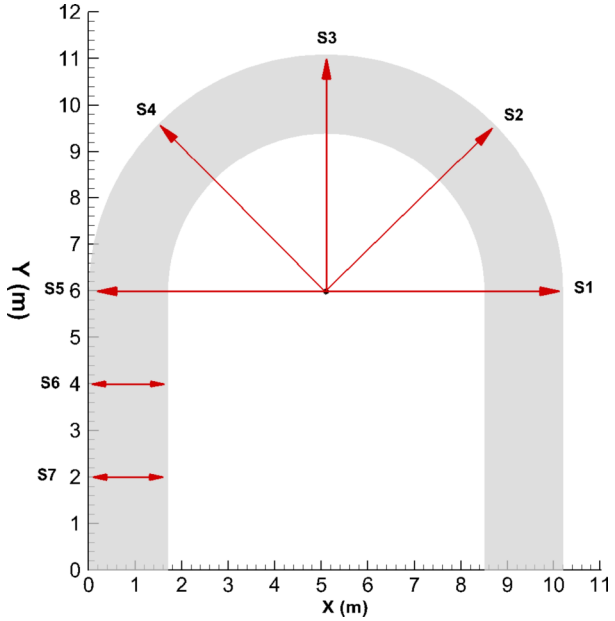

Figure 2. Sections for extracting modelled velocity magnitude

As mentioned in Section II the U-shaped channel simulated here is based on the laboratory experiment of De Vriend. The comparison between measured and modelled velocity magnitude is presented at seven cross-sections, S1 to S7, as shown in Fig. 2. Additionally the variation of water surface elevation along the inner bank, middle of the channel and the outer bank for the aforementioned cross-sections is compared with the measured data once the numerical simulation is converged. The horizontal and vertical position where the water surface elevation and velocity magnitude is compared with the measured data is shown in Fig. 3

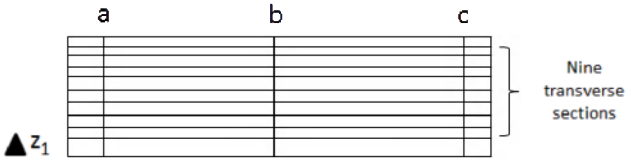

Figure 3. Vertical and horizontal points where modelled data is observed

The simulated water surface elevation at the inner bank is compared with the measured value at point "a" shown in Fig. 3 which lies 0.1 m from the inner bank, at point "b" which is in the middle of the channel and point "c" which is again 0.1 m from the outer bank. Additionally, along points a, b and c (Fig. 3) velocity magnitude is extracted at 9 distinct vertical

points. The bottom most point (Δz_1) is at 0.025 m from the bottom of the channel and succeeding points are evenly placed at a height of 0.020 m from each other.

The computational mesh for the aforementioned simulation was constructed with the help of the gridding software Bluekenue (Bluekenue (2012)). Three different mesh resolutions were used to examine the impact of different grid resolutions on simulation results. Mesh construction started with fifteen nodal points on horizontal inlet and outlet edges, the number of nodal points on inner and outer channel boundary was fifty. Mesh refinement was accomplished by changing the edge length of the triangular elements in the unstructured mesh. The number of nodes and elements in three different meshes used for the simulation is presented in Table II.

TABLE II. MESH RESOLUTION USED FOR THE SIMULATION

Mesh	Edge Length	No. of Nodes	No. of Elemts
I	0.10	1292	2280
II	0.15	2267	4141
III	0.20	4695	9326

In the simulation presented here, the method of characteristics was used for advection. Turbulence closure in vertical and horizontal was accomplished by using the k-ε model. The number of horizontal level used was 21. For the law of bottom friction, option 5 Nikuradse law with friction coefficient value set at 0.0008 was used. The time step used for all the simulations presented here was 0.1 seconds.

A. Comparison between measured and modeled data with TELEMAC-3D hydrostatic version

As mentioned above, the comparison between measured and modelled velocity is carried out at three distinct positions along the transverse direction, (point a, b and c - Fig. 3) and at nine different vertical points. The usage of three dimensional models also provides an insight into the flow structure in the simulated domain.

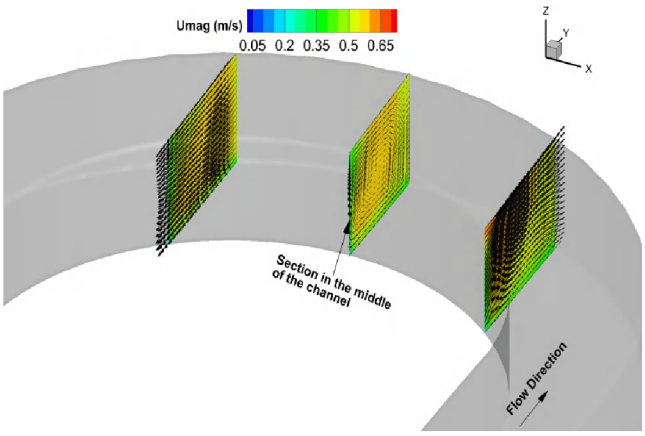

Figure 4. Velocity vectors in sections at the bend of the channel

To that end, the velocity vectors are plotted at sections halfway along the channel, as well as at a distance of 2.1 m more towards the inflow boundary and 2.1 m more towards the outflow boundary of the domain. As shown in Fig. 4 the velocity vectors in the section towards the inflow side are oriented from the inner to the outer bank. As the flow traverses further, the velocity vectors in the section halfway along the channel exhibit a circulatory pattern, flow at the surface is pushed towards the outer bank, whereas at the bottom flow direction is towards the inner bank. Beyond the centre of the channel the flow vectors in the section, shown in Fig. 4, change direction again and are now oriented from outer to inner bank. As regards to free surface elevation the modelled and measured data are compared at the inner bank, centre and the outer bank of the seven sections (Fig. 2).

It can be clearly seen from Fig. 5 and Fig. 6 that successive refinement of the computational mesh brings the simulated surface elevation closer to the observed free surface elevation. The agreement between modelled and measured free surface elevation is better for the centre of the channel and it improves further for the outer bank as shown in Fig. 7. Also worth noting is that the comparison between measured and simulated data is better for the latter sections away from the inflow. This might be attributed to the boundary effect which might be contaminating the solution. As regards to the velocity the for the sake of brevity the comparisons are only presented for sections 2, 3 and 4 and in the centre of the channel.

Although the match between the measured and simulated velocity magnitude is not exact, the model is able to reproduce the trends in the variation of velocity magnitude. The velocity magnitude is less near the bed and increases in logarithmic fashion as the distance from the bed increases (Fig. 8, 9 and 10). It should be mentioned that the velocity magnitude for the purpose of comparison at designated points from the bottom was extracted and interpolated from Tecplot with the help of a post-processing subroutine. This interpolation procedure might contaminate the numerical solution to some extent. The mesh refinement improved the results in all the sections (2, 3 and 4) examined and presented here.

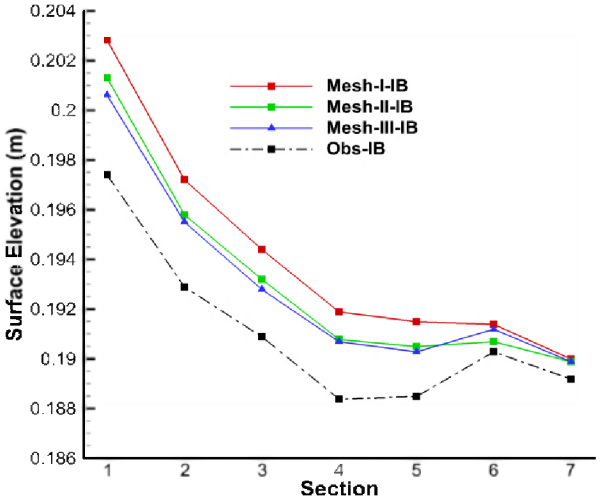

Figure 5. Comparison between simulated and measured free surface elevation at the inner bank (IB) for various mesh resolutions

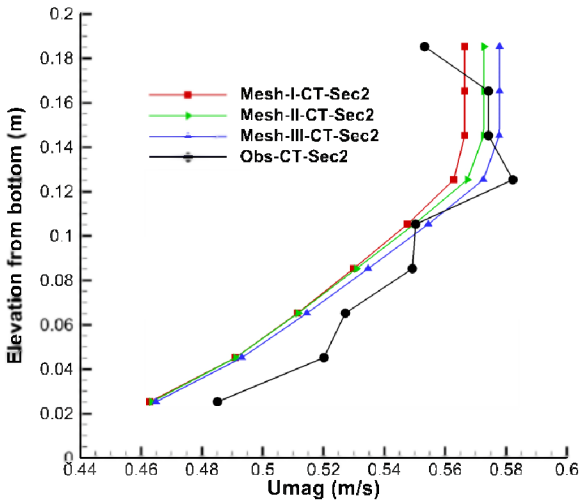

Figure 8. Comparison between simulated and measured velocity magnitude at the centre (CT) of the channel at section 2

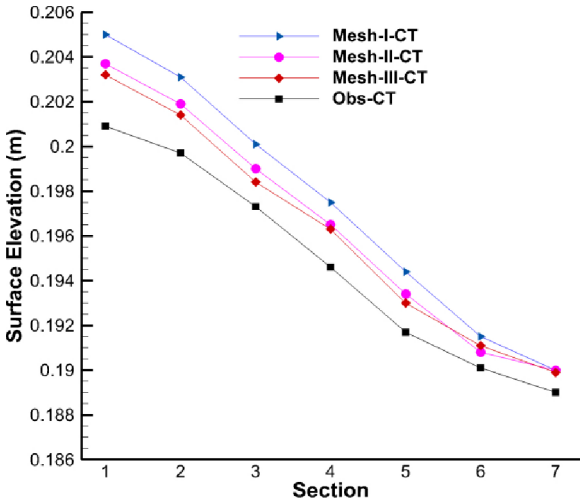

Figure 6. Comparison between simulated and measured free surface elevation at the centre (CT) of the channel for various mesh resolutions

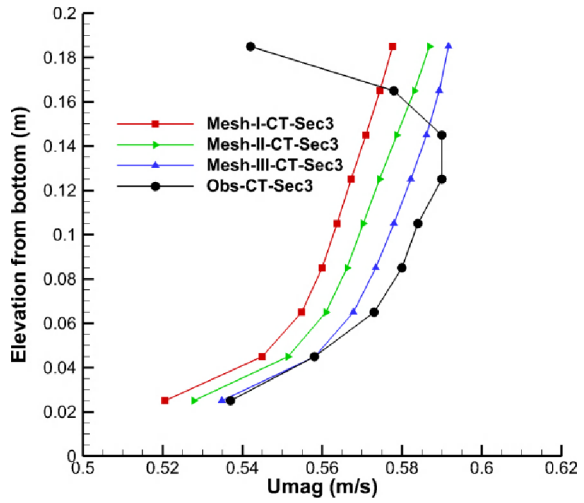

Figure 9. Comparison between simulated and measured velocity magnitude at the centre (CT) of the channel at section 3

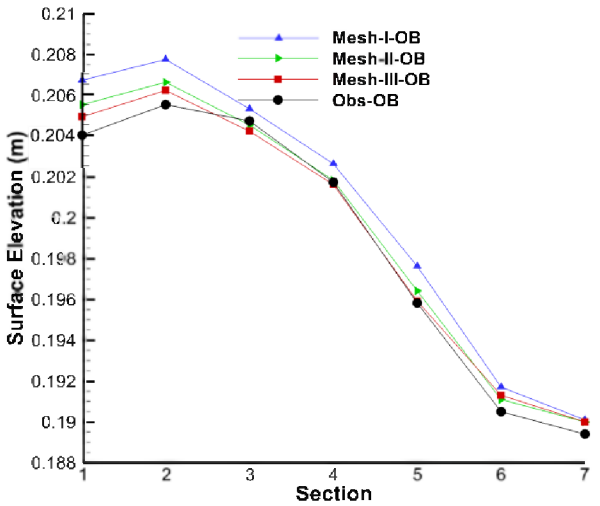

Figure 7. Comparison between simulated and measured free surface elevation at the outer bank (OB) of the channel for various mesh resolutions

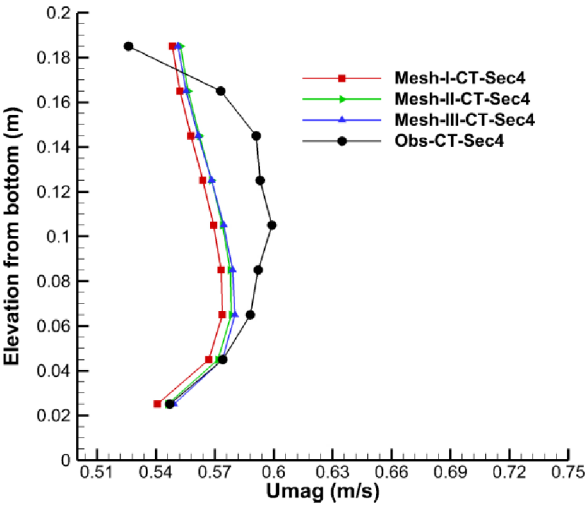

Figure 10. Comparison between simulated and measured velocity magnitude at the centre (CT) of the channel at section 4

B. Comparison between measured and modeled data with TELEMAC-3D nonhydrostatic version

As mentioned in section II, the simulation for the same configuration (U-shaped channel) was also conducted with the non-hydrostatic version of TELEMAC-3D. The free surface elevation and velocity magnitude were extracted at the same points for the purpose of comparison.

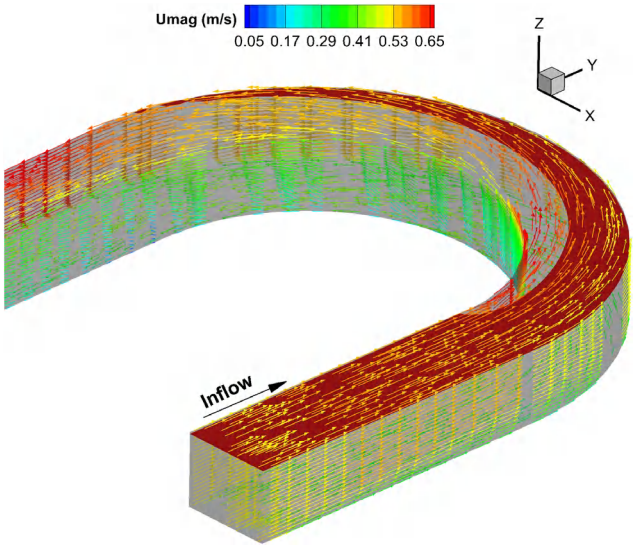

Figure 11. Simulation with non-hydrostatic version of TELEMAC-3D, velocity vectors are coloured with magnitude, also depicted is iso-surface at 0.2 m from the bottom

The simulation conducted with the non-hydrostatic version also reproduces the same flow physics. As shown in Fig. 11, the higher velocity is towards the inner bank of the channel, whereas the higher elevation, also known as super elevation is observed towards the outer bank. The contour plot of free surface, plotted at 0.2 m from the bottom of the bed is shown in Fig. 11. As expected when the flow enters the U-turn the contour of 0.2 m free surface is concentrated towards the outer bend, also commonly known as superelevation. As regards to the comparison of free surface elevation between the modelled and measured data, once again the model was able to reproduce the trends in the variation of free surface elevation. The comparative plot between simulated and measured free surface elevation at the inner bank (IB), centre (CT) and outer bank (OB) for the seven sections examined here (Fig. 2) is presented in Figs. 12, 13 and 14. It is important to point out that in comparison to the hydrostatic version (Figs. 5, 6 and 7) results don't improve significantly. The match between the modelled and measured data is best for the outer bank as shown in Fig. 14. The simulated results almost always improved with mesh refinement and once again the match between modelled and measured surface elevation is better for the latter sections away from the inflow. The same trend was also noticed in simulation conducted with the hydrostatic version of TELEMAC-3D.

As regards to the velocity comparison, the measured and modelled data were compared at the centre of the channel for section 2, 3 and 4. The comparative plots are presented in Figs. 15, 16 and 17; once again the mesh refinement improves the results. Both the hydrostatic and non-hydrostatic version of the model were not able to capture the decrease in the velocity magnitude at the free surface as observed in the measured data. As in the case of the hydrostatic version of the model the velocity magnitude increased in logarithmic fashion away from the channel bed with minimum velocity near the bed and maximum near the free surface. All the simulations presented in this research were conducted with the parallel version of TELEMAC and used 60 processors. The simulation time for the finest mesh was as low as 3 minutes and even lesser for the coarser mesh.

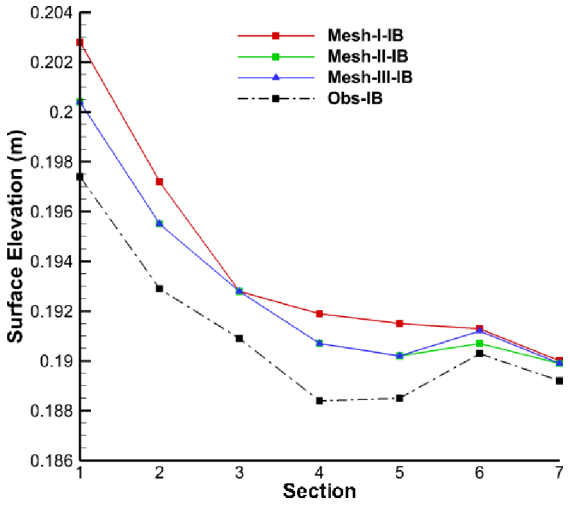

Figure 12. Comparison between simulated and measured free surface elevation at the inner bank (IB) for various mesh resolutions with non-hydrostatic TELEMAC-3D

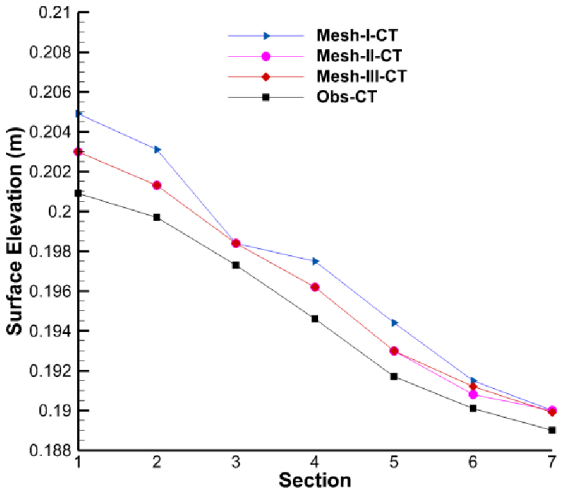

Figure 13. Comparison between simulated and measured free surface elevation at the centre (CT) for various mesh resolutions with non-hydrostatic TELEMAC-3D

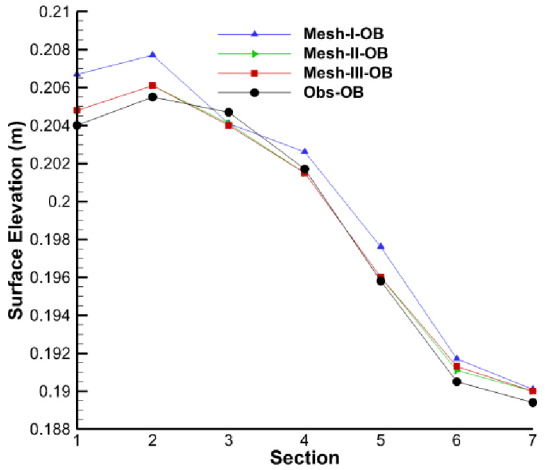

Figure 14. Comparison between simulated and measured free surface elevation at the outer bank (OB) for various mesh resolutions with non-hydrostatic TELEMAC-3D

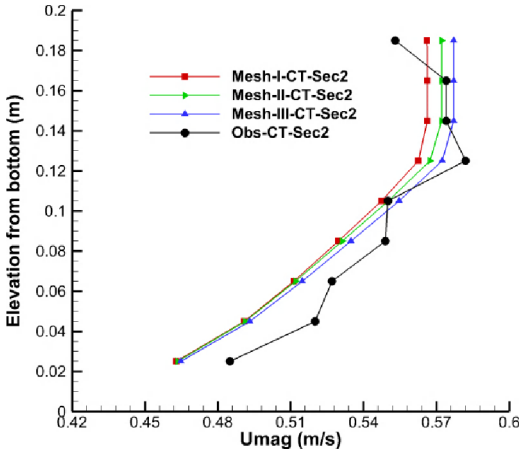

Figure 15. Comparison between simulated and measured velocity magnitude at the centre (CT) of the channel at section 2 with non-hydrostatic TELEMAC-3D

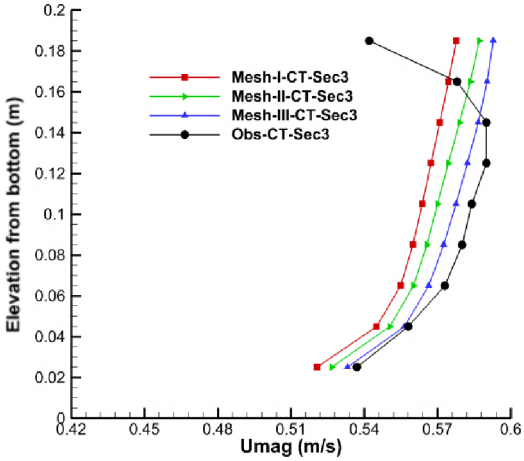

Figure 16. Comparison between simulated and measured velocity magnitude at the centre (CT) of the channel at section 3 with non-hydrostatic TELEMAC-3D

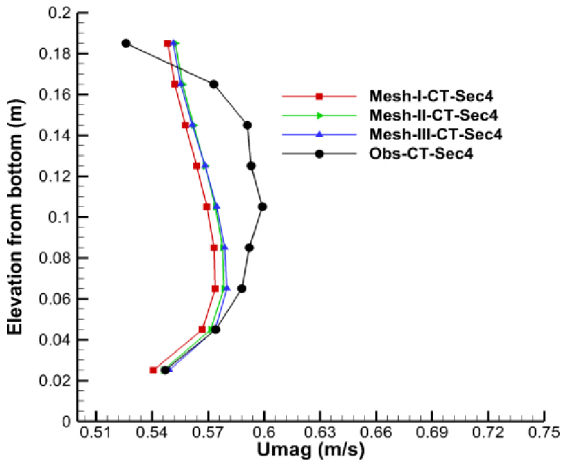

Figure 17. Comparison between simulated and measured velocity magnitude at the centre (CT) of the channel at section 4 with non-hydrostatic TELEMAC-3D

IV. SUMMARY & CONCLUSION

Three dimensional hydrostatic and non-hydrostatic simulations of the flow in a U-shaped channel were conducted using TELEMAC-3D. Both the free surface elevation and velocity magnitude were compared against the measured data. The finest mesh with 4695 nodes and 9326 elements showed the best match with the measured data for both the hydrostatic and non-hydrostatic version of TELEMAC-3D. Although the model is able to capture the qualitative trend of the hydrodynamics simulated, some key features like reduced velocity at the free surface and the free surface elevation at the inner bank could be improved further.

ACKNOWLEDGEMENT

The author would like to extend his gratitude towards the cluster team of Helmholtz Centre for Environmental Research (UFZ), Leipzig, Germany for their help compiling and porting the code. Dr. Talia E. Tokyay is also acknowledged for her help with post-processing of the simulation result.

REFERENCES

[1] Bluekenue, "Visualization and Analysis for Hydraulic Modeling", Canadian Hydraulics Centre/National Research Council. EnSimCore Version 3.3.25, 2012.

[2] D. J. De Vriend, "Flow measurements in a Curved Rectangular Channel", Laboratory of Fluid Mechanics, Department of Civil Engineering, Delft University of Technology, Internal Report No. 9-79, 1979.

[3] F. Alcrudo, "A state of review on mathematical modeling of flood propogation", IMPACT project.

[4] G. W. Brunner, "HEC-RAS River Analysis System Hydraulic Reference Manual (Version 4.1)", US Army Corp of Engineers, Hydrologic Engineering Center (HEC), Davis California, USA, 2010.

[5] J. M. Hervouet, "Hydrodynamics of free surface flows- Modelling with finite element method", John Wiley & Sons 341 pp ISBN 978-0-470- 03558-0, 2007.

[6] S.C. Kramer, G. S. Stelling, " A conservative unstructured scheme for rapidly varied flows", International Journal for Numerical Methods in Fluids, 58 (2), 183-212, 2008.

[7] "Telemac Modelling System – TELEMAC-3D CODE OPERATING MANUAL", December 2007.

[8] S. S. Y. Wang, P. J. Roache, "Verification and validation of 3D free-surface flow models", ASCE publication 2009.

TUC 2013, 16-18/10/2013, Karlsruhe - Kopmann, Goll (eds.) - © 2013 Bundesanstalt für Wasserbau ISBN 978-3-939230-07-6

Influence of numerical schemes in representing flow over and around groynes

M. Baron
Ingenieurbüro Baron
Vorholzstr. 50
76137 Karlsruhe, Germany
manuela.baron@web.de

R. Patzwahl
Department of Hydraulic Engineering, Section W2
Federal Waterways Engineering and Research Institute
76187 Karlsruhe, Germany
regina.patzwahl@baw.de

***Abstract*—Assessing the influence of small geometry changes in trained rivers is becoming a more and more common task at the Federal Waterways Engineering and Research Institute (BAW). In order to validate the impact on water levels and velocity distribution of such modifications, a flume and a detailed measuring program in 2D and 3D was set up. The resulting dataset was applied to validate the numerical models in use at BAW. In this paper, the results from TELEMAC-3D 6.1 are presented. The study shows that horizontal flow in a emerged groyne field in a numerical model is mostly influenced by the advection scheme properties, whereas good representation of the vertical eddy behind submerged groynes essentially needs an appropriate turbulence model.**

I. INTRODUCTION

German waterways are maintained according to river training concepts. Within these inter-regional concepts, presently rather minor modifications in training structures (e.g. re-emptying of silted groyne fields) become more and more frequent. These changes aim at either improvement of navigational and/or ecological conditions. In order to get a reliable assessment of quality and quantity of the impact of such small changes, a flume test was set up and a detailed measuring campaign covered relevant aspects [1]. This flume dataset was then applied to assess the quality of prediction of the numerical models in 2D and 3D, which are in use at BAW as standard modelling tools. A comprehensive data set resulted from this study. In this paper we will focus on certain aspects of numerical modelling of emerged and submerged training structures and on the results from 3D-modelling with TELEMAC-3D 6.1.

II. THE REFERENCE DATA SET

The flume has an experimental length of 62 m and is 2.5 m wide. The slope is realized by inserting a non-movable gravel bed at a targeted grade. The following measuring techniques were used: magnetic inductive discharge measuring device to guarantee a reproducible discharge (MID), ultrasonic measuring devices for perpetual recording of water levels during experiment, 3D-photogrammetric camera-systems [2], 3D-particle tracking (PTV) for extensive measurements of surface flow velocities and water levels, correlation measurements: extensive measurements of bottom and training structure topography; magnetic inductive sensor for point measurements (P-EMS [3]) of flow velocities in two spatial directions (bottom near to surface near) and acoustic Doppler velocimeter (ADV) for point measurements of flow velocities in three spatial directions.

The following variants are investigated so far:

- V00: Flume with graded gravel bed, no training structures inserted.
- V01: Flume trained at full length with 40 schematized groynes (0.08 m height, 1.20 m long, placed at 1.50 m distance to each other).
- V02: Partial variation of trained flume within the groyne assembly: embankment of 12 m length.

Discharges (water depths respectively) which result in emerged, slightly submerged and fully submerged groynes (Tab I) are taken into this investigation.

TABLE I. LIST OF MEASURED DISCHARGES AND WATER-DEPTH

	Discharge [l/s]		
Water depth H [m]	***V00***	***V01***	
0.07	42	21	Emerged
0.12	100	56	Slightly submerged
0.16	157.8	92	Fully emerged

III. THE NUMERICAL MODEL BASED ON TELEMAC-3D 6.1

Tab. II summarizes the key data for the numerical model. The two-dimensional base grid of TELEMAC-3D was set up as unstructured triangular grid. In vertical sigma-layering with a logarithmic distribution was applied.

TABLE II. MODEL DESCRIPTION

Parameter	
Number of nodes	approx. 54000
Number of elements	approx. 106000
Min. / Max. length of edges	0.05/ 0.1 m
Min. /Max. height of vertical planes	0.002/ 0.005 m
Time step	0.1 s
Number of time steps / Duration	120000 / 33,3 h

The numerical modelling included the investigation of several combinations of advection schemes and turbulence models available in TELEMAC-3D [4]. A combination of constant horizontal viscosity and Prandtl mixing length PML approach or a full three-dimensional k-ϵ-model was applied. For the advection stage characteristics or MURD-scheme are taken [4].

A. Calibration

In the calibration process measured water levels, horizontal near-wall velocities and several vertical velocity profiles were compared to computational results. During this process an optimal equivalent sand roughness k_s after Nikuradse could be found for variant V00 valid for all discharges. The agreement between measurement and computational results are quite satisfying and could be validated with measurements from other variants [1].

A dependency of the roughness parameter on the turbulence model can be noted. For PML a lower k_s-value is needed than for a k-ϵ-model to reach the same water level. The vertical velocity profile using PML showed good agreement with the measured profile whereas the vertical velocity profile from computations with k-ϵ-model showed too low velocity in the lower half and, in consequence, too high velocities in the upper half of the vertical profile. Accordingly, the vertical profile of computed viscosity for the k-ϵ-model is not parabolic.

Interestingly, the lateral non-dimensional wall-friction parameter AUBOR [5] also played an important role in the calibration process due to interdependencies of the wall-friction with advection scheme and turbulence model.

B. Scaling effects

Systematic reference data sets at real scale are difficult and very expensive to obtain. Therefore numerical modelling at laboratory scale is a possibility for validation. In order to investigate scaling effects, tests with an up-scaled numerical model (length scaling factor L*50) were performed. The results from the real-scale model were down-scaled (velocity scaling factor v/7.071)

Fig. 1 shows the results of the numerical model for flume -scale (top), for real-scale model (bottom) and the down-scaled results from the real-scale model (middle). Comparing the results between directly flume-scale calculated (top) and down-scaled real-scale (middle) the computations show minor differences in velocity distribution at the leeside of the groyne as well as above the groyne crest. Nonetheless, the small differences in the obtained results legitimate the approach of numerical modelling at laboratory scale and formulating conclusions for the real scale.

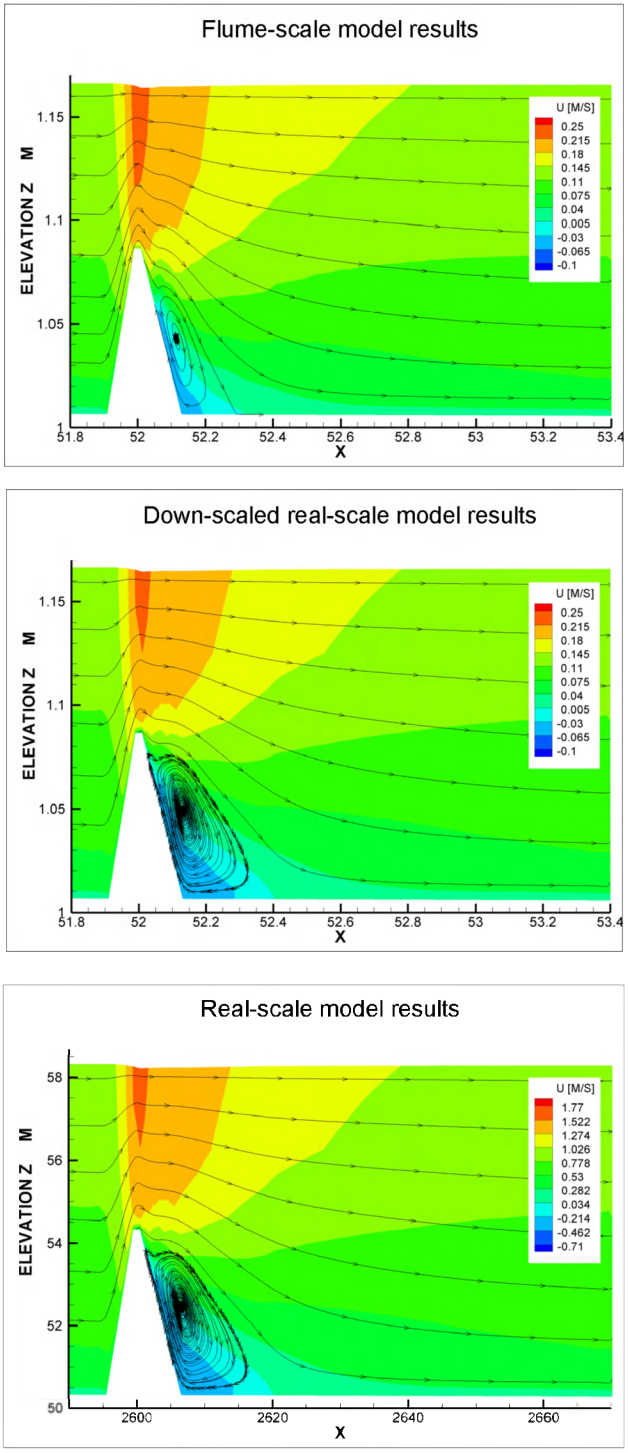

Figure 1. Scaling effects in the longitudinal distribution of computed velocities over groynes (TELEMAC-3D 6.1 simulation of V01)

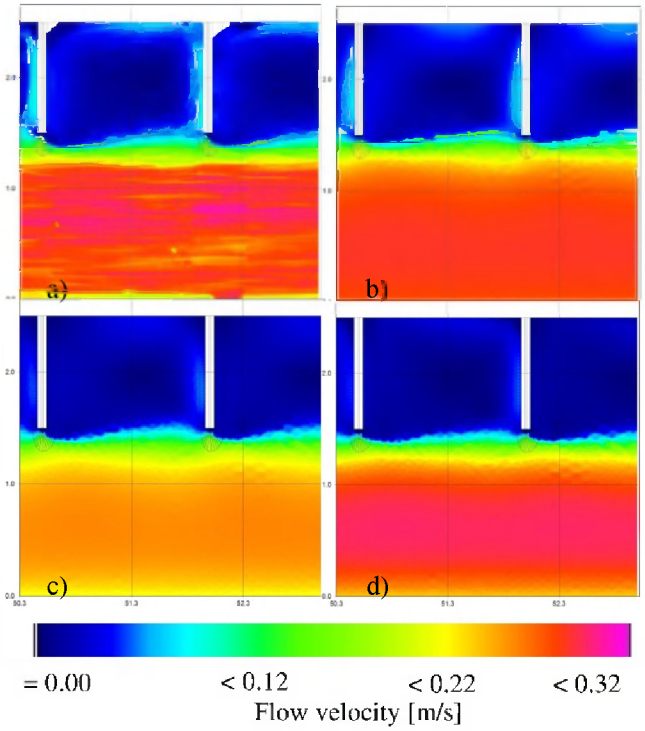

Figure 2. Measured (3D-PTV) and computed surface flow velocities in the main channel and groyne field for different types of advection schemes and turbulence models. a) Laboratory measurements, b) MURD-scheme and k-ϵ-model, c) characteristics and PML and d) characteristics and k-ϵ-model

IV. HORIZONTAL FLOW IN EMERGED GROYNE FIELDS – A PROCESS MOSTLY INFLUENCED BY THE ADVECTION SCHEME

Knowing the influence of groynes on the water level is the key importance to river engineering. However, when it comes to estimating sediment transport into and out from a groyne field it is also important to get a correct distribution of flow velocities between main channel and groyne field as well as in the groyne field itself. For this purpose surface velocities were measured in the flume for the case of emerged groynes (H=0.07 m). Fig. 2 shows the measured data set as well as results from various numerical simulations in the main channel and the groyne field. The flow is predominantly horizontal. A well expressed groyne field eddy rotating on the outer edge at approximately 1/3 of the speed of the main channel is clearly visible (Fig. 2). A closer look at groyne field flow can be taken in Fig. 3. The apparently large differences in surface velocities in the main channel (Fig. 2c and Fig. 2b and d) result from differences in the computed vertical velocity profiles, as already mentioned in chapter III A. The k-ϵ-model leads to lower velocities near the bottom and thus, higher velocities near the surface compared to the measured vertical distribution.

The advection scheme based on the concept of characteristics seems to suppress the transport of momentum into the groyne field (Fig. 2c) and Fig. 3d). The MURD-scheme gives better agreement with the measured flow field (Fig. 3c) and supplies a good basis for the k-ϵ-turbulence model (Fig. 3b) to further improve the results.

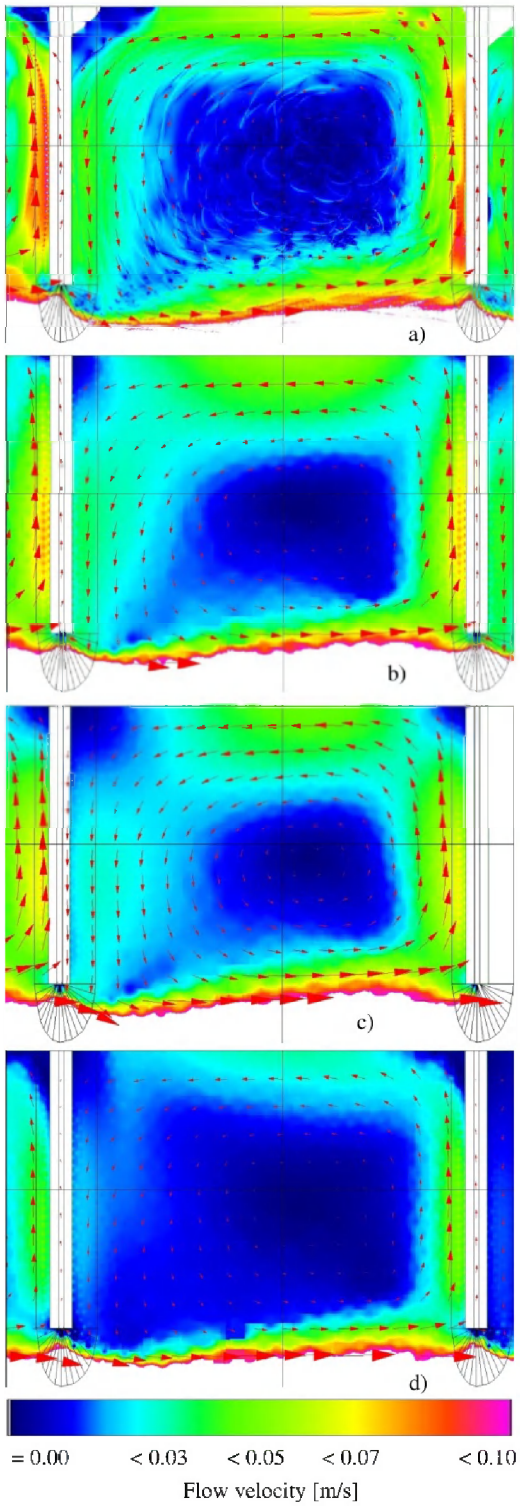

Figure 3. Surface velocities in a groyne field in detail. a): Laboratory measurements, b) MURD-scheme and k-ϵ-model, c) MURD-scheme and PML and d) characteristics and PML

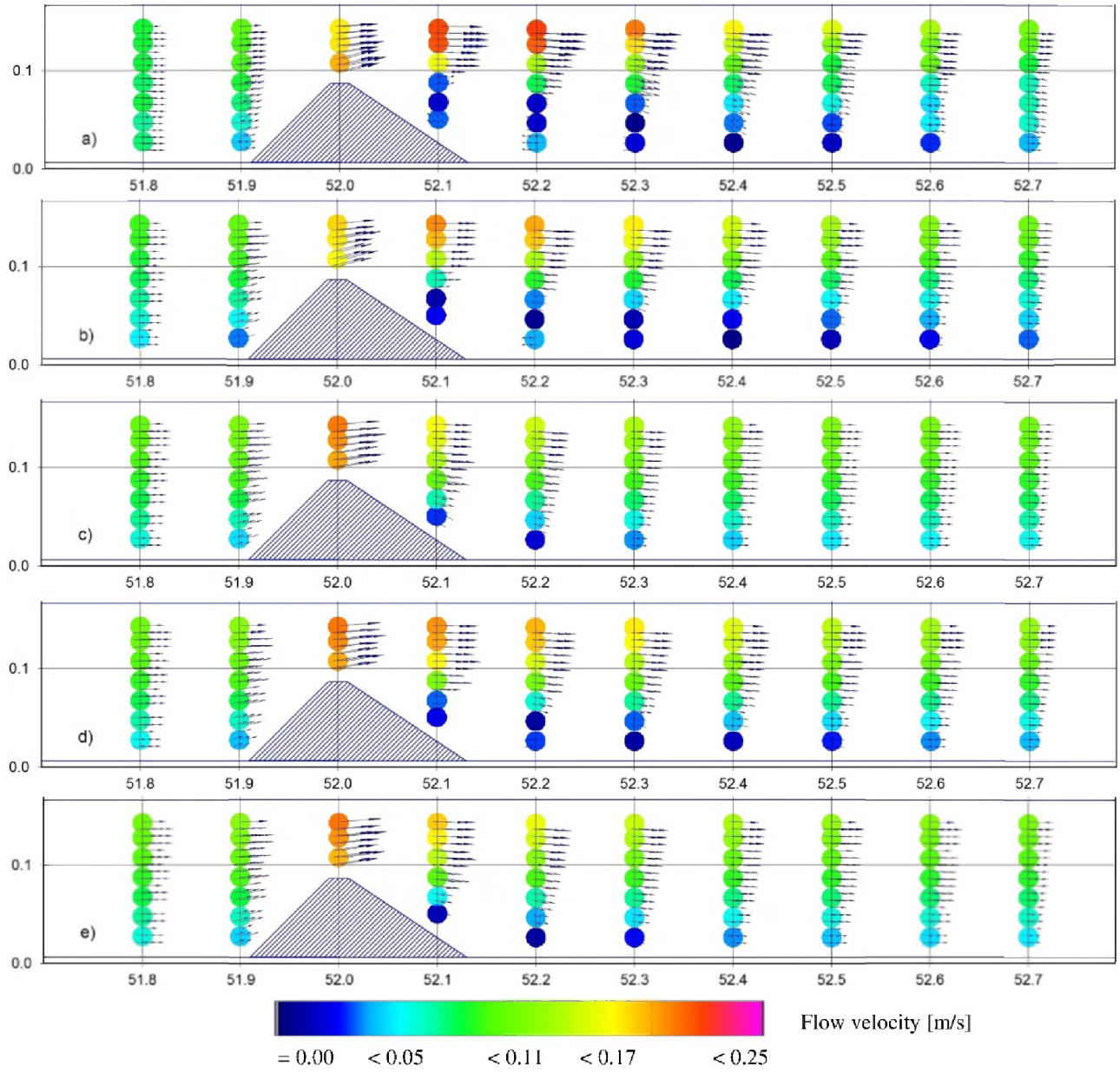

Figure 4. Flow over a groyne presented in a vertical section. a): Laboratory measurements (side looking vectrino), others: TELEMAC-3D 6.1 b) MURD-scheme and k-ε-model, c) MURD-scheme and PML, d) Characteristics and k-ε-model and e) Characteristics and PML

V. FLOW OVER SUBMERGED GROYNES – A PROCESS MOSTLY INFLUENCED BY THE TURBULENCE MODEL

Even more challenging than groyne field flow is modelling the flow field behind submerged groynes. When the groyne is submerged, a vertical eddy develops right downstream the groyne. A longitudinal transect of vertical velocity profiles, crossing a groyne were measured (H=0.16 m). It shows a vertical recirculation zone lee side of the groyne, which extends almost to the mid of the groyne field (Fig. 4). Above the groyne the dataset shows higher velocities closer to the crest than to the surface and the highest velocities were measured directly downstream the groyne ridge near the surface. First of all, non-hydrostatic computations are necessary in order to not only get the right change in water-levels but also in order to allow the vertical recirculation as a low pressure field has to develop right behind the groyne as trigger to it.

The computations using the k-ϵ-model (both characteristics and MURD scheme) show the recirculation zone at a shorter extension into the groyne field and flow velocities are slightly too low. Besides, no inversion of velocity distribution over the groyne ridge can be found. Using the characteristics scheme, the velocity distribution above and lee side of the groyne does not fit the measured pattern very well: highest velocities are found above the groyne and not directly downstream. With the MURD scheme the results are more satisfying. Apparently, the highest velocities were computed right downstream the groyne. The velocity distribution above the groyne crest observed in the experiments can also be found. On the other hand, the MURD scheme underestimates the velocities at the upstream foot of the groyne probably leading to too low velocities on top of the groyne.

VI. CONCLUSIONS

The advection scheme has a dominant influence on the horizontal flow pattern developing in emerged groyne fields. A two-equation turbulence model like a k-ϵ-model can improve the representation of the shear zone and turbulent energy transport. In the submerged case, the numerical simulation of the vertical recirculation zone is mainly governed by the turbulence model. Again k-ϵ-model can be an adequate tool for modelling this situation. The advection scheme can lead to further improved reproduction of the overall measured flow field. The combination of MURD-scheme and k-ϵ-model gave agreeable results for both submerged and emerged groynes. It seems to be an adequate choice for 3D-modelling of groyne field flows with TELEMAC-3D 6.1.

ACKNOWLEDGEMENT

We thank the BAW Hydraulic Laboratory Team of W2 for providing us with a carefully prepared and valuable data set. We also would like to thank our colleagues Jacek A. Jankowski and Frank W. Platzek for discussion and support.

REFERENCES

[1] Th. Hüsener, P. Faulhaber und M. Baron, „Modifikationen in bestehenden Stromregelungssystemen an Wasserstraßen“, Proceedings, Wasserbausymposium 2012 TU Munich, ETH Zürich and TU Graz, 12.-15.09.2012, Graz, Austria

[2] Henning, M.; Sahrhage V.; Hentschel, B. (2007). 3D-PTV- Ein System zur optischen Vermessung von Wasserspiegellagen und Fließgeschwindigkeiten in physikalischen Modellen. Mitteilungsblatt, Bundesanstalt für Wasserbau, Nr. 90

[3] WL delft hydraulics (2001). P-EMS programmable electromagnetic liquid velocity meter, Users Manual

[4] J.-M. Hervouet (2007), Hydrodynamics of free surface flows: modelling with the finite element method. Chichester: Wiley, Formerly CP

[5] www.opentelemac.org, TELEMAC-3D Manual

TUC 2013, 16-18/10/2013, Karlsruhe - Kopmann, Goll (eds.) - © 2013 Bundesanstalt für Wasserbau ISBN 978-3-939230-07-6

A Variational Data Assimilation Algorithm to Estimate Salinity in the Berre Lagoon with TELEMAC-3D

S. Ricci, A. Piacentini, A.T. Weaver
Sciences de l'Univers au CERFACS, URA1875
Toulouse, France
ricci@cerfacs.fr

R. Ata, N. Goutal
Laboratoire national d'Hydraulique et d'Environnement
Chatou, France
riad.ata@edf.fr

***Abstract*—Variational assimilation of in-situ data for the description of the salinity field in the Berre lagoon is explored. The Berre lagoon is a receptacle of 1000 Mm^3 where salty water from the Mediterranean Sea meets fresh water discharged by the hydroelectric plant at Saint-Chamas and by natural tributaries. Its dynamics are represented by a 3D hydraulic model that simulates the mean tracer and current fields. This simulation should be further improved to allow for the optimization of the operation of the hydroelectric production while preserving the lagoon ecosystem. A 3D-Var FGAT data assimilation algorithm is used to correct the initial salinity state over a 1-hour time window assimilating observations at three fixed buoys each equipped with 5 XBT sensors in the vertical every 15 minutes. The minimization is performed in a space spanned by vectors of the size of the observation vector in order to reduce both memory usage and computational cost. The background error covariance matrix for salinity is modelled using a diffusion operator. The sequential correction of the salinity state improves the representation of the strongly stratified salinity field over the assimilation window as well as in the short-term forecast. The sensitivity of the assimilation to the background error horizontal and vertical length scale was investigated in single observation experiments as well as in a real case study.**

I. INTRODUCTION

The Berre lagoon is a receptacle of 1000 Mm^3 where salty water from the Mediterranean Sea, through the Canal de Caronte, meets fresh water discharged by the hydroelectric plant at Saint-Chamas and by natural tributaries (Arc and Touloubre rivers). The Laboratoire National d'Hydraulique et d'Environnement (LNHE) aims at optimizing the operation of the hydroelectric production while preserving the lagoon ecosystem. To achieve this objective, improving the quality of the simulation and more specifically the description of the salinity state is essential. The hydrodynamics of the lagoon is modelled with a 3D resolution of the shallow water equations using the TELEMAC-3D (T3D) software developed by Electricité De France (EDF R&D) coupled with the water quality model DELWAQ developed by DELTARES. The proper representation of the stratified salinity and temperature fields as well as the 3D currents was identified as a valuable research objective with direct applications for both electricity production and ecological matters. These fields drive the time of residency for the water masses in the lagoon and thus the phytoplantonic bloom. Indeed, the haline stratification is intensified by the inflow of the salty waters from the Mediterranean Sea and of the fresh waters from the hydroelectric power plant. The deep waters are thus anoxied and the nutriments are trapped in the deep waters of the lagoon. When the wind blows, mixing occurs, the entire water column is oxygenized and the nutriments are consumed by the phytoplancton. Three fixed buoys in the lagoon and one in the Canal de Caronte are equipped with five XBT (eXpendable BathyThermograph) sensors along the vertical that measure the temperature and salinity every 15 minutes. These data are gathered by the GIPREB (Groupement d'Intérêt Public pour la Réhabilitation de l'étang de Berre) and allow, since 2005, the European Comission to ensure that France is applying the decree issued in 1987 to protect the Mediterranean waters against pollution.

Preliminary studies on the calibrated 11 vertical plan T3D model [1] were carried out to quantify the difference between a reference simulation and the observations on a test period. Most uncertainty comes from the maritime, fluvial and meteorological boundary conditions. More specifically the fresh water input from the Touloubre and the Arc influents is under-estimated, some fresh water inputs from minor influents are neglected and the evapotranspiration is over-estimated. The temporal variability of these errors in fresh water inputs was partly corrected by adding an artificial input at Caronte ranging from 3.5 to 15 m^3s^{-1}. With this correction, the lagoon mean salinity drift was reduced by 30% over September-December 2006. Still, the temporal intra- and inter-annual variability of this artificial correction is difficult to estimate and the hydraulics state simulated by the model remains imperfect: the currents tend to be under-estimated and the difference between the simulated salinity and the observations can reach up to several g/l. These uncertainties could be corrected with a data assimilation (DA) algorithm.

Significant advances have been made in recent years in hydraulic DA for water level and discharge prediction [2], as well as for parameter estimation [3], using in-situ as well as

remote sensing data [4]. Recent studies have showed the benefits that hydrology and hydraulics can draw from the progress of DA approaches using either variational methods [5], particle filtering [6], Extended Kalman Filter [7], Ensemble Kalman filter for state updating [8], or for dual state-parameter estimation [9]. Some studies are formulated in an operational setting and demonstrate the performance gained from DA for operational flood and inondation forecasting [10,11,12]. DA offers a convenient framework for integrating observations into a numerical model in order to provide optimal estimates of poorly known parameters and simulated model states and thus, to improve predictions. The key idea is that, when used alone, neither measurements nor numerical models can provide a reliable and complete description of the real state of the physical system. While the merits of DA have been largely demonstrated in the global and coastal ocean fields [13,14] they are yet to be fully taken advantage of in lakes and lagoon hydrodynamical modelling systems.

In this paper, a collaborative work between LNHE and CERFACS (Centre Européen de Recherche et de Formation Avancée en Calcul Scientifique) is described to develop a DA algorithm for T3D that exploits the continuous in-situ salinity measurements at three locations in the Berre lagoon. Similarly to the meteorological and oceanographic approaches [15], the observations are used sequentially to update the hydrodynamic state. More specifically, a 3D-Var FGAT algorithm presented in Section 2, is used to correct the salinity state at the beginning of an assimilation window (or cycle) over which several observations are available. This incremental variational assimilation algorithm relies on the hypothesis that corrections to the model state are approximately constant over a chosen time window. Sensitivity experiments show that in order to cope with this constraint, the analysis time window should be at most 3h. With the current T3D Berre model, as the number of observations over an assimilation window is significantly smaller than the size of the model state vector (less than 100 observations compared to approximately 70000 cells), the minimization is performed in a space spanned by vectors of the size of the observation vector. This allows us to reduce significantly both memory usage and computational cost [16]. The background error covariance matrix for salinity is modelled using a diffusion operator [17]. Preliminary results from the 3D-Var FGAT system are presented in Section 3. The sequential correction of the salinity state improves the representation of the strongly stratified salinity field over the assimilation window as well as in the short-term forecast. The sensitivity to the horizontal and vertical length scale was investigated in single observation experiments as well as in a real case study.

II. VARIATIONAL DATA ASSIMILATION ALGORITHM

3D-Var FGAT (3D variational method with First Guess at Appropriate Time) can be derived as a simplification of 4D-Var in which the temporal dependence of the analysis is neglected. The 4D-Var algorithm formulates the difference between the numerical model outputs and the observations over the assimilation window $[t_0,t_T]$ as a function of the initial state of the system $\mathbf{x}=\mathbf{x}(t_0)$, called the control vector (n-dimensional). This cost function is regularized by a background term that penalizes the distance to the background state $\mathbf{x}^b$ which is the model estimate of this initial condition (prior to the assimilation). The statistics of its errors are described by the background error covariance matrix **B**. The observation vector $\mathbf{y}^o$ is a vector of size N that gathers the observations available in space and time over the assimilation window. The statistics of its errors are described by the observations error covariance matrix **R** (assumed to be diagonal in the following). The inverse of the background and observation covariance error matrices define the weighting matrices of the quadratic terms in the cost function

$$J(\mathbf{x})=\frac{1}{2}(\mathbf{x}-\mathbf{x}^b)^T\mathbf{B}^{-1}(\mathbf{x}-\mathbf{x}^b)+\frac{1}{2}(G(\mathbf{x})-\mathbf{y}^o)^T\mathbf{R}^{-1}(G(\mathbf{x})-\mathbf{y}^o). \quad (1)$$

In order to compute the model equivalent of the observation vector, the initial state **x** is propagated over the assimilation window by the dynamical model $M_{t0,tT}$, then mapped to the observation space using the observation operator H. The composition of H and $M_{t0,tT}$ is the generalized observation operator denoted by G; it is non linear as the dynamical model is non linear with respect to the control vector. The initial state that minimizes the cost function is called the analysis $\mathbf{x}^a$. It can be integrated forward in time to produce a forecast beyond the assimilation time window.

The minimization of the non-quadratic cost function J is usually achieved as a sequence of minimizations of approximated quadratic functions where a local linearization of the generalized observation operator is used. This is the incremental formulation that aims at identifying a correction $\delta\mathbf{x}$ to the background state such that $\mathbf{x}^a = \mathbf{x}^b + \delta\mathbf{x}^a$. The generalized observation operator is linearized around a reference state, usually chosen as the background, that requires the formulation of the tangent-linear $\mathbf{M}_{t0,tT}$ and **H** of the nonlinear model $M_{t0,tT}$ and of the observation operator H with respect to **x** so that

$$\mathbf{G}(\mathbf{x})=\mathbf{H}\,\mathbf{M}_{t0,tT}. \quad (2)$$

The incremental cost function J_{inc} reads:

$$J_{inc}(\delta\mathbf{x})=\frac{1}{2}\delta\mathbf{x}^T\mathbf{B}^{-1}\delta\mathbf{x}+\frac{1}{2}(\mathbf{G}\delta\mathbf{x}-\mathbf{d})^T\mathbf{R}^{-1}(\mathbf{G}\delta\mathbf{x}-\mathbf{d}) \quad (3)$$

where **d** is the innovation vector that denotes the difference between the observation vector and the background trajectory integrated from the background state with $M_{t0,tT}$. The 3D-Var FGAT algorithm lies on the hypothesis that the tangent-linear $\mathbf{M}_{t0,tT}$ can be approximated by the identity matrix, meaning that the dynamics of a perturbation to the state vector is represented by a persistence model. The first reason for choosing this approach is that, as of today, the tangent-linear model of T3D with respect to the initial state is not yet available. The second reason is that the cost of the 3D-Var FGAT is much smaller than that of the 4D-Var while still providing

satisfying results (for instance in the fields of meteo and ocean) when the **B** is properly described.

The exact solution of (3) is obtained by setting the gradient of J_{inc} to zero, which yields [18]

$$\delta \mathbf{x}^{a} = (\mathbf{B}^{-1} + \mathbf{G}^{T}\mathbf{R}^{-1}\mathbf{G})^{-1}\mathbf{G}^{T}\mathbf{R}^{-1}\mathbf{d} \quad (4)$$

Since the matrices in (4) are large and only available in operator form (i.e., as a matrix-vector product), an approximate solution is usually found by iteratively solving a linear system. The minimization of J_{inc} can either be solved in the primal space spanned by vectors of the size of the model control vector, or, using the Sherman-Morrison-Woodbury formula [19], in the dual space spanned by vectors of the size of the observation vector. The dual approach is advantageous in the present study since the size of observation space is significantly smaller than the size of the control vector. The analysis in the dual formulation reads

$$\delta \mathbf{x}^{a} = \mathbf{B}\mathbf{G}^{T}(\mathbf{G}\mathbf{B}\mathbf{G}^{T} + \mathbf{R})^{-1}\mathbf{d} \quad (5)$$

which is solved iteratively with a conjugate gradient method applied to the N*N linear system

$$(\mathbf{G}\mathbf{B}\mathbf{G}^{T} + \mathbf{R})\lambda = \mathbf{d} \quad \text{and} \quad \delta \mathbf{x} = \mathbf{B}\mathbf{G}^{T}\lambda \quad (7)$$

This linear system can be preconditioned by $\mathbf{R}^{-1}$ in order to accelerate the convergence. The algorithm is known as PSAS [20]. A prohibitively large number of iterations may be required to obtain an acceptable solution with PSAS. [21] proposed an alternative way to solve this problem while ensuring that during the minimization process the current iterate is the same as the one found when minimizing in the primal space with a conjugate gradient algorithm preconditioned by **B**. The details and the implementation of this algorithm called RBCG are given in [16].

The **B** operator is described by the integral equation

$$B(\zeta(\mathbf{z})) = \int B(\mathbf{z},\mathbf{z}')\,\zeta(\mathbf{z}')\,d\mathbf{z}' \quad (8)$$

with $\mathbf{z}=(z_1, z_2, z_3)$ representing the spatial directions and $B(\mathbf{z},\mathbf{z}')$ the covariance function for any variable $\zeta(\mathbf{z})$. The modelling of the covariances is usually separated into two operators: one for the variance and one for the correlations. The correlation operator is modelled using an implicitly formulated 3D diffusion equation. This method and its implementation with an implicit scheme are presented in [22]. In the present framework, the correlation functions are described applying the diffusion operator with different diffusion coefficents in the vertical and horizontal directions that relate to the vertical and horizontal correlation length scales. Ad-hoc estimates (isotropic and homogeneous) for these length-scales are used here but objective estimates should be further investigated with an ensemble approach.

III. RESULTS

A. *Single observation validation experiment*

In order to validate the 3D-Var FGAT algorithm, a single observation is assimilated at the closest grid point to SA1 (point A), at -5m deep for January 1st 2008 with a diagonal **B** matrix. Here, the DA procedure comes down to computing a weighted average where the background and observation weights are given by the background and observation error variances. When these are both arbitrarily set to 0.25 psu^2, and given that the observed salinity is equal to 26.434100 psu while the simulated salinity is 26.6386 psu, the analysis increment given by the RBCG (Restricted B-preconditioned Conjugate Gradient) minimization is $\delta\mathbf{x}$ =-0.1022501 psu, which is, as expected half of the BmO (Background Minus Observation computed for salinity) value. It should be noted that the RBCG converges in one single iteration and it was also verified that when the variances are modified, the analysis changes accordingly: it remains close to the background when the observation error variance increases and gets closer to the observation when the background error variance increases.

When the **B** matrix is not diagonal, the difference between the simulated and observed salinity at the observation points translates into a correction at the neighbouring points. The horizontal and vertical spatial repartition of the information is prescribed by the background error correlation functions; more specifically by the horizontal and vertical correlation length-scales L_h and L_v. Fig. 1 presents the horizontal correlation function for point A when L_h=600m. It should be noted that the 0.5 isocontour plotted in white describes a circle of radius equal approximately to 600m, centered in A. It should also be noted that the maximum correlation in A is not exactly equal to 1 (as it should be in theory) because of a normalization procedure within the diffusion operator method that is beyond the scope of this paper.

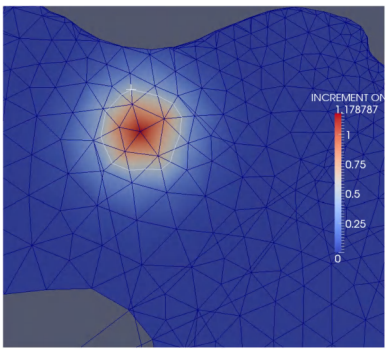

Figure 1: Correlation function (dimensionless) prescribed for point A with L_h=600m over the Berre Lagoon area where SA1 is located.

Similarly, the vertical repartition of the increment relates to L_v that prescribes the shape of the vertical correlation function. The increment is presented in Fig. 2 when L_v=0.5m.

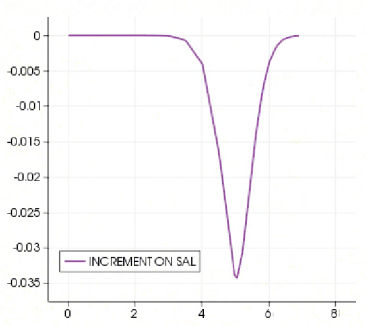

Figure 2: Salinity increment (in psu, on the y-axis) for the single observation experiment, plotted at point A along the vertical (in m, on the x-axis).

In the following, the observations are used at their real measurement location (generally, not at a grid point), meaning that the computation of BmO implies a spatial interpolation (horizontal and vertical) that represents the observation operator *H* presented in Section 2.

The observations at SA1, at 5 m deep are now assimilated every 15 minutes with an assimilation window of 1 hour, meaning that a correction to the initial salinity state is computed from the 3D-Var FGAT algorithm using 4 observations in the minimization process. This analysis is cycled over 24 hours and the results are presented in Fig. 3a- for L_h=200 m and L_v=0.5 m and in Fig. 3b- for L_h=200 m and L_v=2 m. For each panel, the salinity is represented at SA1, at different vertical depths that correspond to the 5 XBT sensors positions, as a function of time over 24 h, at observation times only. The observations are represented in red, the T3D Free Run (no assimilation) is plotted in black, the background (for the current cycle) is plotted is green and the analysis is plotted in blue. First, it should be noted that at 5 m deep (where the observations are assimilated), the salinity is significantly improved and brought closer to the observations (the background and observation errors variances are set to 4 psu^2). The difference between the analysis and the observation is systematically reduced at the beginning of the assimilation window when the correction is applied, then the model is integrated over 1 hour and deviates from the observations. The analysis salinity value at the end of the assimilation window is the background initial salinity state for the following cycle. The 1-hour integration of the background state can thus be considered as a 1-hour prevision following the 1-hour assimilation window. It should then be noted that the 3D-Var FGAT algorithm improves the salinity over the assimilation period as well as over a forecast period of 1 hour.

When Lv=0.5 m (Fig. 3a-), the assimilation of the observations at 5m deep has no impact on the rest of the water column at SA1 where no observations are assimilated. On the contrary, when Lv=2 m (Fig. 3b-), the salinity is corrected over the entire water column. Whether this correction improves or not the salinity depends on the coherence between the spatial correlation of the errors in the simulated salinity field and the correlation function prescribed in B. It also depends on the dynamics of the increment injected at the initial time, this issue will be addressed in the next subsection. Finally, it should be noted that the minimization for each cycle now converges in a small number of iterations, the cost function Jinc (3) is reduced and its gradient is brought to zero.

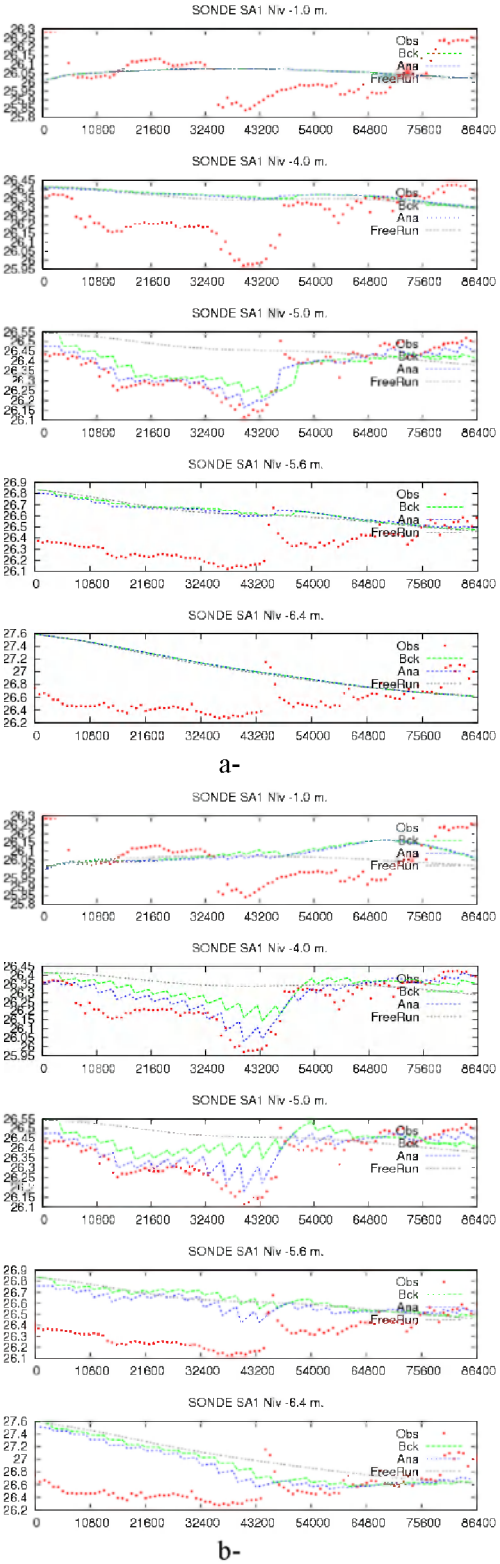

Figure 3: Salinity (in psu) at the 5 observation points at SA1 along the vertical for L_h=200m, a- L_v=0.5m and b- L_v=2m over 24 assimilation cycles of 1 hour. Only the observation at 5m deep are assimilated.

B. Real-case study: Assimilation of all SA1 observations

Fig. 4a- displays the results of the assimilation of all the observations at SA1 for the 5 vertical levels, over 24 hours with a 1-hour assimilation window when L_h=200m and L_v=0.5 m. At each level, the salinity is brought closer to the observations over the assimilation and the forecast period. Still, it should be noted that the effect of the increment applied at the beginning of the cycle can lead to an over-correction as observed at 1m deep for t in [54000 s, 72000 s] where the forecast (the background plotted in green) exceeds the Free Run so that the distance to the observation is increased by the DA procedure. This might be due to the too simple description of L_v that is here constant along the vertical and too large close to the surface as the salinity errors in the mixed layer (down to 3 or 4 m deep) are weakly correlated with the salinity errors in sub-surface where the stratification is strong. Under the mixed layer, as the salinity errors are strongly correlated, the correction from the assimilation at one level has a positive impact on the other levels. In order to account for the spatial variability of the salinity errors in the DA process, on-going developments aim at allowing for an inhomogeneous description of the correlation length scales. Preliminary tests showed that the spurious correction at 1m is significantly reduced when L_v=0.25 m, but on the other hand, the improvement for deeper level is slightly reduced as illustrated in Fig. 4b-.

The 3D-Var FGAT salinity increment for the first assimilation cycle at 1 m deep is shown in Fig. 5a- for Lh=600 m and Lv=0.25 m and the resulting corrected salinity field at the t=0 s is shown in b-. The pink triangle represents the T3D grid element that contains the observation point SA1. As expected, the spatial repartition of the correction is prescribed by the correlation length scale, still the evolution of this increment when the model is integrated from the corrected initial condition should be further investigated as spurious changes to other variables as the pressure, temperature and current could occur thus leading to over corrections. A common way to limit these effects is to spread the correction over the assimilation window instead of applying it, at once, at the initial time for the cycle. This procedure, called IAU Incremental Analysis Updates), was implemented with a basic division of the correction in equal increments applied at each time step over the 1-hour assimilation window. It allows to significantly reduce the over-correction at 1m deep (not shown here) and the shape of the repartition function should be further investigated.

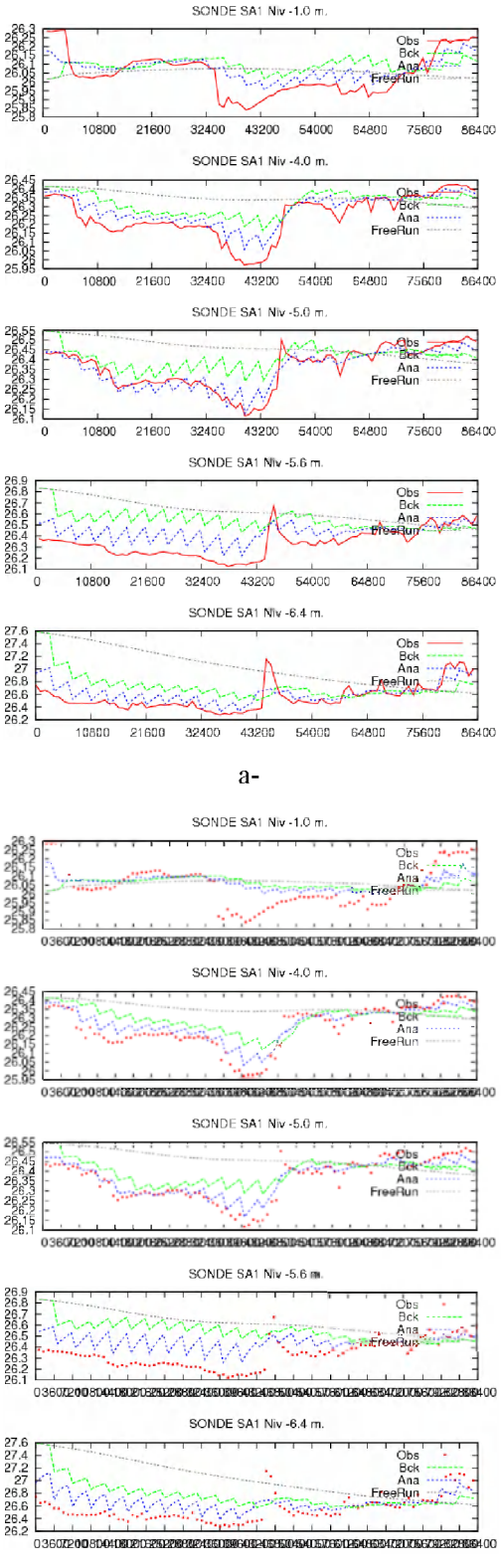

Figure 4: Salinity (in psu) at the 5 observation points at SA1 along the vertical for L_h=200m, a- L_v=0.5m and b- L_v=0.25m over 24 assimilation cycles of 1 hour. All observations at SA1 are assimilated.

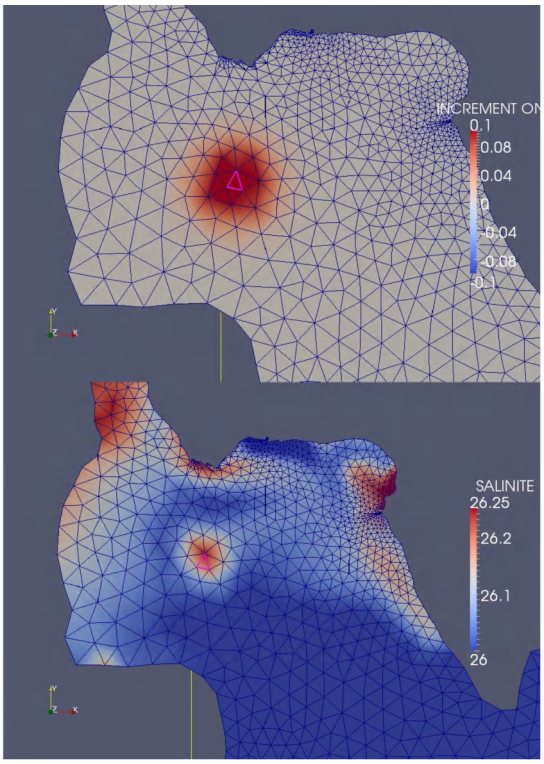

Figure 5: Salinity increment (in psu) for the first assimilation cycle a- L_h=600m and L_v=0.25m, b- analysis salinity field (in psu) for L_h=600m and L_v=0.25m.

CONCLUSION

A 3D-Var FGAT algorithm was implemented in the dual space in order to improve the salinity field description assimilating in-situ salinity observations with a T3D model for the Berre lagoon. The analysis is achieved over a 1-hour window and is applied sequentially every hour. It was shown that the corrected field is closer to the observations over the assimilation and 1-hour forecast periods at the assimilation points. The horizontal and vertical spread of the correction around the observation point depends on the correlation length-scales prescribed in the background error covariance matrix modelled using an implicit 3D diffusion operator. The impact of the vertical length scale was studied and it was shown that in order to avoid spurious correction between the vertical assimilation locations, the correlation length scale should be depth-dependent. This could be achieved using an ensemble-based estimate of the correlation length-scales, eventually with a temporal variability. In further work, the evolution of the salinity increment over time should also be investigated in order to verify that the balance between the other state variables (temperature, currents) is preserved.

REFERENCES

[1] N. Durand, E. Razafindrakoto. "Synthèses et conclusions des études sur la modélisation numérique TELEMAC-3D de l'évolution des courants, de la salinité et de la température dans l'étang de Berre." , Note Interne EDF-LNHE, H-P74-2011-02289-FR, 2011.

[2] Schumann, G., Bates, P.D., Horritt, M.S., Matgen, P., and Pappenberger, F.: Progress in integration of remote sensing-derived flood extent and stage data and hydraulic models, Rev. Geophys., 47, RG4001, doi:10.1029/2008RG000274, 2009.

[3] Durand, M., Lee-Lang, F., Lettenmaier, D.P., Alsdorf, D.E., Rodriguez, E., and Esteban-Fernandez, D.: The Surface Water and Ocean Topography Mission: Observing Terrestrial Surface Water and Oceanic Submesoscale Eddies, IEEE, 98, 766--779, 2010.

[4] Neal, J., Schumann, G., Bates, P., Buytaert, W., Matgen, P., and Pappenberger, F.: A data assimilation approach to discharge estimation from space, Hydrol. Process., 23, 3641—3649. doi: 10.1002/hyp.7518, 2009.

[5] Valstar, J.R., McLaughlin, D.B., te Stroet, C.B.M., and van Geer, F.C.: A representer-based inverse method for groundwater flow and transport applications, Water Resour. Res., 40, W05116, doi:10.1029/2003WR002922, 2004.

[6] Matgen, P., Montanari, M., Hostache, R., Pfister, L., Hoffmann, L., Guingla, D.P., Pauwels, V., De Lannoy, G., De Keyser, R., and Savenije, H.H.G.: Towards the sequential assimilation of SAR-derived water stages into hydraulic models using the Particle Filter: proof of concept, Hydrol. Earth Syst. Sci, 14, 1773--1785, 2010.

[7] Thirel, G., Martin, E., Mahfouf, J.-F., Massart, S., Ricci, S., and Habets, F.: A past discharges assimilation system for ensemble streamflow forecasts over France, Hydrol. Earth Syst. Sci., 14, 1623--1637, 2010.

[8] Weerts, A.H., and El Serafy, G.Y.H.: Particle filtering and ensemble Kalman filtering for state updating with hydrological conceptual rainfall-runoff models, Water Resour. Res., 42, W09403, doi:10.1029/2005WR004093., 2006.

[9] Moradkhani, H., Sorooshian, S, Gupta, H.V., and Houser, P.-R.: Dual state-parameter estimation of hydrological models using ensemble Kalman filter, Advances in Water Resources, 28, 135--147, 2005a.

[10] Madsen, H., and Skotner, C.: Adaptive state updating in real-time river flow forecasting - a combined filtering and error forercasting procedure, J. Hydrol., 308, 302--312, 2005.

[11] Jean-Baptiste, N., Malaterre, P.-O., Dorée, C. and Sau, J.: Data assimilation for real-time estimation of hydraulic states and unmeasured perturbations in a 1D hydrodynamic model, Journal of Mathematics and Computers in Simulation, Vol. 81, Issue 10, 2201-2214, 2011.

[12] Ricci, S., Piacentini, A., Thual, O., Le Pape, E., and Jonville, G.: Correction of upstream flow and hydraulics state with data assimilation in the context of flood forecasting, Hydrol. Earth Syst. Sci, Vol. 15, 1--21, 2011.

[13] Weaver A.T., Vialard J., Anderson D.L.T.: Three- and four-dimensional variational assimilation with a general circulation model of the tropical Pacific ocean. Part 1: formulation, internal diagnostics and consistency checks. Mon. Weather Rev. 131: 1360—1378, 2003.

[14] Moore, A.M., Arango H.G., Broquet G., Powell B.S., Zavala-Garay J., Weaver A.T.: The Regional Ocean modelling System (ROMS) 4-dimensional variational data assimilation systems. Part I: System overview and formulation. Prog. Oceanogr. 91: 34–49, 2011a.

[15] Daley, R.: Atmospheric data analysis. Cambridge atmospheric and space science series. Cambridge University Press, 1991.

[16] Gurol, S., A. T. Weaver, A. M. Moore, A. Piacentini, H. G. Arango and S. Gratton. " B-Preconditioned Minimization Algorithms for Variational Data Assimilation with the Dual Formulation", Q. J. R. Meteorol. Soc. , in print.

[17] Weaver, A.T, P. Courtier, P.: Correlation modelling on the sphere using a generalized diffusion equation, Q. J. R. Meteorol. Soc., 127, 1815--1846, 2001.

[18] Tarantola A.: Inverse Problem Theory and Methods for Model Parameter Estimation. SIAM, Philadelphia, 2005.

[19] Nocedal, J., Wright, S.J.: Numerical Optimization. Series in Operations Research, Springer Verlag: Heidelberg, Berlin, New York, 2006

[20] Cohn, S., Da Silva, A., Guo, J., Sienkiewicz, M., Lamich, D.:Assessing the effects of data selection with the DAO physical-space statistical analysis system. Mon. Weather, 126, 2913--2926, 1998.

[21] Gratton, S., Tshimanga, J.: An observation-space formulation of variational assimilation using a Restricted Preconditioned Conjugate-Gradient algorithm. Q. J. R. Meteorol. Soc., 135, 1573—1585, 2009.

[22] Mirouze, I., Weaver, A.T.: Representation of correlation functions in variational assimilation using an implicit diffusion operator. Q. J. R. Meteorol. Soc., 136, 421--1443, 2010.

TUC 2013, 16-18/10/2013, Karlsruhe - Kopmann, Goll (eds.) - © 2013 Bundesanstalt für Wasserbau ISBN 978-3-939230-07-6

Reverse engineering of initial & boundary conditions with TELEMAC and algorithmic differentiation

U. Merkel
Ingenieurbüro Merkel
Karlsruhe, Germany
info@uwe-merkel.com

J. Riehme, U. Naumann
STCE at RWTH Aachen University
Aachen, Germany
riehme@stce.rwth-aachen.de,
naumann@stce.rwth-aachen.de

***Abstract*—The TELEMAC-SUITE with Algorithmic Differentiation (TELEMAC-AD) calculates the impact of a high number of spatially distributed parameters on flow conditions. This technique is a revolutionary step forward in open channel flow simulations, as it solves previously unsolvable or computationally very expensive problems. Classic simulation methods return the combined impact of many parameters, whereas the adjoint version of TELEMAC-2D returns the individual influence of every single parameter in one run. A wide range of new applications is now possible with the TELEMAC-SUITE: Automatic optimization and calibration of flow relevant shapes, data assimilation, high resolution sensitivity analysis or inverse modelling.**

I. INTRODUCTION

This article describes a new method for open channel flow software which solves inverse flow problems. Instead of traditional forward questions like

„Put water in here, how will it be distributed within our project area?“

we solve inverse questions of the type

„We want specific flow conditions here, where and how do we have to modify our project area?“.

See Fig. 1 for a simple example comparison.

- Left: The traditional forward projects few input parameters have influence on many target parameters.
- Middle: The inverse problematic projects many input parameters have influence on a few target parameters.

Many input parameters means, specific values in many geometric points (e.g. bed roughness, bathymetry), or global parameters (e.g. discharge). Each has an individual influence. We want to quantify for all parameters their relevance for the resulting discharge Q. The relevance is described by the gradient of the output Q with respect to the inputs, which is the vector of partial derivatives ∂ Q / ∂ input(i).

If the hydraulic problem is based on a large number of influence factors, then the adjoint model of the TELEMAC-SUITE (TELEMAC-AD) is the most efficient solver: The complete gradient can be computed by one run of the adjoint model. TELEMAC-AD was generated semi-automatically by the differentiation-enabled NAG FORTRAN compiler, a joint development of the institute STCE at RWTH Aachen University, Germany, NAG, UK, and the University of Hertfordshire, UK.

After a short introduction (Chapter 1) two examples illustrate the potential of TELEMAC-AD (Chapter 2). A basic introduction of the AD concept follows in (Chapter 3). More detailed Information can be found in [1] and [2].

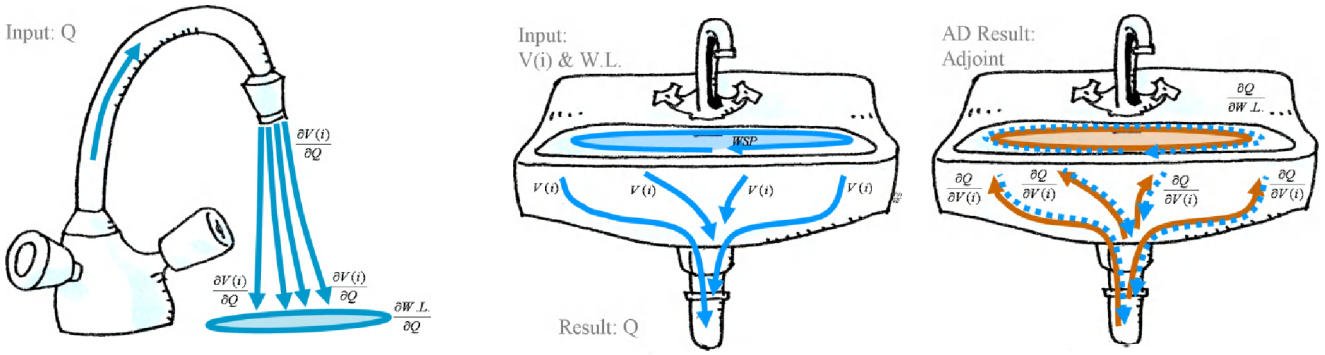

Figure 1. Left: common forward problem: Few Parameters influence many, dependency easy to calculate. Middle: inverse problem. Few parameters depend on many, sometimes millions of geometry points. Both, physical and numerical models overlay the single dependencies on the results. Right: The adjoint method solves until now unsolvable inverse problems by interpreting the forward problem backward.

A. *A wide field of new applications*

This new method opens a door to a new range of hydraulic models. Typically applications are the impact quantification for any point of a TELEMAC-2D -3D or SISYPHE model.

Any point *I* (and its connected parameters velocity V, water level W.L., manning's n ...)

- influences the flow conditions at a power plant intake and the maximum energy level which results in more or less electrical energy.
- influences robustness and sensitivity of hydraulic relevant structures and hydraulic driven processes of all kinds (like dams, bridges, flood protection measures, morphological aspects, a.o.) [3].

In combination with gradient based optimization methods the adjoint technology can be used for

- automatic calibration of thousands of roughness values at the same time, e.g. to fit water levels to measured values (until today an unsolved every day problem).
- semiautomatic modification of single point coordinates to modify flow conditions according to a target function. Airfoils and drag coefficients of cars have already been optimized with AD in mechanical engineering (shape optimization).

B. *Using the classic forward calculation*

The influence of boundary & initial conditions like W.L. and V(i), i=1...N, on a target parameter like Q for questions as in Fig. 1 (middle) is described with the gradient (left part of formula 1):

$$\nabla Q = \left[\frac{\partial Q}{\partial V(1)}, \ldots, \frac{\partial Q}{\partial V(N)}, \frac{\partial Q}{\partial W.L.}\right]^T \approx \left[\frac{\Delta Q}{\Delta V(1)}, \ldots, \frac{\Delta Q}{\Delta V(N)}, \frac{\Delta Q}{\Delta W.L.}\right]^T \quad (1)$$

Until today the differential analysis is the common way to analyze and optimize the flow field or morphology (right part of formula 1). Every element of the gradient approximation has to be computed separately with slightly different input parameters. For millions of points millions of calculations are necessary or the points have to be grouped, what will bias the results.

Since the early days of physical flow models the real target is to minimize the difference between a real and a desired flow field (maximum erosion, water levels, velocity field etc.). The main question in many cases is that one few parameter (the difference) depends on many.

This can be any mathematically relevant variable, but especially for open channel flow it is the spatial distribution of parameters in big FE meshes. But an analysis for millions of points (each one is a bathymetric feature) is too expensive normally.

C. *Backward interpretation with adjoint models*

The adjoint model of TELEMAC-AD computes the entire gradient from formula 1 in only 1 forward run and its following backward interpretation.

In the adjoint mode, TELEMAC-AD records every relevant instruction during a forward evaluation in the so called "tape". At the end of the forward run all target values and the process flow is stored in the tape. The backward interpretation propagates the adjoints (derivatives) from the target parameters (at the end of the tape) to the input parameters (at the beginning of the tape). During this process every single instruction is interpreted by its adjoint version. The adjoints obtained for the input parameters can now be used as dependency information, for robustness or sensitivity analyses or in a next step for gradient based optimization methods.

II. EXAMPLES

Two examples with TELEMAC and SISYPHE illustrate the potential of the AD technology. Both are based on the open source version of TELEMAC v6p2.

- A morphodynamic 2D SISYPHE flume model with 92 roughness zones is automatically calibrated.
- A hydraulic 2D TELEMAC river model is examined to quantify the influence of 95000 spatially distributed parameters on the shear stress in 1 specific point.

Further example cases can be found at [3] and www.uwe-merkel.com/TELEMAC-ad.

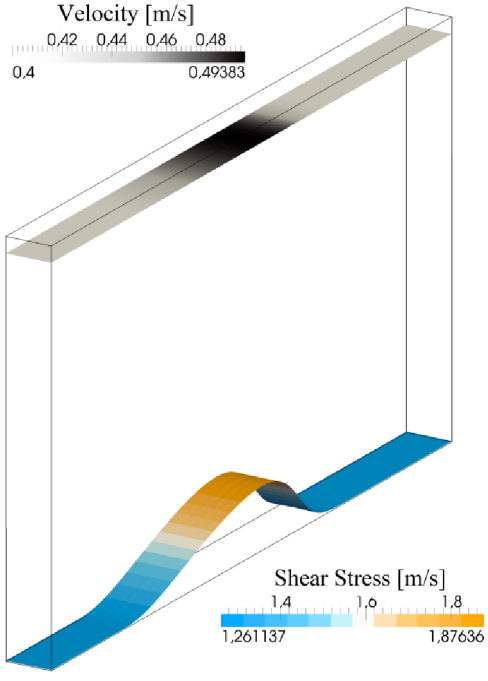

Figure 2. Setup of the flume: LxWxH: 16m x 1,1m x 0,6m; dune height: 0,1m; runtime: 14400 s

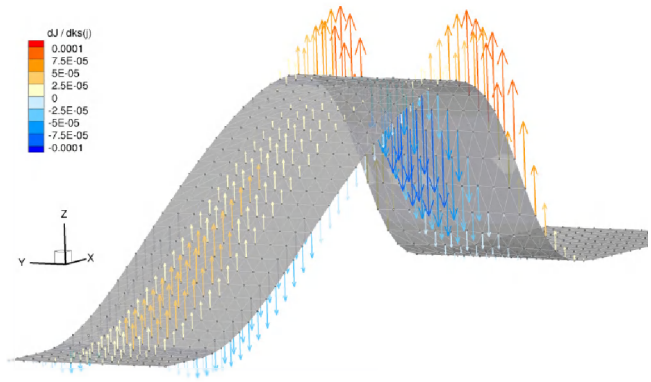

Figure 3. Arrows show direction and magnitude for the influence of a mesh points roughness zone on the cost function (sum of quadratic errors).

A. Automatic calibration of 92 morphological parameters

As introduction example serves a simple lab flume. Adjoints are calculated with the SISYPHE-AD version, and they are used to perform a simple Least Square Root (LSQR) optimization. 92 zones have been defined as relevant to the resulting evolution. Fig. 2 shows the setup, a straight flume with moving sediments in a dune shape. 92 local zones are defined for the roughness ks_j, $j=1,...,92$, which itself is a combination of the boundary roughness and the grain roughness. The calculated morphological evolution $E_i = E_i(ks), i=1,..,891$ has to be optimized to match the observation values in all mesh points i.

A LSQR problem is formulated by introducing a cost functional J:

$$J = \sum_{i=1}^{891} \left(E_{OBS,i} - E_{IST,i} \right)^2 \tag{2}$$

The adjoint model computed the gradient of J with respect to all roughness coefficients ksj, $j=1,...,92$:

$$\nabla_{ks} J = \left[\frac{\partial J}{\partial ks_1}, \ldots, \frac{\partial J}{\partial ks_{92}} \right]^T \tag{3}$$

Therefore the adjoint version of SISYPHE calculates the evolution E(i) values after 14400 s as usual, and the cost functional J in addition. Backward interpretation calculates the gradient from (4) describing the dependency of J on ks_j.

Fig. 3 shows the 92 elements of the gradient as arrows along the 891 mesh points. The arrows show direction and magnitude of the dependency and must not be misunderstood as flow vectors.

In the next step this information is used to fit the calculation results to the observation results:

The observation result in this case is a SISYPHE simulation itself, whose final evolution is set as the ideal case. This is called a twin experiment, which allows evaluating the behavior of the optimization algorithm without the influence of measurement uncertainties or design wishes that might turn out as utopia. The twin experiment suits best for validating SISYPHE-AD and the optimization algorithm.

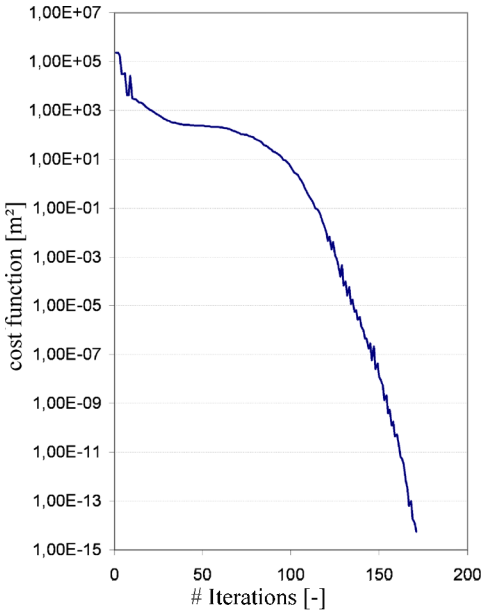

Figure 4. The adjoint based optimization of the roughness parameters, based on the grain diameter, converges until the cost function drops below J < 10-14 (Roughness: Strickler; Algorithm: BFGS).

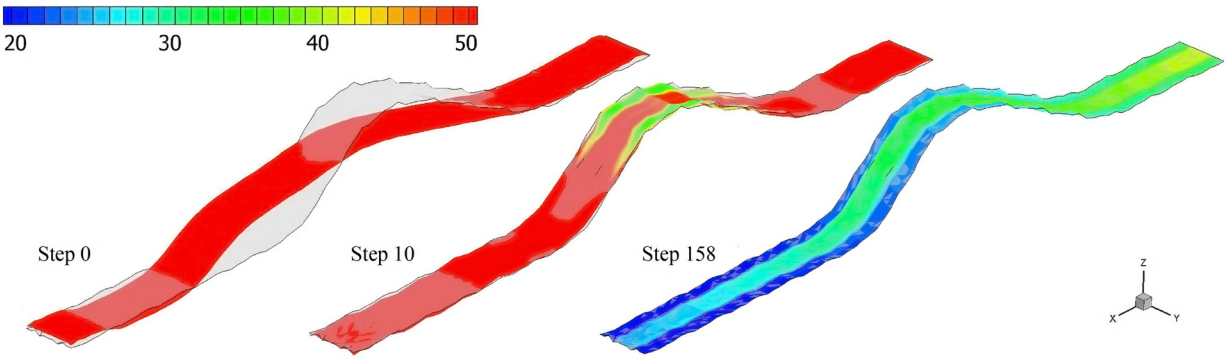

Figure 5. Development of the cost function during the optimization (Initial state, 10 steps, 158 steps): Grey shaded; optimization target. The color indicates the development of the roughness which respects grain size and boundary influence.

The target function J is reduced in each iteration step, which means that for each step a full SISYPHE-AD run is executed and its resulting gradient is used in a wrapping minimization program. This mantle program calls CG, BFGS or SLSQP algorithms, which are part of the MINPACK optimization library [10]. The optimization terminates if the cost function goes below a threshold or doesn't converge. The master thesis of Monika Schäfer focuses on the performance of these algorithms [4].

Fig. 4 shows the progress of the optimization, Fig. 5 the development of bathymetry and roughness during the optimization process. The observation bathymetry (transparent gray) is converging very fast, while the roughness (grain size roughness) is developing slower. But after 158 full calculations of SISYPHE-AD the cost function J is below the terminating threshold 10-14.

B. Dependency of shear stress in a groyne head scour

221_Donau is a public validation example for TELEMAC-2D and it is available at OPENTELEMAC.ORG. It is used here to analyze how the surrounding bathymetry and the neighborhoods roughness distribution influence flow conditions in a certain point of a real river. The shear stress τ (taken from 12 points in the middle of the groyne head scour, see marker in Fig. 6 is the target of this analysis.

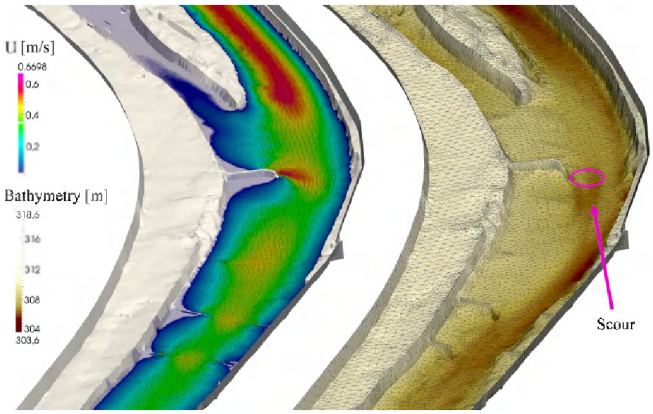

Figure 6. Perspective view of the 221_Donau model, with a dominant groyne and its head scour. Right: Geometry defined with approx. 47500 mesh points. Left: Scalar velocities.

In difference to the first example this real world example has highly complex multidimensional flow conditions with islands, groynes, tidal flats, and many other flow interacting features. The spatial interaction is broken down to local values for every point with TELEMAC-2D-AD, here with focus on the roughness and elevation values of the 47500 points in the 2D mesh. The dependency is individually quantified in total for 95000 parameters. This example is chosen to proof the usability for practical purposes.

1) Classic solution with finite differences (FD):

Solving per point independent dependency analysis requires a base calculation and 95000 full TELEMAC-2D calculations with a slight modification of one input parameter. Only this will proof spatial independent input-output dependencies.

See formula 4 and 5:

$$\frac{\delta\tau}{\delta z(i)} \approx \frac{\tau(z(i)+h)-\tau(z(i))}{(z(i)+h)-z(i)} \quad (4)$$

$$\frac{\delta\tau}{\delta ks(i)} \approx \frac{\tau(ks(i)+h)-\tau(ks(i))}{(ks(i)+h)-ks(i)} \quad (5)$$

One calculation runs 5min on a up to date desktop computer, this means 330 days for all calculations or a very expensive outsourcing on a bigger cluster.

And the result is only valid for:

- one parameter set (discharge, bathymetry, roughness, turbulence setting ...)
- the simulated time span
- very limited extrapolation, due to the nonlinearity in many sub models (see Fig. 8!).

Practical projects usually observe many variants, optimization projects even more, which leads to very expensive computational costs, making this technology economically unusable for most small and medium size projects.

2) Adjoint solution (AD):

TELEMAC-AD calculates the full forward run and backward interpretation in 678 min on the same desktop computer, and returns all 95000 adjoints for the shear stress τ. The gain of computational speed equals the usage of an approx. 1000-core cluster when using the classic FD method. Some results are displayed in Fig. 7. At the time of writing TELEMAC-2D-AD is still not parallelized, and not optimized for speed, which means that a further speedup is expected after completion of these ongoing developments.

3) Interpretation of the resulting adjoints:

Adjoints computed by TELEMAC-2D-AD describe the change of the output τ as a linear relation of its specific input. Therefore extrapolations for other input parameter sets can only be done with great care.

The dependency of the bathymetry on τ at the simulated flow conditions is dominated by the obvious separation of the 2 arms around the upstream island. If the southern arm, which has low flow, is lifted, then more water is pushed to the main channel (1). The same happens if the surrounding of the groyne and the opposite site (2) of the cross section are elevated. A kind of funnel effect increases the shear stress. Decreasing the scour itself increases the shear stress as well (3).

The perspective view from downstream (4) reveals that some other groynes have a high impact, as they influence with their back draft the water level in the examined area. The lower groynes, which are smaller and shaded by the bigger ones therefore don't influence the examination zone anymore. Again the reader shall be warned that only a change of few decimeters in any topographic feature might

change the result totally. The general noise in the adjoints origins from bumps and holes in the bathymetry. Following the direction of the adjoints will smoothen the main channel and therefore accelerate flow and increase the shear stress.

On the contrary for bed roughness a clear tendency is visible: the smoother the bed along the main channel, the higher the shear stress at the groyne head scour. If the roughness gets higher on the opposite shore (5), more water is pressed to the scour. Classic methods (numerical and physical) would have given a rough idea about this dependency, but for the first time a hydraulic model can exactly define the spatial limits of the relevant area. The scour itself has a different tendency (6): Increasing the roughness in the target point obviously increases the local shear stress.

III. ALGORITHMIC DIFFERENTIATION

Algorithmic differentiation (AD) is a mathematical method that extends existing computer programs in a way that for a priori chosen results their dependency to a priori chosen input variables is additionally calculated. AD tools work on the original source code, and not as a new implementation of the mathematic model. Differentiated models obtained by AD compute derivatives in machine precision for a given input parameter set.

Since some time aerospace, mechanical engineering and meteorology are working successfully with adjoint models. They use AD for uncertainty quantification, data assimilation, optimization strategies and inverse problems. Inverse problems in hydraulic engineering are for example the quantification of boundary and initial conditions for given results.

The principles of AD are based on the fact, that every calculation is finally a combination of basic operations (+, -, *, /, exp, sin,...) with well known differentiation rules. All more complex formulas are a sequence of these; derivatives of basic operations are combined by the chain rule to derivatives of sequences.

Two basic techniques are used for first order derivatives:

- Tangent linear models (forward models) work the same direction as finite difference (FD) approximations of derivatives, but at machine precision. Fig. 8 shows this advantage against FD, which has to use 2 calculation results for each derivative.
- Adjoint models (inverse interpretation of the forward model) propagate the adjoint (derivative) from the final results back to initial and boundary conditions. For the backward interpretation the full path of the forward calculation has to be recorded. If the forward model has just a single target parameter value, the vector of derivatives (the gradient) can be calculated in only one backward interpretation.

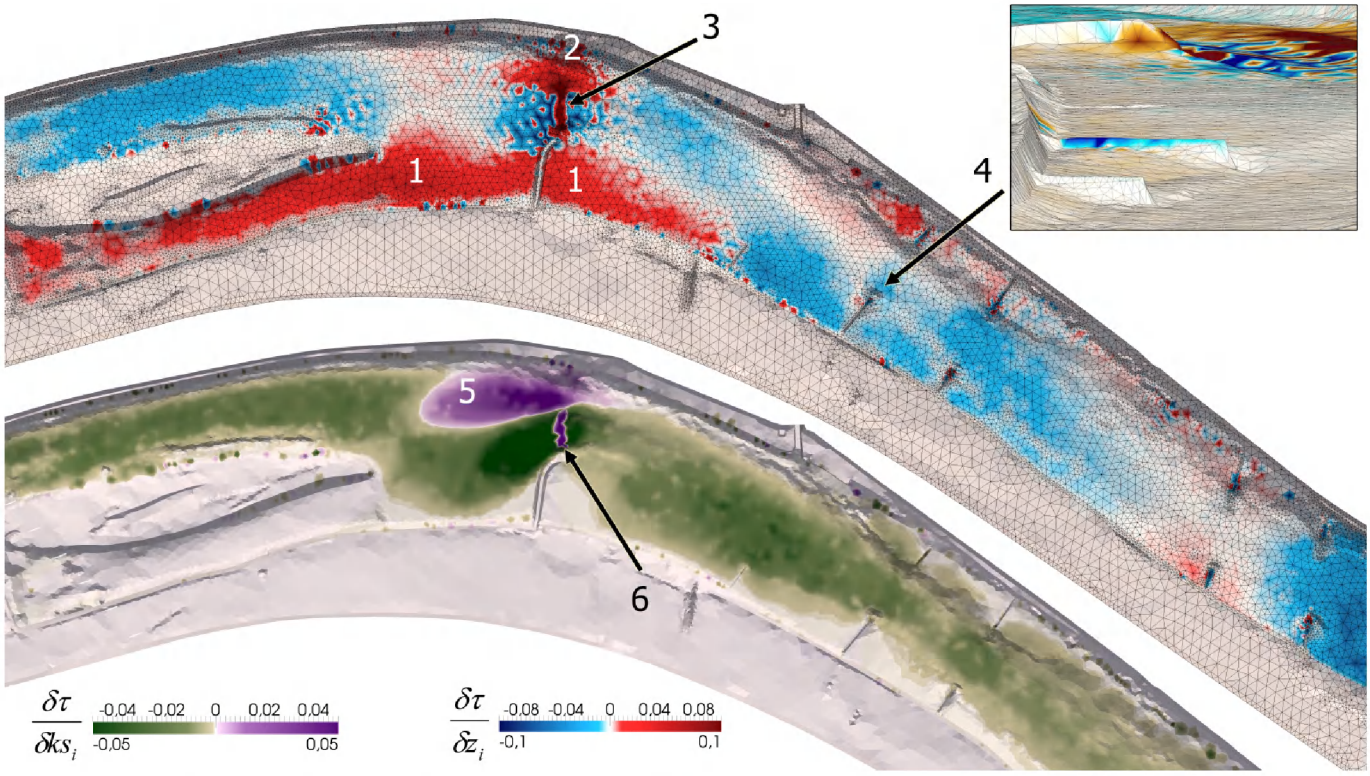

Figure 7. Result of a single TELEMAC-2D-AD calculation. Top: Dependency of the shear stress in the scour (marked) to neighbouring geometry information. Bottom: Influence of the roughness on the shear stress [values per m²]. Values are only valid for the current flow conditions and setup!

Second or higher order derivatives can be calculated by combining the basic techniques. Higher order derivatives might speed up optimization processes significantly. For further information see [5].

The AD-enabled NAG Fortran Compiler [7], developed at the Institute"Software and Tools for Computational Engineering" (STCE, University RWTH Aachen) is a commercial extension of the NAG FORTRAN compiler (Numerical Algorithm Group, Oxford, UK). It uses a hybrid technique of source code transformation and an efficient overloading based run time library. [6] discusses this methods in detail. The hybrid approach allows an efficient differentiation of large projects like the TELEMAC-SUITE.

For practical usage the recording of all iterations and all operations within these iterations is a memory consumption problem. For the 221_Donau example 10TB of RAM would be necessary. Therefore TELEMAC had to be extended by a so called checkpointing technology. What means that every calculation can be saved to RAM and restarted from RAM with binary identically results at any point in time, with only a minimum recording of variables.

For the backward propagation of the adjoints (backward time step wise) the necessary detail information about subprogram internal operations is recalculated from the checkpoints in reverse order. This increases calculation effort by 200%, but reduces the RAM usage, as the minimum checkpointing system only needs 300MB for 1000 time steps in the 221_Donau example, plus 10GB for the current time step.

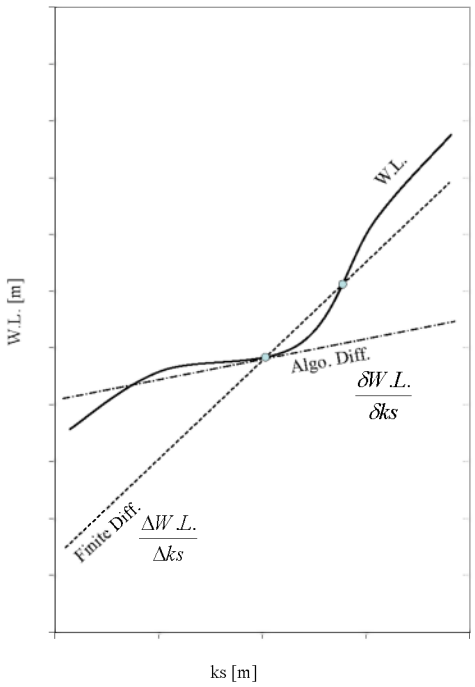

Figure 8. Water level as a function of the roughness ks. Normally the dependency is not linear. Dependency is described as first derivation, this means the ascent of the tangent is defined in only one point for algorithmic (~analytic) differentiation and in two for finite differences.

IV. CONCLUSIONS

The methods of reverse interpretation and algorithmic differentiation enable a very fast quantification of dependency gradients with millions of influence parameters! The dependency of any numerical result (energy, evolution, transport rates, risk ...) on any numerical input value (spatial or global) can be quantified independently within only one run of the adjoint model. For hydraulic modelling especially the ability to dissolve spatial interactions opens a gate to a new generation of models, which solve until now unsolved problems. Spatial independent sensitivity and robustness information helps to understand complex flow situations and can be used for gradient based optimization processes [3]. This method is currently unique for open channel flow software, and the growing number of new examples will be continuously updated on www.uwe-merkel.com/TELEMAC-ad.

This first project was funded by the BAW with participation of the EDF. Their aim is to have a tool that dissolves the interaction between morphology, flow and constructions.

REFERENCES

[1] Villaret, C. 2013. Hervouet, J.M. Kopmann, R. Merkel, U. Morphodynamics modelling using the TELEMAC finite-element System. Computers and Geosciences. Heft 53, S.105-113. (2013)

[2] Kopmann, R. Merkel, U. Drei Jahre TELEMAC Open Source. In: Wasserwirtschaft (2013), Heft 12

[3] Kopmann, R. Merkel, U. Riehme, J. Using Reliability Analysis in Morphodynamic Simulation with TELEMAC2D / SISYPHE. Proceedings: TELEMAC Users Club 2012, Oxford, (2012)

[4] Schäfer, M. Optimierungsalgorithmen für LSQR Optimierungsprobleme mit dem algorithmisch differenzierten TELEMAC-2D AD. Diplomarbeit (2013)

[5] Griewank, A., Walther, A. Evaluating Derivatives: Principles and Techniques of Algorithmic Differentiation. 2d ed. SIAM. Philadelphia. . (2008).

[6] Rauser, F. Riehme, J. Leppkes, K. Korn, P., Naumann, U. On the use of discrete adjoints in goal error estimation for shallow water equations. Procedia Computer Science, 1, 107–115.(2010).

[7] AD-enabled NAG FORTRAN compiler: Users manual. http://www.stce.rwth-aachen.de/files/nagfor_ad/userguide_v0.2.pdf (03/2013).

[8] Naumann, U. The Art of Differentiating Computer Programs. An Introduction to Algorithmic Differentiation. Software, Environments, and Tools, SIAM, (2012).

[9] Naumann, U., Riehme, J. A differentiation-enabled Fortran 95 compiler. ACM Transactions on Mathematical Software, 31(4):458–474. (2005).

[10] Nocedal, J. Wright, S.Numerical Optimization. 2nd ed. Springer. (2006).

TUC 2013, 16-18/10/2013, Karlsruhe - Kopmann, Goll (eds.) - © 2013 Bundesanstalt für Wasserbau ISBN 978-3-939230-07-6

Numerical simulation of flow structures in the presence of alternate and transverse bars: application to the Loire river (France)

B. Magnier[1,2], N. Claude[2, 3], C. Villaret[2], S. Rodrigues[4] and P. Tassi[2]

[1] Institut de Physique du Globe de Paris
Paris France

[2] EDF R&D - Laboratoire Saint Venant
Chatou, France

[3] Ecole des Nationale des Ponts et Chaussées
Champs sur Marne, France

[4] E.A 6293 GéHCO, Université François Rabelais
Tours, France

***Abstract*—In this study, the module TELEMAC-3D is used to analyse the flow behaviour in the presence of alternate and transverse bars. This particular bar organization has been poorly studied in the literature and presents great interest for the planing of dredging operations in rivers like the Loire in France. Three-dimensional numerical results showed that the main flow structure is defined by the channel planform and bars configurations. The roughness-length distance strongly influences the velocity near the bed and the increasing of the mesh resolution impacts the bed resistance mechanisms and, in consequence, the distribution of the velocity profiles.**

I. INTRODUCTION

Bars are ubiquitous morphological macroforms that interact with the flow and sediment transport processes in rivers with important bedload transport rates [2]. Alternate bars, whose structure is characterized by a sequence of steep consecutive diagonal fronts and deep pools at the downstream face, have been extensively investigated both theoretically and through flume studies, e.g. [1, 2, 3, 4]. More complicated macroform patterns, such as transverse, central or multiple configurations can be found in wider reaches, e.g. [5, 6].

Bars can be classified as forced or free. Forced bars arise from a forcing effect that can have an anthropic or natural origin, such as channel curvature, width variations or the presence of confluence/diffluence zones in the channel. Free bars, on the other hand, can arise from an inherent instability of the erodible bottom subject to a turbulent flow [5]. Further details can be found in the companion paper presented in this conference [7].

Depending on the forcing mechanism, bar patterns show different configurations. Forced bars that are associated with a flow in a variable-width channel appear as mid-channel bars or transverse bar, or as two symmetrical lateral bars [8]. The formation of central or transverse bars could be associated to an antisymmetric forcing such as a channel curvature, while alternate bars can appear as a response to instability in the channel bed or by the presence of a repetitive sequence of width variations.

Furthermore, Wu *et al.* [8] pointed out that the presence of free bars in a "forced bar" configuration could give rise to a "mixed" organization (free + forced), arranged in alternate or transversal configurations. Coexisting free and forced bars have been extensively studied in meandering channels. In contrast, the presence of mixed bars in widening/narrowing channels has received little attention [9].

As highlighted by Claude *et al.* [10], the site of Bréhémont in the middle reach of the Loire river in France presents forcing effects caused by channel width variations that induce the presence of alternate and transverse bars over short periods of time, even in a slow hydrodynamic context. To the best of our knowledge, this particular bar organization has been poorly studied in the literature.

In this work, the three-dimensional (3D) hydrodynamic models TELEMAC-3D is calibrated for the site of Bréhémont on the Loire River from a large dataset of high-quality field surveys based on Acoustic Doppler Current Profiler (ADCP) measurements. The validated model is then used to analyze the flow behaviour in the presence of alternate and transverse bars. The plan form and variable bed topography (obtained from multibeam echosoundings) present a complex hydrodynamic behavior in which a number of physical processes are investigated, such as the impact of roughness-length treatment due to "sub-grid" or non-resolved effects of bed roughness [11].

II. SITE AND FIELD MEASUREMENTS

The Loire River, the largest river in France, is 1,020 km long and drains a catchment area of 117,000 km^2. The study site is located at the village of Bréhémont (47°17'43.31''N, 0°20'33.80''E) in the middle reaches of the Loire River. At the study site, the Loire system presents a multiple-channel pattern. Bed materials are constituted by sands and gravels. The main channel is composed of an expansion zone followed by a contraction area occupied by migrating bars (Fig. 1). These macroforms can adopt successively an alternate or a transverse configuration (Fig. 1) [9]. The channel width varies between 175 and 300 m.

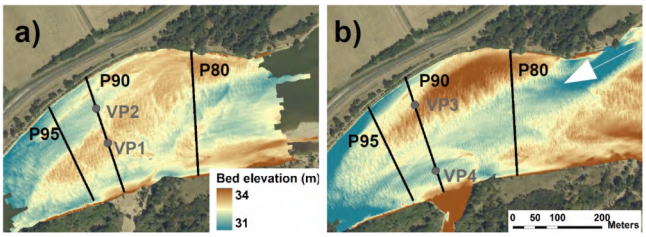

Figure 1. Study site. Black lines: ADCP profiles. Grey points: location vertical velocity profiles. (a) Transverse (22/06/10); (b) alternate (27/12/10) bar configuration. The white arrow indicates the direction of the flow.

Nineteen daily field measurements were performed during the study with a multibeam echosounder and an ADCP. Thus, three floods were monitored with a high temporal resolution: one annual flood in June 2010 (maximal discharge of 1030 m^3/s) and two 2-year floods in December 2010 (maximal discharge of 1950 m^3/s). More details are given in [9].

III. MATHEMATICAL MODEL AND NUMERICAL TOOL

The 3D hydrodynamics field is computed with the 3D hydrodynamics code belonging to the open source TELEMAC-MASCARET system (TMS), TELEMAC-3D. The TMS is currently developed by the R&D department of Electricité de France (EDF) and TELEMAC Consortium members.

TELEMAC-3D solves the 3D Navier-Stokes equations with a finite element discretization under a non-hydrostatic approximation. The code has been fully parallelized using the Message Passing Interface paradigm (MPI). The non-hydrostatic approximation is based on the pressure tained in the first plane above the bottom, with u and v the components of the 3D velocity field, and κ the von Karman's constant (= 0.4). Turbulent stresses and turbulent fluxes are modelled using turbulent viscosity and turbulent gradient diffusion hypothesis, which respectively introduce eddy viscosity and eddy diffusivity. Several turbulence-closure models are available in TELEMAC-3D, see e.g. [12]. In this study, the standard k-ε turbulence model is used.

IV. MODEL CALIBRATION AND 3D NUMERICAL RESULTS

A. Mesh description

The 3D finite element mesh is obtained by first dividing a two-dimensional domain with non-overlapping linear triangles (with a mean size of 10 m) and then by extruding each triangle along the vertical direction into linear prismatic columns that exactly fit the bottom and the free-surface. In doing so, each column can be partitioned into non-overlapping layers, requiring that two adjacent layers comprise the same number of prisms.

B. Model calibration

Model calibration is performed by comparing model predictions with averaged ADCP velocity measurements of streamwise velocities and velocity profiles at different cross-sections surveys, see Fig. 1. The optimization of model prediction is done by using a roughness-length representation based on the Nikuradse coefficient k_s. The decomposition into hydrostatic and hydrodynamic parts, allowing an accurate computation of the vertical velocity, which is coupled to the whole system of equations.

In the present study, boundary conditions are specified as follows: at the domain inflow all flow components are prescribed by imposing a velocity profile to provide a certain inflow discharge. At the domain outlet the normal gradients of all variables are set equal to zero. On the solid boundaries the velocities tangential and normal to the boundary are set to zero. Inflow and outflow boundary conditions used for the different models and configurations are shown in Table I.

The parameterization of bed shear stress is done by assuming the validity of the « law of the wall », which applies on a relatively thin layer near the bed ($z/h < 0.20$, with h the mean flow depth) [11]. In TELEMAC-3D, this approximation is used to determine the shear velocity u_* (subroutine `tfond.f`) at a distance equal to the altitude of the first plane above the bottom z':

$$u_* = \frac{\kappa |u|_r}{\ln(z'/z_0)} \quad (1)$$

where z_0 is a characteristic length scale. For hydraulically rough flows, which is the situation commonly found in natural channels $z_0 = k_s/30$, with k_s the Nikuradse's effective roughness-length. In (1), $|u|_r = (u^2 + v^2)^{1/2}$ is the magnitude of the velocity con

friction coefficients used in the models are presented in Table I.

TABLE I. BOUNDARY CONDITIONS AND BED ROUGHNESS COEFFICIENTS USED IN THE MODELS

Mesh	Flow rates (m^3/s)	Downstream water surface elevation (m)	Roughness coefficient (m)
Transverse Bar	400	34.38	0.07
	700	35.19	0.12
	1000	35.77	0.3
Alternate Bars	700	35.21	0.275
	1000	35.91	0.125
	2000	37.39	0.0975

In general, streamwise velocities are well represented by the model for the different flow discharges (Fig. 2a and 2c). Concerning the velocity profiles, for the transverse bar configuration, comparisons between measurements and numerical results are done on P90 (Fig. 1a) on VP1 (over the bar) and VP2 (thalweg). For the alternate bars configuration, comparisons are performed on P90 (Fig. 1b) on VP3 (over the right bar) and VP4 (thalweg). For both configurations,

the numerical results are in agreement with field measurements (Fig.3a and 3c), except at low discharge (400 m³/s) for the transverse bar configuration and high discharge (2000 m³/s) for the alternate bar configuration (Fig. 3b and 3d).

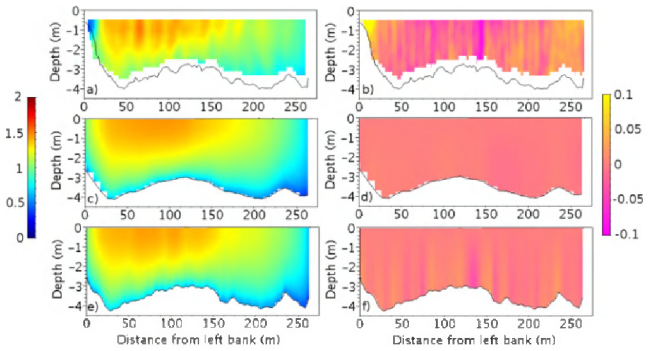

Figure 2. Cross-sectional and vertical distribution of velocities (m/s) and vertical velocities (m/s) on P90 with a transverse bar configuration for 1000 m³/s and *ks*= 0.3 m; a) measured velocities, b) measured vertical velocities, c) velocities predicted by the model with the basic mesh (element size of approx. 10 m), d) vertical velocities predicted by the model with the basic mesh, e) velocities predicted by the model with the refined and re-interpolated mesh (element size of approx. 2.5 m), f) vertical velocities predicted by the model with the refined and re-interpolated mesh. Positive vertical velocities are for upwelling, negative vertical velocities are for down welling.

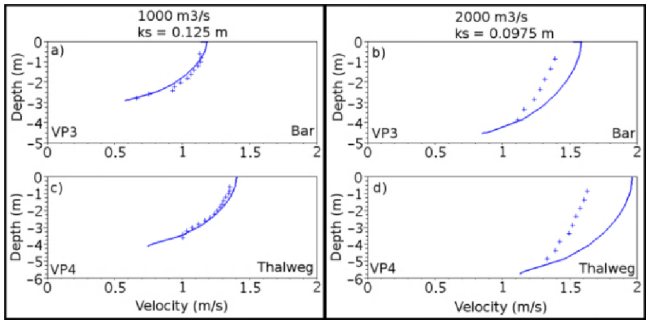

Figure 3. Measured (+) and predicted (solid lines) vertical velocity profiles for the alternate bar configuration, a) over the bar at 1000 m³/s, b) over the bar at 2000 m³/s, c) over the thalweg 1000 m³/s, d) over the thalweg 2000 m³/s.

C. *3D numerical results*

1) *Influence of the roughness-length*

Fig. 4 presents a comparison between measurements and numerical results of velocity profiles for different values of k_s. These plots show that the shape of the vertical velocity profiles depends on the roughness coefficient. This parameter strongly influences the velocity near the bed and through a significant portion of the water column, while its impact on the velocity close to the surface decreases with a deeper depth. As expected, the effect of decreasing the Nikuradse's roughness-length values will produce larger velocity gradients near the bottom. Furthermore, for the same water discharge, the *ks* do not have the same influence on the velocity profile in pools and on bars (Fig. 4a and 4b).

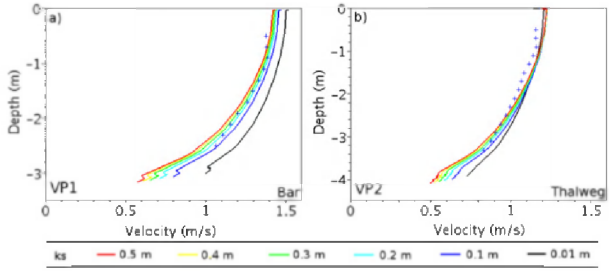

Figure 4. Vertical velocity profiles for different roughness coefficients for the transverse bar configuration at 1000 m³/s; a) over the bar, b) in the pool close to the right bank. Field data are indicated with +.

2) *Influence of the mesh resolution and convergence of the model*

The convergence of the model and mesh dependency is studied by analyzing the distribution of the velocity profiles. Fig. 5 presents the velocity profile predictions obtained with a mesh size of approx. 10 m and a mesh refined by a factor of 16 in the horizontal plane, resulting in a mesh size of approx. 2.5 m in the study zone. For this case, the finer mesh has not been re-interpolated. The results show that the velocity profiles remain almost unaffected to the mesh refinement. For a horizontal mesh discretization with a mesh size of approx. 10 m, the convergence of the model to the refinement in the vertical direction show little impact on the model results (Fig. 5). Further analysis showed that, in our study, a distribution of eight vertical planes is an optimal compromise between model efficiency and accuracy.

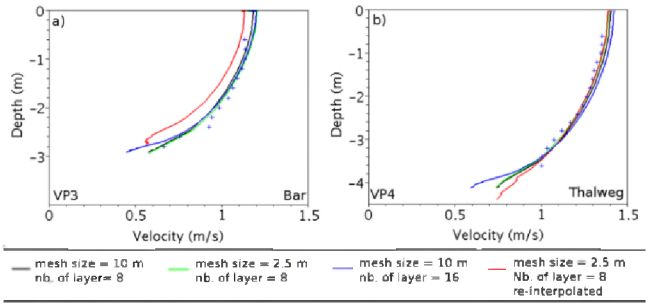

Figure 5. Influence of mesh refinement and reinterpolation on vertical velocity profiles at 1000 m³/s in alternate bar configuration. a) over the bar, b) over the thalweg. Field data are indicated with +.

Re-interpolating the topographic information into the nodes of a spatially refined mesh can lead to significant changes in the model results, as is shown in Fig. 2e, 2f and 5. Generally, the refinement and re-interpolation of the meshes do not improve significantly the magnitude of the velocities and the vertical velocities (Fig. 5b). Also, refinement and re-interpolation can give worse predictions (Fig. 5a). However, the horizontal resolution of a mesh size of approx. 2.5 m incorporates small scale topographic features that cannot be captured with a horizontal mesh resolution of 10 m (Fig. 2e and 2f). Therefore, the increase in mesh resolution impacts the bed resistance mechanisms and, in consequence, the distribution of the velocity profiles. Moreover, vertical accuracy can be further improved with the increasing of grid resolution and re-interpolating topographic information. Fig. 2a-f shows a comparison of measured ADCP vertical

velocities and model results for a horizontal mesh resolution of 10 m and a mesh reduced by a factor of 4, respectively. These results show how the mesh resolution affects dramatically the velocity distribution. In this case, the coarse mesh "filters" topographic features that are well captured by the high resolution mesh, with important consequences on the prediction of energy losses and therefore, on the correct evaluation of the shear stresses.

3) Analysis of the flow structure for the transverse and alternate bars configurations

For the transverse and alternate configurations, the streamwise and crosswise velocities are presented respectively in Fig. 6 and 7 for a discharge of 1000 m^3/s. Numerical simulations show that the flow structure and distribution remains almost identical for both the alternate and transverse bars configuration, with higher speeds located in the thalweg, between the left bank and the top of the bars (Fig. 6a and 6b). However, small differences exist between both configurations, as the transverse bar concentrates the flows more to the left part of the channel, leading to higher velocities.

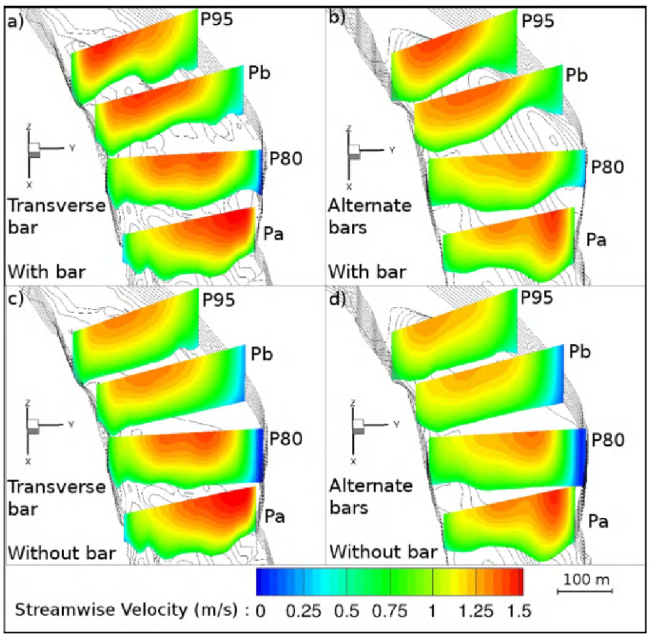

Figure 6. Cross-sectional and vertical distribution of streamwise velocities at 1000 m^3/s; a) transverse bar configuration, b) alternate bars configuration, c) transverse bar configuration with the bar deleted, d) alternate bars configuration with the bars deleted.

The analysis of the crosswise velocities shows a flow divergence zone near the left edge of the bars and convergence zones coincident with the position of the right edge of the bars (Fig. 7a and 7b). Flow convergence is also found in the thalweg. The projection of the flow field onto the crosswise section shows a clear difference between the magnitude of the transversal velocity component in the deeper depth zone of the channel with respect of the portion occupied by the bars (see P80 and P95).

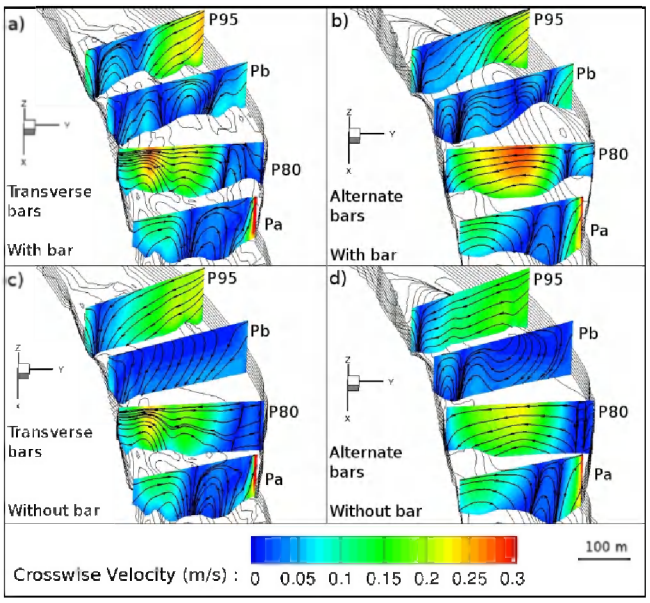

Figure 7. Cross-sectional and vertical distribution of crosswise at 1000 m^3/s; a) transverse bar configuration, b) alternate bars configuration, c) transverse bar configuration with the bar deleted, d) alternate bars configuration with the bars deleted. Arrows represent the direction of the crosswise velocities.

To study the influence of the bars on the streamwise and crosswise velocities, two new models were built. These models present similar characteristics than the models presented previously, except that the macroforms were removed from the topographic information. Simulation results are presented in Fig. 6c, 6d, 7c and 7d for a discharge of 1000 m^3/s. Fig. 6 shows that the absence of the bars causes a decreasing of the intensity of the streamwise velocity. Nevertheless, the zones of higher velocities remain almost identical when comparing with those of the topography with the bars.

The effect of the absence of bars seems to be more important for the distribution of the crosswise velocities (Fig. 7). For the profile P80, the absence of the macroforms motorizes a projection of the flow towards the divergence zone near the right bank. On the left bank, crosswise velocities present a lower intensity. At the Pb profile (between profiles P80 and P95), the zones of convergence and divergence of the flow over the bars disappear. Finally, at the profile P95 the transversal velocities exhibit higher velocities than in the presence of bars, while the velocities direction remains almost identical.

V. DISCUSSION AND CONCLUSIONS

Our numerical results showed that the predicted velocities evolve differently according to the water depth when the roughness coefficient is changed (Fig. 4). These observations, similar as those of Sandbach *et al.* [11], show that the influence of the roughness coefficient on the hydrodynamic differs for the different morphological units (bars, thalweg, pool, etc…). This means that during floods (when the values of *ks* change significantly), the the hydrodynamic and the sediment dynamics associated with the bars and the thalweg could follow different evolutions,

and, like for the hydraulic reversal theory (velocity shear stress), could affect the formation of pools and riffles [13].

Furthermore, for a water discharge and a bar configuration, the vertical velocity profiles obtained from the models are in relative agreement with the field measurements according to their location (thalweg or bar) (Fig. 3a, 3c and 5). These results may indicate a spatial variability of the bed roughness. Thus, the bars and the thalweg could be associated to different roughness-lengths in order to improve the hydrodynamic calibration. This observation is supported by the results of a study on the dunes dynamic on the site [9] which show that the mesoforms adopt different sizes on the thalweg and on the bars. Using several bed roughness on the domain is probably more pertinent.

No relationship seems to link the bed roughness coefficients obtained after the calibration and the water discharge (Table I). This illustrates the complexity of the interactions between hydrodynamic and bed roughness (characterized during floods by complex hysteresis [14]), which depends strongly to the dunes dynamic (in sand-bed rivers as the Loire). The present study highlights this point by showing the influence of the small dunes on the bed roughness and the flows. Indeed, only the dunes longer than 10 m have been integrated in the spatial discretization. It is admitted that the influence of the bedforms smaller than the elements of the meshes is parameterized through the roughness length coefficient [11]. Sensitivity analysis have shown that for a constant k_s, the use of refined meshes and re-interpolated on a more detailed bed topography, gives values of velocities similar to those predicted by calculations with the basic meshes (Fig. 5b). Normally, the bed roughness of the refined meshes should be increased (roughness of the small dunes + *ks* of the models) and the velocities decreased. As it is rarely the case, the results of the sensitive tests indicate that the small dunes seems to not contribute significantly to the bed roughness. Nevertheless, in general, the integration of the small bedforms in the meshes improves the representation of the flow structure. Thus, with the refined and re-interpolated meshes, the distribution of the velocities follow vertical and crosswise variations close to those observed in the field data (Fig. 2e). The integration of the small dunes also improves significantly the calculation of the vertical velocities (Fig. 2f). This indicates that the small bedforms strongly influence the vertical velocities; the latter being linked to the turbulences generated by these small dunes. Thus, if the turbulence affects significantly the sediment dynamics (especially for the suspended sediment and therefore, the von Karman constant), and by extension the morphology of the bed, it seems necessary to integrate the small bedforms into the morphodynamic models. However, it should be noticed that in some cases, the refinement of the mesh modified the bed topography so much that the results of the simulation can be locally degraded.

Calibration and sensitivity tests have showed a systematic overestimation of the velocities predicted for a discharge of 2000 m^3/s applied on alternate bars configuration (Fig. 3b and 3d). This can be explained by the not-representation of a secondary channel in the models on the left bank close to the profile P90. Indeed, this secondary channel is totally connected above 1700 m3/s [9]. Thus at 2000 m^3/s, the connection of the secondary channel should decrease the water discharge in the main channel (from P90). As the reducing of the water discharge in the models is no considered, the predicted velocities are overestimated compared to the field data. A deeper investigation of the influence of the connection/disconnection of the secondary channel on the main channel's hydrodynamic should improve our understanding of bifurcations.

The results of the models show that the general flow is defined by the channel planform. However, the bars modify the hydrodynamic. Indeed, the macroforms deflect the streamlines and concentrate the flows in the thalweg. Thus, the large flow velocities (Fig. 6) are constrained on the edge of the bars which follow the thalweg. It also seems that the macroforms constitute a physical limit which gives the currents a different structure on either side of the bars. The bars control the location of the divergence and convergence zones, respectively caused by the channel widening and narrowing (Fig. 7). Thus, the separation and the mixing of the currents always take place, respectively, on the crest and downstream of the macroforms. The bars' configurations (i.e. alternate or transverse) in the channel partly determine the location of the large flow velocities and those of the divergence and convergence zones.

This study allowed the validation of TELEMAC-3D to reproduce the hydrodynamics in a complex morphological environment in the presence of transverse and alternate bars. Future work include the coupling to the morphodynamic model (SISYPHE) in order to simulate the sedimentary processes around the bars, for a better understanding of their formation and evolution in natural systems [7].

ACKNOWLEDGEMENT

The measurements were funded by the Master Plan Loire Grandeur Nature-FEDER (Presage n° 30809). The authors thank Philippe Jugé, Yann Guerez, Vincent Bustillo, Benoît Delplancque, Benjamin Gandubert and Olivier Guillemet for their help during the measurements. The four month research scholarship of Benjamin Magnier is gratefully acknowledged.

REFERENCES

[1] M. Colombini, G. Seminara and M. Tubino (1987). "Finite-amplitude alternate bars." Journal of Fluid Mechanics, 181, 1, pp. 213-232.

[2] G. Seminara and M. Tubino (1989). "Alternate bars and meandering: free, forced and mixed interactions." River meandering, S. Ikeda and G. Parker, Washington, American Geophysical Union - Water Resources Monographs 12, p. 267-320.

[3] M. Tubino (1991). "Growth of alternate bars in unsteady flow." Water Resour. Res., 27, 1, pp. 37-52.

[4] S. Lanzoni (2000). "Experiments on bar formation in a straight flume: 1. Uniform sediment." Water Resour. Res., 36, 11, pp. 3337-3349, doi:10.1029/2000WR900160.

[5] M. Tubino, R. Repetto and G. Zolezzi (1999). "Free bars in rivers." Journal of Hydraulic Research, 37, 6, pp. 759-775.

[6] A. Crosato and E. Mosselman (2009). "Simple physics-based predictor for the number of river bars and the transition between

meandering and braiding." Water Resour. Res., 45, 3, pp. W03424, doi:10.1029/2008WR007242.

[7] F. Mattia, D. Wang, J.-M. Hervouet, A. Leopardi, K. El Kadi Abderrezzak and P. Tassi (2013). "Numerical simulations of bar formation and propagation in straight and curved channels." XXth TELEMAC-MASCARET Users conference, Karlsruhe, Germany.

[8] F. C. Wu, Y. C. Shao and Y. C. Chen (2011). "Quantifying the forcing effect of channel width variations on free bars: Morphodynamic modeling based on characteristic dissipative Galerkin scheme." J. Geophys. Res., 116, pp. F03023, doi:10.1029/2010JF001941.

[9] N. Claude (2012). "Processus et flux hydro-sédimentaires en rivière sablo-graveleuse : influence de la largeur de section et des bifurcations en Loire moyenne (France)." PhD, University of Tours, Tours, p. 366.

[10] N. Claude, S. Rodrigues, V. Bustillo, J.-G. Bréhéret, P. Tassi and P. Jugé (2013). "Interactions between flow structure and morphodynamic of migrating bars in a channel expansion/contraction, Loire River, France.", unpublished.

[11] S. D. Sandbach, S. N. Lane, R. J. Hardy, M. L. Amsler, P. J. Ashworth, J. L. Best, A. P. Nicholas, O. Orfeo, D. R. Parsons, A. J. H. Reesink and Szupiany R.N. (2012). "Application of a roughness-length representation to parameterize energy loss in 3-D numerical simulations of large rivers." Water Resour. Res., 48, 12, doi:10.1029/2011WR011284.

[12] J.-M. Hervouet (2007). "Hydrodynamics of free surface flows, modelling with the finite element method", John Wiley & Sons.

[13] E. A. Keller (1971). "Areal sorting of bed-load material: the hypothesis of velocity reversal." Bulletin of the Geological Society of America, 82, 3, pp. 753-756.

[14] R. M. Frings and M. G. Kleinhans (2008). "Complex variations in sediment transport at three large river bifurcations during discharge waves in the river Rhine." Sedimentology, 55, 5, pp. 1145-1171, doi:10.1111/j.1365-3091.2007.00940.x.

TUC 2013, 16-18/10/2013, Karlsruhe - Kopmann, Goll (eds.) - © 2013 Bundesanstalt für Wasserbau ISBN 978-3-939230-07-6

Modelling the eddy pattern in the harbour of Zeebrugge

W.A. Breugem, B. Decrop, J. Da Silva, and G. Van Holland
IMDC NV
Berchem, Belgium
abr@imdc.be

C. Martens
afdeling Maritieme Toegang
Departement Mobiliteit en Openbare werken van de Vlaamse overheid
Antwerpen Belgium

***Abstract*—The eddy patterns in the harbour of Zeebrugge are studied using TELEMAC-3D and compared to available measurement data. It was found that during flood a clockwise eddy exists, generated by a strong jet near the eastern side of the harbour entrance. This eddy generates a second counter-clockwise eddy, which persists in the harbour during the ebb phase, whereas the primary eddy disappears. A sensitivity study was performed to investigate the influence of the turbulence model, the bed roughness and the advection scheme. It appeared that the modelled eddy patterns are quite sensitive to the settings that are used for all these three parameters.**

I. Introduction

The harbour of Zeebrugge is one of the most important Belgian seaports. The area surrounding Zeebrugge is characterised by strong tidal flows, with a tidal amplitude up to 5m during spring tide. In the harbour, complex eddy flow patterns are found, varying throughout the tidal cycle. Understanding these patterns is important for navigation purposes and for increasing our understanding of the siltation of the harbour, especially with respect to the redistribution of suspended sediment through the harbour.

In order to understand this process, the eddy pattern in the harbour is studied using TELEMAC-3D. The results of the TELEMAC model are compared with measurements, and a sensitivity test is performed with respect to the eddy formation by varying the bed roughness, the advection scheme and the horizontal turbulence model.

II. Phenomenology of the Eddy Currents in the Harbour of Zeebrugge

In order to study the phenomenology, an existing data set of ADCP (Acoustic Doppler Current Profiler) measurements was used [1]. These measurements were taken on different locations in the harbour and the navigation channel on various days between November 2009 and March 2010. Because the data were taken on different occasions, we put together the data from various measurement days, sorting them with respect to the time after high water (from now on abbreviated as HW) and according to the spring-neap tidal cycle. In this paper, we will only study the data from spring tide conditions. In the analysis, we focus on what happens in the period around the occurrence of high water, when the strongest eddies are formed.

The ADCP data show the following pattern (Fig. 1; note that additional arrows have been added to aid interpretation of the data):

- 2 h before HW: There is a net flux of water into the harbour in the form of a jet at the eastern harbour dam. The jet increases in length and strength with time. This jet generates an eddy in clockwise direction, which we will call the primary eddy.
- 1 h before HW: A smaller secondary eddy with a counter clockwise rotation is also generated by the jet.
- Around HW: From this moment, there is no net inflow of water in the harbour. Hence the eddy is decoupled from the flow at sea and it follows its own dynamics. It appears that the primary eddy starts decreasing in size and magnitude.
- 1 h after HW: Only the counter clockwise secondary eddy remains present in the harbour. It moves slowly towards the harbour entrance and gradually becomes weaker.

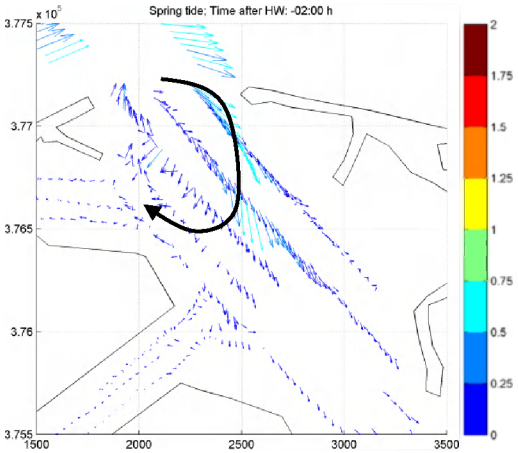

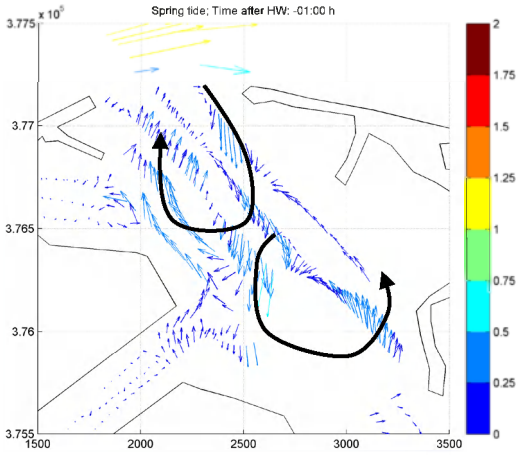

Figure 1. Overview of the eddy development in the harbour of Zeebrugge from ADCP measurements.

Comparable eddy patterns are found in the measurements during average tide, whereas the formation of this pattern is much less pronounced during neap tide.

One must take care when interpreting the measured data, because the presented data was collected during different measurement days. There is always some error associated with the matching procedure, because the tidal amplitude and period are not completely the same for the different measurement days. Nevertheless, the discussed pattern seems to be representative for the conditions occurring in the harbour, since earlier data [2] show similar results for the observed eddy patterns.

III. MODEL SETUP

The model was set up in a circular domain centred around the harbour of Zeebrugge, starting from Dunkirque (France) in the West to Goeree-Overflakkee (the Netherlands) in the East (Fig. 2). The Eastern and Western Scheldt estuaries are included in the model, although the most upstream part of the Western Scheldt was schematized using straight prismatic channels. The resolution varied from 30 m inside the harbour to 5000 m close to the open boundary (Fig. 3). Vertically, ten non-equidistant sigma layers were used to represent the water column.

Boundary conditions for velocity and water level were obtained from the Zuno [3] model, which has a resolution comparable to our model at the location of these boundaries. These boundary condition were applied as a time series (with a time interval of 10 min) at each location on the open boundary. Additional discharge boundary conditions were applied to schematise fresh water influxes into the model. Note that one of the sources of fresh water was located inside the harbour.

The model was run in TELEMAC-3D for a period of 15 days using a time step of 20 seconds using the Smagorinsky scheme for the horizontal eddy viscosity and a mixing length model using the mixing length parameterization of Nezu and Nakagawa [4] for the vertical eddy viscosity.

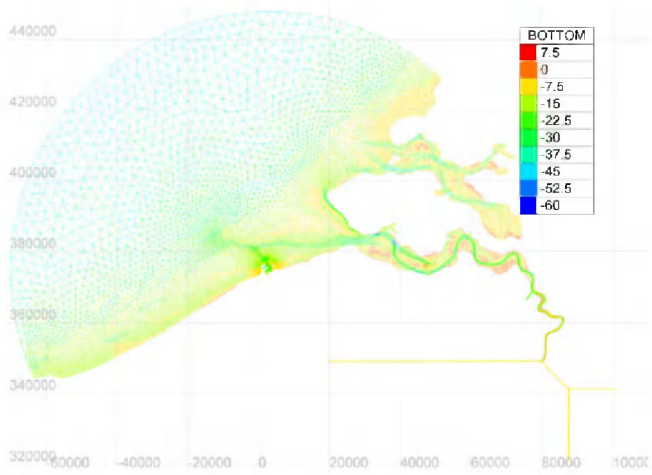

Figure 2. Mesh and bathymetry of the model

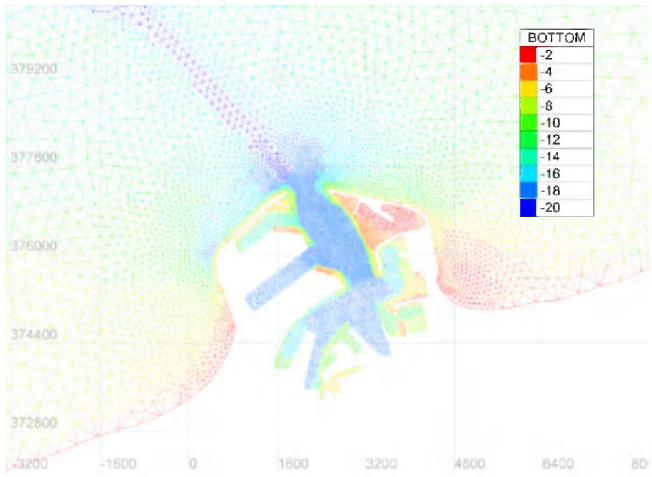

Figure 3. Detail of the mesh close to the harbour

The model was calibrated using water level and velocity data at sea. This leads to a Manning roughness coefficient of 0.02 s/m$^{1/3}$. Close to the harbour entrance, the friction coefficient was increased, in order to represent the effect of the friction due to the large concrete elements of the breakwater (Fig. 3).

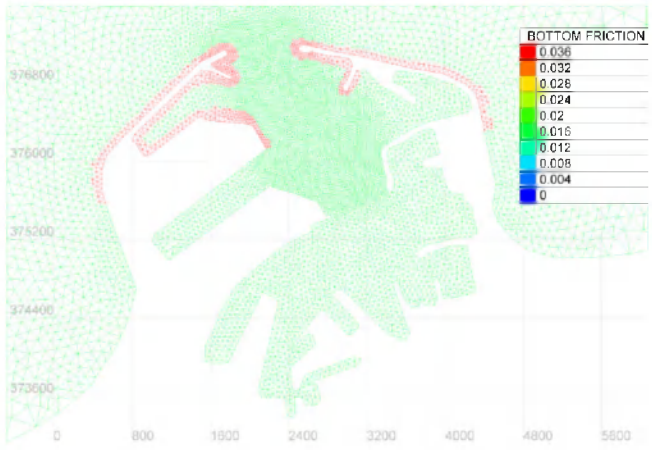

Figure 4. Manning roughness coefficient close to the harbour

A comparison of measurement data and model results for the water level time series showed typical bias of 0.1 m, and a root mean squared error (rms) of 0.15 m. The depth averaged velocities have a bias of -0.04 m/s and a rms error of less than 0.13 m/s. A comparison of high water and low water levels shows typical rms errors of 0.13 m, while a comparison of the high and low water levels resulted in a typical rms error of 10 min. These errors compare well with those of the Zuno model that was used for the open boundaries [3] and they were considered sufficiently accurate for our purposes.

IV. RESULTS

The results of the model are shown in Fig. 5. The model reproduces the strong jet found in the measurements, although it occurs somewhat later in the tide (Fig. 5a). In the model, the jet seems to be even more pronounced than in the measurements. However, the jet is located somewhat more to the east in the model than in the measurements. The model also shows a strong primary eddy. Further, the jet also generates a secondary circulation which is weaker than the primary eddy (Fig. 5b).

Approximately one hour after high water both the primary and secondary eddy are present in the model results (Fig. 5c). With the course of time, the primary eddy elongates and decreases strongly in strength, while the decrease of the secondary eddy is less. As a result of this process, the primary eddy disappears completely, just as seen in the measurements (Fig. 5d). However, in the model a very weak tertiary eddy developed north of the primary eddy, with the same direction of rotation as the secondary eddy. This eddy could not be observed in the measurements. The reason for this is probably that it is to weak and small to be observed with the relatively limited spatial resolution provided by the ADCP measurements.

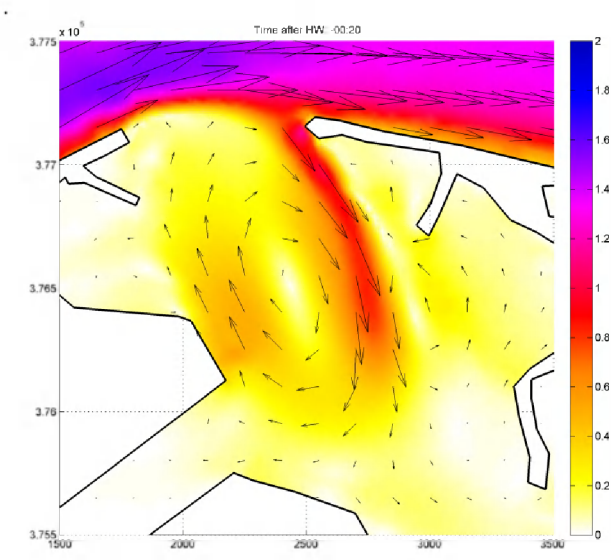

a.

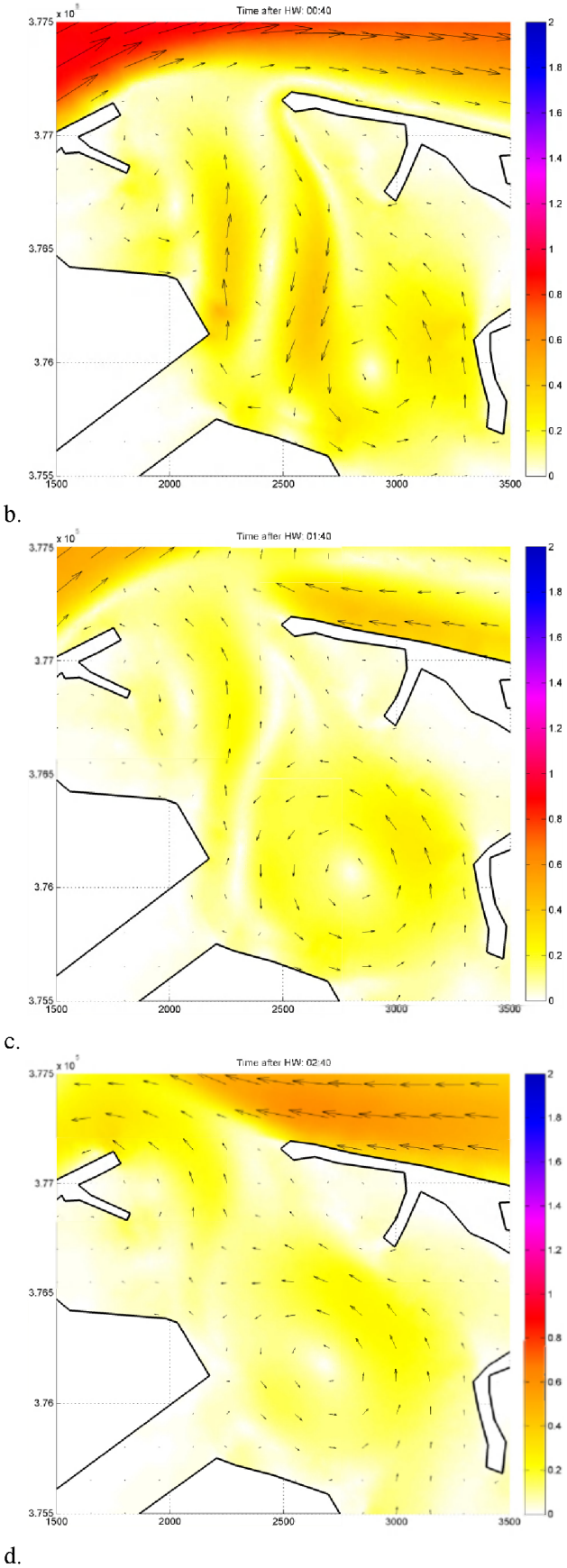

V. SENSITIVITY ANALYSIS

A. Bed roughness

In order to assess the sensitivity towards the bed roughness on the formation of the eddy patterns, we eliminated the increased bed roughness at the harbour entrance. Thus the simulation was done using a constant Manning roughness coefficient of 0.02 s/m$^{1/3}$. The modelled eddy pattern changes dramatically in comparison with the base run (Fig. 6). At first, we see the same jet developing (Fig. 6a). However, it has a slightly different location. This gives the primary eddy a slightly stronger circulation and the secondary circulation that develops is slightly weaker than in the base run (Fig. 6b). Consequently, the primary eddy does not disappear with time (Fig. 6c). Thus we end up with two eddies in the harbour during the ebb phase, rather than one (Fig. 6d), which does not correspond to the measurements.

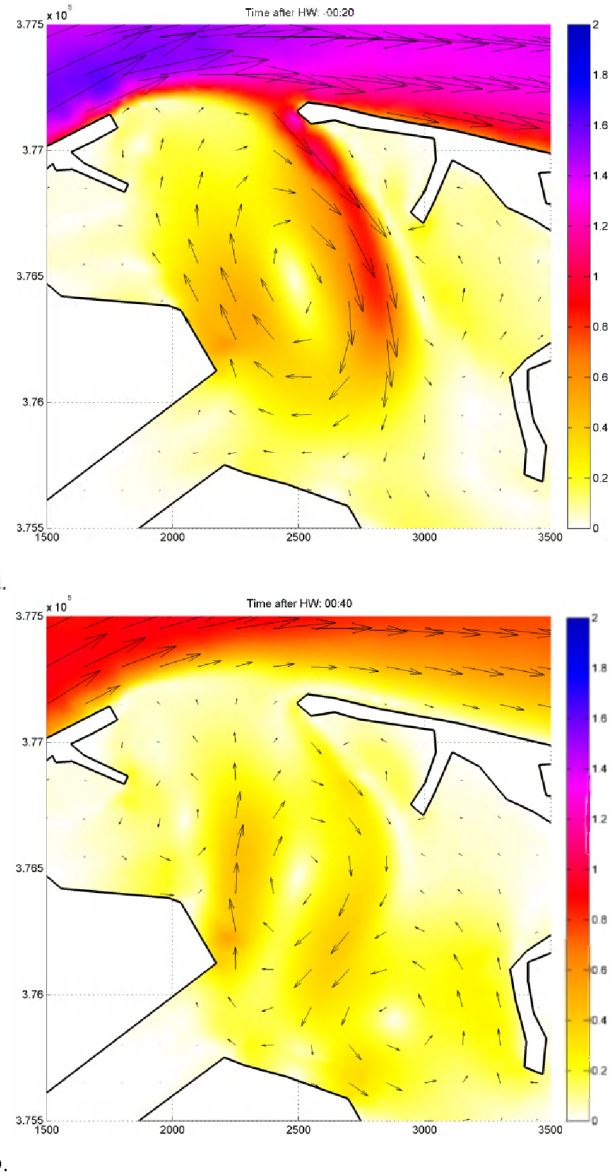

Figure 5. Development of the modelled eddy pattern (base run)

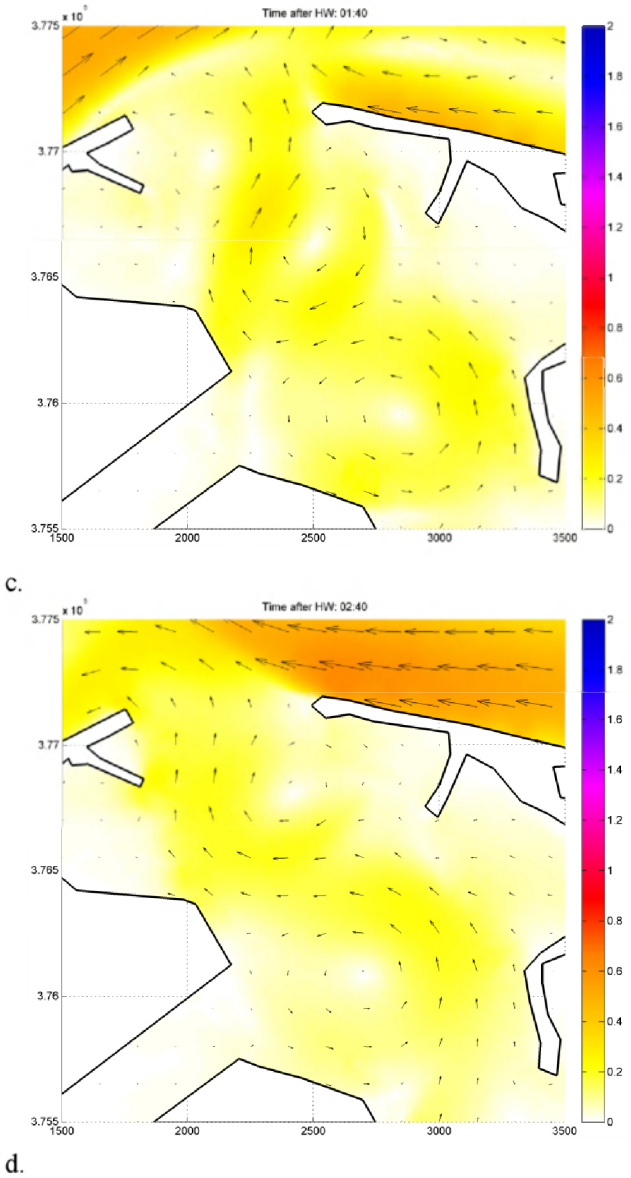

Figure 6. Modelled eddy patterns, without increased bottom friction at the break waters.

B. *Advection scheme*

The previous simulations were done using the characteristic method as advection scheme for the advection of velocity. In order to test the sensitivity toward the used advection scheme, computational runs were performed using the two schemes that were especially suited to use in combination with the use of tidal flats: the "Leo Postma scheme" and the "N-scheme".

Once again, the resulting eddy patterns change dramatically compared to the base run (Fig. 7) Note that for brevity, only two time steps for the N-scheme are shown. The Leo Postma scheme gave qualitatively similar results). In fact, the eddy pattern that develops is rather similar to the simulation without bottom friction at the breakwaters (section V.A). We see both a primary eddy and a secondary eddy, with the primary eddy being slightly stronger than the secondary eddy.

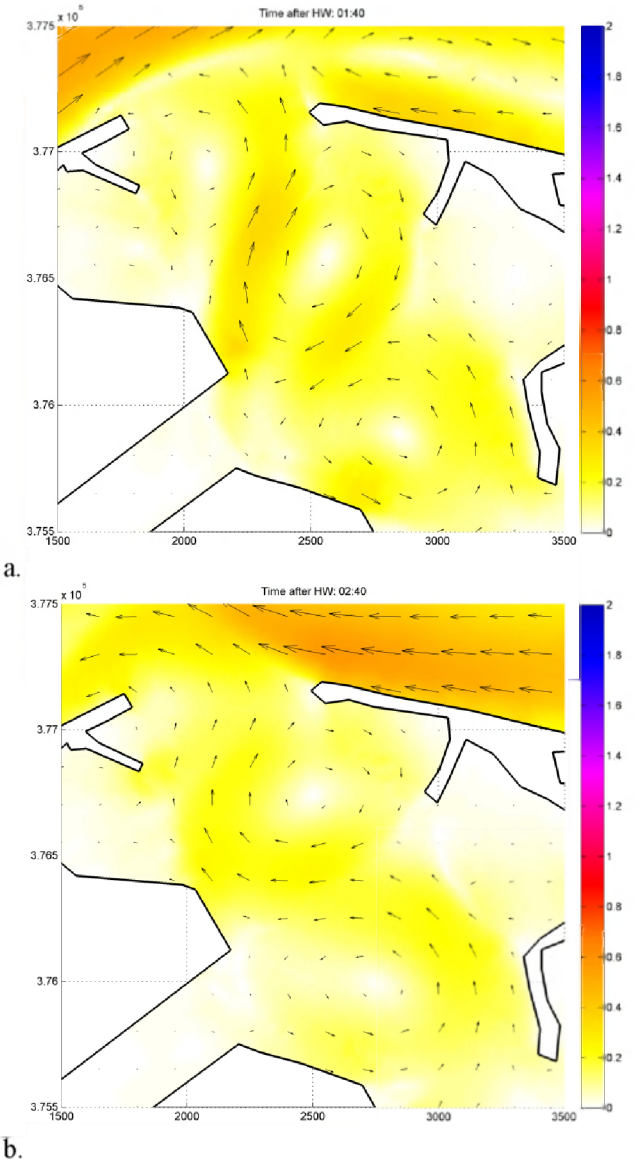

Figure 7. Modelled eddy patterns using the "N-scheme"

C. *Turbulence modeling/eddy viscosity*

In order to test the sensitivity toward the used horizontal turbulence model a model with a constant horizontal eddy viscosity of 1.0 m^2/s was used. This value is somewhat higher than those calculated using the Smagorinsky scheme used in the other runs, which were in this area in the order of 10^{-2} m^2/s.

The use of a high eddy viscosity coefficient weakens the jet at the harbour entrance (Fig. 8a). The secondary eddy develops but is weaker than the primary eddy (Fig. 8b). Therefore, in this situation only the primary eddy remains in the harbour during the start of the ebb phase (Fig. 8c), and it is stronger than the secondary eddy. Nevertheless, the primary eddy disappears eventually, leading to a flow direction that corresponds to the measurements (Fig. 8d).

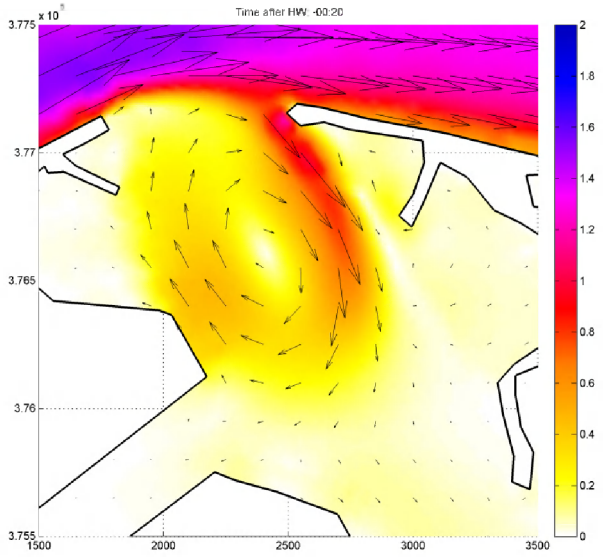

a.

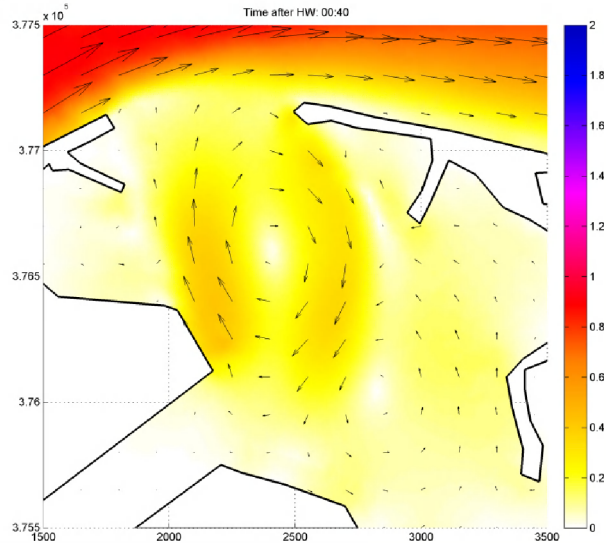

b.

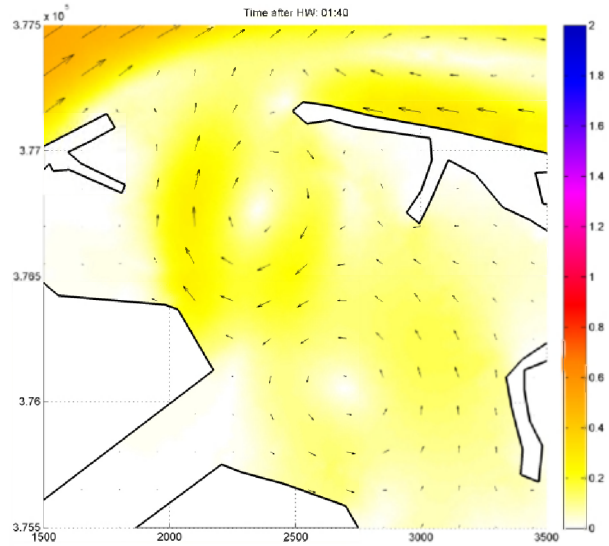

c.

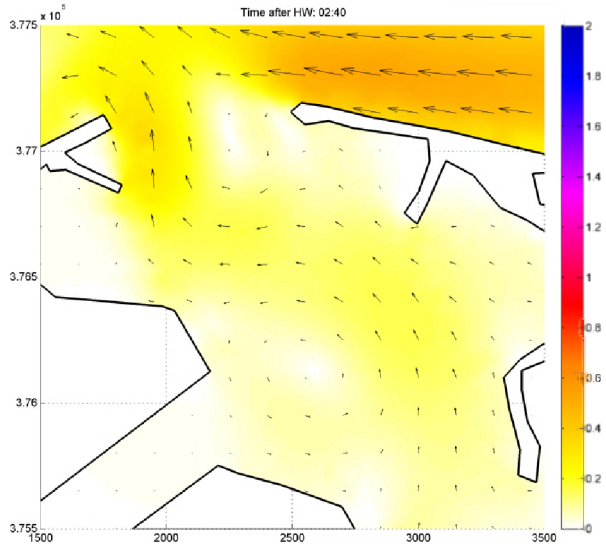

d.

Figure 8. Model results with a constant eddy viscosity of 1.0 m^2/s

Note that simulations with a constant eddy viscosity of 0.01 m^2/s (thus comparable with those calculated using the Smagorinsky model) gave similar results for the eddies as the base run.

VI. SUMMARY AND CONLUSIONS

A TELEMAC-3D model was developed in order to study the eddy patterns occurring in the harbour of Zeebrugge. It appears that a strong jet is formed some time before high water during the moment of strongest inflow. The jet generates a clockwise and a counter clockwise eddy, from which only the counter clockwise eddy remains visible during the ebb phase. A comparison between ADCP measurements and the model showed that this behaviour could be simulated using TELEMAC. A sensitivity analysis showed that the results are very sensitive to the bed friction close to the edges of the harbour. The used advection scheme and the calculation method for the horizontal eddy viscosity, and the variation of these parameters could lead to a different number of eddies present in the harbour.

ACKNOWLEDGEMENT

Project funded under project number '16EF201116.' assigned by the Maritime Access Division (aMT) of the Department of Mobility and Public Works of the Flemish Government.

REFERENCES

[1] Eurosense and Aquavision, “Stroomatlas Zeebrugge Verwerkingsrapport” 2011 (in dutch)

[2] Ministerie van de Vlaamse Gemeenschap, “Stroomatlas haven van Zeebrugge” 1998 (in dutch)

[3] Vanlede, J.; Leyssen,G.; Mostaert, F., (2011) Modellentrein CSM-ZUNO. Deelrapport 1: opzet en gevoeligheidsanalyse. WL Rapporten WL2011R753_12rev1_1 (in dutch)

[4] I. Nezu and H. Nakagawa "Turbulence in Open-Channel Flows", IAHR Monographs, A.A. Balkema, 1993, 281 pages

TUC 2013, 16-18/10/2013, Karlsruhe - Kopmann, Goll (eds.) - © 2013 Bundesanstalt für Wasserbau ISBN 978-3-939230-07-6

Tropical Cyclone Modelling with TELEMAC-2D

A. Cooper, M. Turnbull, S. Grey, P. Loilier
HR Wallingford Ltd
Wallingford, UK
a.cooper@hrwallingford.com

***Abstract*—Model testing has shown that the use of schematic wind models can reproduce well the observed rotating wind field in a tropical cyclone. Imposing the wind field and air pressure field in TELEMAC-2D has been found to give good results in comparison with observed storm surge levels at tide gauges during a cyclone.**

The purpose of this study was to validate the capability of TELEMAC-2D to model the storm surge due to a tropical cyclone. These storms are also referred to as hurricanes and typhoons in different parts of the world. The surge arises as a result both of the pressure drop in the middle of the cyclone and also because of the resulting rotating wind. The effects on the flows of the wind and the atmospheric pressure variation are included in TELEMAC-2D. Storm surge is important as flooding is often the greatest danger to life due to a cyclone.

Because of the large amount of data available, cyclone Yasi (Australia, Queensland, 2011) was selected for this study. Available data included wind speed and direction at 12 sites near to the cyclone's track measured throughout the cyclone's passage. Tide gauge data at a number of ports was also available (see Fig. 1).

Data from the Australian Bureau of Meteorology included the cyclone's track, and the central pressure and maximum wind speed during the storm's passage. Cyclone Yasi had a track (see Fig. 1) making landfall near Clump Point. A minimum pressure of 929mB was measured at Clump Point and a maximum wind speed of 57m/s was estimated. The maximum recorded storm surge was 5.33m at Cardwell.

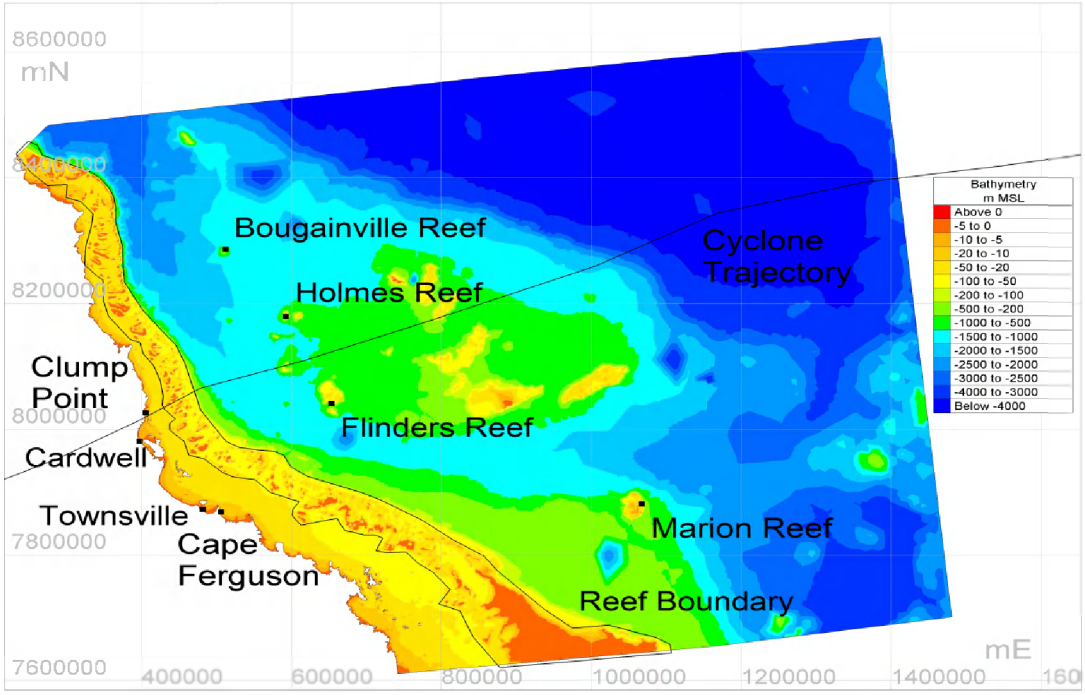

Figure 1. Observation locations (wind and surge).

Tropical cyclones are characterised by a strong, circular wind field that can be represented approximately in a 1D model as the wind and pressure vary mostly in the radial direction. The atmospheric pressure is a minimum at the centre of the storm.

The available information on a cyclonic storm is likely to include that given above (track, central pressure, maximum wind speed and sometimes radius to maximum wind speed) although the radius to maximum wind is not always known. Under these circumstances it is usual to create a schematic wind and pressure model and compare it as far as is possible with any wind and pressure data that are available. Another possibility could be to use a detailed atmospheric model to simulate the wind and pressure fields, but that was not the method chosen in this case.

Flow model simulations carried out included the following:

- *Using a wind field from Holland (1980) or Jelesnianski and Taylor (1973)*

At each location in each wind field, the wind speed was determined based on the parameters of the cyclone at the time and the distance of the point from the centre of cyclone. Both Jelesnianski and Taylor (1973) and Holland (1980) formulations were implemented in the model.

The relation used from Jelesnianski and Taylor (1973) is:

$$U_i = \frac{2rR_{\max}}{r^2 + R_{\max}^2} U_{\max} \qquad (1)$$

where U_i (m/s) is the speed at location i, r is the distance of i (km) from the centre of the cyclone, U_{max} is the maximum wind speed (m/s) and R_{max} is the radius of the maximum wind speed (km).

The wind velocity given in Holland (1980) is:

$$U_i^2 = U_{\max}^2 \exp\left(1 - \frac{R_{\max}^{\beta}}{r^{\beta}}\right) \frac{R_{\max}^{\beta}}{r^{\beta}} \qquad (2)$$

The β coefficient is calculated from the central pressure drop P_{drop} (Pa) and the maximum wind velocity U_{max} (m/s) as:

$$\beta = U_{\max}^2 \rho e / P_{drop} \qquad (3)$$

with ρ is density of air and e the base of natural logarithms.

The representation of the wind was best achieved using the Holland (1980) wind formulation (see Fig. 2). This is partly because the Holland beta coefficient allows for reproducing different profile shapes of the radial wind speed distribution.

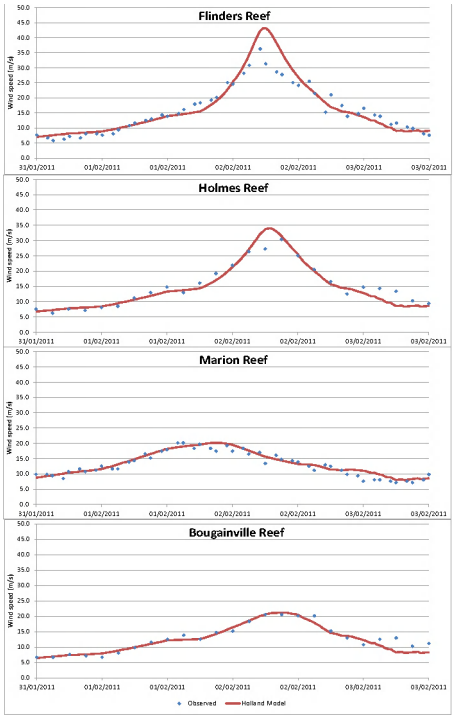

Figure 2. Comparison of modelled and observed wind speed time histories.

- *Including/excluding the forward tracking speed in computing the wind field*

The forward tracking speed of the cyclone is added into the cyclone wind field based upon a formulation of McConochie et al (2004). This method allows the contribution of the forward tracking speed to decrease with increasing distance from the centre of the storm. By adding in the forward tracking speed the wind speed on one side of the cyclone is increased and that on the other side decreased so the cyclone is no longer circularly symmetric.

- *Including/excluding the inward angle of the wind*

It is expected that the wind close to the ground will have a component of flow towards the centre of the cyclone driven by the low pressure there.

The winds circulate clockwise around a southern hemisphere cyclone. The direction of the wind is assumed to be close to a circular wind field but with an inflow angle dependent on the distance from the centre. The wind inflow angle, β, follows the relation:

$$\begin{array}{cc} 0 \le r < Rmax & \beta = r/Rmax \times 10° \\ Rmax \le r \le 1.2\ Rmax & \beta = 10° + 5(r/Rmax - 1) \times 15° \\ r > 1.2\ Rmax & \beta = 25° \end{array} \qquad (4)$$

- Including/excluding the effect of the tide

The TELEMAC-2D simulation shows a large surge spread along the coast (Fig. 3). The surge was strong due to the particularly high speed cyclone winds and the broad continental shelf. At Cardwell which lies close to where the wind was strongest the surge was also enhanced by constriction of the surge within the bay.

In the case of cyclone Yasi the best schematic wind representation was using the Holland (1980) model with time varying beta value. The best simulation of the peak surge levels (Fig. 4) at the tide gauge locations included:

- adding the forward tracking speed of the storm (so the wind field is not symmetrical)
- an inward angle of the wind near the ground.
- The flow modelling included the tide (but it did not make a great difference if the tide was not modelled)
- an enhanced friction at the location of the Great Barrier Reef (location shown in Fig. 1).

In this best simulation the mean value over 7 tide gauges of the absolute error in the predicted peak storm surge was 0.33m.

REFERENCES

[1] G. Holland, "An analytic model of the wind and pressure profiles in hurricanes", Monthly Weather Review, Vol 108, p1212-1218,1980

[2] C.P. Jelesnianski and A.D. Taylor, "A preliminary view of storm surges before and after storm modifications", NOAA, 1973, Technical Memorandum ERL, WMPO-3 p23-33

[3] J.D. McConochie, T. A. Hardy and L. B. Mason, "Modelling tropical cyclone over-water wind and pressure fields", Ocean Engineering 31 (2004) p1757-1782

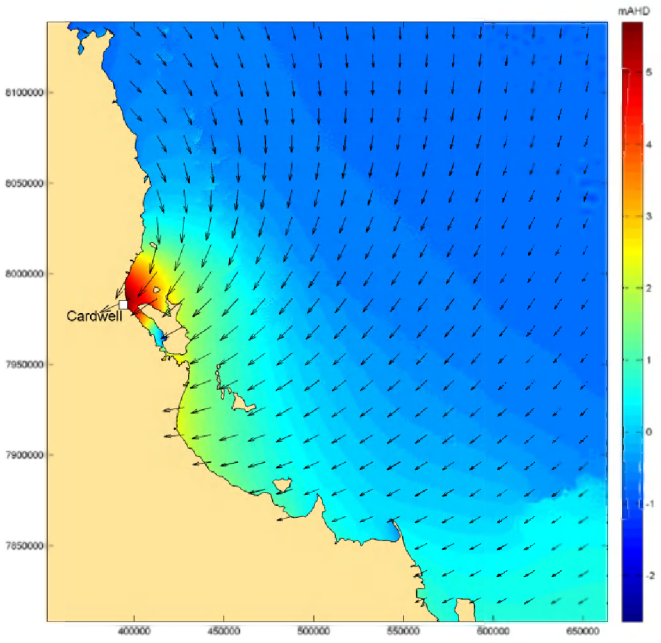

Figure 3. TELEMAC-2D simulation of water level due to Cyclone Yasi at the time of maximum surge at Cardwell. The arrows show wind vectors.

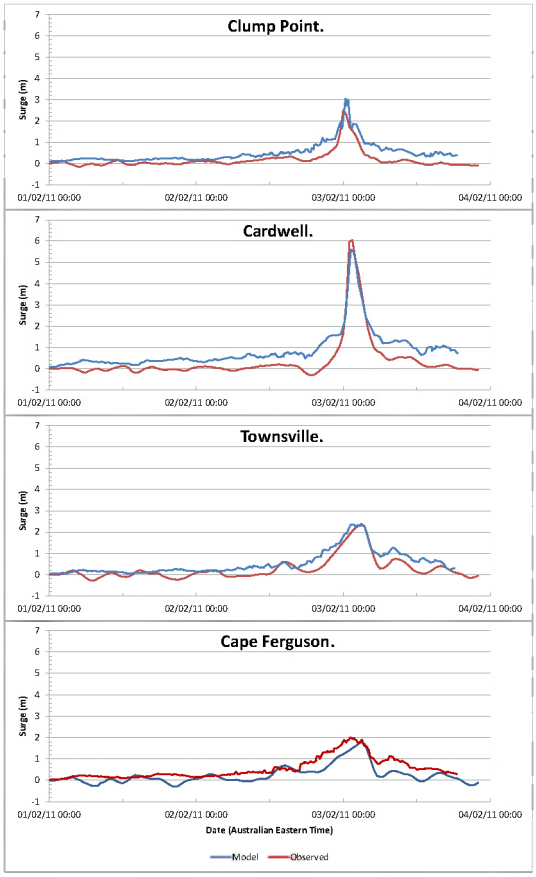

Figure 4. Comparison of modelled and observed storm surge water levels.

TUC 2013, 16-18/10/2013, Karlsruhe - Kopmann, Goll (eds.) - © 2013 Bundesanstalt für Wasserbau ISBN 978-3-939230-07-6

Comparison of 1D and 2D models for Dam Break flow: Simulations for Two Different River Systems

P. Grover, A. Naumov, Y. Khayer
4DM Inc.
Toronto, Canada
pgrover@4dm-inc.com

***Abstract*—The simulation of dam-break flows are an important component of dam safety programs and used to establish the dam's hazard classification and develop emergency response plans. Within North America, 1D models such as DAMBRK and HEC-RAS, have been the models of choice for conducting these dam break studies. Although 2D models are widely available and the barriers to their application have been mostly eliminated due to improved computer performance and availability of detailed topographic data, their use in dam break studies is still not as widespread as 1D models. This study is a comparison of HEC-RAS (1D) and TELEMAC-2D (2D), for the simulation of dam-break flows along two different river systems. The first river system is located within a well defined river valley in an urban environment and the second is located within a flat-bottomed valley in a rural environment. The results of the 1D and 2D models are compared along with an examination of practical considerations of interest to practitioners.**

I. INTRODUCTION

Hydrotechnical studies involving dam breach and floodwave routing are an important part of periodic dam safety reviews performed in North America [1][2]. Within a dam safety framework, hydrotechnical studies are used to determine the hazard classification of the dam through analysis of life-safety, socio-economic, environmental and cultural losses. The hazard classification is used to identify the Inflow Design Flood (IDF) and the Design Earthquake as well as to establish monitoring and inspection requirements for the dam. The results of hydrotechnical studies are also used to prepare emergency response plans and distributed to emergency response stakeholders. Both of these activities require accurate predictions of the floodwave travel times, the extent of the inundation as well as the depths and velocities of the flows.

Simulation of dam break flows is a complex problem and there are a number of challenges that engineers and their models must address. Firstly, dam break models require specialized numerical techniques to handle the highly unsteady, rapidly varied flows including discontinuities such as bores and hydraulic jumps [3]. Improper selection of the numerical techniques can lead to solutions that are too diffusive or unstable due to numerical oscillations. Another challenge in simulating dam break flows is that the magnitude of the breach hydrographs are typically an order of magnitude greater than typical flood events and often result in complex flows (e.g. flow splitting, flow through urban environments) and flows that are temporarily unconfined and 2D. Finally, there is often limited data available to conduct a proper calibration of the model for the magnitude of the flows being simulated.

Current 2D hydraulic models offer many advantages over 1D models for modeling dam break flows. Many 2D models offer advanced numerical techniques specifically developed for handling rapidly varied flows. 2D models also more accurately reproduce the flood wave dynamics that occur during high flows over complex terrains [4] and they reduce the need for model empirically-based parameterization to account of 2D flows.

Within North America, 1D models such as DAMBRK and HEC-RAS are still commonly used for the simulation of dam breach floodwave propagation. 2D models are only requested in special cases where it is obvious that a 1D model is not appropriate. Despite the advantages of 2D models as well as advances in computing power and the wide availability of high-resolution elevation data collected from LiDAR and photogrammetry there still is a bias towards the use of 1D models.

This paper compares the results of two of previous dam break studies modelled in 1D using HEC-RAS with the result from using the TELEMAC-2D 2D model. For both these river systems, the assumption of 1D flow during the dam breach is reasonable and therefore the purpose is to quantify the differences between the model results and examine the advantages and disadvantages of each approach from a practical perspective.

II. STUDY AREAS

Two study areas were used in this investigation. For both study areas, the dams were modelled in 1D using HEC-RAS by the authors as part of hazard classification and inundation mapping projects. The dams are located in two different locations in Canada.

A. Study Area 1 - Confined Parkland/Urban River

The dam for Study Area 1 (SA1) is an earthen embankment dam used for flood control with a height of 16.5 m and reservoir storage of 5,000,000 m^3. The sunny-day failure scenario of the dam was assumed to be due to piping/seepage with a time-to-failure of 1 hour.

The river valley downstream of the dam is well defined with a width of approximately 500 m and steep banks of approximately 30 m. The river is approximately 5 m width and less than 1m deep with an average slope of 0.006. The land use in the river valley is parkland consisting of both grassed fields and forested areas (see Fig. 1). Additionally, the river crosses two residential neighbourhoods located 3.8 km and 8.1 km downstream from the dam. There are a total of ten road crossings ranging from small residential roads to multi-lane highways.

The dimensions of the study area are approximately 10.5 km x 1.2 km and the distance from the dam to the end of the study area along the river centreline is 15.6 km.

Figure 1. View of the dam and downstream valley for Study Area 1.

B. Study Area 2 - Flat Bottom Rural Valley

The dam for Study Area 2 (SA2) is located in the prairies region of Canada in south-western Saskatchewan. The dam is an earthen embankment dam used for irrigation with a height of 14.1 m and a reservoir storage of 7,929,579 m^3. The sunny-day failure scenario of the dam is assumed to be due to piping/seepage with a time-to-failure of 1 hour and produces a peak flow of 2357 m^3/s.

The dam is located along the side of a wide flat-bottom valley and the outflow from the dam joins up with a small creek before continuing downstream (Fig. 2).The width of the valley varies from 0.5 km to 1.3 km. The creek is approximately 5 m wide with a slope of S=0.00024. The land use downstream of the dam consists of agricultural fields for grain crops and cattle grazing. The valley also includes a complex system of irrigation canals and road and rail embankments.

The dimension of SA2 is approximately 19.8 km x 4 km and the distance from the dam to the end of the study area is 40.3 km along the creek centreline.

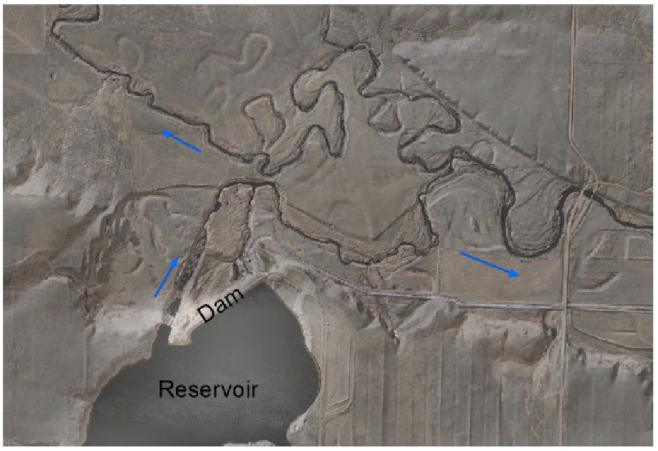

Figure 2. View of the dam and downstream valley for Study Area 2.

III. NUMERICAL MODELS

A. HEC-RAS

HEC-RAS version 4.1.0 was used for the 1D simulations. HEC-RAS is developed by the US Department of Defence, Army Corps of Engineers at the Hydraulic Engineering Center (HEC) in Davis California. The unsteady routines in HEC-RAS were adapted from the UNET model [5] and use a four-point implicit finite difference scheme. The temporal and spatial derivatives for this scheme are:

$$\frac{\partial f}{\partial t} = \frac{f_m^{n+1} + f_{m+1}^{n+1} - f_m^n + f_{m+1}^n}{2\Delta t} \quad (1)$$

$$\frac{\partial f}{\partial x} = \theta\left(\frac{f_{m+1}^{n+1} - f_m^{n+1}}{\Delta x}\right) + (1-\theta)\left(\frac{f_{m+1}^n - f_m^n}{\Delta x}\right) \quad (2)$$

where f represents some variable, n is the time index, m is the spatial index and θ is a weighting factor ($0.5 < \theta \leq 1$). The weighting factor is used to adjust between a backwards implicit scheme ($\theta = 1$) which is most stable but least accurate to a box scheme ($\theta = 0.5$) which is most accurate but least stable [6]. The recommended value for theta is $\theta = 0.6$ to be used once the model has been stabilized.

B. TELEMAC-2D

TELEMAC-2D version v6p2 was used for the 2D simulation. The model was configured to run as a Finite-Volume model using the HLLC solver. The HLLC (Harten-Lax-Van Leer with contact discontinuities) solver is a shock capturing, approximate Riemann solver developed by [7]. This class of solvers was developed specifically for modelling of rapidly-varying-flows with discontinuities such as shock waves and bores and the HLLC solver has been used in a number of dam break studies [8], [9], [10]. Fig. 3 illustrates the wave structure of the HLLC solver where S_L and S_R are the left and right waver speeds, S^* is the speed of the middle wave and F_L, F_{*L}, F_{*R} and F_R are the inter-cell fluxes.

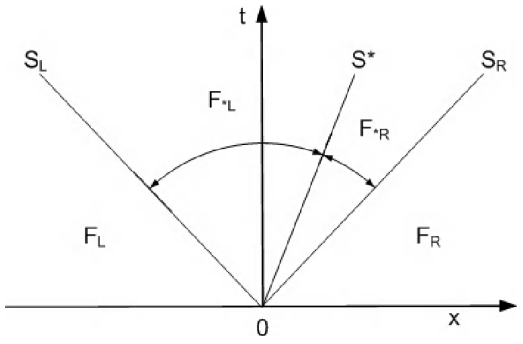

Figure 3. Wave structure of the HLLC solver for sub-critical flow conditions.

IV. Model Development

A. Study Area 1

1) Data Preparation

A 1m digital elevation model (DEM) was prepared for SA1 using breaklines and mass-points generated by photogrammetry. Additional breaklines to represent the channel bathymetry were created from previous flood studies and incorporated into the DEM. Data regarding the hydraulic structures and water crossings were collected from engineering drawings and previous hydraulic modelling studies.

2) HEC-RAS Model Development

The geometry for the HEC-RAS model was developed using the HEC-GeoRAS extension for ArcGIS. This extension allows the user to generate the HEC-RAS geometry input file within a GIS environment. Cross-sections were placed at approximately 75 m intervals (Fig. 4). Bridges and culverts were assumed not to have failed. Ineffective flows areas, used to define areas of the cross-sections that contain water that is not actively conveyed, were applied upstream and downstream of road crossings assuming 1:1 and 1:4 contraction and expansion ratios. Elevations for the ineffective flow areas were initially set based on steady flow experiments and iteratively adjusted to ensure a smooth transition throughout the floodwave.

Although HEC-RAS allows the use of very detailed variations of the roughness values along each cross-section, this can create problems in unsteady models and is not recommended as abrupt changes of the roughness values can cause the model to become unstable. For this reason uniform Manning's n values were assigned for the overbanks ($n = 0.08$) and the main channel ($n = 0.035$). Hydrometric data was only available to calibrate the roughness in the main channel.

The dam reservoir was modelled as a level-pool using the stage-storage curves developed for the dam. The dam breach was simulated using the built-in dam breach routines in HEC-RAS. A steady inflow equal to 2.5 m^3/s was set as the upstream boundary condition and normal depth was assumed at the downstream boundary. The model was run for a mixed flow regime with a time step of 10 seconds and the duration of the simulation was 4 hours. The total runtime for the simulation was approximately 2 minutes.

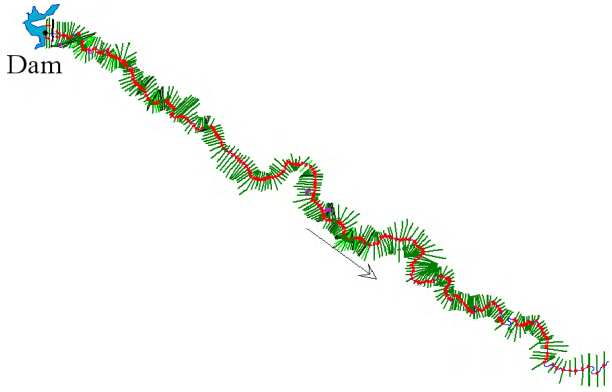

Figure 4. HEC-RAS geometry for Study Area1.

3) TELEMAC-2D Model Development

The mesh for the 2D model was created using the BlueKenue software and contains approximately 184,000 nodes (Fig. 5). The mesh was constructed using a graded mesh resolution. The mesh size (edge length) along the channel was set to 5m with a default mesh size of 15m. Linear topographic features such as roads and the stream banks were captured in the mesh as breaklines. Bridges and culverts were not explicitly modelled as with the HEC-RAS model (e.g. the decks of the bridges and culverts were removed from the DEM). A single value for the roughness was used in the model. The manning's roughness was set to n = 0.07, slightly lower than the value used for the overbanks in the HEC-RAS model. The selection of a slightly lower value was based on the study by [4] who found that the 2D model needed a lower roughness value compared to the 1D. Turbulence was modelled using the k-ε model. The breach hydrograph generated by the HEC-RAS model was used as the inflow boundary condition at the foot of the dam. A constant water elevation boundary condition was imposed at the downstream end of the model and far enough downstream to not impact the results at the locations of interest in the study.

The initial conditions for the model consisted of a baseflow of 2.5 m^3/s. The model was run with a variable time-step such that the maximum courant number was 0.25. The duration of the simulation was 4 hours and the runtime on a desktop workstation was 4 hours and 13 minutes.

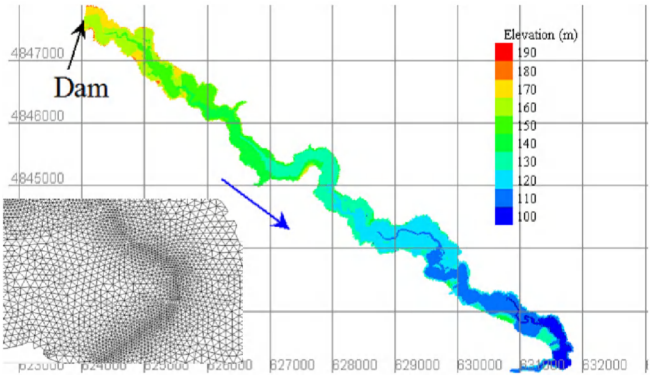

Figure 5. Computational mesh for Study Area 1. Inset shows detail of mesh.

B. Study Area 2

1) Data Preparation

High-resolution 20 cm orthophotography and airborne LiDAR were available for SA2. The LiDAR point cloud was processed by our team to generate 3D breaklines along the banks of the creek. The breaklines were merged with the point cloud to create a hydro-flattened DEM. Data regarding the various hydraulic structures and water crossings were collected from field measurements or extracted from the LiDAR data. The channel bathymetry was not included in the model as the channel depth was assumed to be negligible.

2) HEC-RAS Model Development

The HEC-RAS model for SA2 was developed using a similar approach as for SA1. Due to the smaller slope, cross-section intervals of 150 m were used. A number of storage areas and lateral structures were added to the model to simulate the road and rail embankments running parallel to the floodway (Fig. 6). The embankments act as levees and the overtopping flows are directed into the storage areas. Manning's n values were set to n = 0.05 for the overbanks and n = 0.032 for the main channel. No data was available to calibrate the model. Slightly higher roughness values were used immediately downstream to stabilize the model. The dam and reservoir for SA2 were modelled in the same was as for SA1. A steady inflow of 2.5 m^3/s was set as the inflow boundary condition for the reservoir. A small inflow of 1 m^3/s was also added to the storage area upstream of the confluence to maintain flow in the creek upstream of the confluence. Normal depth was assumed at the downstream boundary. The model was run with a time-step of 20 seconds and the duration of the simulation was 24 hours. The total runtime for the simulation was 2 min 22 s.

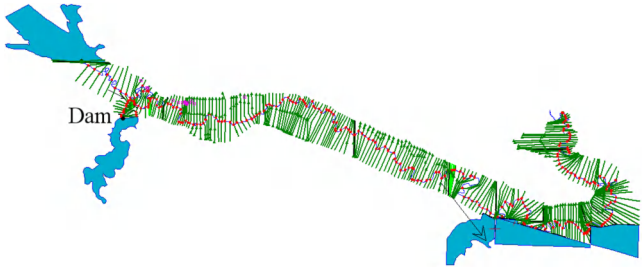

Figure 6. HEC-RAS geometry for Study Area 2.

3) TELEMAC-2D Model Development

A uniform 15m mesh was used for SA2 and incorporated breaklines for features such as the road and rail embankments, stream centreline and the irrigation canals (Fig. 7). Bridges and culverts were treated similar to the 2D model for SA1. The mesh contains approximately 342,000 nodes.

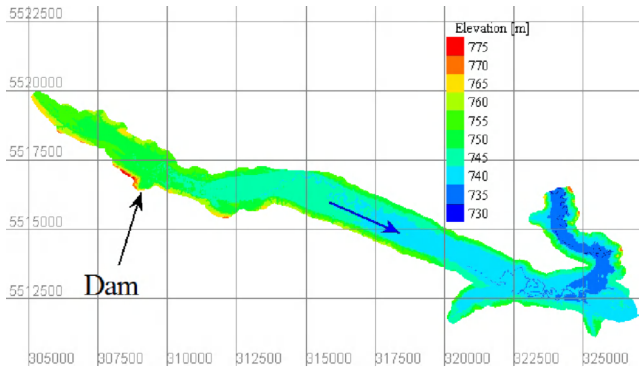

Figure 7. Computational mesh for Study Area 2.

The manning's roughness was set to n = 0.04. The breach hydrograph from the HEC-RAS model was used as an inflow boundary condition at the location of the dam spillway. A water elevation was specified at the downstream end of the model. A dry bed was assumed for the initial conditions. The model was run with a variable time-step with a maximum courant number of 0.25. The duration of the simulation was 24 hours and the runtime on a desktop workstation was 12 hours and 59 minutes.

V. Results

A. Floodwave Statistics

Table 1 and 2 provide a comparison of the key floodwave statistics of importance in dam safety studies for study areas 1 and 2 respectively. The flood arrival time and the time-to-peak is the time measured between the initiation of the dam breach and the initial rise and peak stage respectively. The maximum depth is based on the maximum stage measured within the main channel. Comparisons of the maximum water surface profiles are provided in Fig. 8 and Fig. 9.

For SA1, the floodwave travel times between the two models are similar with TELEMAC-2D predicting slightly longer travel times. There is a much greater difference in the

predicted maximum depth with TELEMAC-2D predicting much deeper inundation depths particularly at stations 2.58 km and 3.86 km, after which the elevation difference decreases. This difference in the depths may be partially attributed to differences in the approaches used in the modelling of the bridges as can be seen in Fig. 8. Further refinement of the 2D mesh at the road crossings and/or the use of the bridge/culvert elements available in TELEMAC-2D should be performed to see if the difference in the water surface elevations is minimized.

TABLE I. FLOODWAVE STATISTICS FOR STUDY AREA 1.

Station	*Parameter*	*HEC-RAS*	*TELEMAC 2D*	*Diff*
2.58 km	Flood Arrival Time [hh:mm]	0:20	0:24	-0:04
	Time-to-peak [hh:mm]	0:50	0:52	-0:02
	Maximum depth [m]	12.96	14.94	-1.98
3.86 km	Flood Arrival Time [hh:mm]	0:25	0:32	-0:07
	Time-to-peak [hh:mm]	0:55	1:00	-0:05
	Maximum depth [m]	9.42	11.07	-1.65
7.15 km	Flood Arrival Time [hh:mm]	0:45	1:03	-0:18
	Time-to-peak [hh:mm]	1:20	1:25	-0:05
	Maximum depth [m]	10.47	9.96	0.51
9.06 km	Flood Arrival Time [hh:mm]	0:55	1:17	-0:22
	Time-to-peak [hh:mm]	1:35	1:48	-0:13
	Maximum depth [m]	6.58	6.91	-0.33

For SA2, the differences in the floodwave travel times predicted by the two models are much greater than in SA1. The flood arrival times predicted by HEC-RAS are much shorter than predicted by TELEMAC-2D; however TELEMAC-2D generally predicts a shorter time-to-peak. It was hypothesized that the dry-bed initial conditions used in the 2D model would have resulted in a faster arrival time compared to the wet bed conditions used in the 1D model, consistent with the analytical solution for dam break flows over rigid beds by [11]. The coarse mesh used along the channel could be partly responsible for the slower travel times. The faster time-to-peak predicted by TELEMAC-2D indicates that the wave front of the floodwave is travelling slower than the wave predicted by HEC-RAS but the hydrograph is steeper. This could be the result of excessive numerical diffusion within HEC-RAS and further study is warranted. Interestingly, the two models both predict very similar maximum water depths with TELEMAC-2D generally predicting slightly greater depths as was found in SA1.

TABLE II. FLOODWAVE STATISTICS FOR STUDY AREA 2.

Station	*Parameter*	*HEC-RAS*	*TELEMAC*	*Diff*
2.1 km	Flood Arrival Time [hh:mm]	0:10	0:20	-0:10
	Time-to-peak [hh:mm]	1:15	1:35	-0:20
	Maximum depth [m]	5.63	6.01	-0.38
13 km	Flood Arrival Time [hh:mm]	1:40	2:55	-1:15
	Time-to-peak [hh:mm]	4:30	3:50	+0:40
	Maximum depth [m]	4.31	4.71	-0.40
22.4 km	Flood Arrival Time [hh:mm]	3:05	5:45	-2:40
	Time-to-peak [hh:mm]	9:09	7:25	+1:44
	Maximum depth [m]	4.55	4.34	+0.21
29.2 km	Flood Arrival Time [hh:mm]	5:00	8:30	-3:30
	Time-to-peak [hh:mm]	15:00	10:10	+4:50
	Maximum depth [m]	2.94	3.34	-0.40
36.8 km	Flood Arrival Time [hh:mm]	6:05	10:55	-4:50
	Time-to-peak [hh:mm]	17:55	14:05	+3:50
	Maximum depth [m]	3.56	3.81	-0.25

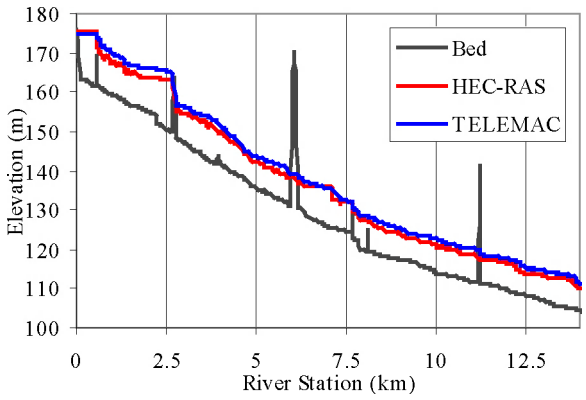

Figure 8. Comparison of the maximum water surfaces for Study Area 1.

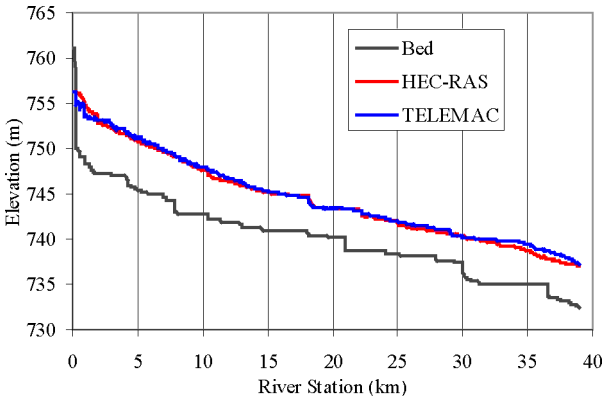

Figure 9. Comparison of the maximum water surfaces for Study Area 2.

VI. Conclusions

In this paper, two dam break studies originally modelled in 1D using HEC-RAS were re-modelled in 2D using TELEMAC-2D model. The differences between the floodwave characteristics predicted by the two models have been compared.

Due to the fact that there is no data to validate these models against, it is difficult to state which model was more accurate in simulating the floodwaves. The 2D models generally predicted higher maximum water levels than the 1D models consistent with the findings of [4] and predicted shorter times for the floodwave to peak. Both of these findings should be further investigated because if confirmed they would mean that the application of 1D models are not sufficiently conservative and could result in miss-classification of the dams and have implications on evacuation strategies used in emergency preparedness plans. From a practical perspective, the 2D models do not make as many assumptions as the 1D models and require less empirically-based parameterization reducing the subjectivity in the modelling.

The authors found that the construction of the 2D models was far more intuitive than the 1D models. Flow expansion and contractions are implicitly determined by the model (see Fig. 10) as well as areas of ineffective flow. Similarly, modelling areas where the assumption of 1D flow is not valid can present significant challenges using a 1D model but are not a problem with a 2D model (see Fig. 11). Finally, the ability to quickly visualize the flow fields using tools such as BlueKenue helps the modeller to quickly identify problems and also are extremely powerful in conveying the model results to clients and stakeholders.

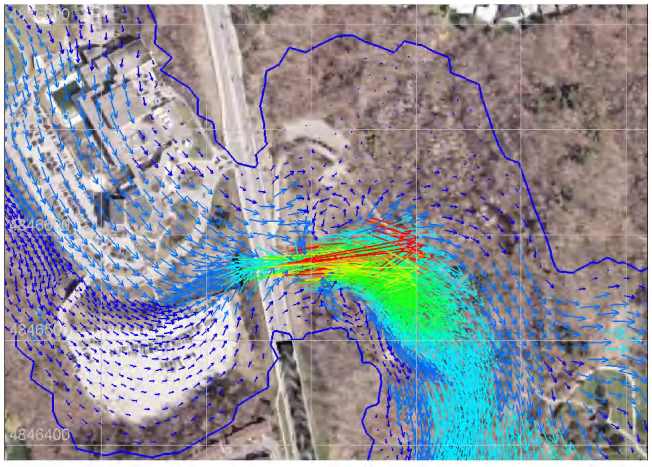

Figure 10. Velocity field generated by major road crossing in SA1. Blue line represents the inundation extent.

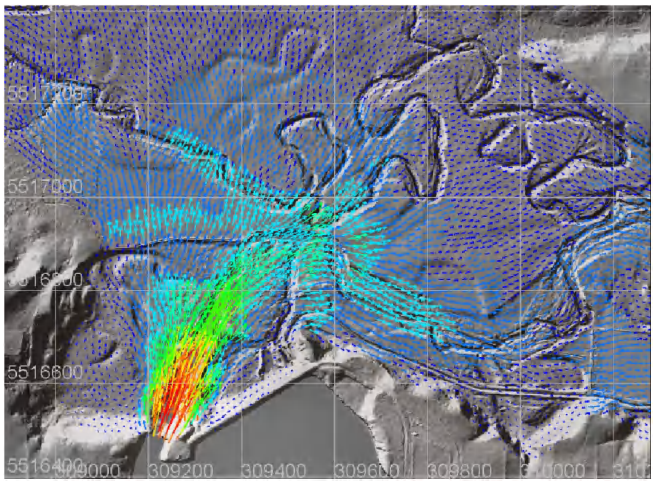

Figure 11. Velocity field at the peak outflow from the dam breach for SA2 showing the complex 2D flow generated by the topography.

Acknowledgement

The authors would like to thank Agriculture and Agri-Food Canada for use of the data used in this study.

References

[1] CDA (Canadian Dam Association), "Dam Safety Guidelines," 2007.

[2] FERC (Federal Energy Regulatory Commission), "Chapter 14. Dam Safety Performance Monitoring Program. Monitoring the Performance of Dams," 2005.

[3] W. Wu, "Computational river dynamics," CRC Press Taylor & Francis Group, 2007.

[4] J.-M. Hervouet and A. Petitjean, "Malpasset dam-break revisited with two-dimensional computations," Journal of Hydraulic Research, vol. 37, no. 6, pp. 777–788, Nov. 1999.

[5] R. L. Barkau, "UNET One-Dimensional Unsteady Flow Through a Full Network of Open Channels User Manual," USACE, Generalized Computer Program Manual, CPD-66, Version 2.0,Davis, CA, 1992.

[6] D. L. Fread, "Numerical properties of implicit four-point finite difference equations of unsteady flow," NOAA Technical Memorandum NWS Hydro-18, U.S. Department of Commerce, NOAA, NWS, Silver Spring, MD, 123pp. 1974.

[7] E. F. Toro, M. Spruce, and W. Speares, "Restoration of the contact surface in the HLL-Riemann solver," Shock Waves, vol. 4, no. 1, pp. 25–34, Jul. 1994.

[8] S. Soares- Frazão, "HLLC scheme with novel wave-speed estimators appropriate for two-dimensional shallow-water flow on erodible bed," Int. J. Num. Meth. Fluids 66(8), pp.1019–1036. 2011.

[9] Z. Cao, G. Pender, S. Wallis, and P. Carling, "Computational Dam-Break Hydraulics over Erodible Sediment Bed," Journal of Hydraulic Engineering, vol. 130, no. 7, p. 689, 2004.

[10] S. Soares-Frazão, J. Lhomme, V. Guinot, and Y. Zech, "Two-dimensional shallow-water model with porosity for urban flood modelling," Journal of Hydraulic Research, vol. 46, no. 1, pp. 45–64, Jan. 2008.

[11] J. J. Stoker, "Waterwaves,". New York: Interscience Publications,Wiley, 1957.

TUC 2013, 16-18/10/2013, Karlsruhe - Kopmann, Goll (eds.) - © 2013 Bundesanstalt für Wasserbau ISBN 978-3-939230-07-6

Numerical and experimental study of Favre waves after hydropowerplant trigger with TELEMAC-3D

D. Alliau, T. Fretaud, M. Genin
Engineering department
Compagnie Nationale du Rhône
Lyon, France
d.alliau@cnr.tm.fr

P. Lang
Expertise et structure
INGEROP
Grenoble, France
pierre.lang@ingerop.com

***Abstract*—CNR is the first producer of exclusively renewable energy in France, operating and managing 18 hydroelectric power plants on the Rhône River. When turbines shut down because of electric incidents, the stop is very sudden and generates a wave that raises the upper channel water level. This step is called trigger or disjunction.**

To improve the knowledge of these wave phenomena is essential for CNR in order to implement suitable actions both at the barrage and power plant with respect to each specific development constraint (warning of sudden water release in the downstream reach, automatic backup, intrinsic security).

Previous modelling studies with 1D and 2D models of the actual trigger test carried out with a 500 m^3/s discharge at Chautagne scheme in April 2010 showed some limitations including excessive dampening of reflected waves and underestimation of secondary waves amplitude. The aim of this study is to carry out the modelling of this test with the TELEMAC-3D software in order to get better results. Tasks consist of 3D model meshing, model calibration for trigger conditions, comparison of results with real test measurements, discussion on methods, analysis of the main parameters and extrapolation to a trigger test with a 700 m^3/s discharge.

I. INTRODUCTION

The of hydro-electric development scheme of the Rhone River is based on a regulation barrage and a power plant equipped with turbines. Electrical incidents (mechanical failure in the turbine or in the electrical network, etc…), or unfavourable hydraulic conditions can lead to a quick stopping of one or more turbines and thus stop the plant and its production. This phenomenon is also called trigger or disjunction. To avoid destruction of the machines due to overspeed, the flow that supplies hydraulic turbines is automatically cut off by valves. The discharge is then suddenly reduced to zero, creating a positive wave propagating in the upstream channel and a negative one in the downstream channel of the plant. The wave is called wave disjunction or swelling. As a consequence, the positive wave will temporarily increase the standard water level of the upper channel (i.e. the usual operating water level) and consequently affects security issues (e.g. flooding of banks equipments and structures, spillage over levees). The numerical study of this phenomenon is crucial for CNR in order to improve the understanding of the wave propagation and to prevent occurrence of any incidents.

The paper is divided in four parts. First, the Chautagne development scheme features are explained. Second, the experimental trigger is described. Third, the TELEMAC modelling is presented. Finally, 2D and 3D results are analysed, limits of optimization are listed and improvements are proposed.

II. OBJECTIVES

The simulation of disjunction waves using TELEMAC-2D model (shallow water or Boussinesq equations) gives a good representation of the first passage of the primary wave amplitude and frequency. This model also has its limitations:

- The dampening of reflected waves is too strong;
- The amplitude of the wave from the second pass at the plant is underestimated compared to the expected results.

In addition, the secondary waves are not modelled by the Saint Venant equations, because these assume a hydrostatic pressure distribution. That's why 3D modelling seems necessary to reproduce this phenomenon.

Study objectives are:

- to realize a 3D exploratory approach from the existing 2D model and evaluate it by comparing with the experimental test data recorded on 29 April 2010 (500 m3/s);
- To extrapolate the trigger test to the maximum discharge of the power plant.

III. CHAUTAGNE SCHEME

Chautagne hydropower plant is located in the Rhône River valley (in the eastern part of France), between Geneva (Switzerland) and Lyon. It was built in 1980. Chautagne follows the typical CNR development scheme. Indeed, it is composed of the following structures:

- A hydropower plant (Usine d'Anglefort: US) with a total installed capacity of around 90 MW. It comprises two bulb-upstream units with a maximum power station discharge of 700 m^3/s.

- A barrage (BarraGE de retenue de Motz: BGE) equipped with five sector gates. When upstream discharge is higher than the power plant maximum discharge, the gates start opening. During major floods, the gates cannot regulate the water level anymore since they are completely opened.
- A lock for yachting navigation purposes (US).
- A reservoir (retenue RE) which is 5.7 km long. The tributary Fier River (FI) converges into this part of the river course.
- A headrace channel (Canal d'amenée CA) from reservoir to hydropower plant which is 5.3 km long.
- A tailrace channel (Canal de Fuite: CF) which is 3.4 km long.
- The natural river course (Vieux Rhône: VR) in which a minimal discharge has always to be maintained during dry season. During floods most of the flow goes through this natural river.

IV. EXPERMIENTAL TRIGGER

A. *Hydraulic scheme*

The model is delimited by the CNR works:

- Upstream: barrage/hydropower plant of Seyssel (SY) and the tributary FIER River (FI);
- Downstream: barrage of Motz (BGE) and hydropower plant of Chautagne.

B. *Disjunction test in April 2010*

1) *Chronology*

TABLE I. DISJUNCTION CHRONOLOGY

Initial conditions, before disjunction	
Initial incoming discharge at 9:37 am	759 m^3/s
Initial turbine discharge in hydropower plant of Chautagne	500 m^3/s
Discharge through the barrage of Motz	185 m^3/s
Initial water level upstream hydropower plant	251.74 m NGFO
Disjunction	
Turbines stopping	09 :37 :03
Barrage opening	09 :54 :00

2) *Experimental measurements*

7 sensors with an adapted frequency sampling rate (Δt = 1 s) were implemented along the Chautagne scheme (Fig. 1). Therefore the short period secondary waves phenomenon could be recorded. During study the comparison was always done regarding these measurement points.

3) *Experimental results*

The speed of wave propagation was 9.8 m/s, the period was 49 min for the primary waves and 15 seconds for the secondary waves. The waves reached the headrace channel inlet in about 13 minutes (where secondary waves could be clearly recorded).

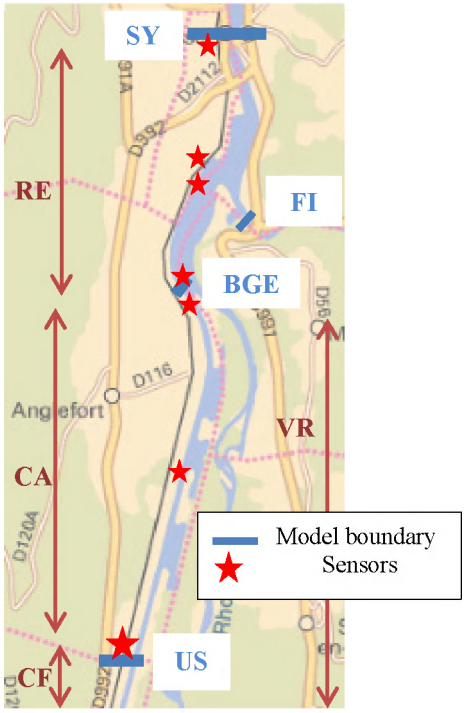

Figure 1. Chautagne scheme

V. THEORETICAL ASPECT CONCERNING THE FAVRE WAVES

Different physical phenomena are distinguished:

- Primary waves (which are related to the propagation along the channel of rapidly changing boundary conditions of flow);
- The secondary Favre waves overlapping primary waves;
- Other "side effects" phenomena such as the amplification of the wave to the right bank (which are a consequence of modulation and primary waves)

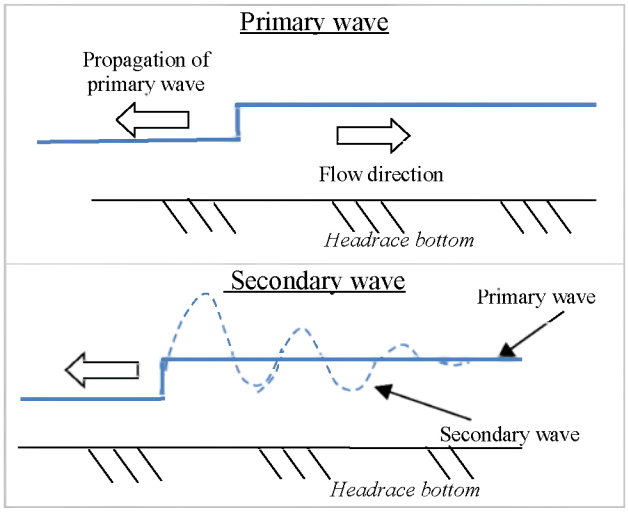

Figure 2. Schematic representation of Favre waves.

VI. SCHEME MODELLING

1. Mesh

The domain is 15 km long and is meshed with node located every 15 m (Δx). This resolution was calculated according to the wave speed (C) and the time for stopping the hydropower plant. The secondary waves are very quick and have a runtime of 15 s (T). It was assumed that between 5 and 10 observations (n) during plant stopping were enough to measure waves. Consequently the mesh resolution was calculated with:

$$\Delta x = \frac{C.T}{n} \underset{n=10}{\Longrightarrow} \Delta x = 15.6\ m \qquad (1)$$

The 2D grid comprises about 26 000 nodes and 50 000 elements. This mesh has been generated by Matisse. With regard to the 3D model, 6 horizontal levels are generally used in this study. Consequently, the 3D grid comprises about 150 000 nodes and 750 000 elements. 4 liquid boundary segments (SY, FI, BGE, and CE) are applied.

A. Calibration

The model calibration is very important because it determines numerical model reliability. At first, the calibration is done with the 2D model. Then 2D calibration coefficients are reused in the 3D model after a validation step (dependent to the water depth discretization, i.e. horizontal level number). For the calibration process five steady state discharges ranging from 436 m^3/s to 1300 m^3/s and two flood events with peak flows of 2400 m^3/s and 2070 m^3/s were selected. Water levels were imposed at the downstream hydropower plant (CE) and at the other three liquid boundaries (SY, FI and BGE).

The modelling of the turbulence was realised with a constant viscosity of 5.10^{-3}m^2/s. Calibration was focused on the bottom coefficient, which was computed following Strickler's law. The model was divided into different Strickler zones as specified in Fig. 3.

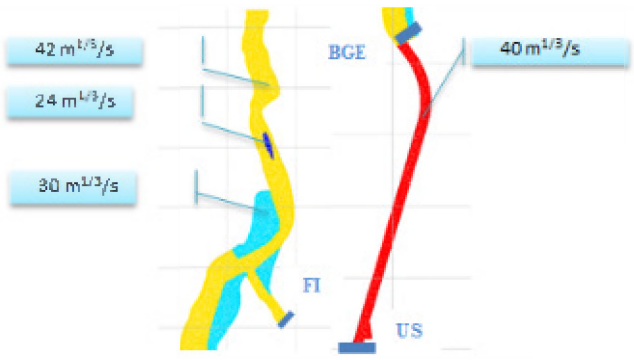

Figure 3. Strickler coefficients

The comparison of computed and measured water levels shows a maximal error of 15 cm for the steady state conditions, however for the lowest discharge the error is less than 5 cm. For the flood events the upstream power plant water level during the peak flow is overrated with 15 cm,. Nevertheless the results match the measurements fairly well allowing to validate the numerical model. For the next step of the study, an average error between 5 and 15 cm has to be taken into account.

The Strickler coefficients from the 2D calibration were used in the 3D model, and the calibration procedure was applied again in order to check the model behaviour in 3D. A similar calibration quality could be reached.

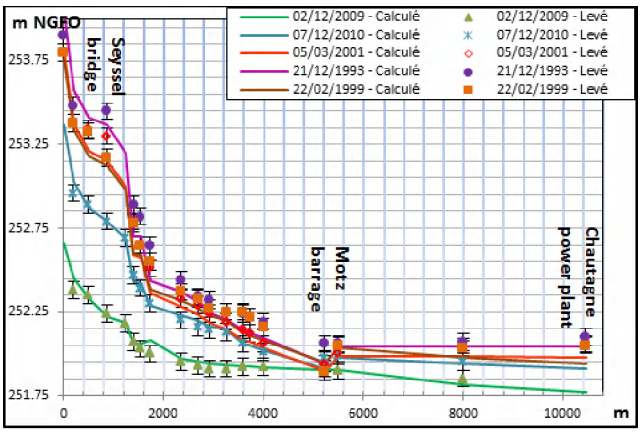

Figure 4. Calibration of steady state in 3D model

VII. DISJUNCTION TEST MODELLING

The disjunction is studied in this part. Water levels throughout the model were calculated to improve the knowledge about these phenomena. During the disjunction, the model was controlled by flow boundary condition. Thus, 2 different kinds of boundary condition setups were used. On the one hand, the initialization (normal boundary conditions), on the other hand the disjunction (only flows).

A. Initialization

A hydraulic model in subcritical flow is controlled by a downstream water level, consequently a water level was imposed on the power plant. For the initialization the unsteady state before the disjunction took place was taken from measurements. The model simulated a whole day prior to the disjunction until 9:30 a.m. The simulation of these 30 hours took only 8 minutes on 32 computational cores.

At first the initialization was run with TELEMAC-2D. The difference between the models will be explained later. The comparison of computed and measured water levels (ΔZ) for the initialization run is presented in Table II for different locations of the model (Fig. 1).

At 9:30 a.m the water level. is close to the reality (average ΔZ about 3 cm). Moreover, the headrace channel discharge calculated at 9:30 am is about 500 m^3/s, similar to the ADCP measurements. Therefore the last time step of this initialization was used as the first of the trigger modelling.

TABLE II. INITIALIZATION SUMMARY

Measurement Point/Station	Z [m NGFO]		Init 5 [m NGFO]			
	08:30	09:30	08:30	ΔZ	09:30	ΔZ
P1 Seyssel Bridge	252.33	252.53	252.47	*0.14*	**252.56**	***0.02***
P2 leisure center	251.96	252.06	252.13	*0.17*	**252.09**	***0.03***
P5 BGE upstream	251.96	252.03	252.09	*0.13*	**252.04**	***0.01***
P7 CA entrance	251.94	252.02	252.04	*0.10*	**252.01**	***0.00***
P8 mi- CA	251.84	251.94	251.82	*-0.02*	**251.87**	***-0.06***
P9 lock upstream	251.57	251.73	251.64	*0.07*	**251.78**	***0.05***
P13 100m CE upstream	251.54	251.70	251.59	*0.05*	**251.76**	***0.06***
P14 CE upstream	251.59	251.74	251.67	*0.08*	**251.74**	***0.00***

B. *Disjunction*

To start disjunction modelling, simulation was run with TELEMAC-2D to get an idea of the results. Then a simple 3D model was run with default setup parameters in TELEMAC-3D. The optimization of this case has been studied in a second phase. Again only flow boundary conditions were used (Fig. 5). Default setup parameters were chosen for TELEMAC-2D run.

- Strickler's friction law with different zones as shown in Fig. 3.
- Constant turbulence model with a constant viscosity of 5.10^{-3} m^2/s.
- The solver was chosen by default with "solving normal equation".
- Shallow water equations were used in this model. A quick sensitivity test between Saint Venant and Boussinesq did not show any significant difference.

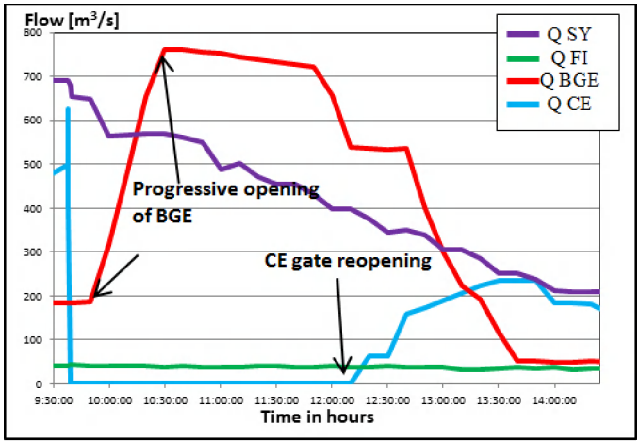

Figure 5. Boundary conditions during trigger test

For the TELEMAC-3D run, parameters were chosen similarly. Additional key-words like 2D continuation, 6 horizontal levels and no friction on lateral boundaries were added to the 3D model.

The time step (Δt) has been calculated according to Courant number C_r. This number must be less than 1 for rapidly changing flows.

$$C_r = C.\frac{\Delta t}{\Delta x} < 1 \underset{\Delta x=15m}{\Longrightarrow} \Delta t < 1.4\ s \qquad (2)$$

Consequently, **Δt = 1s**.

Both simulations (2D and 3D) were run with continuation on 2D or 3D initialization. Results were extracted at different locations; the study mainly focused on the upstream US sensor (6) and on the inlet of CA sensor (7).

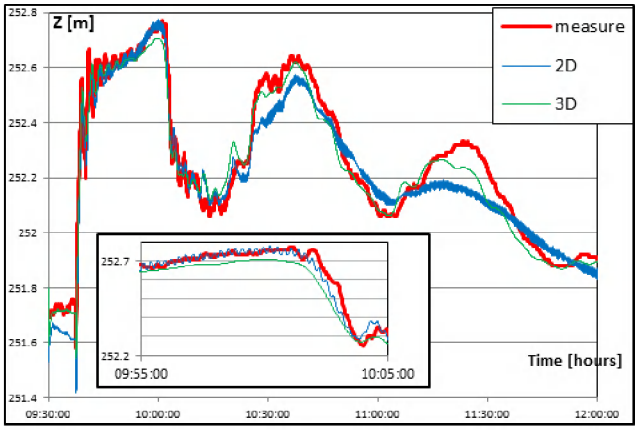

Figure 6. Comparison 2D vs. 3D models at upstream powerplant.

The 2D model shows attenuation of the reflected waves and underestimated amplitude. The first wave peak is perfectly reached by the 2D model; the 3D model is also close even if there is a Δz of 5 cm. Generally the 3D model reproduces the waves better than 2D model. Amplitude and frequency of the model results are almost in line with the measured signal. The amplitude of the reflected wave is quite acceptable even if the model results show a small attenuation; this could be improved with an optimization program.

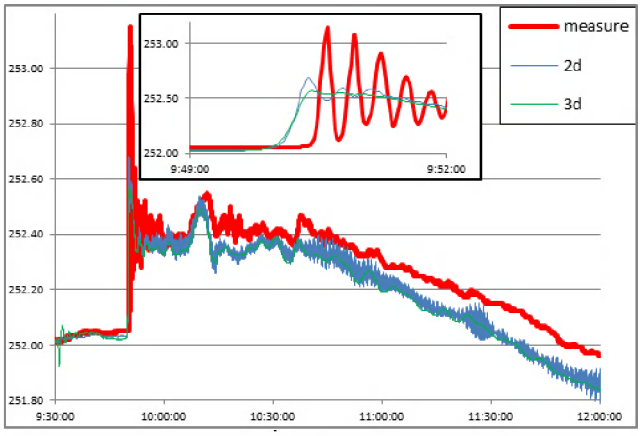

Figure 7. Comparison 2D vs. 3D models at inlet of headrace channel.

The 2D model shows instabilities on the secondary waves (see the zoomed detail in Fig. 7). Some oscillations appear overlaying the general curve, but they might be linked to numerical instability. The primary wave is well

simulated by the 3D model. Afterwards a specific study is performed on the representation of secondary waves.

VIII. Optimisation program (1)

A. Key-words effect

A large optimization program is set up to improve the representation of the disjunction wave and to mitigate the difference between simulation and measurements. This program is based on different key words available with TELEMAC-3D:

- Number of horizontal levels: 6 to 10;
- Horizontal levels position: equidistant or close to free surface;
- Modelling continuation: 2D or 3D;
- Non-hydrostatic or hydrostatic version;
- Horizontal and vertical turbulence model: constant viscosity, mixing length, Smagorinsky, K-Epsilon, K-Omega;
- Solvers.

Most of the tests are displayed on Fig. 8 and Fig. 9. Not all the tests performed with the different solvers are shown, because the results are almost the same.

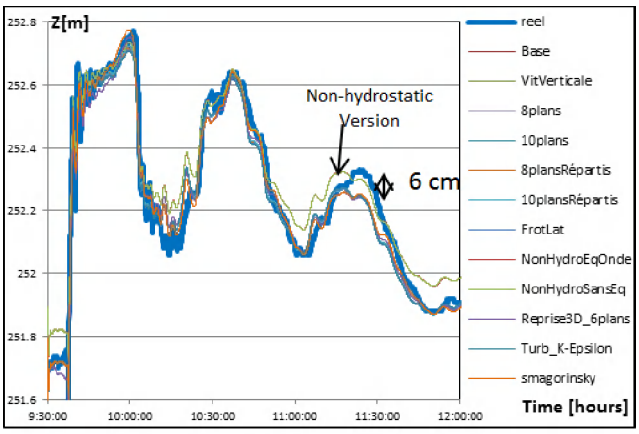

Figure 8. CE upstream models comparison

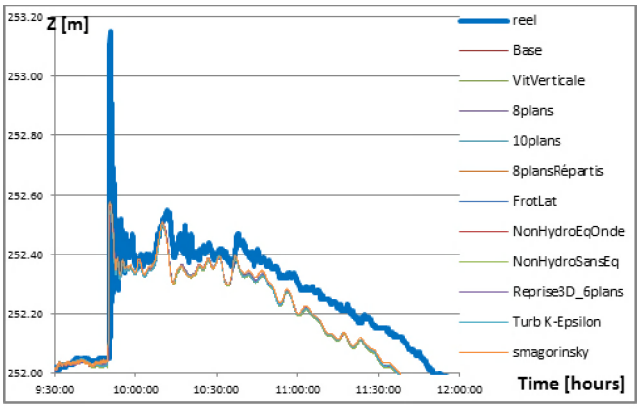

Figure 9. Inlet of headrace channel models comparison.

From the analysis shown in Fig. 8 some configurations could be dismissed:

- Particular level distribution is not appropriate to this test;
- Friction on lateral boundaries has no influence on the free surface level.

Further investigations:

- 3D continuation with restart file (equations solved at last time step);
- Non-hydrostatic version (starting hypothesis);
- Horizontal turbulence model: constant viscosity (5.10^{-3} m^2/s);
- Vertical turbulence model: mixing length;
- Steering word "Velocity profiles" at the discharge boundaries were calculated considering the water height.

At the inlet of the headrace channel, only the primary waves could be calculated by TELEMAC-3D: it should be necessary to find an alternative set of parameters to investigate this phenomenon.

B. Key-words coupling

These selected key words are gathered in one simulation. A quick test showed that considering only 6 horizontal levels was enough for this trigger test. Besides boundary conditions were modified and shifted to +10 minutes, because records gave average on last 10 minutes. The values of coefficient diffusion for velocity and depth were fixed to 1 in accordance with the calibration done on v5p9 version. Moreover, free surface gradient compatibility was reduced to 0.9 to avoid instabilities.

A new simulation was run with TELEMAC-3D considering the mentioned key-words concerning coupling and boundary conditions. The 2D model was also modified with the same key-words matching on TELEMAC-2D. Results were matching very well with the measurements as shown on Fig. 10 and Fig. 11.

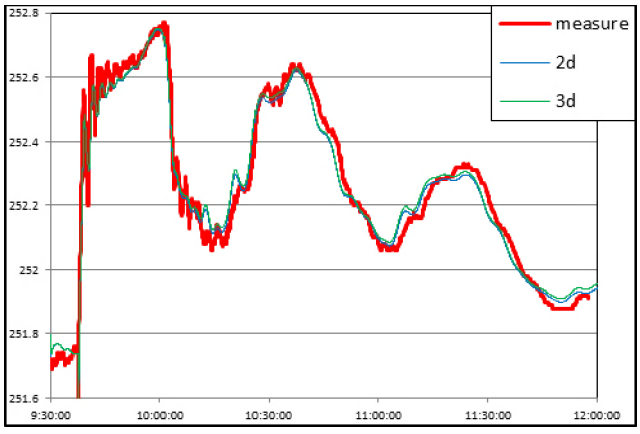

Figure 10. Comparison 2D vs. 3D optimized models at upstream of power plant

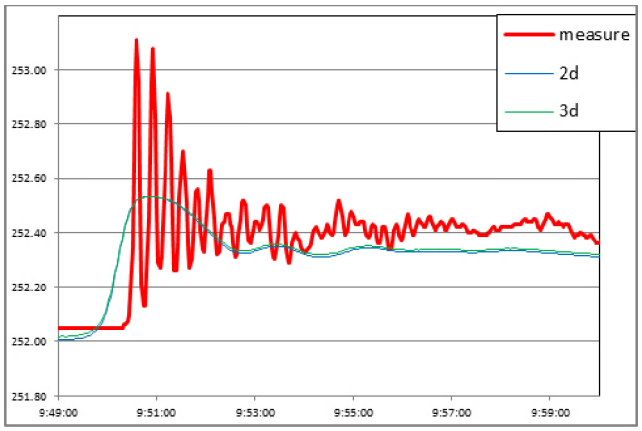

Figure 11. Comparison 2D vs. 3D models at inlet of headrace channel.

Due to optimization steps, the primary wave upstream of the plant is very well represented. Indeed, the period of the signal is correctly calculated for three oscillations visible in the Fig. 11 and the difference in the maximum amplitude is about 2 cm. The curves of 2D and 3D models overlap. The optimized 2D modelling converges to the same results as the 3D model. However, the results provided by TELEMAC-3D take the non-hydrostatic pressure distribution in the vertical axis into account; the model should in theory represent these secondary waves. The optimization of the 3D model must be continued in order to obtain these secondary waves.

IX. Optimisation program (2)

Besides the coefficients of velocity and water level diffusion imposed by the version and used for the calibration of the model, a refined mesh could be an alternative solution to get a better hydraulic behaviour. The alternative meshes were:

- Mesh modified at $\Delta x = 5$ m and $\Delta t = 0.5$ s with 588,378 nodes and 4,238,535 elements;
- Mesh modified at $\Delta x = 1$ m all along CA, as for the remaining area $\Delta x = 15$ m and $\Delta t = 0.1$ s and $\Delta t = 0.01$ s with 5,676,066 nodes and 28,197,810 elements.

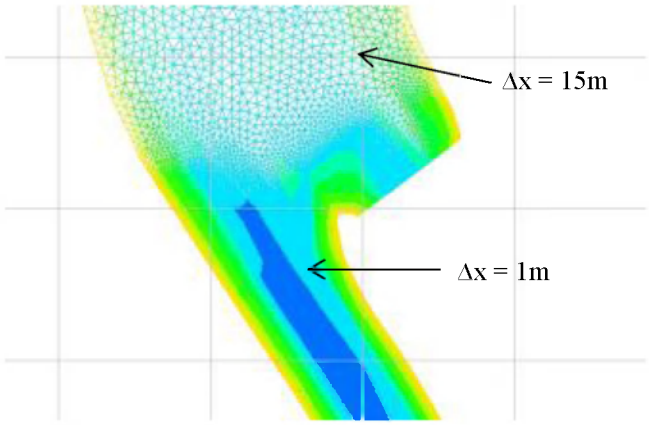

Figure 12. 3D models alternative meshed at inlet of headrace channel.

Only a refined mesh at 1 m with $\Delta t = 0.01$ s led to better results concerning Favre's waves modelling (Fig. 13). Indeed the frequency of the secondary waves is now visible in the 3D model results. However, the amplitude is not reached by this last run. A difference of about 50 cm occurred between the computed and measured peak amplitude.

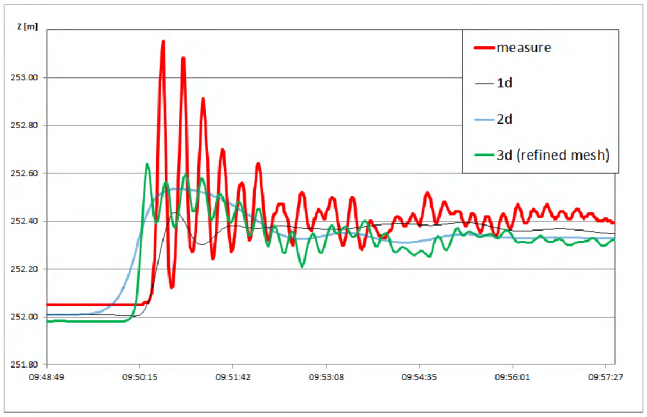

Figure 13. Best 3D Favre's waves representation at inlet of headrace channel.

X. Conclusion

The primary wave phenomenon is perfectly calculated by 2D and 3D models (with 6 horizontal plans only). However, the secondary wave phenomena could only be covered with an extremely refined mesh. This led to huge computing time. For 30 min simulation time with a time step of 0.1 s using 32 computational cores the server required 96 h and about 500 h with a time step of 0.01 s for the most refined model. Another future optimization is to refine the discretization of the water column by increasing the number of horizontal planes. Computation times observed here are probably incompatible with the engineering constraints. CNR wants to study the possibility of HPC (High Performance Computing) in the coming months.

Improved knowledge of waves disjunction, including secondary waves, on facilities of the Rhone valley is crucial for CNR to secure the safety for people and facilities. Farmers do not want to take responsibility for the real tests for trigger at high discharge. Also, the real tests mobilize a lot of resources and people. The numerical approach is a suitable way for the study of these phenomena in current operations. Today, as shown in Fig. 13, the calculations 1D-2D-3D do not supply conservative results. It would be promising to continue the study with further model configurations on Chautagne or with an alternative geometry of headrace channel (other development scheme on the Rhône River).

References

[1] FAVRE H. (1935), Etude théorique et expérimentale des ondes de translation dans les canaux découverts, Dunod, Paris.

[2] CNR (2007), Modélisation d'un déclenchement, Notice hydraulique et proposition de méthodologie.

[3] CNR (2010), Compte rendu de l'essai de déclenchement du 29/04/2010 et extrapolation à un déclenchement de 700 m3/s.

[4] CNR (2012), Modélisation hydraulique sous Telemac-2D, Construction d'un modèle bidimensionnel de la retenue de Chautagne.

TUC 2013, 16-18/10/2013, Karlsruhe - Kopmann, Goll (eds.) - © 2013 Bundesanstalt für Wasserbau ISBN 978-3-939230-07-6

Wave and hydrodynamics modelling in coastal areas with TELEMAC and MIKE21

A. G. Samaras, M. Vacchi
CIRI - EC, Fluid Dynamics Research Unit
University of Bologna
Bologna, Italy
achilleas.samaras@unibo.it

R. Archetti, A. Lamberti
Dept. of Civil, Chemical, Environmental and Materials Engineering
University of Bologna
Bologna, Italy

***Abstract*—Wave and hydrodynamics modelling in coastal areas is nowadays an indispensable tool for both research and engineering/environmental design. The selection among the various available models is equally essential and should be done cautiously, taking into consideration both the models' capabilities and the actual modelling needs. In the above context, results of ongoing research on the comparison between TELEMAC and MIKE21 are presented in this work. The test study area is located near the Port of Brindisi in South Italy. TELEMAC simulations were performed using TOMAWAC for wave propagation and TELEMAC-2D for the hydrodynamics; MIKE21 simulations were performed using the MIKE21-SW and MIKE21-HD modules respectively. Model output is compared on the basis of wave/current fields and wave propagation along linear trajectories from the offshore to the shoreline; analysis shows an overall satisfactory agreement between the two models.**

I. INTRODUCTION

Accurate predictions of wave climate, current patterns and sea level variations are essential for a wide range of research and operational applications, as they govern sediment and pollutant transport, coastal morphology evolution and interactions with structures in the coastal field. Accordingly, numerical models that can serve the above purposes have become the main tool for researchers, engineers and policy planners around the world. The range of available models is wide; the selection of the most suitable for each application should be based on models' evaluation with regard to the case-specific modelling needs.

In the present work, the open-source TELEMAC suite is compared with the well-known MIKE21 commercial software (developed by DHI Group) in a fundamental wave and hydrodynamics modelling application. The study area is located near the Port of Brindisi in South Italy; the models used are briefly described, as are the steps of their setup for the final applications. Results are compared on the basis of wave/current fields and wave propagation along linear trajectories from the offshore to the shoreline. Analysis shows an overall satisfactory agreement between the two models and is deemed to provide a useful insight on their comparative evaluation, setting the basis for future work in this direction.

II. MATERIALS AND METHODS

A. Grid Generation

Blue Kenue is a data preparation, analysis, and visualization tool for hydraulic modellers developed by the Canadian Hydraulics Centre (National Research Council). In the present work it was used to create the variable-density triangular mesh of the study area. The respective work for MIKE21 was done using MIKE Zero, the DHI tool for managing MIKE projects.

The bathymetric and shoreline data of the wider study area resulted from the digitization of nautical charts acquired from the Italian National Hydrographic Military Service ("Istituto Idrografico della Marina Militare").

B. Wave Propagation

Wave propagation with TELEMAC was modelled using TOMAWAC. By means of a finite-element type method, TOMAWAC solves a simplified equation for the spectro-angular density of wave action. The physical processes modelled comprise [1]: (a) energy source/dissipation processes (wind driven interactions with atmosphere, dissipation through wave breaking / whitecapping / wave-blocking due to strong opposing currents, bottom friction-induced dissipation), (b) non-linear energy transfer conservative processes (resonant quadruplet interactions, triad interactions), and (c) wave propagation-related processes (wave propagation due to the wave group / current velocity, depth-/current-induced refraction, shoaling, interactions with unsteady currents).

Wave propagation with MIKE21 was modelled using MIKE21-SW. MIKE 21-SW is a third generation spectral wind-wave model that simulates the growth, decay and transformation of wind-generated waves and swells. The discretisation of the governing equation in geographical and spectral space is performed using a cell-centred finite volume method, while in the geographical domain is discretized by unstructured triangular meshes [2]. MIKE-SW models the same physical processes as TOMAWAC, offering however less options for their parametrization.

C. Hydrodynamics

Hydrodynamics with TELEMAC were modelled using TELEMAC-2D. TELEMAC-2D solves the Saint-Venant equations using the finite-element or finite-volume method, and is able to perform simulations for both transient and permanent conditions [3]. Due to its capabilities, the model is widely used in free-surface maritime and river hydraulics; in the present work, the objective was to test the simulation of wave-current interactions through its direct coupling with TOMAWAC.

Hydrodynamics with MIKE21 were modelled using MIKE21-HD. MIKE21-HD simulates unsteady flow taking into account density variations, bathymetry and external forcings; it is based on the numerical solution of the two-dimensional incompressible Reynolds averaged Navier-Stokes equations, subject to the assumptions of Boussinesq and of hydrostatic pressure. The spatial discretisation of the primitive equations is performed using a cell-centred finite volume method [4]. As mentioned in the previous section for TOMAWAC and MIKE21-SW, MIKE21-HD also offers less parametrization options than TELEMAC-2D.

III. Model Setup

A. Study area

The study area is located northwest of the city and port of Brindisi (Puglia region, South Italy). The selected rectangular outline of the test field for the model applications, also shown in Fig. 1, measures about 21km in the longshore and 8km in the cross-shore direction.

B. Grid Generation

The triangular mesh in Blue Kenue was created defining two density zones: the one below 10m of depth where the "default edge length" was set to 20m, and the rest of the field where the respective value was set to 250m. The "edge growth ratio" parameter that governs the transition between the two in the meshing algorithm was set to 1.2. The resulted mesh, presented in Figure 2a, consists of 55,521 nodes forming 109,490 elements. The same approach was followed using MIKE Zero as well, with the two density zones divided by the 10m depth isoline. However, due to the fact that in MIKE Zero the generation of mesh elements is based on element area rather than "edge length" (as in Blue Kenue), repetitive testing resulted to a mesh of 61,861 nodes forming 122,110 elements (see Fig. 2b) which for this case was considered satisfactory. The effect of the mesh differences on the results will be the subject of future evaluation.

C. Coupled Wave and Hydrodynamics Simulations

Both TELEMAC and MIKE21 were set-up to run coupled wave and hydrodynamics simulations through the direct coupling of TOMAWAC – TELEMAC-2D and MIKE21-SW – MIKE21-HD respectively. Based on previous analysis of the wave regime for the wider area (wave data from the buoy of Monopoli, part of the Italian wave metric network "RON" [5, 6]), the test simulation in this work was selected to run for an extreme NE wave of significant wave height H_s=4m and peak period T_p=8sec imposed to the upper field boundary (see Fig. 2).

Figure 1. Wider study area and outline of the test field for the model applications (base images from Google Earth; privately processed).

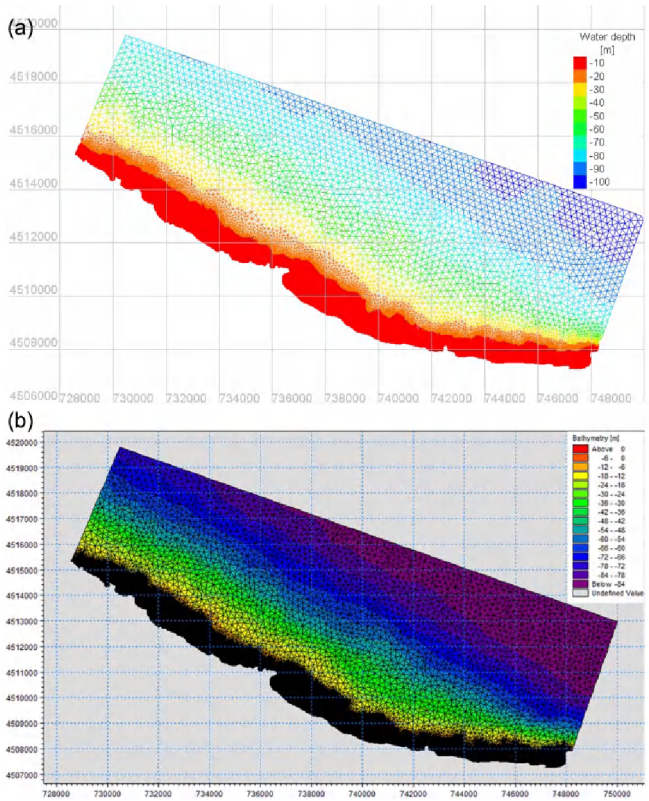

Figure 2. Triangular mesh and bathymetry for the test field as resulted from: (a) Blue Kenue and (b) MIKE Zero.

For the TOMAWAC – TELEMAC-2D simulation, the keywords that were modified in the steering files of the models are presented in Tables I and II respectively. For the MIKE21-SW – MIKE21-HD simulation, basic model parameters are presented in Table III.

TABLE I. MODIFIED KEYWORDS IN TOMAWAC

Keyword	Value
TIME STEP	6
NUMBER OF TIME STEPS	450
TYPE OF BOUNDARY DIRECTIONAL SPECTRUM	6
BOUNDARY SIGNIFICANT WAVE HEIGHT	4
BOUNDARY PEAK FREQUENCY	0.125
MINIMAL FREQUENCY	0.067
NUMBER OF FREQUENCIES	16
BOUNDARY MAIN DIRECTION	225
BOUNDARY DIRECTIONAL SPREAD	5
NUMBER OF DIRECTIONS	16
CONSIDERATION OF SOURCE TERMS	TRUE
DEPTH-INDUCED BREAKING DISSIPATION	1

TABLE II. MODIFIED KEYWORDS IN TELEMAC-2D

Keyword	Value
TIME STEP	3
NUMBER OF TIME STEPS	900
COUPLING WITH	TOMAWAC
COUPLING PERIOD FOR TOMAWAC	2
SOLVER	1 (conjugate gradient)
TREATMENT OF THE LINEAR SYSTEM	2 (wave equation)
WAVE DRIVEN CURRENTS	TRUE

TABLE III. MODEL PARAMETERS IN MIKE21-SW AND MIKE21-HD

Keyword	Value
Duration time [s]	2700
Wave	
Mode	2
EQUATION / Formulation	2
EQUATION / Time Formulation	2
SPECTRAL / Type of frequency discretization	2
SPECTRAL / Number of frequencies	15[a]
SPECTRAL / Minimum frequency	0.067
SPECTRAL / Frequency factor	1.1
SPECTRAL / Type of directional discretization	1
SPECTRAL / Number of directions	16
BOUNDARY CONDITIONS / Type	4
BOUNDARY CONDITIONS / Wave Height	4
BOUNDARY CONDITIONS / Peak period	8
BOUNDARY CONDITIONS / Wave direction	45
BOUNDARY CONDITIONS / Directional spread	5
WAVE BREAKING / Type	1
WAVE BREAKING / Type of gamma	1
WAVE BREAKING / Alpha	1
Hydrodynamics	
EQUATION / Formulation	2
EQUATION / Time Formulation	2
RADIATION STRESSES / Type	2
SOLUTION / Scheme of time integration	1
SOLUTION / Scheme of space discretization	1
SOLUTION / Type of entropy fix	1
SOLUTION / CFL critical HD	0.8
SOLUTION / CFL critical AD	0.8

a. The difference form the respective value in Table I is explained by the different definition of frequency distribution in TOMAWAC and MIKE-SW [1, 2].

IV. RESULTS AND DISCUSSION

Fig. 3a shows the wave height distribution and wave direction vectors over the entire field, as resulted from the coupled TOMAWAC – TELEMAC-2D run; Fig. 3b shows a detail of these results for a particular area of interest. The respective results of the coupled MIKE21-SW – MIKE21-HD run are presented in Figs. 4a and 4b. Model estimates are quite close for both wave height magnitude and distribution, focusing especially in the surf zone. The difference depicted in MIKE21 results (Fig. 4) for the onshore propagating waves is in fact not significant; all the values exceeding 4m in this area are below 4.1m, while the respective ones for TOMAWAC (Fig. 3) are only slightly smaller than 4m. Local peaks of wave height close to the breaker line reach ~4.2m in both models' results.

Fig. 6a shows the current speed distribution and current direction vectors over the entire field, as resulted from the coupled TOMAWAC – TELEMAC-2D run; Fig. 6b shows a detail of these results for the particular area of interest (same as in Figs. 3b and 4b). The respective results of the coupled MIKE21-SW – MIKE21-HD run are presented in Figs. 5a and 5b. In Figs. 5 and 6 insignificant current direction vectors (for speeds lower than 0.1 m/s) were omitted to enhance figures' clarity. Current circulation patterns and magnitude agree satisfactorily between model runs, with the prevailing longshore current (E-SE to W-NW direction) affected by shoreline morphology and local bathymetry. Current speed peaks appear in the same areas in both Figs. 5 and 6, approaching 2.5m/sec for the TOMAWAC – TELEMAC-2D run and reaching 2.8m/sec for the MIKE21-SW – MIKE21-HD run.

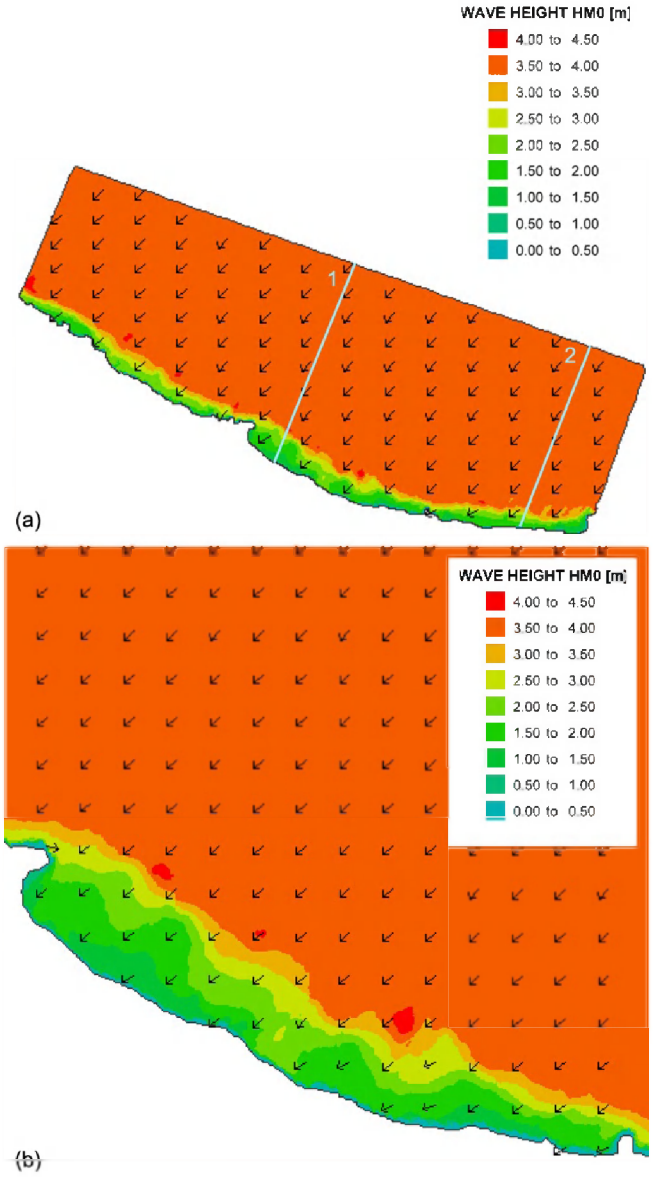

Figure 3. Wave height distribution and wave direction vectors as resulted from the coupled TOMAWAC – TELEMAC-2D run: (a) over the entire field and (b) for a particular area of interest. Wave height evolution along the line trajectories depicted in the upper figure, is presented in Fig. 7.

Figs. 7a and 7b show wave height evolution results of both the coupled TOMAWAC – TELEMAC-2D and MIKE21-SW – MIKE21-HD runs, along two linear trajectories from the offshore field boundary to the shoreline. Wave height profiles for Trajectory 2 (Fig. 7b) practically overlap inside the surf zone, with minor differences for the onshore-propagating wave behind the breaker line (located at ~5800m along the trajectory). On the other hand, results for Trajectory 1 (Fig. 7a) show differences regarding wave breaking and height evolution inside the surf zone. As the underlying theory is similar in both models, these can be attributed to differences in the triangular meshes (see Section III.B) and local anomalies in nearshore water depth interpolation (also affected by mesh properties). The aforementioned issues are undoubtedly among the ones to be further investigated in future research.

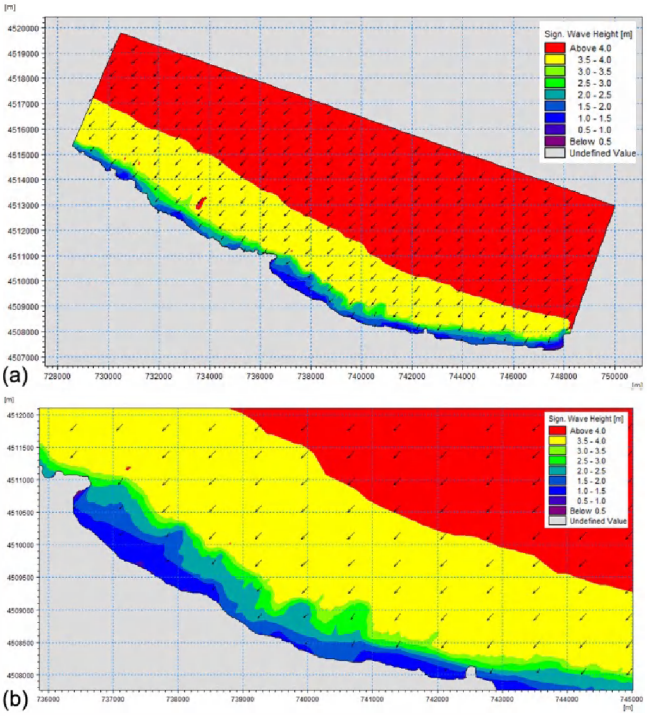

Figure 4. Wave height distribution and wave direction vectors as resulted from the coupled MIKE21-SW – MIKE21-HD run: (a) over the entire field and (b) for a particular area of interest.

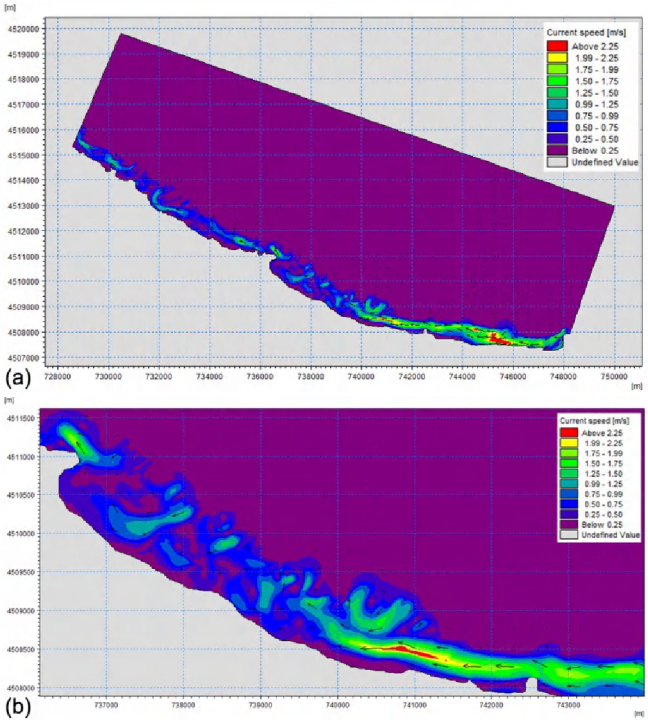

Figure 5. Current speed distribution and current direction vectors as resulted from the coupled MIKE21-SW – MIKE21-HD run: (a) over the entire field and (b) for a particular area of interest.

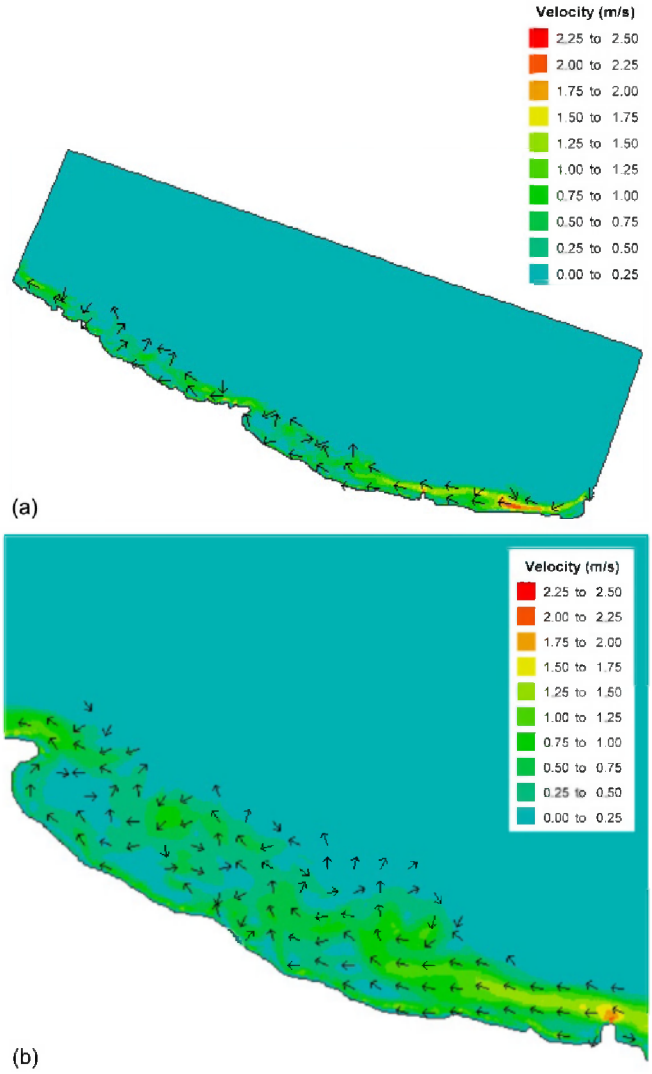

Figure 6. Current speed distribution and current direction vectors as resulted from the coupled TOMAWAC – TELEMAC-2D run: (a) over the entire field and (b) for a particular area of interest.

V. CONCLUSIONS

The present work was the first authors' step towards a comprehensive comparison of TELEMAC and MIKE21 on wave and hydrodynamics modelling. The results of the fundamental applications presented above show a satisfactory agreement between the two models. Having overcome some of the main obstacles in model setup, ongoing research comprises the investigation of the effect of all the wave- and current- related processes – modelled by TELEMAC and MIKE21 – on wave-current interaction. In future work, focus will be also given to identifying and implementing methods of analytical comparison of the models' results.

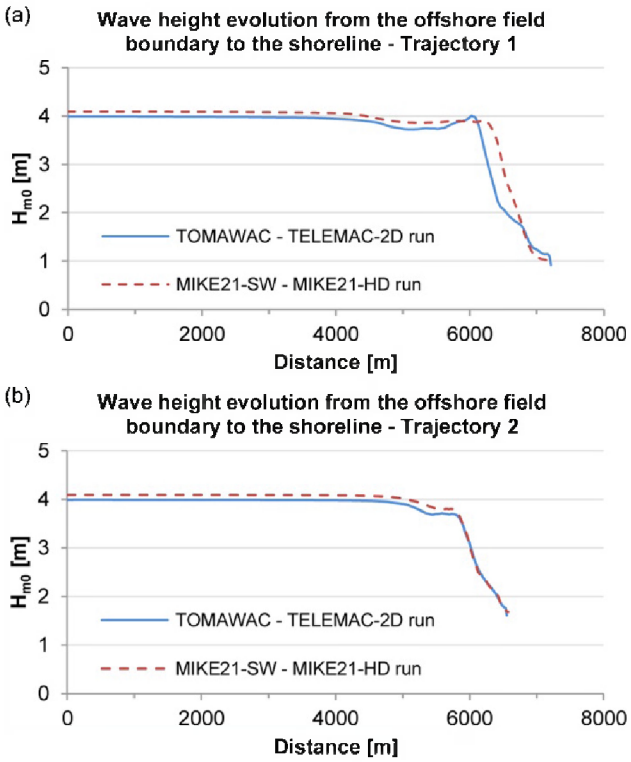

Figure 7. Wave height evolution along two linear trajectories from the offshore field boundary to the shoreline (see Fig. 3, (a) = Trajectory 1 and (b) = Trajectory 2), as resulted from both the coupled TOMAWAC – TELEMAC-2D and MIKE21-SW – MIKE21-HD runs.

ACKNOWLEDGEMENTS

This work was performed and funded in the framework of the Italian Project "TESSA – Development of Technologies for the Situational Sea Awareness" / PON01_2823.

REFERENCES

[1] EDF R&D, "TOMAWAC software for sea state modelling on unstructured grids over oceans and coastal seas. Release 6.1", 2011, p. 144.

[2] DHI, "MIKE 21 WAVE MODELLING / MIKE 21 SW - Spectral Waves FM / Short Description", Denmark, 2013, p. 14.

[3] P. Lang, "TELEMAC modelling system / 2D hydrodynamics / TELEMAC-2D software / Version 6.0 / USER MANUAL", 2010, p. 118.

[4] DHI, "MIKE 21 & MIKE 3 FLOW MODEL FM / Hydrodynamic Module / Short Description", Denmark, 2013, p. 12.

[5] Idromare. www.idromare.it.

[6] S. Corsini, R. Inghilesi, L. Franco, R. Piscopia, "Italian Waves Atlas", APAT-Università degli Studi di Roma 3, Roma, 2006, p. 134.

TUC 2013, 16-18/10/2013, Karlsruhe - Kopmann, Goll (eds.) - © 2013 Bundesanstalt für Wasserbau ISBN 978-3-939230-07-6

Two-dimensional hydrodynamic model of the port of Terneuzen (Scheldt estuary, The Netherlands)

T. Maximova[1,2], J. Vanlede[1], S. Smolders[3,1]
[1]Flanders Hydraulics Research, Berchemlei 115, 2140 Antwerp-Borgerhout, Belgium
Joris.Vanlede@mow.vlaanderen.be
[2]Free University of Brussels, Pleinlaan 2, 1050 Brussels, Belgium
[3]University of Antwerp, Universiteitsplein 1, 2610 Antwerp-Wilrijk, Belgium

***Abstract*—This paper describes the development and calibration of a two-dimensional hydrodynamic model of the port of Terneuzen. The model is calibrated using a cost function against a combination of water level, discharge and ADCP data. The calibrated model is used to calculate flow fields for the ship manoeuvring simulator of Flanders Hydraulics Research (FHR). The use of an unstructured grid allows for local grid refinement in the study area.**

I. INTRODUCTION

The lock complex at the port of Terneuzen provides access from the Western Scheldt to the port of Ghent located in Belgium (via the canal of Ghent – Terneuzen). Each year, about 10.000 seagoing vessels, 50.000 inland vessels, and about 3.000 pleasure crafts pass the locks.

The ship manoeuvring simulator of FHR consists of a mathematical model that calculates the effect of different forces on a sailing vessel, and a navigation bridge from where the pilot can see how the vessel behaves and can steer it. It is possible to simulate different types of vessels, tugboat assistance, movement of other ships, etc. The ship manoeuvring simulator is used for training purposes for river pilots and for research on the feasibility of an extension of the lock complex. The numerical model is used to calculate accurate velocity maps with a high spatial resolution, which are provided as flow fields for the simulator.

Before setting up the TELEMAC model presented here, the best hydrodynamic model for the port of Terneuzen was the NEVLA model [1], [2], which includes the entire Scheldt estuary in a curvilinear grid. The grid resolution of the NEVLA model is 130 x 50 m near Terneuzen, which is too coarse for a meaningful application of the model results in the ship simulator. The use of an unstructured grid allows for local grid refinement in the study area, which is necessary to take the complex geometry of the study area into account (e.g. accurate representation of the quay walls).

II. THE NUMERICAL MODEL

A. Model grid

A 2D model for this project is developed in the TELEMAC software, which is based on the finite element method. The model domain is discretised into an unstructured grid of triangular elements and it is locally refined in the study area.

Google Earth and Blue Kenue [3] were used to define the outline of the model. Afterwards, the triangular computational mesh was generated in the Blue Kenue software. The model domain is shown in Fig. 1. The downstream boundary of the TELEMAC model is located at Vlissingen; the upstream boundary is located at Liefkenshoek.

The final grid has a resolution of 100 m at the model boundaries, 50 m in the area around the port of Terneuzen and 10 m at Terneuzen (Fig. 2). The total number of nodes in the grid is 95.105 and the total number of the elements is 186.877.

Figure 1. Numerical model domain

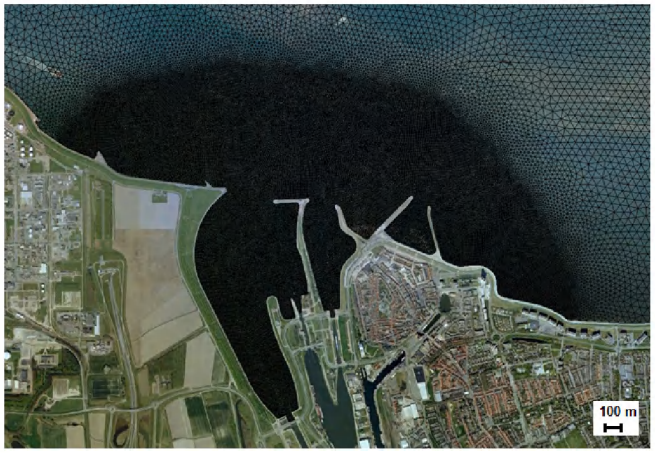

Figure 2. A detail of the mesh for the port of Terneuzen

B. Bathymetry

The bathymetry of the Western Scheldt and Lower Sea Scheldt is defined based on the samples from 2011 provided by Rijkswaterstaat and Flemish Hydrography respectively. Bathymetry for the port of Terneuzen and its surroundings is taken from the Scheldt ECS server (data for 2010 – 2012). TAW (Tweede Algemene Waterpassing, the standard vertical reference in Belgium) is used as a vertical reference.

The bathymetric samples are not available for a number of relatively small areas located far from the area of interest (e.g., port of Hansweert and Vlissingen). The bathymetry for these areas was defined based on the maps of Flemish Hydrography (2011).

C. Boundary conditions

The boundary conditions for the TELEMAC model in this study are generated by nesting the model in the NEVLA model. A 10 minute time series of total discharge at Vlissingen is imposed at the downstream boundary and a 10 minute time series of water level at Liefkenshoek is imposed at the upstream boundary.

D. Simulation period

Based on the tidal conditions during which ADCP and discharge measurements are available (see further), the model is run from 28/07/2009 00:00 to 28/08/2009 00:00.

III. AVAILABLE MEASUREMENT DATA

Measured water levels are available in 9 different stations (location in Fig. 3). 10 minute time series of water level were retrieved from the Hydro Meteo Centrum Zeeland database (HMCZ) for the stations on the Dutch territory and from Hydrologisch Informatie Centrum (HIC) for station Liefkenshoek in Belgium.

Six different ADCP measurement campaigns are available (Table I and Fig. 3). During such a measurement campaign, a ship-mounted ADCP measures continuously during one tidal cycle, while the ship follows a fixed transect across the river. The resulting dataset consists of velocity vectors distributed over the transect and over the water depth, during one tidal cycle. Four of these datasets are used for the model calibration, two are used for the model validation.

TABLE I. ADCP MEASUREMENTS USED FOR THE MODEL CALIBRATION

Measurement	Date	Tidal Conditions	Used for
R7 Everingen	04/06/2008	spring tide	calibration
Terneuzen port	21/03/2007	spring tide	calibration
Waarde	23/03/2006	neap tide	calibration
Waarde	28/09/2006	average tide	calibration
R7 Everingen	05/07/2011	spring tide	validation
R7 Terneuzen	06/07/2011	average tide	validation

Discharge data are obtained by integration of ADCP data over the cross section, and are available for 15 cross sections in the Western Scheldt. Discharge data are used during the model calibration.

Figure 3. Available measurement data

IV. MODEL CALIBRATION

A. Methodology

The main objective of the model calibration is to optimize the representation of the flow velocity in the port of Terneuzen. Bed roughness and velocity diffusivity are used as calibration parameters. The results of model simulations are compared with measured water levels, velocities and discharges.

Comparison between modelled and measured water levels is done by comparing the time series, the individual high and low waters, and the harmonic components obtained from a harmonic analysis.

For ADCP measurements and discharge data, comparison with the model results is done for a selected modelled tide that is comparable to the tidal conditions during the measurements (Table I). Working with comparable tides means that differences between the calculated and measured velocities and fluxes are expected when the agreement between the measured and modelled tides is not sufficient. Differences between the model bathymetry and the actual bathymetry during the measurements can be another reason for the differences in discharges.

B. Cost function

In order to select the best calibration run, a cost function (1) is calculated for each simulation. The cost function is intended to get one value that represents model performance. The factors in the cost function are defined in such a way that a lower value represents better model performance. The cost function is made dimensionless in relation to a reference run, so a value lower than 1 indicates an improvement over that reference run [2]. The model run with the best accuracy has the lowest score.

$$Cost = \sum \frac{Factor_i}{Factor_{i,ref}} * Weight_i \quad (1)$$

Several parameters are selected as factors for the calculation of the cost function (Table II).

TABLE II. FACTORS FOR THE CALCULATION OF THE COST FUNCTION

Factor	Weight	
RMSE water level time series	7%	Total weight for WL = 28%
RMSE high waters	7%	
RMSE low waters	7%	
Vector difference[a]	7%	
RMSE velocity magnitude R7 Everingen	8%	Total weight for velocities and discharges = 72%
RMSE velocity direction R7 Everingen	8%	
RMSE velocity magnitude Terneuzen port	8%	
RMSE velocity direction Terneuzen port	8%	
RMSE velocity magnitude Waarde 23/03/2006	8%	
RMSE velocity direction Waarde 23/03/2006	8%	
RMSE velocity magnitude Waarde 28/09/2006	8%	
RMSE velocity direction Waarde 28/09/2006	8%	
RMSE discharge	8%	
Sum	100%	

a. Vector difference combines the evaluation of both amplitude and phase between the observed and modeled tidal components.

In the cost function more weight is given to velocities than to water levels because the main objective of this project is to improve the model accuracy for the flow velocities.

C. *Results*

In order to improve the representation of water levels, the upstream boundary condition was corrected by subtracting 6 cm from the water level at Liefkenshoek calculated in the NEVLA model. The model was further calibrated by varying the roughness and diffusivity parameters. The adaptation of the bed roughness resulted in an improvement of the M2 amplitude.

Run simTZ_44 produces the best results. A varying roughness field (0.023 $m^{-1/3}s$ in the downstream part of the model and 0.021 $m^{-1/3}s$ upstream) and a velocity diffusivity of 2 m^2/s are used in this simulation.

V. QUALITY ASSESSMENT OF THE FINAL MODEL

This paragraph gives a quantitative assessment of the performance of model run simTZ_44 during the calibration.

A. *Water levels*

The RMSE (root mean square error) of high, low waters and complete water level time series is about 10 cm for most stations. The RMSE of high and low water phase is smaller than 10 min.

The M2 harmonic component has the highest amplitude in the zone of interest, implying that the tidal amplitude will depend to a large extent on the amplitude of M2. The difference between the calculated and measured M2 amplitude is very small (1 to 2 cm) at most stations (Fig. 4). The biggest difference (4 cm) is observed at Borssele and Terneuzen. These stations are located in the downstream part of the model near the discharge boundary. The difference in the M2 phase is 3 degrees at Liefkenshoek and 1 to 2 degrees at other stations (Fig. 5).

B. *ADCP velocities*

An example of the plot of time series of the measured and modeled velocities at Everingen is shown in Fig. 6. Each point on this plot represents a depth-averaged velocity magnitude or direction for a certain transect measured with ADCP or calculated in the model. Fig. 7 presents a vector plot of the modeled and measured velocities for one of the transects in the port of Terneuzen.

The absolute value of bias of the velocity magnitude at Everingen is smaller than 10 cm/s for most transects. The RMSE of velocity magnitude varies between 7 and 20 cm/s over a tidal cycle. The total RMSE for all transects is 16 cm/s. The RMSE of velocity direction is smaller than 20 degrees for most transects. It is maximal during slack.

The bias of the velocity magnitude at Terneuzen varies between -9 and 11 cm/s. The total RMSE of velocity magnitude is 11 cm/s. The RMSE of velocity direction changes from 13 to more than 100 degrees (in the beginning of flood). The model accuracy for the velocity direction is good when the velocity magnitude is high. It worsens in the areas where velocity magnitude is very small. This results in an increase of the RMSE value of the entire transect.

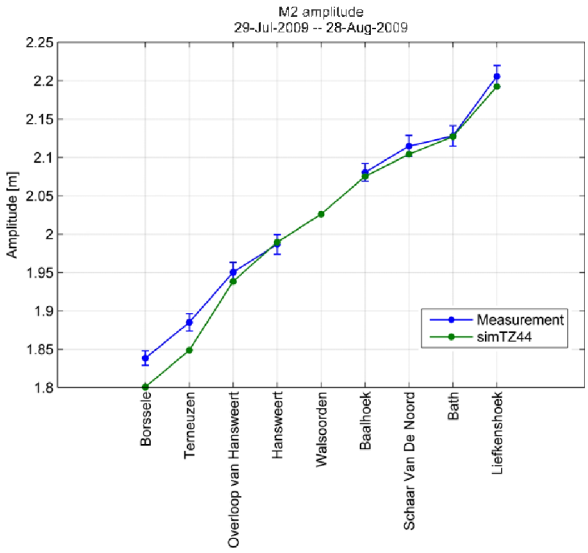

Figure 4. M2 amplitude

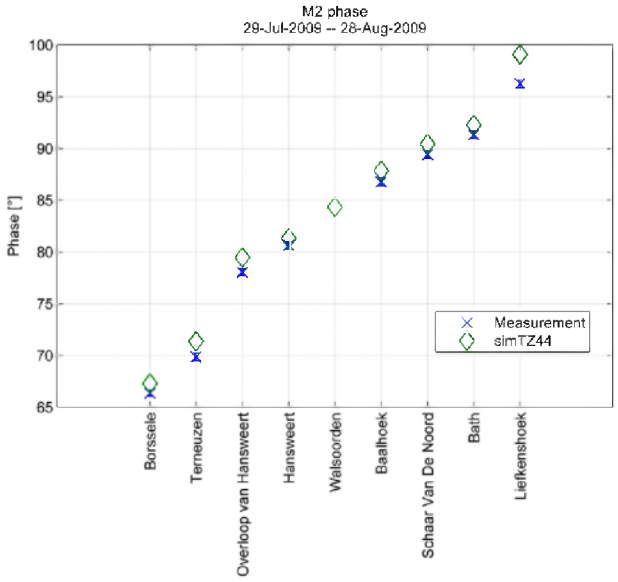

Figure 5. M2 phase

The modelled velocities at Waarde are slightly underestimated in the model for most transects. The total RMSE of velocity magnitude is 14 cm/s; the total RMSE of velocity direction is 32 degrees. During ebb and in the beginning of flood this RMSE increases up to 40 to 60 degrees. This is related to uncertainties in the ADCP measurements.

C. *Discharges*

The shape of the discharges is well represented in the model for most cross sections. The RMSE of the discharge time series is 4 to 13% of the maximum discharge at a certain location. An example of the measured and calculated discharge time series is shown in Fig. 8 for R7 Pas van Terneuzen. The model results and measurements are analysed for the comparable tides.

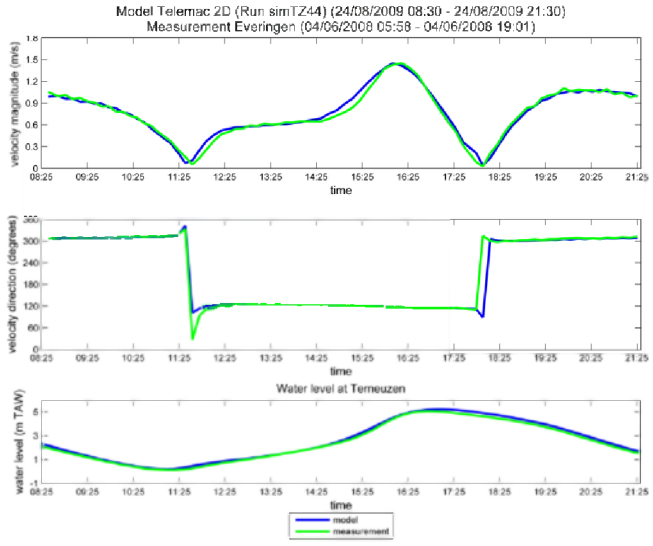

Figure 6. Time series of the measured and modeled velocity magnitude and direction at R7 Everingen

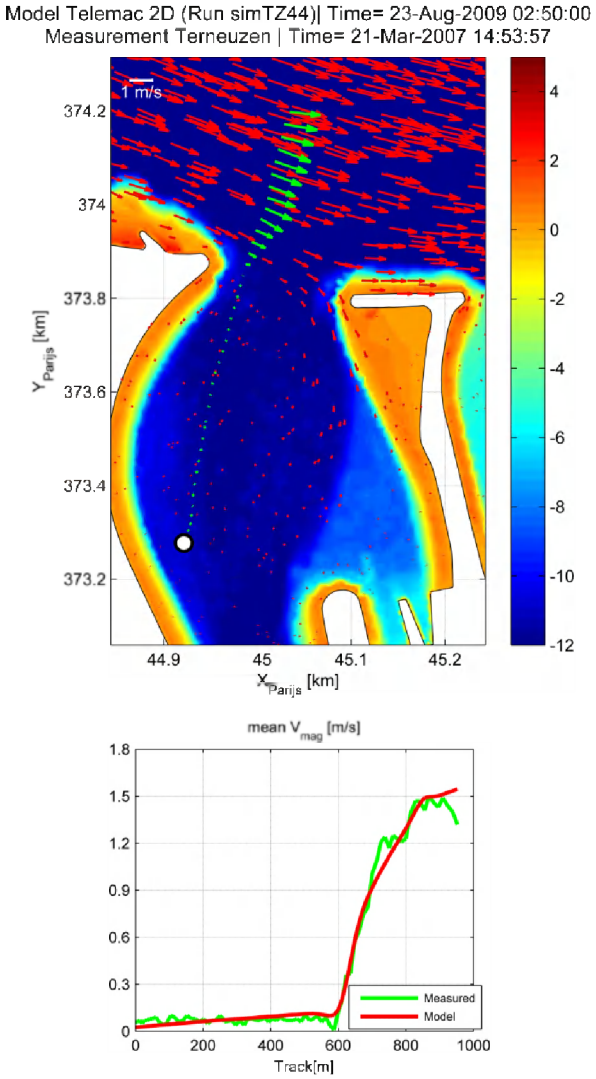

Figure 7. Vector plot of the modeled and measured velocities at Terneuzen (white circle on the figure shows the location of the first measurement (0 m))

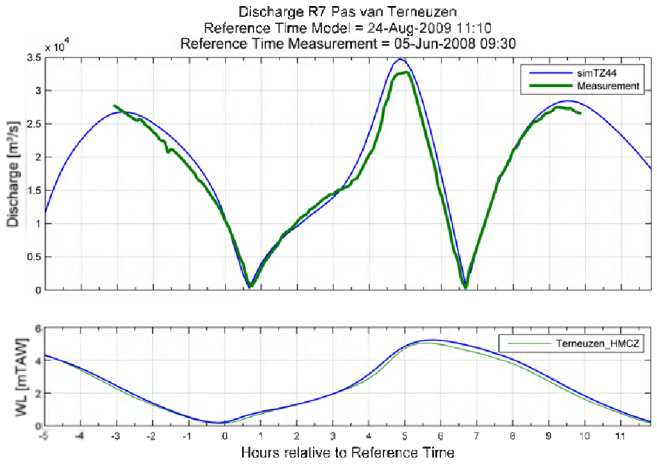

Figure 8. Measured and modeled discharges at R7 Pas van Terneuzen

VI. MODEL VALIDATION

For verification purposes, an independent set of ADCP measurements that were not used for the model calibration is used. The measurement campaigns are listed in Table I.

The model performance during the validation period is comparable with the performance during the calibration. The absolute value of bias of the velocity magnitude at Everingen is smaller than 10 cm/s for most transects. The total RMSE of velocity magnitude is 14 cm/s. The RMSE of velocity direction is smaller than 20 degrees for most transects. It increases around slack. The total RMSE for all transects is 24 degrees.

The flow velocities at R7 Terneuzen are underestimated in the model during ebb (the bias varies between -1 and -16 cm/s). The model accuracy is better during flood. The total RMSE for all transects is 18 cm/s. The RMSE of velocity direction is 35 degrees. The maximum differences are observed around slack.

VII. APPLICATION OF THE FLOW FIELDS IN THE SHIP SIMULATOR

A. *Export of the modelled velocity maps*

The calibrated model was used to calculate the velocity maps for the ship simulator of FHR. The model maps were calculated every 10 min from 25/08/2009 16:00 to 26/08/2009 8:00 (spring tide).

Since a 2D model was used for this study, no depth averaging was implemented. The modeled velocities were exported only for the points with a water depth larger than 1 m. For the points with a smaller depth, velocities were set to NaN (not a number).

B. *Research in the simulator*

The modelled velocity fields are used in the ship manoeuvring simulator of FHR for the training of canal pilots and for testing specific proposals for the design of new infrastructure (e.g. new sea lock in Terneuzen). This lock will improve the access for seagoing vessels to the ports of Ghent and Terneuzen and will ensure a smooth transit of inland vessels between the Netherlands, Belgium and France [4].

Qualified pilots can assess whether a new design does not hinder navigation so that the limits for safe traffic can be defined (e.g. the maximum dimensions of the vessels calling at a port, the maximum allowed wind or current on entry, what action to take by poor visibility etc.) [5].

It is also possible to examine if new nautical procedures and auxiliary resources improve safety (e.g. use of tugboats, moving of buoys etc.) [5].

It is possible to simulate sailing into and out of the lock, assistance of tug boats, different weather conditions, interaction with other vessels etc. The evaluation of simulations is based on the recorded trajectory, the values of important parameters during the simulation and the reactions of the pilots after the simulations [6].

The following documents are used for the evaluation of simulation results:

- Sailing course plots that describe the trajectory of the simulated ship (including an indication of the positions where a contact occurred between the ship and a hard structure).
- Summary graphs with information about the ship parameters and the use of tugboats etc.) [6].

The view of the port of Terneuzen in the ship manoeuvring simulator is shown in Fig. 9. An example of the sailing course plot is presented in Fig. 10. It shows positions of the simulated ship and tug boats every 60 seconds.

The simulator can be used for the training of river pilots. They can sail into locks and carry out anchoring manoeuvres; approach various jetties and moor to these; learn to work with tugboats; etc. The position, velocity components and forces acting upon the vessel during simulation runs can be saved and can thereafter be used for further analysis [5].

VIII. CONCLUSIONS

A TELEMAC model was developed for the port of Terneuzen. After calibration and validation it was used to calculate velocity fields for the ship simulator of FHR. The TELEMAC model was successfully integrated into the existing software of FHR for the statistical analysis during calibration and validation. This model was calibrated based on the available water levels, velocity and discharge measurements.

The model accuracy for high and low waters and harmonic components of the tidal wave was improved during the calibration process. Discharges are well represented in the model at most locations. For the model calibration the calculated velocities were compared with the ADCP measurements at R7 Everingen, port of Terneuzen and Waarde.

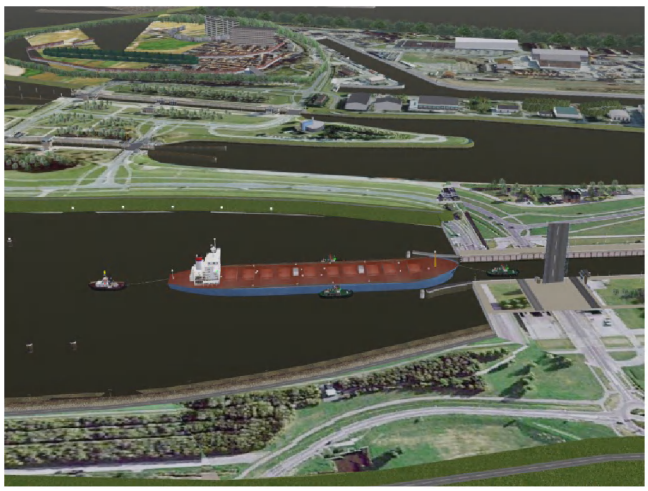

Figure 9. View of the port of Terneuzen in the ship manoeuvring simulator

Figure 10. Sailing course plot: vessel entering the port of Terneuzen

The model accuracy is good at all three locations. The RMSE varies between 11 cm/s at the port of Terneuzen and 16 cm/s at Everingen.

The ADCP measurements from 2011 at R7 Everingen and R7 Terneuzen were used for the model validation. The RMSE of velocity magnitude is 14 cm/s at Everingen and 18 cm/s at R7 Terneuzen.

The modeled velocity fields will be applied in the ship manoeuvring simulator of FHR for the training of river pilots and for testing specific proposals for the design of new infrastructure.

REFERENCES

[1] T. Maximova, S. Ides, T. De Mulder, and F. Mostaert, (2009). Verbetering 2D randvoorwaardenmodel. Deelrapport 4: Extra aanpassingen Zeeschelde. WL Rapporten, 753_09. Flanders Hydraulics Research, Antwerp, Belgium.

[2] B. Verheyen, G. Leyssen, J. Vanlede, G. Schramkowski, and F. Mostaert, (2013, concept version). Verbetering randvoor-waardenmodel: Deelrapport 7: Afregeling van het 3D Scheldemodel. WL Rapporten, 753_09. Flanders Hydraulics Research & IMDC: Antwerp, Belgium.

[3] Canadian Hydraulics Centre, (2011). Blue Kenue. Reference manual.

[4] Port of Ghent, (2013). Engineering office to design new sealock in Terneuzen [online]. Available from: http://en.havengent.be/nieuwsdetail.aspx?id=3247 [Accessed 02/08/2013].

[5] Flanders Hydraulics Research, (2010). Nautical research. Towing tank and ship manoeuvring simulator. D/2010/3241/119. Antwerp, Belgium.

[6] J. Verwilligen, K. Eloot, and F. Mostaert, (2010). KGT – Zeesluis binnen complex: Simulatiestudie. Versie 2_0. WL Rapporten, 803_05. Waterbouwkundig Laboratorium: Antwerpen, België.

TUC 2013, 16-18/10/2013, Karlsruhe - Kopmann, Goll (eds.) - © 2013 Bundesanstalt für Wasserbau ISBN 978-3-939230-07-6

Harvesting the currents power on the Southern Brazilian Shelf

E. de Paula Kirinus; C. Eadi Stringari
Instituto de Oceanografia
Universidade Federal do Rio Grande - FURG
Rio Grande, Brazil
ekirinus@gmail.com

W. Correa Marques; H. Barreto Matzenauer
Instituto de Matemática, Estatística e Física
Universidade Federal do Rio Grande - FURG
Rio Grande, Brazil
wilian_marques@yahoo.com.br

***Abstract*—Application of marine currents for electricity generation could offer a distinct advantage over other renewable energy sources due to the regular and predictable nature of the resource. This paper details the design of a turbines farm containing ten helicoidal turbines. With three grids a study computing one year of simulation with the TELEMAC-3D model coupled with the energy conversion module was carried out. It was possible to indicate an interest area for trial tests of modelling a turbine farm. The conversion pattern is highly dominated by the wind-driven circulation and for the passage of frontal systems. The configuration settled for this study predicted an annual power output of 59,39 GWh which is equivalent to 0.22% of the whole energetic consumption of the Rio Grande do Sul State in 2010.**

I. INTRODUCTION

The continuous growth of the world population increases the demand and competition for energy, requiring an immense effort for making non-renewable energy sources availability. Therefore, in addition to promoting the development of new technologies, global policies for the generation of renewable and clean energy are being strengthened. Several methods of energy conversion have been developed over the years, especially the turbine-based current energy converter, which demonstrated high energy generation capacity and is already in operation.

The technique used can be described as an underwater wind turbine, having approximately the same principles of function. In Brazil, there is no mapping of the coastal zones regarding the energetic potential viable for conversion using hydrokinetic turbines, however, recent studies have showed two spots of high power availability off the shores of the Rio Grande do Sul state, that can generate 3.5 MW/year of power [1]. [2] studied the influence of hydrodynamic and morphodynamic processes of the installation of six hydrokinetic turbines reaching 5 GW/year annual power.

The Southern Brazilian Shelf (SBS), located between 28°S and 35°S (Fig. 1), continentally bounded with the Rio Grande do Sul State, has a slightly rugged shoreline, which is oriented Northeast - Southwest. The bathymetry of this region is quite soft, with the higher slope and shelf break located near the 180 m isobath [3]. Located near the Brazil-Malvinas Confluence zone, this region is known for the high spatial and temporal variability and also for the meeting of several water masses [4]. In addition, the Southwest Atlantic

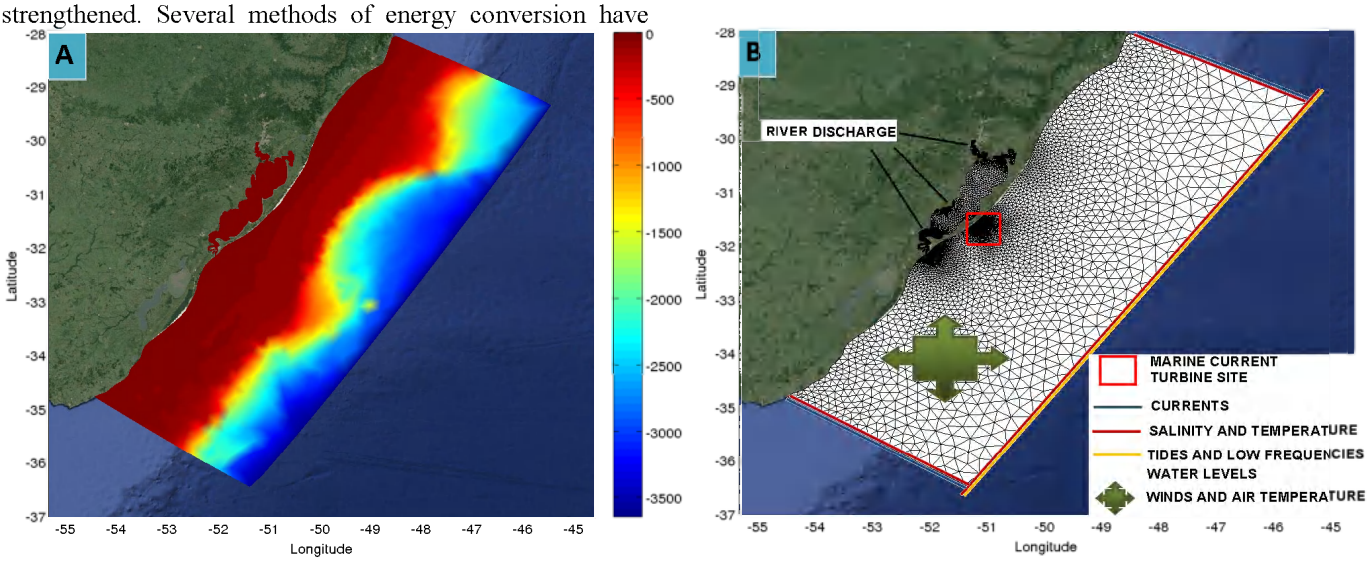

Figure 1. A) Southern Brazilian Shelf, with maximum depth around 3.500 m. B) Grid used on the site simulation. The red square represents the spot of the hydrokinetic turbines farm. Also, the finite elements mesh highlighting the liquid and surface boundaries conditions for the TELEMAC-3D model.

Ocean is one of the most dynamic regions of the global ocean [5], characterized by large thermohaline contrasts and intense mesoscale activity [6].

The high seasonality in the wind fields [7] contributes for dominance of Northeast (NE) winds during Summer and Southwest (SW) winds during Winter, which drive the coastal circulation through the SW and NE, respectively [2,4,8].

Recently, the annual energy report of the Rio Grande do Sul state [9] have briefly mentioned the energy from the marine currents as a possible source for harvesting power, which could easily enhance the Brazilian matrix of energy. Following, the aim of this paper is to study the potential of using energy converters (as turbine type) along the Southern Brazilian Shelf, applying a three-dimensional model of ocean circulation coupled with an energy model, in order to evaluate the energy conversion and the local circulation pattern of a converters farm.

II. METHODOLOGY

A. Hydrodynamic Model

The TELEMAC system, developed by the Laboratoire National d'Hydraulique et Environnement of the Company Eletricité de France (CEDF), was used for the hydrodynamic simulations. The TELEMAC-3D model solves the Navier Stokes equations by considering local variations in the free surface of the fluid, neglecting density variations in the mass conservation equation, and considering the hydrostatic pressure and Boussinesq approximations to solve the motion equations. The model is based on finite element techniques to solve the hydrodynamic equation [10] and relies on the sigma coordinate system for the vertical discretization in order to follow the surface and bottom boundaries [11].

A time step of 90s and a Coriolis coefficient of -7.70 x 10^{-5} rad.s^{-1} (latitude 32°S) were used in all the simulations. The horizontal turbulence process was performed using the Smagorinsky model. This closure turbulent model is generally used in maritime domains with larger-scale eddy phenomena, calculating the mixing coefficient by considering the size of the mesh elements and the velocity field [12].

The mixing length model for buoyant jets was implemented to assess vertical turbulence processes. This model takes into account density effects via a damping factor that depends on the Richardson number to calculate the vertical diffusion coefficients.

B. Energy Conversion Module

The power of the oceanic currents can be transformed, by using converters with similar technology of wind converters, through a submerged rotor that is forced to rotate by the fluid surrounding it. According to [13], in a recent study of equipments available to capture hydrokinetic energy, it was found 76 equipments, among them, turbines in operation or still in the early stages of research were studied.

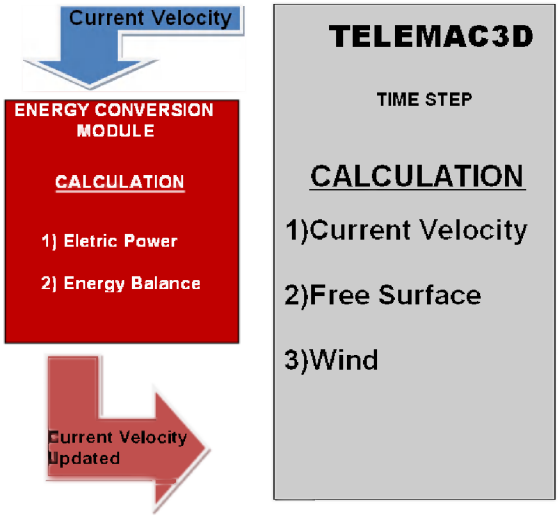

Figure 2. Fluxogram of the interactions between the TELEMAC-3D and the energy module (adapted from [2]).

The hydrodynamic simulations used in this work were performed using TELEMAC-3D model, and the investigations that involved the energy conversion from currents into electrical power were performed with the energy module [2]. This module uses the turbine standard equation to calculate the electric power converted in watts (W), from the incident flow velocity.

Based on the principle of energy conservation, during each time step of the hydrodynamic model (Fig. 2) the current velocity is calculated and transferred to the energy conversion module that converts some part of the energy of the currents into power through the electric power equation (1). In the energy conversion module the current velocity is updated to maintain the energy balance of the TELEMAC-3D model.

According to [2,4,8], among others, the region of the SBS presents a multidirectional and highly dynamic pattern of circulation, which are strongly influenced by the passage of frontal meteorological systems. Due to this pattern, in this work the Gorlov converter will be used [14] because of its advantages on capturing energy in multidirectional currents.

Furthermore, the helicoidal turbine of Gorlov has a sectional area corresponding to a rectangle (h*D) and its efficiency coefficient (η) is smaller, being equal to 0.35 [14]. Therefore, Equation (1) controls the power gained from a helicoidal converter. Table I indicates the turbine technical parameters used into the energy conversion module.

$$P(W) = 0.5.\eta\rho(h*D)v^3 \quad (1)$$

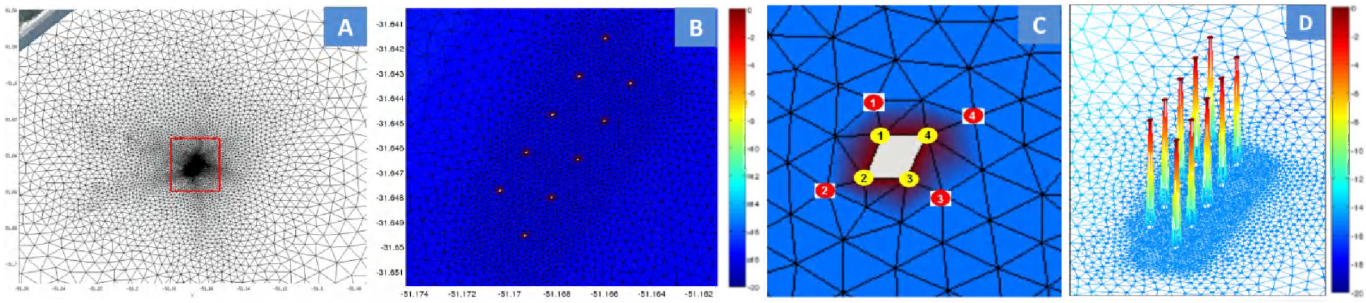

Figure 3. Region of the turbines on the study area. (A) Numerical grid with high degree of refine on the interest region. (B) Converters farm with 10 helicoidal turbines represented with 2 arrays parallel to the coast. (C) Scheme showing the interactions between the energy conversion module and the turbines. (D) Conversion structures represented in a three dimensional shape. The depth of this site is around 18m.

C. *Scenario Study*

To investigate the potential for energy conversion and the influence of the installation of energy converters in the natural hydrodynamic processes of the SBS, three simulations were carried out over 365 days, applying the physical parameters established in the upcoming section. The simulated period covers from January 1st to December 31st of a climatologic year.

One simulation was conducted using only the hydrodynamic processes. After indicating the interesting areas, another mesh was created with ten turbines (Fig. 3.a).

The farm grid direction (Fig.3.b) was idealized to be parallel to the coast, with 200 m of distance between each turbine on x and y directions. Due to computational limitations the best shape for a turbine was with 4 nodes (Fig. 3.c), with 10 m distance between each node.

The conversion model interacts with the turbine, acquiring the velocity at the node (red bullet at Fig. 3.c), this velocity is converted into power and the loss of kinetic energy is released on the turbine node, represented for the yellow bullets.

In order to improve this scenario, the energy sink for conversion was implemented for two simulations with the farm grid (according to the interactions above). One simulation was without the conversion structures and another simulation contained the three-dimensional physical structure of the turbines (Fig. 3.d), where the turbine nodes depth was changed in the FORTRAN source code.

D. *Initial and Boundary Conditions*

In order to study the tendency of power generation and the understanding of the processes occurring within a farm of turbines, for this study we used climatology data to impose the initial and boundary conditions. This data was created from long scale data base from the Brazilian National Water Agency (ANA), the Ocean Circulation and Climate Advanced Modeling Project (OCCAM) and also from Reanalysis (National Oceanic Atmospheric Administration - NOAA).

The climatological changes were performed through a monthly mean of temporal data series of discharge since January of 1940 until December 2006. The OCCAM data were treated from 1990 to 2004 for the velocity components, temperature, salinity and sea surface height. The wind and air temperature fields from Reanalysis were gathered from 1948 to 2012 [15].

The oceanic boundary was forced by the astronomical tides, water levels, current velocity, salinity and temperature fields (Fig. 1.b.). Along the surface boundary, the temporal and spatial variability of the winds and air temperature were prescribed. The air temperature data along the ocean's surface have also been used in order to consider the process of heat exchange with the atmosphere in the model calculations.

The numerical model was initialized from the rest and with an initial elevation of 0.50 m, the approximate average tide in the region [16]. Along the oceanic border the amplitude and phase data were also prescribed, through the calculation by the Grenoble Model FES95.2 (Finite Element Solution v. 95.6).

TABLE I. TURBINE TECHNICAL PARAMETERS

Start-in Speed	0.2 m.s^{-1}
Cut-in Speed	1.5 m.s^{-1}
Nominal Power	170 kW
Turbine Height	14 m
Turbine Ray	10 m

E. Calibration and Validation

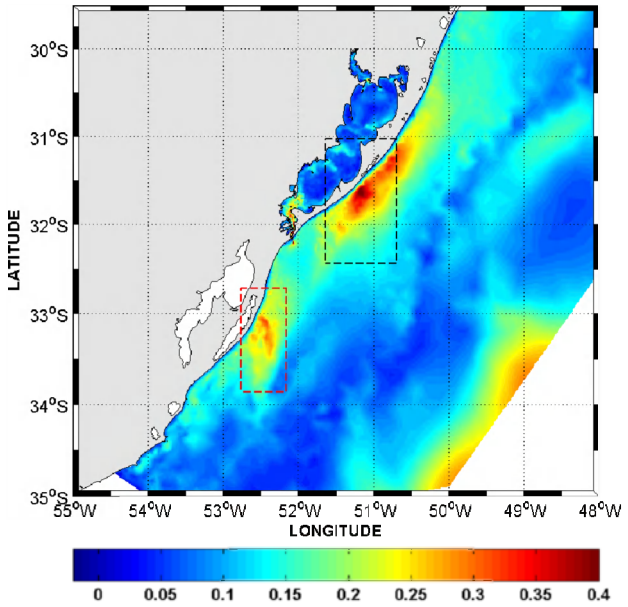

Figure 4. A) Average current velocity (m/s) during the whole period of simulation. In detail, the southern region in the red-dashed area, and the northern region in the black-dashed area.

Reference [17] presented results for calibration and validation of the two-dimensional model in the Patos Lagoon estuary. Subsequently, one can find in references [2,8] that a set of simulations for the calibration and validation of the three-dimensional numerical model along the area covered by the Patos Lagoon and the adjacent coastal region has been done. The results of these calibration and validation tests indicated that the TELEMAC-3D model can be used for studies on the SBS with an acceptable degree of accuracy. As a result of these studies of calibration and validation, values of a number of physical parameters (such as wind influence coefficient, friction coefficient and turbulence models) were used to conduct this study.

III. RESULTS

The hydrodynamic conditions of this region are characterized by the clash of different water masses. In these regions the average velocity of the current (Fig 4) was analyzed, and mean values reaching extremes of 0.4 m.s^{-1} in these two highlighted regions were observed.

This mean value is associated with some variability, and thereby the standard deviation of the current velocity is distributed by the same regions of high mean values (Fig 4). This result suggests that: while these regions are appropriate for the location of energy converters, they can also go through periods of low power generation, since the velocity deviation has a closer value to the average.

Reference [1], in previous study, concluded that the southern region has less viability for installation of marine turbine currents in the SBS, while the northern region has emerged as a significant potential power producer reaching mean values of 10 kWday^{-1}. Therefore, only the northern region is investigated.

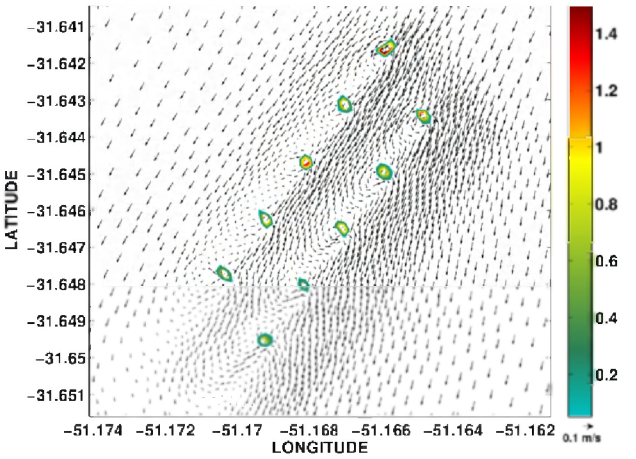

(A)

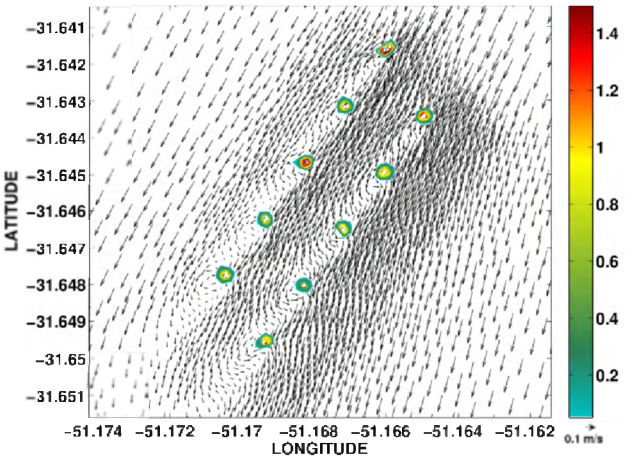

(B)

Figure 5. Residual velocities and the mean power (kW) generated for the turbines as isolines. (A) Site without the barriers. (B) Site with the presence of the barriers.

A. Current Pattern and Energy Conversion

In order to define which scenario delivers the most efficiency for a farm of turbines (with or without the presence of the structures), the spatial variability analysis was performed considering the temporal variation of the simulation. This analysis relies on the quantification of each turbine on its own capacity of converting the current energy into power according to the hydrodynamic pattern.

The average behaviour of the power generation on both sites was analyzed considering the residual velocity field associated with the mean field power converted (showed in isolines of power in Fig. 5).

The average power converted reaches values higher than 1.4 kW (Fig. 5.a and Fig. 5.b) in some turbines. The simulation without the structure presence (Fig. 5.a) shows the higher mean power on the turbines 1, 2, 3 and 6 (counting from the North-West turbine as first and the South-East as tenth). Despite this, the simulation with the presence of the structures (Fig. 5.b) shows enhanced power generation at the turbines 7, 8 and 10, in addition those cited before.

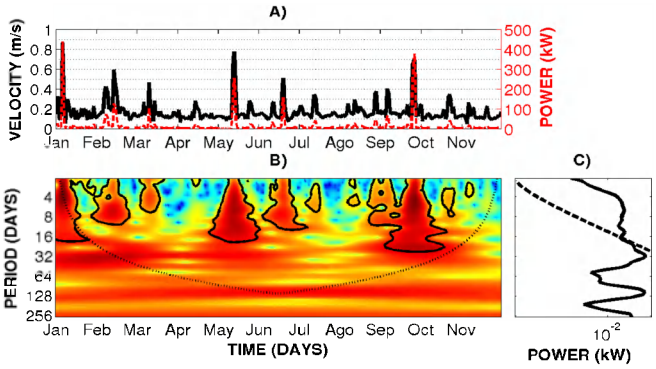

Figure 6. Integrated current velocity and electric power time series (A) used for the cross-wavelet analysis, as well as, the local (B) and the global (C) wavelet power spectrum of the time series using Morlet wavelet. Thick contour lines enclose regions of greater than 95% confidence for a red-noise process with a lag-1 coefficient of 0.95. Cross-hatched regions indicate the cone of influence where edge effects become important.

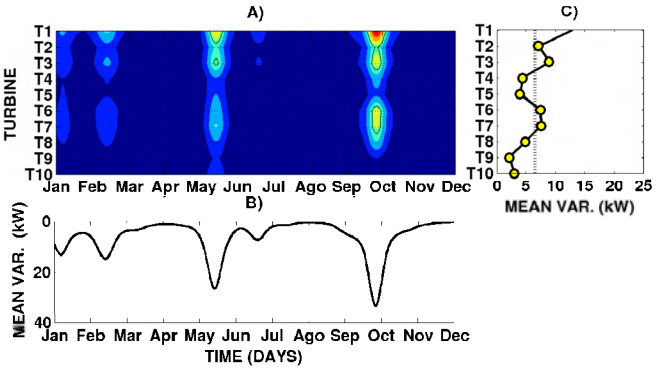

Figure 7. (A) Cross-spectral analysis between power (kW) and current velocity (m/s), for events with scale period higher than 1 day and lower than 30 days. Thick contour lines enclose turbines of greater than 95% confidence for a red-noise process with a lag-1 coefficient of 0.27. (B) Mean variance of the studied period, where values beneath the tendency line represents 95% of confidence. (C) Temporal series of the spacial mean variance of each turbine.

The same South-West circulation pattern can be observed on both simulations, which can be explained by the North quadrant winds dominance during the analyzed period. Besides, there is a slightly intensification at the residual velocity on the simulation that consider the structure effects (Fig. 5.b), with enhanced vectors between the turbine arrays and around them.

Behind the turbines we can observe a "shadow zone" in the circulation pattern, which can be related with the wake generated by the adjacent turbines. On the simulation without the barrier presence, this wake effect is purely hydrodynamic, where variations on the velocity fields occurs due to the conversion of the energy which inputs changes on the local vorticity pattern. On the other hand, on the simulation with the structure effect, this process shows as a contribution of the alterations into the hydrodynamic processes and the effect of the turbine body shape.

B. *Temporal Variability Analysis*

In order to analyse the temporality of the energy conversion regarding the entire turbines farm, time series (Fig. 6.a.) of electric power accounting for the ten converters were taken to perform the wavelet method described by [18] and [19]. The wavelet method is able to demonstrate the occurrence of events of energy conversion regarding time scales through local and global wavelet power spectrum.

At the analysis of the local power spectrum (Fig. 6.b) positive correlations (red-colored contours) are enhanced for the occurrence of velocities higher than 0.5 m.s^{-1}, increasing the energy conversion. It also shows that the physical processes maintaining the behaviour of the turbines farm are controlled by two main groups of temporal scales. The first group with occurrence around 6 days dominate the period, forced by the cyclic changes of the wind pattern direction.

Otherwise, the second group of temporal scales consists of correlations covering periods above 16 days, suggesting that the physical processes shorter than 20 days were the main mechanisms controlling the electric energy conversion along the inner continental shelf. The global spectrum of energy (Fig. 6.c) corroborate this hypothesis, indicating with 95% of confidence, the occurrence of processes with time scales above 16 days and may be extended in some moments, throughout the study period.

This pattern is similar to the obtained by [2] with respect to the occurrence of the processes and cycles of occurrence. Thus are strongly influenced by the passage of frontal meteorological systems generating further changes in wind direction and intensity of currents.

C. *Spatial Variability Analysis*

In order to define the importance of each turbine in the farm structure, the correlation between the incident current velocity and the power was performed along the turbine arrays. With this analysis, the efficiency of each turbine was studied in different time scales behalf the usage of bi-dimensional cross-spectral wavelet analysis, considering that the dominant processes occurring on the turbines site have temporal scale higher than 1 day and lower than 30 days.

The importance of each turbine and its variance in time is defined by the high correlation (red colored contours) in the Morlet Wavelet. Values on the right of the tendency line indicate with 95% of confidence the best placed turbines.

For the simulation considering the presence of the structures, through the cross-spectral (Fig. 7a.) it can be observed intensification on the power conversion in several turbines during the main conversion events. The temporal series of mean variance (Fig. 7b.), indicated with 95% of confidence that the four events of great power conversion sustain high power and are also intensified in this scenario.

Variance values above 35 kW (Fig. 7b.) can be observed during the October extreme event, enhancing the greatest power capacity of this scenario. The mean variance of each turbine (Fig. 6 c.) indicates that the higher correlation between the variables maintain average power around 7 kW. Moreover, it suggests that the turbines 1, 2, 3, 6 and 7 are the most efficient of the farm, considering only the energy conversion.

This discrepancy between the turbines efficiency relies on their positions on the farm and the influence of the incident current into the wake patterns.

IV. CONCLUSIONS

The Southern Brazilian Shelf is highly dynamic and constantly influenced by cycling winds (North-East/South-West) and the wind-driven coastal currents. This condition makes the usage of marine current turbines viable, although the recommended helicoidal turbine is to be applied. From this work we can conclude that:

The comparison between the simulations with and without the presence of the physical converting structure demonstrated that, regarding the numerical aspect of these simulations, the effect of the structure does not input changes on the temporal pattern of the energy conversion. The structures presence acted in a positive way in order to promote the intensification of the velocity field surrounding the turbines farm, also increasing the energy conversion.

The presence of the energy converters, on the other way, removed some part of the kinetic energy from the coastal currents, generating divergence and convergence zones in accordance with the dominant direction of the currents. The changes into the hydrostatic balance generated instability on the fluid motion, - part due to the converting energy, and part due to the presence of the structure – generating the wake effect behind the turbines. This effect decrease the energy conversion on the subsequent turbine, although, it also creates an intensification on the surrounding velocity fields.

The turbines farm shows great capacity for converting the currents energy, principally during the four main energetic events observed. Regarding the annually energy capacity, this turbine farm can reach 59,39 GWh (16,5 MW) with ten turbines, which is equivalent to 0.22% of the whole energetic consumption of the Rio Grande do Sul State in 2010.

Further studies shall improve the geometry of the farm and also promote trial test to implement a diffuser structure nearby the turbines to intensity the incident current fields.

ACKNOWLEDGEMENTS

The authors are grateful to the “Agência Nacional do Petróleo” - ANP and Petrobras for the fellowships regarding the “Programa de Recursos Humanos” (PRH-27) that sponsored the participation at the XXth TELEMAC-MASCARET User Conference. The authors are also greatful to the “Fundação de Amparo à Pesquisa do Estado do Rio Grande do Sul” (FAPERGS) for sponsoring this research under contracts: 1799 12-3 and to the “Coordenação de Aperfeiçoamento de Pessoal de Nível Superior” (CAPES) under contract: 23038.00773/2011-56. Further acknowledgments go to the Brazilian Navy for providing detailed bathymetric data for the coastal area; the Brazilian National Water Agency and NOAA for supplying the fluvial discharge and wind data sets, respectively.

REFERENCES

[1] E P Kirinus, W C Marques, and C E Stringari. Viabilidade de conversão da energia de correntes marinhas na Plataforma Continental Sul do Brasil. Vetor, 22, 2012.

[2] W C Marques, E H L Fernandes, A Malcherek, and L A O Rocha. Energy converting structures in the Southern Brazilian Shelf: Energy Conversion and its influence on the hydrodynamic and morphodynamic processes. Journal of Geophysical Research, 2012.

[3] S Zembruscki. Geomorfologia da margem continental sul brasileira e das bacías oceânicas adjacentes. Technical report, Projeto REMAC, Rio de Janeiro, 1979.

[4] O O Jr. Möller, A R Piola, A C Freitas, and E J D Campos. The effects of river discharge and seasonal winds on the shelf southeastern South America. Continental Shelf Research, 2008.

[5] A R Piola and R P Matano. Brazil and Falklands (Malvinas) currents, 2001.

[6] A L Gordon. Brazil - Malvinas Confluence - 1984. Deep-Sea Research, 36:359-384, 1989.

[7] M F Braga and N Krusche. Padrão de ventos em Rio Grande, RS, no período de 1992 a 1995. Atlântica, 22:27-40, 2000.

[8] W C Marques, E H L Fernandes, and O O Möller. Straining and advection contributions to the mixing process of the Patos Lagoon coastal plume, Brazil. Journal of Geophysical Research, 115(C6), 2010.

[9] G. J. Capeletto and G. H. Z. De Moura. Balanço Energético do Rio Grande do Sul 2010: ano base 2009., 2010.

[10] J M Hervouet. Free surface Flows: Modelling with the finite element methods, 2007.

[11] J M Hervouet and L Van Haren. Recent advances in numerical methods for fluid flows. In M G Anderson, D E Walling, and P D Bates, editors, Floodplain processes, pages 183-214. Wiley, Chichester, 1996.

[12] Smagorinski, J., 1963. General circulation experiments with the primitive equation, I. The basic experiment. Weather Review. 91, 99-164.

[13] M J Khan, G Bhuyan, M T Iqbal, and J E Quaicoe. Hydrokinetic energy conversion systems and assessment of horizontal and vertical axis turbines for river and tidal applications: A technology status review. Applied Energy, 86(10):1823-1835, 2009.

[14] A Gorlov. Helical Turbine and Fish Safety. Pages 1-14, 2010.

[15] E Kalnay, M Kanamitsu, R Kistler, W Collins, D Deaven, L Gandin, et al. The NCEP/NCAR 40-Year Reanalysis project. Technical report, Bulletin of the American Meteorological Society, 1996.

[16] O O Möller, P Castaing, J C Salomon, and P Lazure. The influence of local and non-local forcing effcts on the subtidal circulation of Patos Lagoon. Estuaries, 24:297-311, 2001.

[17] E H L Fernandes, K R Dyer, and O O Möller Jr. On the hydrodynamics of the world's largest choked coastal lagoon: Patos Lagoon (Brazil). Estuaries, 2001.

[18] C Torrence and G P Compo. A practical guide to wavelet analysis. Technical report, Bulletin of the American Meteorological Society, 1997.

[19] P A Morettin. Ondas e ondaletas: da análise de Fourier à análise de ondaletas. Edusp, São Paulo, 2004.

TUC 2013, 16-18/10/2013, Karlsruhe - Kopmann, Goll (eds.) - © 2013 Bundesanstalt für Wasserbau ISBN 978-3-939230-07-6

Validation of a 1D simplified model of Gironde Estuary based on a database of TELEMAC simulations

V. Laborie, F. Hissel, P. Sergent
Research Department
CETMEF
Margny-Lès-Compiègne, France
vanessya.laborie@developpement-durable.gouv.fr

***Abstract*—Within THESEUS European project, on the one hand, an overflowing model of Gironde Estuary, based on TELEMAC software, has been used to create a database of water lines along the estuary depending on a large range of hydrometeorological situations. In this study, no breaching and no modification in the elevation of the dikes were considered in TELEMAC model. This database was then used to validate the construction of a 1D numerical model whose aim is to provide in less than one minute both water heights and propagation of tide along the Estuary.**

The model based on TELEMAC-2D was fed by several data sources, a tide signal at Le Verdon and a large range of discharges of the Garonne (at La Réole), the Dordogne (at Pessac), the Dronne (at Coutras) and the Isle (at Libourne). Simulations were led without considering any wind in the Estuary. The tide signal imposed at the mouth of the Estuary, near Le Verdon, was divided into two parts: a sinusoidal signal characterized by its amplitude added to a hydrometeorological surge level. Both amplitudes and surge levels belonged to a large physical range of values. Water levels along the axis of Gironde Estuary were then analyzed with a FFT decomposition to extract the tide amplitude and phase at each point along the axis and also to obtain the value of mean water levels.

On the second hand, a permanent 1D shallow water numerical model and a 1D numerical model of tide propagation were obtained developing shallow water equations with the assumption of Gironde Estuary having an exponential increasing width. Its results are mean water depths and tide amplitude along Gironde Estuary from Le Verdon to Ambes. Overflows are supposed to have an influence only on tide amplitudes.

Results were compared with TELEMAC database both for mean water levels along Gironde Estuary and tide amplitude. Results for mean water levels along Gironde Estuary show the necessity to complete the equations taken into account. For several hydrometeorological scenarios, the simplified tide amplitude model well represent tide amplitudes along the estuary as overflows occur.

I. INTRODUCTION

Within THESEUS European project [1], on the one hand, an overflowing model of Gironde Estuary, based on TELEMAC software, has been used to create a database of water levels along the estuary depending on a large range of hydrometeorological situations.

This database was then used to validate the construction of a 1D numerical model whose aim is to provide in less than one minute both water heights and propagation of tide along the Estuary to evaluate the efficience of mitigation options towards climate change.

II. STUDY SITE AND DESCRIPTION OF THE TELEMAC NUMERICAL MODEL

A. The study site

Gironde Estuary is the study site. To establish a database giving mean water levels and the first harmonic tide at specific locations along the Estuary, a bidimensional numerical model of Gironde Estuary based on shallow water equations has been used [2]. This model is currently integrated in the inundations repository of Gironde. It permits to test the impact of new buildings in the estuary and is based on TELEMAC-2D.

B. TELEMAC numerical model of Gironde Estuary

The model covers the entire estuary from La Réole on the Garonne River and Pessac on the Dordogne River [3]. Its maritime boundary is located at Le Verdon. Upstream, the model takes into account the flow rates of the river Isle at Libourne (at its confluence with the Dordogne River) and extents on the Isle River downstream of its confluence with the river Dronne.

The particularity of this bidimensional model is to take into account overflows from the minor bed of the rivers Dordogne, Garonne, Isle and Dronne into the floodplain. The model has 21304 finite elements and is composed of 13621 nodes. Its mesh is represented on Fig. 1 just below. It is about 115 km long from east to west.

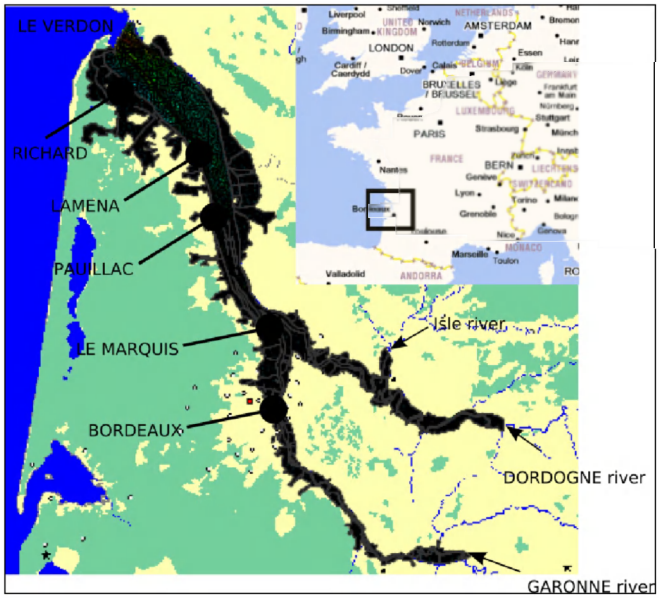

Figure 1. extension and location of the numerical model of Gironde Estuary

III. CONSTRUCTION OF A DATABASE BASED ON TELEMAC RESULTS

A. *Parameters of simulaions*

The model has to be fed by several kinds of data [4]:

- at the upper part of the model, the flow rates of the Garonne and the Dordogne rivers, as well as those of the Isle;
- the global signal at the maritime boundary of the model located at Le Verdon. It is the sum of two components: the predicted tide, characterized by the amplitude and the period of the signal and the meteorological surge level.

The impact of winds and pressure fields has not been considered in this study.

B. *Data used for simulations*

A large range of data has been used to evaluate mean water levels from Le Verdon to Bordeaux obtained with the TELEMAC numerical model.

For all simulations, flow rates of the Isle and the Dronne rivers are maintained constant, respectively equal to 37.4 and 24.6 m^3/s, which correspond to the mean discharges for these rivers.

Three flow rates have been chosen for each mean river, i.e. the Garonne and Dordogne rivers (respectively [20 m^3/s; 634.5 m^3/s; 5666.0 m^3/s] and [23.6 m^3/s; 253.10 m^3/s; 1640 m^3/s]. These values respectively correspond to the minimum, the average and the maximum discharges observed on these rivers.

Tide amplitudes at le Verdon mostly belong to the n-uplet [1.15 m; 1.30 m; 1.7 m; 1.9 m; 2.125 m]. For average flow rates of the Garonne and the Dordogne rivers, tide amplitudes were chosen between 1.15 m and 2.10 m using an increment of 0.05 m. The value of 2.125 m was also considered in this case.

The mean sea level was considered at Le Verdon. At this mean sea level was added a storm surge whose value belongs to the range [-0.1 m ; 0 m ; 0.2 m ; 0.4 m ; 0.5 m]. For the Garonne and the Dordogne rivers' average flow rates, storm surges between -0.1 m and 0.5 m were considered with an increment of 0.05 m.

The combination of those boundary conditions led to 465 simulations with the Gironde Estuary's TELEMAC-2D numerical model.

C. *Extraction and analysis of results*

For each simulation, TELEMAC-2D water levels were extracted at 48 nodes (24 nodes along in the Estuary, 19 along the Garonne River and 5 along the Dordogne River).

For each hydraulic scenario and each of these 48 nodes:

- the mean water level was calculated and the mean water profile along the estuary thus obtained (cf. Fig. 2 below);
- a FFT analysis was realised to obtain the tide first harmonic amplitude and its evolution along the estuary (cf. Fig. 3 below).

Fig. 2 and Fig. 3 also show mean water levels and tide amplitudes from Le Verdon to Ambès for the scenario 95, for which flow rates of Garonne and Dordogne rivers are respectively 5666 m^3/s and 1640 m^3/s, tide amplitude equals 1.9 m and the storm surge equals 0.5 m.

These results constitute the TELEMAC-2D database for mean water levels' and tide amplitude' propagation along Gironde Estuary.

In this study, this database is considered as a reference for the construction of a simplified decision support system, based on a 1D numerical model described in the following paragraphs, whose aim is to quantify effects of mitigation solutions towards climate change in a few minutes.

IV. CONSTRUCTION OF THE 1D NUMERICAL MODEL OF GIRONDE ESTUARY

A. *Equations implemented in the decision support system dedicated to Gironde Estuary*

Considering the following assumptions ([5]):

- the width of the estuary follows a decreasing exponential law :

$$B(\xi) = B_0\, \varepsilon\xi\pi(\xi/\beta) \quad (1)$$

where x is the curvilinear abscissa along Gironde Estuary (upstream to downstream), $B(x)$ is the width of the estuary, $B0$ the width of the Estuary at Ambès and h is a shape parameter characterizing Gironde Estuary.

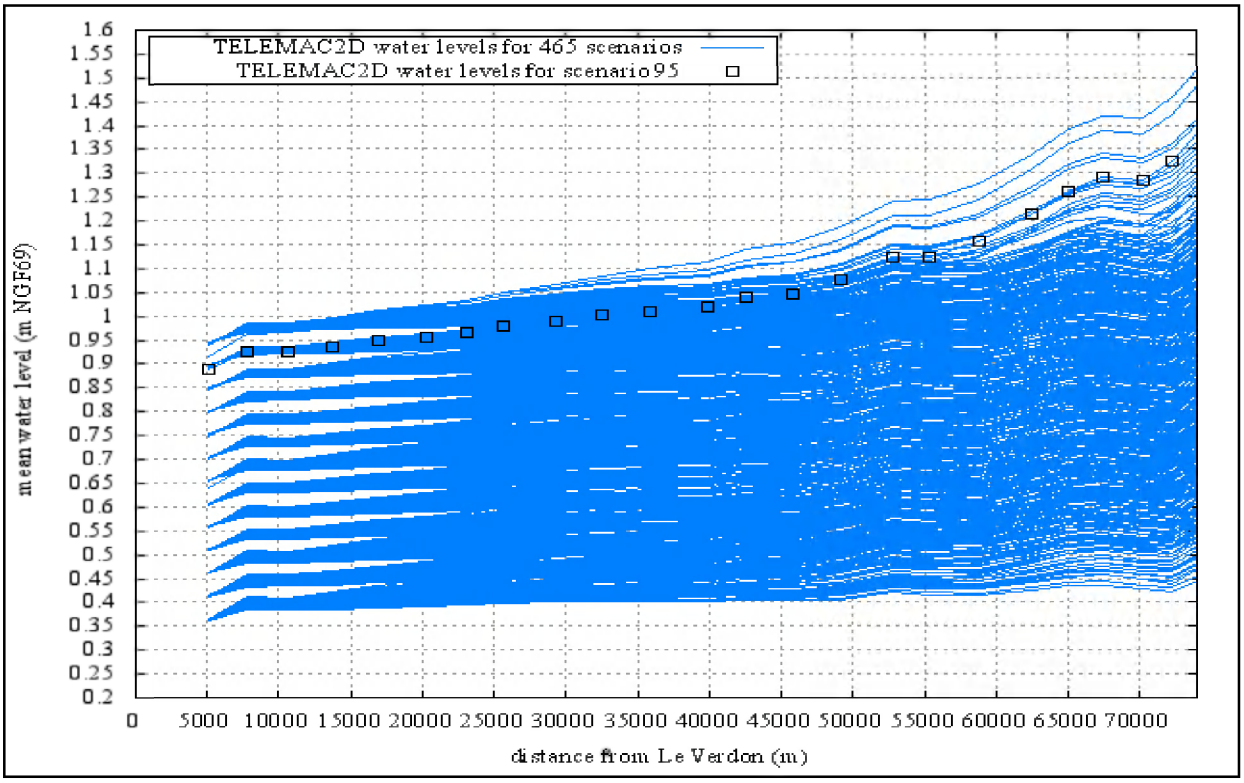

Figure 2. Water level profiles along the estuary (from Le Verdon to Ambès) for 465 hydraulic scenarios computed with TELEMAC-2D – scenario 95 constitute identification marks

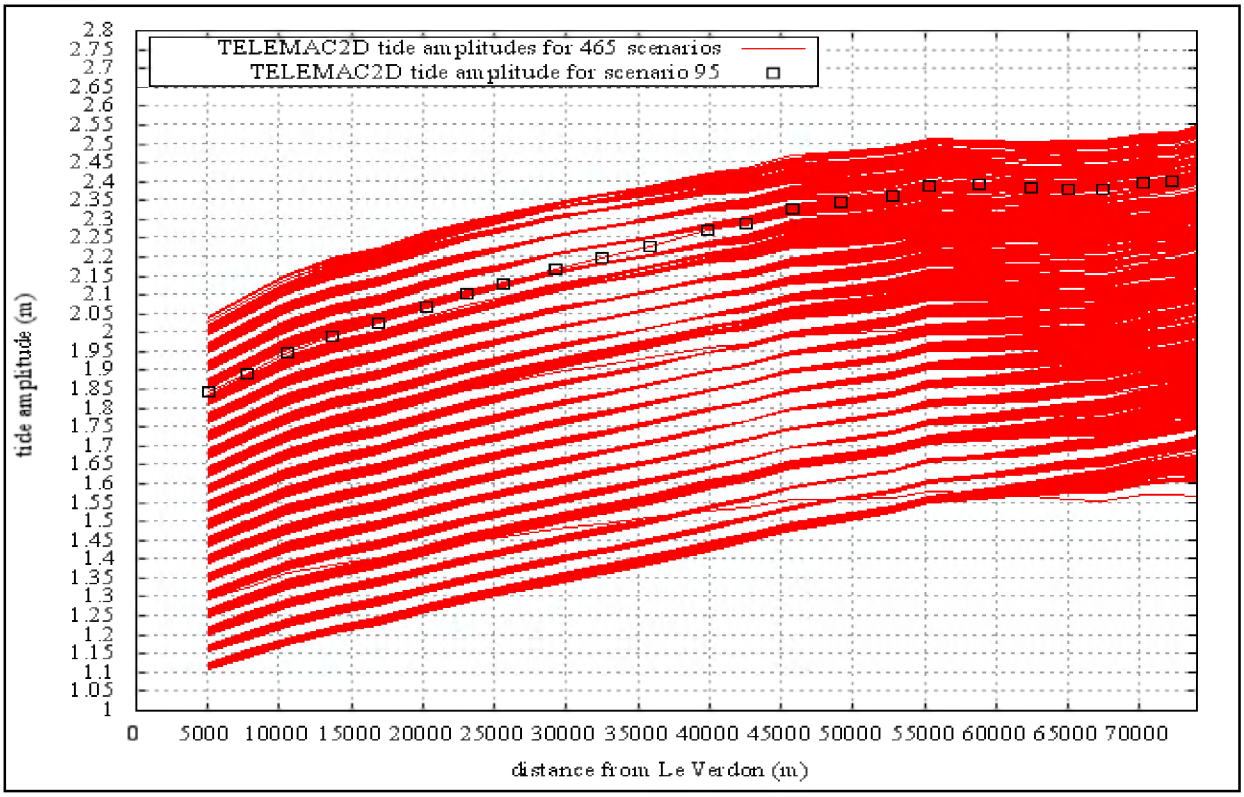

Figure 3. Tide harmonic amplitudes along the estuary (from Le Verdon to Ambès) for 465 hydraulic scenarios obtained with T2D

- the bottom of the estuary follows a 1/x law :

$$\zeta(\xi) = \zeta 0 + \delta/(\Lambda - \xi) \tag{2}$$

- where *z(x)* is the bottom elevation at the curvilinear abscissa *x*, z_0 and d are constant and L is the distance between Ambès and Le Verdon,

A 1D permanent numerical model based on 1D shallow water equations and the 1D momentum equation of has then been developed in Gironde Estuary.

B. Mean Sea level

Mean water levels along the estuary are obtained with the following equation:

$$\frac{\partial h}{\partial x}(x) = \frac{\dfrac{-q^2}{gbh^2} + sin(\gamma) - \dfrac{q^2}{K^2 h^{10/3}}}{cos(\gamma) - \dfrac{q^2}{gh^3}} \tag{3}$$

where *h(x)* is the water depth (m), *g* the gravity, *γ* the bottom slope (-), *K* the Strickler coefficient and *q* the averaged linear discharge (m²/s).

From Ambès to Bordeaux, the same assumptions and equations have been used, except for the bottom supposed, in this part of the estuary, to be a linear function of the curvilinear abscissa.

C. Amplitude of the first tide harmonic and overflows

To calculate tide amplitudes along the estuary, a first attempt of Fourier decomposition of water levels' and flow rates' signal has aborted.

Hence, as Fig. 3 above shows that curves representing tide amplitudes nearly remain parallel, tide amplitudes in Gironde Estuary have been calculated using an interpolation function.

In this study, it has been considered that overflows over dikes only affect tide amplitude at the curvilinear abscissa considered. If $h_1(x)$ is the tide amplitude at x and $h_2(x)$ the tide amplitude after overflows, it can be shown that:

$$\begin{aligned}\hat{h}_2(x) = \hat{h}_1(x) - \frac{\omega}{sin(\omega T_2') - sin(\omega T_1')} \frac{V_{\text{overflow}}}{\hat{u}(x) B(x)} \\ + \hat{h}_1 \frac{(x)}{\omega} \left(sin(\omega T_1') - sin(\omega T_1) \right) \\ + (T_1' - T_1)(h(x) + z_f(x) - Z_c)\end{aligned} \tag{4}$$

where ω is the pulsation of Gironde Estuary, $V_{overflow}$ the overflowing volume and $\hat{u}(x)$ is the periodic velocity, T_1 is the time at which the initial periodic signal equals Z_c, the dike crest level; T'_1 and T'_2 have the same definition for the signal obtained after overflows.

Considering the following assumptions:

$$h = \bar{h} + \hat{h} e^{(i\omega t)} \tag{5}$$

where $\bar{h}$ is the time-averaged water depth, $\hat{h}$ is the tide first harmonic

$$q = \bar{q} + \hat{q} e^{(i\omega t)} \tag{6}$$

where $\bar{q}$ is the time-averaged flow rate, $\hat{q}$ is the flow rate first harmonic.

If $q = u \cdot h$, where u is the velocity, using the momentum equation:

$$\begin{aligned}\frac{-\partial u}{\partial t} + g\, sin(\gamma) - g\, cos(\gamma) \left(\frac{\partial \bar{h}}{\partial x} + \frac{\bar{h}}{2b} \right) \\ + \frac{B\bar{h}\, sin(\gamma)}{2} g \frac{\partial \gamma}{\partial x} = 0\end{aligned} \tag{7}$$

leads to:

$$\begin{aligned}-i\omega\hat{q}\bar{h} + -i\omega\bar{q}\hat{h} + 2g\, sin(\gamma)\bar{h}\hat{h} - 2g\, cos(\gamma)\bar{h}\hat{h}\frac{\partial \bar{h}}{\partial x} \\ - g\, cos(\gamma)\bar{h}^2 \frac{\partial \hat{h}}{\partial x} = 0\end{aligned} \tag{8}$$

Neglecting bottom friction and convection gives:

$$\begin{aligned}+g\, sin(\gamma) - g\, cos(\gamma)\frac{\partial \bar{h}}{\partial x} = 0 \\ \frac{\partial \bar{h}}{\partial x} = tan(\gamma)\end{aligned} \tag{9}$$

Injecting (9) in (8) gives:

$$\frac{\partial h}{\partial x} + \frac{i\omega}{g\, cos(\gamma)} \frac{\hat{q}}{\bar{h}} - \frac{i\omega}{g\, cos(\gamma)} \frac{\bar{q}}{\bar{h}^2} \hat{h} = 0 \tag{10}$$

and

$$\frac{\partial \bar{q}}{\partial x} - \frac{\bar{q}}{b} = 0$$

with

$$\frac{\partial \hat{q}}{\partial x} - \frac{\hat{q}}{b} + i\omega\hat{h} = 0 \tag{11}$$

Finally,

$$|\hat{u}| = \frac{1}{\bar{h}}|\hat{q} - \bar{u}\hat{h}| \tag{12}$$

can be obtained by solving the following linear set of equations:

$$\frac{\partial \bar{X}}{\partial x} = \begin{bmatrix} 0 & -\frac{\bar{q}}{\bar{h}}\frac{\omega}{g\,cos(\gamma)\bar{h}} & 0 & \frac{\omega}{g\,cos(\gamma)\bar{h}} \\ \frac{\bar{q}}{\bar{h}}\frac{\omega}{g\,cos(\gamma)\bar{h}} & 0 & -\frac{\omega}{g\,cos(\gamma)\bar{h}} & 0 \\ 0 & \omega & \frac{1}{b} & 0 \\ -\omega & 0 & 0 & \frac{1}{b} \end{bmatrix} .\bar{X} \tag{13}$$

with:

$$X = \begin{bmatrix} \Re(\hat{h}) \\ \Im(\hat{h}) \\ \Re(\hat{q}) \\ \Im(\hat{q}) \end{bmatrix} \tag{14}$$

Overflows are calculated using the usual weir expression:

$$q_{\text{overflowing}}(x) = \mu\,(h(x,t))^{\frac{3}{2}}\,(2g)^{0.5} \tag{15}$$

where $q_{overflowing}(x)$ is the overflowing flow rate above dikes at x and μ is a flow rate coefficient.

V. VALIDATION OF THE 1D NUMERICAL MODEL OF GIRONDE ESTUARY

A. *Mean sea levels*

Absolute errors on mean water levels between the results obtained with the simplified model and the TELEMAC-2D database are represented on Fig. 4.

Even after the calibration of the model, the maximum absolute error is still about 30 cm at Ambès, with a mean absolute error which equals 15 cm. Nevertheless, the distribution of scenarios gives a predominant weight to hydraulic situations where the flow rate of the Garonne River equals 634.5 m^3/s. However, it appears that for this range the calibration of a part of scenarios has negative impacts on the results obtained with other scenarios.

Moreover, in the maritime part of the Estuary, the influence of tide on mean sea levels should be considered ; this is not the case here, where water level have been divided into a mean water level and a periodic signal.

Fig. 5 below represents absolute errors between the simplified model and the database from Bordeaux to Ambès, using the exact mean water level at Ambès.

The maximum absolute error is less than 0.15 m at Bordeaux, which would be quite acceptable. Ttherefore it is necessary to improve results in the maritime part of the estuary. Indeed, the propagation of the error calculated by the model from Le Verdon to Ambès leads to errors between -0.30 m and 0.30 m at Bordeaux, even after a global calibration.

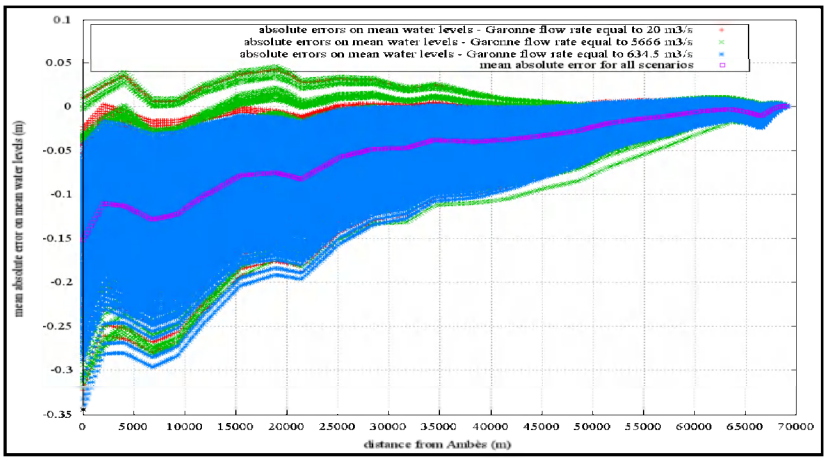

Figure 4. Absolute mean error on time-averaged water levels between the simplified model and TELEMAC-2D results from Le Verdon to Ambès

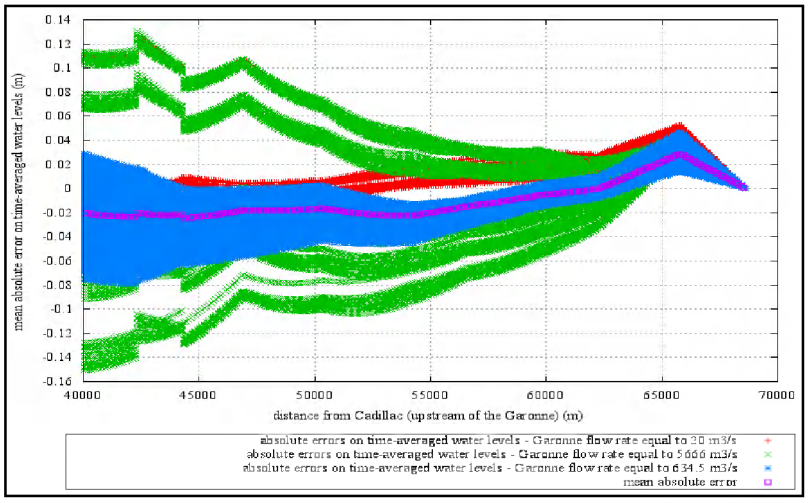

Figure 5. Absolute mean error on time-averaged water levels between the simplified model and TELEMAC-2D results from Bordeaux (x=44000 m) to Ambès (x=68000 m)

B. Tide amplitude and overflows

The flow rate coefficient has been calibrated and tide amplitude has been calculated for scenario 95 described in § III.C.

Fig. 6 represents both tide amplitudes along Gironde Estuary obtained with the simplified model in which overflows have been implemented and obtained with TELEMAC-2D for scenario95.

In this case, differences are less than 0.10 m.

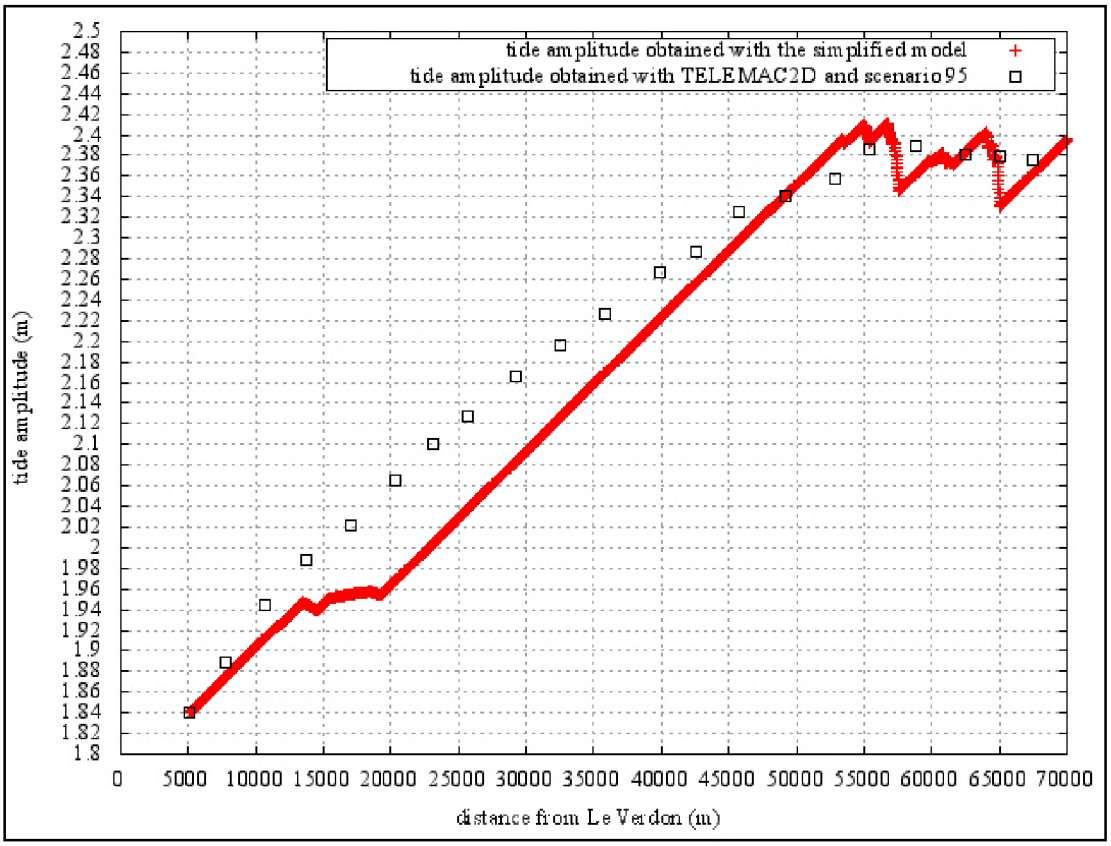

Figure 6. Tide amplitude obtained with the simplified model of Gironde Estuary (in red) and with TELEMAC-2D (black points) for scenario 95

VI. Conclusions and perspectives

A simplified numerical model to calculate the propagation of water levels and tide amplitudes along Gironde Estuary has been developed and compared with a database provided by a 2D numerical model based on TELEMAC2D.

Concerning mean water levels along Gironde Estuary, differences are between 0 and -0.30 m at Ambès with a mean absolute error of 0.15 m. Therefore, results have to be improved not to propagate such a high error to Bordeaux. At Bordeaux, considering the TELEMAC-2D value at Ambès, differences between the simplified model and the database are less than 15 cm, which is quite acceptable, in light of the many assumptions that were made.

For several hydrometeorological scenarios, the simplified tide amplitude model well represent tide amplitudes along the estuary as overflows occur. The results and the methodology have to be applied to all scenarios.

Acknowledgement

This work has been financially supported by the EU through the FP7 project THESEUS.

Special thanks to the CETE South-West, METEOFRANCE, the SPC Littoral Atlantique and SOGREAH.

References

[1] SOGREAH - Référentiel de protection contre les inondations le long de l'estuaire de la Gironde, de la Garonne et de la Dordogne, Rapport d'étape 4 : définition des événements de référence, Version I. *Rapport n° 4310990 –1 74 0638*, 199 p., 2010.

[2] V. Laborie, F. Hissel F., P. Sergent. - Évolution de l'emprise des zones inondables de l'estuaire de la Gironde sous l'influence du changement climatique. Colloque Génie Civil Génie Côtier, Cherbourg, 8 p., 2012.

[3] V. Laborie, F. Hissel F., P. Sergent. - Impact of climate change on Gironde Estuary. 9 p., La Houille Blanche, in press.

[4] V. Laborie, F. Hissel F., P. Sergent. - Évaluation des niveaux d'eau extrêmes du futur sur l'estuaire de la Gironde. Colloque SHF « événements extrêmes fluviaux et maritimes», Paris, 8 p., 2012.

[5] S. Lanzoni, G. Seminara – On tide propagation in convergent estuaries, Journal of Geophysical Research, vol. 103, No C13, pages 30,793-30,812, December 15, 1998.

TUC 2013, 16-18/10/2013, Karlsruhe - Kopmann, Goll (eds.) - © 2013 Bundesanstalt für Wasserbau ISBN 978-3-939230-07-6

Numerical Simulations of Bar Formation and Propagation in Straight and Curved Channels

F. Mattia[1,3], D. Wang[2,3]
[1]Università di Cassino e del Lazio Meridionale, Italy
[2]University of Nice Sophie Antipolis, France

J.-M. Hervouet[3], A. Leopardi[1], K. El kadi Abderrezzak[3], P. Tassi[3,*]
[3]EDF R&D – LNHE and Saint-Venant Hydraulics Laboratory, France - *pablo.tassi@edf.fr

***Abstract*—The capabilities of the TELEMAC Modelling System to reproduce the formation and evolution of free and forced bars in straight and curved channels are investigated by reproducing the numerical experiments by Defina [5], Bernini *et al.* [1], Crosato *et al.* [4] and the laboratory experiences conducted by Whiting and Dietrich [12, 13]. Numerical results showed that the main features of the bars, such as wavelength, amplitude and celerity are well reproduced when the bed slope correction term is considered. Parameterization of secondary currents effects appeared to be an important parameter to mimic accurately the geometrical characteristics of the bars, but it is not crucial for the origin and development of the bars.**

I. INTRODUCTION

Depending on the flow and the sediment conditions, the flow-bottom interaction in natural channels with non-cohesive sediments gives rise to a variety of forms, which may occur on a micro-scale (of the order of sediment size) leading to ripples, or on a macro-scale (of the order of flow depth) leading to the formation of dunes or anti-dunes, or finally on a mega-scale (of the order of channel width) leading to the development of bars [2, 3, 11]. In turn, these modes of interaction not only represent different modes of sediment transport, but also different mechanisms of bed resistance [14].

Alternate bars are a variety of large-scale bed-forms that can be observed in natural or restored rivers. These patterns arise from a perturbation of the non-cohesive channel bed that grows in time until the equilibrium state is achieved; leading to a sequence of riffles and pools in the downstream direction with an alternating transversal amplitude structure [2, 3], see Fig. 1. Typically, the height and wavelength of bars scale with flow depth and channel width, respectively [14].

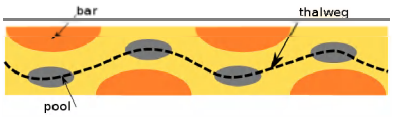

Figure 1. Schematic alternate bars in a straight channel.

Bars can be classified into forced and free bars. Free bars are typically characterized by alternate bars that develop spontaneously on the bottom of straight or weakly curved channels, as a result of inherent instability of the flow-sediment interaction [2, 3]. Forced bars are motorized by the presence of a forcing effect of anthropic or natural origin, such as a perturbation in the channel or in large-amplitude meandering channels [12]. Bars can also be classified into steady or migrating bars. Migrating bars can reach value of celerity in the order of meters per hour. Steady bars are characterized by values of celerity in the order of meters per year.

In this work, the capabilities of the TELEMAC-MASCARET modelling system (TMS) to reproduce the origin, short-term and long-term development of bars in straight and large-amplitude meanders with fixed boundaries are investigated. In order to compare the results obtained with the TMS, we reproduced the numerical experiments in straight channels by Defina [5], Bernini *et al.* [1], and Crosato *et al.* [4]. Numerical experiences in curved channels were based on the experiments conducted in symmetric sine-generated meanders of large amplitude by Whiting and Dietrich [12, 13].

II. MODELLING OF BARS: MORPHODYNAMICS MODEL

To study the behaviour of bars in straight and curved channels with fixed banks we used the hydrodynamics solver TELEMAC-2D, internally coupled to the sediment transport and bed evolution module SISYPHE of the TMS. The hydrodynamics part of the system is based on the solution of the 2D depth-averaged shallow-water equations, with a closure relationship for the turbulence based on a constant-viscosity model, and the Nikuradse friction law to parameterize roughness effects [7]. The evolution of the channel bottom is computed from the sediment mass balance equation and a sediment transport model, with an appropriate parameterisation of two relevant physical processes, such as (i) bed slope effects [9] and (ii) secondary currents effects [6].

1) Bed slope effects

A sloping bottom causes the increase bed-load transport rate in the downslope section, and the reduction in upslope bed-load direction. For taking into account of the bed slope effect it is possible to use the Koch and Flokstra expression [9]:

$$q_b = q_{b0}\left(1 - \beta_* \frac{\partial z_b}{\partial s}\right) \quad (1)$$

where q_{b0} is the unitary solid discharge evaluated for bed-load using a sediment transport closure, β_* is an empirical factor, z_b is the bottom position above datum, and s is the coordinate in the current flow direction.

2) Secondary currents effects

The bed-load movement direction deviates from the main flow direction due to the presence of helicoidally flow effects [6]. For taking into account these effects, a 3D analysis must be performed. Different authors have proposed formulae for modelling the presence of the helicoidally flows in 2D models, Engelund proposed the use of the expression $\tan\delta = 7h/r$ where δ is the angle between the bedload movement and the main flow direction, h is the mean water depth and r is the radius of curvature of the channel.

III. NUMERICAL SIMULATIONS OF BARS FORMATION AND PROPAGATION: STRAIGHT CHANNELS

In this section the capabilities of the TELEMAC Modelling System (TMS) to describe the formation, evolution and migration of alternate free bars in straight channels are investigated. For all simulations, bed slope effects were accounted with the Koch and Flokstra expression, Eq. 1. The influence of the secondary flows on the solid discharge was considered by means of the Engelund formula [6]. Preliminary numerical simulations have yielded the bed slope correction term as a crucial processus for reproducing the formation and propagation of alternate bars in channels, while parameterization of secondary currents effects appeared to be an important parameter to mimic the geometrical characteristics of the bars, but it is n m ot crucial for the origin and development of alternate bars.

IV. DEFINA'S NUMERICAL SIMULATIONS

In [5], Defina presented a 2D finite element model for describing the morphodynamic evolution of cohesion-less bed. To validate their numerical model, Defina performed numerical simulations to analyze the formation, evolution and migration of alternate bars in a straight channel with rectangular cross-section. Defina's numerical simulations were inspired by laboratory experiments by Lanzoni [10] and were focus on the influence of an initial perturbation introduced in the flow field. Here, we focus our attention on a numerical simulation characterized by the presence of an initial erodible bump, 5 mm high, located immediately downstream of the channel inflow.

The numerical experiment was conducted on a straight channel 117.5 m long and 1.5 m wide. The bed of the channel was composed by non-cohesive movable sediment and the perimetral walls were impermeable. The sediment was sand characterized by a median size of $\bar{d} = 0.48$ mm. The initial bedslope was constant and equal to $S_0 = 0.452\%$. The Strickler roughness coefficient chosen was $Ks = 54\ m^{1/3}s^{-1}$.

A. Numerical simulations with the TMS

The unstructured mesh used for the numerical simulations was composed by 9770 triangular elements and 5842 nodes, characterized by a typical mesh size of 0.02 m^2. The time step was set to $t_s = 0.1$ s in order to keep a Courant number lower than 1. For the flow equations, a flowrate $Q_* = 30\ ^{l}/_{s}$ at channel inflow and a water-depth at channel outflow $h_* = 4.4$ cm were imposed as boundary conditions. A constant water-depth value $h_0 = 4.4$ cm was fixed over the domain as initial condition.

a) Symmetric bump simulations

Numerical simulations were performed for a simulated time $t = 48$ h. For triggering the formation of a train of alternate bar, we introduced an erodible bump of 1.5 m length, 0.5 m width, and 5 mm height at 3.0 m from the inlet. The bump was located on the axis of the channel, in a symmetrical position respectively to the banks. Results of the bed evolution from time 0 to 48 h are shown in Fig. 2.

During the early evolution stages, numerical results show the development of a clear train of alternate migrating bars characterized by a symmetrical form. From $t > 16$ h, alternate bars change their geometric configuration and evolve into a configuration in which the downstream face becomes much steeper than the upstream face. A first bar appears after 3 h, a clear train of alternate bar is visible for $t = 8$ h and a state for which the bar geometric dimensions are characterized by slow changes over time is reached after 30 h.

The bars average wavelength, amplitude and celerity at time $t = 36$ h are summarized in Table I. Fig. 3 shows the velocity field near the downstream boundary of the channel. It is evident how the new bottom configuration induces a degree of curvature on the streamlines that could motorize the formation of meanders.

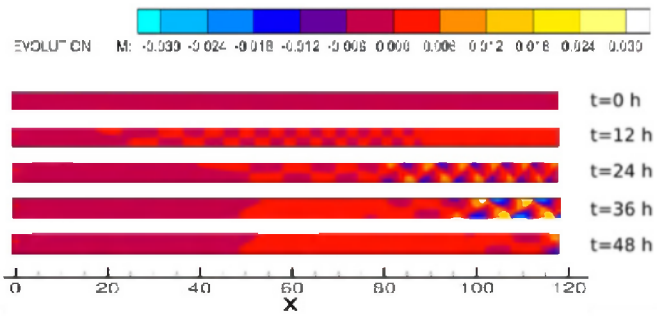

Figure 2. Bottom evolution, symmetric bump 5 mm high.

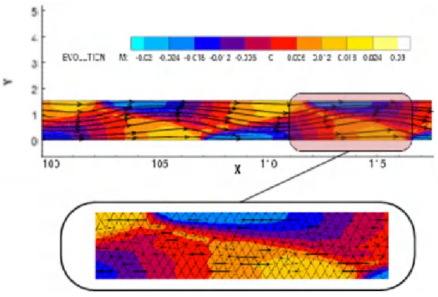

Figure 3. Detail of the mesh and streamlines for t=36h.

b) Numerical simulations in a longer-length channel

A set of numerical simulations were performed in a longer length channel than the previously used (275 m long), for a simulation time $t = 72$ h, with a bottom perturbation located symmetrically respect to the banks.

The new computational domain was discretized using a non-structured mesh composed by 23702 triangular elements, with a median size 0.02 m, and 13235 nodes. Numerical results are shown in Fig. 4. The evolution behavior is close to the one observed in the previous numerical simulations, the bars present first a symmetric shape and subsequently evolve into a configuration characterized by the downstream face being steeper than the upstream face. The values of λ_b, δ_b and c_b at a simulated time $t = 48$ h are summarized in Table I.

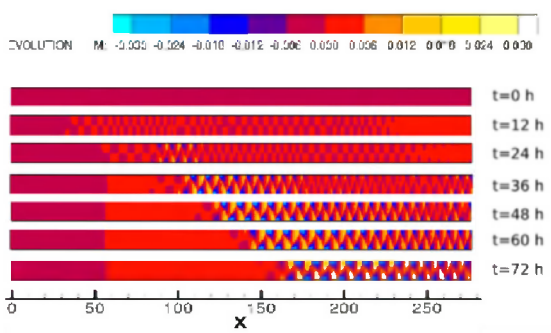

Figure 4. Plan view of bottom evolution: symmetric bump

B. Comparison of results

Both Defina's [5] and our numerical results show a clear train of alternate migrating bar that develops in a straight channel which bed is composed by a movable non-cohesive material. After one hour of simulated time a first bar appears and becomes the trigger for the formation of a well-defined train of free alternate migrating bars and the initial perturbation is eroded. During the first evolution steps the bars are characterized by a symmetrical planimetric shape, subsequently these bed-forms change their geometric pattern into another one, characterized by the downstream face being steeper than the upstream face.

Defina's numerical bars reached a state for which the main features are quasi-steady after a simulated time $t = 25 - 30$h, that value is in accordance with the results obtained with the TMS. For an initial perturbation located in an non-symmetric position, the time for which a quasi-steady state is reached is around $t = 25$ h. For an initial perturbation located in a symmetric position, the time for which a quasi-steady state is reached is around $t = 30$ h. For a numerical simulation without any initial perturbation, the time for which a quasi-steady state is reached is around $t = 40$ h.

Differences between the two numerical simulations can be found comparing the characteristics of Defina's numerical bars after 30 h with the bars calculated with the TMS after had reach the steady state. A comparison between bars average values of wavelenght λ_b, amplitude δ_b and celerity c_b is presented in Table I.

TABLE I. COMPARISON BETWEEN TMS AND DEFINA'S BARS FEATURES [5]

	wavelenght λ_b $[m]$	amplitude δ_b $[cm]$	celerity c_b $[^m/_h]$
Defina [5]	10.00	8.00	2.00
TMS, symmetric bump	9.00	3.80	2.00
TMS, non-symmetric bump	10.00	4.00	1.60
TMS, longer-length channel	10.00	4.00	1.60

V. BERNINI ET AL.'S NUMERICAL EXPERIMENT

In [1], Bernini, Caleffi and Valiani presented a numerical model for the morphodynamic evolution of a cohesionless bed for subcritical and supercritical flow conditions. In this work, we compared our results with those obtained by Bernini et al. for a supercritical flow condition. Numerical simulations were performed in a channel 60 m long and 30 cm wide with an initial constant bed slope equal to $S_0 = 1.4\%$. That bed was composed by a non-cohesive uniform movable material with a median diameter of $\bar{d} = 0.43$ mm. The boundary walls were fixed and impermeable. The domain was discretized using a regular grid with rectangular elements 0.03 cm long and 0.01 cm wide. The velocity profile at the inlet was imposed to be normal to the section, this imposition lead to Froude number, $Fr = \|\vec{v}\|/\sqrt{gh} > 1$, where $\vec{v}$ is the velocity vector of components (u, v). For triggering the bars evolution an asymmetrical perturbation consisting of an erodible bump 9 cm wide, 30 cm long and 0.24 cm high was located at 1.5 m downstream the inlet, near the right bank.

A. Numerical simulations with the TMS

The channel was discretized with a non-structured mesh composed of 16248 triangular elements, characterized by the mean size of 12.5 cm^2, and 9331 nodes. In order to keep the Courant number lower than 1 we set the time step $t_s = 0.01$ s.

The boundary conditions used to solve the flow equations were a prescribed water elevation $h_* = 0.72$ cm and a prescribed water discharge $Q_* = 0.75\ ^l/_s$ at channel inflow. Boundary conditions for the bed evolution model consisted of fixing the bottom elevation at channel inflow and imposing the free boundary condition at channel outflow. The sediment transport was calculated using the Meyer-Peter-Müller formula [8]. Roughness effects were accounted with a Strickler roughness coefficient $Ks = 54$ m$^{1/3}$s^{-1}.

A first simulation was performed by considering $\beta_* = 1.3$ in the Koch and Flokstra (1). The results obtained from the numerical simulations are shown in Fig. 5. For a simulated time $t = 1$ h a clear train of alternate bars developed and started to migrate from upstreasm to downstream. During the first evolution steps bars present a symmetrical planimetric shape. Rapidly the computational bars changes their geometric pattern into another one characterized by the downstream face being steeper than the upstream face.

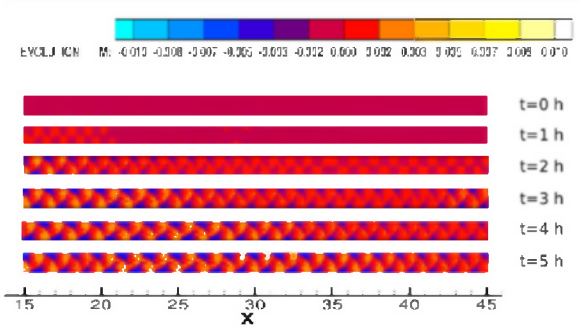

Figure 5. Plan view of bottom evolution: $\beta_* = 1.3$. $\beta_* = 1.3$.

A second simulation was performed considering $\beta_* = 2.6$ in the Koch and Flokstra formula. The results obtained from the numerical analysis are not shown here. No appreciable difference in the main bars features was detected for different values of β_*. The average bars features for a simulated time of $t = 5$ h are summarized in Table II.

B. Comparison of Results

Results obtained using the TMS are in accordance with those obtained by Bernini *et al.* [1]. In both cases, simulations describe the bars formation, evolution and propagation inside a straight channel which bed is composed by movable non-cohesive material, subject to a supercritical flow. The bars obtained are characterized by similar mechanisms of evolution. A first bar can be observed immediately after the beginning of the simulation and for a time $t = 1$ h a train of alternate bars can be detect in the channel. The non-symmetric bump used as the initial perturbation quickly eroded in both the numerical simulations. Bars geometric configuration for the early stages of evolution is characterized by a gentle a symmetric behavior. For a simulated time $t > 2$ h bars evolved into a new geometric configuration characterized by the downstream face being steeper than the upstream face. No appreciable variations in bar main features were observed in the numerical simulations performed with the TMS for different values of the coefficient β_* used in the Koch and Flokstra formula. Table II presents the average characteristics of the bars after a simulated time $t = 5$ h. Bernini *et al.*'s computational bars presented greater values of λ_b and δ_b than the computational bars obtained using the TMS. Nevertheless the values of bar length and height calculated with both numerical models remains on the same order of magnitude.

TABLE II. COMPARISON BETWEEN TMS AND BERNINI ET AL.'S BARS FEATURES [1].

	wavelenght λ_b [m]	amplitude δ_b [cm]
Bernini et al. [1]	2.80	0.60
TMS	1.80	0.90

VI. CROSATO ET AL.'S NUMERICAL EXPERIMENTS

In [4], Crosato, Mosselman, Desta and Uijttewaal performed numerical simulations and long-duration physical experiences to investigate the required conditions for the formation and behavior of migrating or non-migrating alternate bars in straight alluvial channels.

Numerical simulations were performed in a straight channel 20 km long and 150 m wide with an initial bed slope $S_0 = 0.1\%$. These geometric dimensions characterize the Waal River in the Netherlands. The domain was discretized with a finite difference grid with elements 25 m long and 15 m wide. The sediment composing the bed was considered non-cohesive and uniform with a median size $\bar{d} = 0.002$ m. The roughness coefficient, constant in space and time, was $C_f = 0.005\ m$. To describe the sediment transport mechanism, the Engelund & Hansen transport formula was used [8].

Simulations presented here are based on those proposed by Crosato *et al.* [4], in which a permanent finite perturbation in the upstream section of the channel consisting of a groyne 20 m wide and a flat bottom was considered. The initial condition was characterized by a constant value of the water-depth $h_0 = 2.8$ m for the whole domain. At the channel inflow it was imposed a prescribed value of water discharge $Q_* = 300\ {}^{m^3}/_{S}$. At channel outflow a prescribed value of water-depth equal to the value calculated for every time step at the inflow was imposed. The boundary conditions used for the morphodynamic evolution were not described in the article. To reduce the computational cost, Crosato *et al.* [4] performed the numerical simulations with a morphological factor $C_m = 10$.

A. Numerical Simulations with the TMS

The numerical experiment was performed in a straight channel with the same characteristics of the channel used by the authors. Reproduction of migrating bars was forced with a permanent perturbation similar to a transversal groyne 20 m wide and 15 m near the right bank. The channel was discretized with a non-structured mesh composed of 28121 triangular elements and 15410 nodes, characterized by main element size of 112.5 m^2.

To keep a Courant numbers lower than 1 we used a time step $t_s = 1$ s. For taking into account the bed-slope effect we decided to use the Koch and Flokstra formula, with the standard settings used by SISYPHE. The sediment transport was calculated using the Engelund & Hansen formula. According to the value of the roughness proposed by the authors, $C_r = 0.005$, the Strickler coefficient was calculated according to the the Ramette formula, given a value of Ks = 62 $m^{1/3}s^{-1}$. The simulations performed with the TMS were carried out for a simulated time $t = 1500$ days, roughly 4 yr, and no morphological factor was used.

A clear train of alternate bars developed into the computational domain, as it is shown in Fig. 6. During the first days of simulated time it was possible to observe the presence of a train of alternate free bars immediately downstream the groyne. The channel bed in the first half upstream progressively assumes a characteristic alternate pattern in which deep pools follow deposition fronts near the banks. Bars are not observed in the second half of the channel during the first days of simulated time.

Initially the alternate bars migrate from upstream to downstream. For a simulated time $t = 10 - 15$ d, the bars reached values of celerity $c_b = 6 - 7\ ^m/_h$, length $\lambda_b = 300 - 400$ m and height $\delta_b = 1 - 1.5$ m. Subsequently the bar features change, the value of λ_b and δ_b increase and, as it is logical to expect, the value of c_b decrease. For a simulated time of 1460 days, that corresponds to 4 yr, the average main bars features are $\lambda_b \approx 1750 - 1850$ m and $\delta_b \approx 7 - 8$ m. For such values of celerity the bars are not considered migrating, but steady bars.

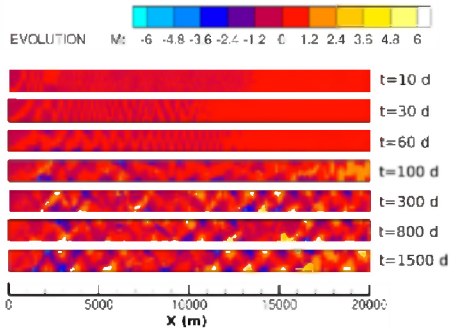

Figure 6. Plan view of bottom evolution bump.

B. *Comparison of results*

As Crosato *et al.* [4], we were able to reproduce a long-term mophodynamics evolution in straight channels, characterized by the formation of alternate bars. In both simulations the bars appeared in the first days of simulated time and immediately, downstream of the finite permanent perturbation. Initially the bars migrated with values of celerity c_b typical of migrating bars. Subsequently the bars augmented their dimensions until a state is reached for which the bar length becomes roughly $10 - 12$ times the value of the channel width and the bar height becomes roughly $2 - 2.5$ times the value used for indicating the initial water-depth. For such values of λ_b and δ_b the alternate bars lost the capacity to migrate from upstream to downstream and evolved into a steady bar configuration.

Some differences are found when comparing the value of λ_b and δ_b obtained by Crosato *et al.* with the one extrapolated by the simulation performed with the TMS. For a simulated time $t = 4$ yr the authors obtained a value of $\lambda_b = 907$ m and a value of $\delta_b \approx 15 - 20$ m. The value of λ_b obtained from our simulation is roughly $1750 - 1850$ m, larger than the value obtained by the authors. Inversely the main value of δ_b is in the range between $7 - 8$ m, lower than the value calculated by the authors.

VII. NUMERICAL SIMULATIONS OF BARS FORMATION AND PROPAGATION: LARGE-AMPLITUDE MEANDERS

According to the review of theories presented by Whiting and Dietrich [12], the development of a sequence of alternate riffles and pools in the downstream direction in a bend can be, in short, due to (*i*) an overshoot response to a first riffle-pool unit in the bend; (*ii*) a forcing effect of the curved planform; or (*iii*) in response to an instability of the flow throughout the curved planform. For this case, pools and riffles do not occur successively on opposite sides of the channel as is observed in straight configurations. Instead, bars present a 'shingled' appearance, with the same sense of curvature [11, 12].

A. *Physical Experiment by Whiting and Dietrich and Numerical Model Set-up*

We simulate here the formation and propagation of bars, bed topography and flow pattern in a large-amplitude meander channel, based on an experimenalt research conducted in symmetric sine-generated meanders channel of large-amplitude by Whiting and Dietrich [12, 13], see Fig. 7. In their experiment, flow and bed topography in large-amplitude meander bends were studied in 25-cm-wide flume channel that followed a sine-generated curve :

$$\phi = \omega \sin[2\pi(s/m)] \qquad (2)$$

with ϕ being the angle the centerline makes with the downvalley direction at point s, ω being the maximum angle between the channel path and the downvalley direction, and m being the total path distance along a single meander. This curve was proposed because it gives a smoothly varying radius of curvature that reaches a single minimum at the apex of a symmetric bend.

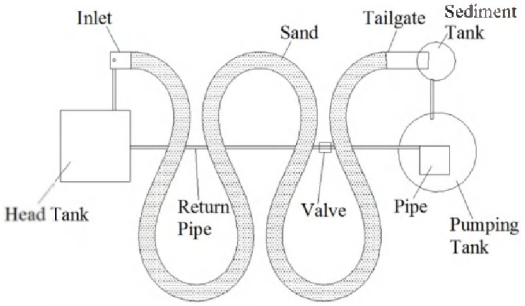

Figure 7. Sketch of the flume and experimental setup (From [12]).

The numerical simulations performed in this section correspond to the channel configuration 115-3 of the Whiting and Dietrich experimental setup [12]. For this case, in (2) $\omega = 115^{\circ}$; $m = 9.1$m and $s = 18.2$ m (corresponding to two wave lengths). The initial water depth was 0.016 m all over the domain. The inlet discharge is set to $0.001\ ^{m^3}/_s$ and the downstream water level is estimated to $h = 0.016$ m. The Fernandez Luque and Van Beek formula was adopted to estimate the sediment transport capacity of the channel. Bed material is well-sorted quartz with median diameter $d_{50} = 0.00062$ m, Shields parameter is 0.032 and bed porosity is set to 0.4. The correction for effect of secondary helical flow follows the formulation by Engelund [6]. The influence of the local bed slope on the direction of bedload motion is accounted as in Blondeaux and Seminara [2], with the Koch and Flokstra formula as the correction factor. Numerical simulations were conducted on an unstructured mesh with 11190 element and 6235 nodes. In accordance with the physical experiences, numerical simulations were run for a total time of 945 minutes.

B. *Numerical Results*

Patterns of simulated water depth, velocity module, sediment transport and bed shear stress are shown in Fig. 8 a-d. In agreement with experimental observations, Fig. 8 (a) shows the presence of multiple pools along the outer bank of the long-amplitude meander. Downstream of the bend apex of the loop (section « B »), distinctive bar units formed by shoals and pools are observed. Bar fronts (highlighted in the figure) are projected towards the right bank by effect of curvature, giving them their characteristic « shingled » appearance. In contrast with observations, the 2D model is not able to capture the presence of a first pool located approximately where the projection of the tangent to the inner bank at section « A » intersects the outer bank. Observed and simulated bar units present the characteristics 'shingled-shape'. These morphological features migrate downstream, evolving to alternate bars when they enter the straight reach between the bends, see downstream of point 'D' in Fig. 8 a. Fig. 8 (b) shows the depth-averaged velocity module. As observed in the experiments, computed patterns of higher velocities are located along the outer bank in the downstream portion of the bend. Fig. 8 c and d present the patterns of bed shear stress and sediment transport, respectively. Upstream of the bend, sediment transport is aligned along the inner bank and then projected towards the outer bank, remaining along this bank to the next bend, in concordance also with the zones of maximum local velocities and boundary shear stresses (Fig. 8 b and c). Computed sediment transport rates are in agreement with observations, with maximum values in the order of $10^{-7}\, m^3/_S$. In [12], the local boundary shear stress was estimated by inverting the bed-load equation of Fernandez Luque and van Beek. Our computed maximum stresses are in agreement with the experimental estimations, with values up to 3 times the critical dimensionless boundary shear stress.

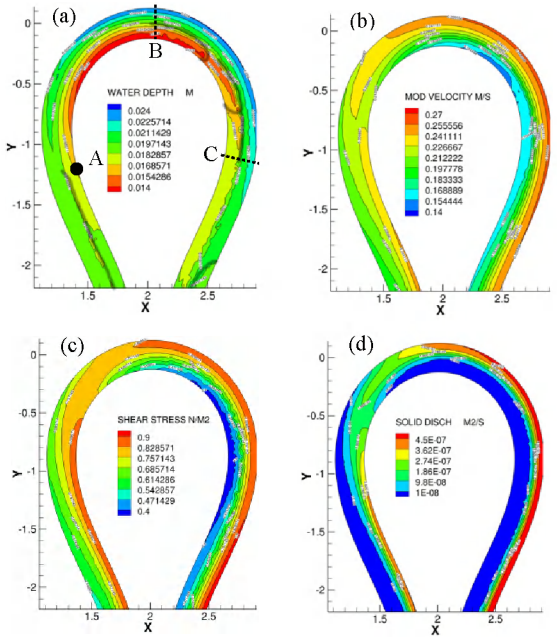

Figure 8. Numerical results of (a) water-depth (bathymetry), (b) velocity magnitude, (c) local boundary shear stress, and (d) local sediment transport rate for experiment 115-3 of Whiting and Dietrich [12].

VIII. CONCLUSIONS

From the results obtained in this work, the capabilities of the TELEMAC Modelling System to simulate the origin, evolution and propagation of alternate bars in straight and curved channels have been demonstrated. By reproducing the numerical and physical experiments presented in literature, the importance of some physical processes was found, such as the influence of the bed slope correction term and the parameterization of secondary currents effects. In agreement with Defina [5], Bernini *et al.* [1] and Crosato *et al.* [4], the importance of the bed slope correction term for reproducing the formation and propagation of alternate bars in linear channels was assessed. Parameterization of secondary currents effects appeared to be an important parameter to mimic accurately the geometrical characteristics of bars, but it is not crucial for the origin and development of bars. An important parameter for all the numerical simulation was the choice of the Strickler roughness coefficient.

The large-amplitude meander setup of Whiting and Dietrich [12, 13] showed to be a severe test for a depth-averaged 2D model. Curvilinear open-channel flows induce centrifugal forces which generate secondary currents and super-elevation of the water surface, which significantly may influence the 3D flow patterns since the cross-flow can be up to $40-50\%$ of the bulk streamwise velocity. However, even if appropriate parameterizations of relevant 3D effects are incorporated into the depth-averaged 2D model, numerical simulations have failure to capture some 3D mechanisms observed in the laboratory experiences, such as a first well-defined pool located approximately where the projection of the tangent at point 'A' in Fig. 8 (a) intersects the external boundary [12]. Preliminary results obtained with the full 3D Navier-Stokes equations previously averaged in the sense of Reynolds are shown in Fig. 9 (a) and (b), in which most of the observed flow and morphodynamics patterns, such as a series of shingled bars with pools along the concave bank and depositional bank fronts along the inner bank are well captured.

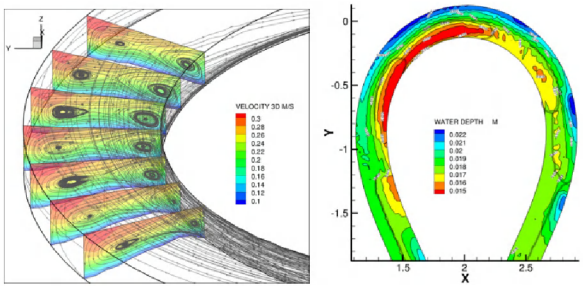

(a) (b)

Figure 9. (a) Three-dimensional flow patterns and cross-section velocities at the channel bend. The formation of two recirculation cells is clearly visible; (b) Water depth results from the 3D model.

REFERENCES

[1] Bernini, A., Caleffi, V., Valiani, A., 2006, Numerical modelling of alternate bars, Braided Rivers: Process, Deposits, Ecology and Management, Special Publication, 36, pp. 153-175.

[2] Blondeaux, P., and Seminara, G., 1985, A unified bar-bend theory of river meanders, Journal of Fluid Mechanics, 157, 449-470.

[3] Colombini, M., Seminara, G., and Tubino, M., 1987, Finite amplitude alternate bars, Journal of Fluid Mechanics, 181, 213-232.

[4] Crosato, A., E. Mosselman, F. Beidmariam Desta, and W.S.J. Uittewaal, 2011, Experimental and numerical evidence for intrinsic nonmigrating bars in alluvial channels, Water Resources Research, 47.

[5] Defina, A., 2003, Numerical experiments on bar growth, Water Resources Research, 39(0).

[6] Engelund F., 1974. Flow and bed topography in channels bends. Journal of the Hydraulics Division.

[7] Hervouet, J-M., 2007, Hydrodynamics of Free Surface Flows, modelling with the finite element method, John Wiley & Sons.

[8] Julien, P.M., 2010, Erosion and Sedimentation, United States, Cambrige, Cambrige University press.

[9] Koch F.G. and Flokstra C., 1981. Bed level computations for curved alluvial channels. XIX Congr. Int. Assoc. Hydr. Res., New Delhi, India.

[10] Lanzoni, S., 2000, Experiments on bar formation in a straight flume. Part 1: Uniform sediment, WRR, 36(11), 3337-3349.

[11] Tubino M., Repetto R. and Zolezzi G. (1999) Free bars in rivers, Journal of Hydraulics Research, 37(6).

[12] Whiting P. and Dietrich W.E., 1993, Experimental studies of bed topography and flow patterns in large-amplitude meanders 1. Observations. Water Resources Research, 29 (11), pp.3605-3614.

[13] Whiting P. and Dietrich W.E., 1993, Experimental studies of bed topography and flow patterns in large-amplitude meanders 2. Mechanisms. Water Resources Research, 29 (11), pp.3615-3622 .

[14] Yalin, S. M., 1992, River mechanics, United Kingdom, Oxford, Pergamon press.

TUC 2013, 16-18/10/2013, Karlsruhe - Kopmann, Goll (eds.) - © 2013 Bundesanstalt für Wasserbau ISBN 978-3-939230-07-6

Comparison of hydraulic and morphological predictions of TELEMAC-3D/SISYPHE and SSIIM in curved laboratory channels

J. Riesterer
Institute for Water and River Basin Management (IWG)
Karlsruhe Institute of Technology (KIT)
Karlsruhe, Germany
jochen.riesterer@kit.edu

T. Grafmüller
Institute for Water and River Basin Management (IWG)
Karlsruhe Institute of Technology (KIT)
Karlsruhe, Germany
thomas.grafmüller@kit.edu

T. Wenka
Federal Waterways Engineering and Research Institute (BAW)
Karlsruhe, Germany
wenka@baw.de

***Abstract*—For planning and optimization of hydraulic structures as well as maintenance measures physical and numerical models are basic tools. This applies to reproduce complex physical processes in the context of hydraulic and morphological problems as accurate as possible. Curved channel sections represent a particular challenge, since both the hydraulics and the morphodynamics are partly significantly affected by so-called secondary flow effects. Due to the complex flow situation and the improved computing power in recent years, three-dimensional numerical models with high-resolution are used increasingly. In the context of the presented comparative considerations based on two laboratory experiments with curved channels the numerical models TELEMAC-3D/SISYPHE and SSIIM were applied. Although there are differences in solving the flow equations and in the turbulence models used, that the results of the hydraulic conditions as e.g. the velocity distribution, the water level or the secondary flow were in close agreement. As to the morphological results mainly a good agreement between the results of TELEMAC-3D/SISYPHE and SSIIM can be observed. In spite of local differences both models reproduced the measured bed evolution quite well.**

I. INTRODUCTION

Within a scientific cooperation of the German Federal Waterways Engineering and Research Institute (BAW) and the Institute of Water and River Basin Management (IWG) of the Karlsruhe Institute of Technology (KIT) the analysis and further development of the existing numerical sediment transport models used as forecast instruments on inland waterways is considered. One focus of the investigations is the analysis of hydraulic and morphological processes in curved sections of waterways. The flow pattern as well as the direction of the sediment transport are affected by secondary flow effects due to the interaction of the centrifugal force, the lateral pressure gradient and the roughness of the bed. Thus, a suitable reproduction of the secondary flow in the numerical model is a basic requirement for a reliable sediment transport modeling in curved channels.

Against this background, hydraulic and morphological simulations of two laboratory experiments of Yen & Lee [23] and Wormleaton et al. [21] with different curved channel geometries were performed. Moreover, two different three-dimensional numerical programs were used. In addition to TELEMAC-3D/SISYPHE developed by EDF ("Electricité de France") the program SSIIM of the University of Trondheim (Olsen [17]) was considered. Both programs are available for free, whereas TELEMAC-3D/SISYPHE is an open-source and SSIIM a freeware program. With the help of comparative considerations the influence of the differences in solving the flow equations as well as the usage of different turbulence models on the hydraulic and morphological results should be analysed.

II. NUMERICAL METHODS

In TELEMAC-3D two different methods for solving the flow equations are implemented. While SSIIM solves the Navier-Stokes equations in all three spatial directions, the standard version of TELEMAC-3D is based on with the hydrostatic pressure assumption in the vertical direction. However, by using the approach of Jankowski [13] it is also possible to use a non-hydrostatic version of TELEMAC-3D, which was applied in these studies.

The horizontal mesh of the TELEMAC-3D model consists of triangles with variable lengths of the edges in horizontal direction. By defining breaklines and local grid refinements it allows an accurate capture of the channel geometry. The horizontal mesh of the SSIIM model is based on structured non-orthogonal rectangular cells. For the

spatial discretisation in the vertical sigma transformation (see e.g. Deleersnijder [5]) is used in both models. The two computer programs offer various methods of turbulence modelling (see Table I), each of them representing statistical turbulence modeling approaches (see Hervouet [12] or Olsen [18]).

TABLE I. SUMMARY OF TURBULENCE MODELS

TELEMAC-3D	*SSIIM*
constant viscosity model	*constant viscosity model*
mixing length model	*keefer model*
smagorinsky model	*spalart-allmaras model*
k-ε model	*k-ε model*
k-ω model	*k-ω model*

Further, the two codes offer the possibility of morphological modeling. The necessary approaches are implemented directly in SSIIM. When using TELEMAC the coupling with the program module SISYPHE is necessary. SISYPHE is a process-based model in which sediment transport, subdivided into bed load and suspended load, is determined on the basis of the flow field and the sediment properties for each node of the computational grid.

In both models the bed evolution is determined by solving the Exner equation (1) by means of finite-element (SISYPHE) or finite-volume (SISYPHE/SSIIM) approach, respectively.

$$(1-n)\frac{\delta Z_f}{\delta t} + Div\left(\vec{Q}_b\right) = 0 \qquad (1)$$

where n = porosity of bed material (n~0.4 for non-cohesive sediments); Z_f = bed level and Q_b = volume of sediment transport per running meter of width.

With the application of different transport formulas (see Table II) the two codes also include different approaches to account for the influence of various factors on the sediment transport. Thus, it is possible to consider the slope effect of the river bed inclination (in SISYPHE: Koch & Flokstra [15]; Soulsby [19] and in SSIIM: Brooks [3]) or the hiding and exposure effects of grain gradation (in SISYPHE: Egiazaroff [6]; Ashida & Michiue [2]; Karim et al. [14] and in SSIIM: Egiazaroff [6]; Wu et al. [22]; Buffington & Montgomery [4]).

TABLE II. SUMMARY OF TRANSPORT FORMULAS

TELEMAC-3D	*SSIIM*
Meyer-Peter-Müller [16]	*Wu et al. [22]*
Einstein-Brown [10]	*Ackers-White [1]*
Engelund-Hansen [9]	*Engelund-Hansen [9]*
Van Rijn [20]	*Van Rijn [20]*

In TELEMAC-3D/SISYPHE the bed shear stress which is relevant for the bed load transport is calculated using the formula of Nikuradse (2).

$$\tau_0 = \rho\left(\frac{\kappa}{ln\frac{z_1}{z_0}}\right)^2 U(z_1)^2 \qquad (2)$$

where τ_0 = bed shear stress; ρ = fluid density; κ = Kármán constant; z_1 = height coordinate; z_0 = Nikuradse bed roughness ($z_0 = k_s/30$) and $U(z_1)$ = velocity at level z_1.

In SSIIM the bed shear stress is calculated, by default, with reference to the existing kinetic energy (3) close to the bed, delivered from the respective turbulence model.

$$\tau_0 = C \cdot \rho \cdot k \qquad (3)$$

where τ_0 = bed shear stress; ρ = fluid density; k = kinetic energy and C = constant (SSIIM: C=0.3).

The investigations described below were carried out with the versions TELEMAC-3D/SISYPHE v6.0 and SSIIM v38.

III. INVESTIGATIONS

In the present work, the possibilities and limitations of morphological modeling and the detection of secondary flows in curved channel should be considered with the aid of the above-mentioned CFD codes. For this purpose, hydraulic and morphological comparative simulations were performed for the two laboratory experiments of Yen & Lee [23] and Wormleaton et al. [21].

A. 180 Degree Cuved Channel

Yen & Lee [23] examined the influence of unsteady flow conditions on the bed evolution in a 180 degree curved and 1 m wide rectangular channel with straight inflow and outflow sections (Fig. 1). The slope of the channel was about 2.0 ‰. At the initial stage with overall water depths of h=0.0544 m and a flow rate of 0.02 m³/s no sediment transport occurs. While for comparison of hydraulic features the initial steady conditions were used. For the morphological analysis unsteady flow conditions were applied, where the flow rate of 0.02 m³/s (h=0.0544 m) was linearly increased up to 0.053 m³/s (h=0.103 m). The average grain diameter of the initial sediment layer was d_m=0.001 m.

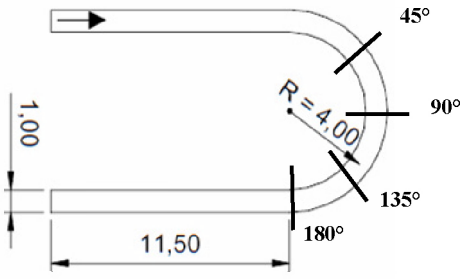

Figure 1. Bathymetry and existing control sections at 45, 90, 135 and 180 degree

B. *Meandering Channel*

The investigations of Wormleaton et al. [21] have been carried out in a flume of the U.K. Flood Channel Facility (FCF) of HR Wallingford (Fig. 2) with a steady discharge of 0.097 m³/s.

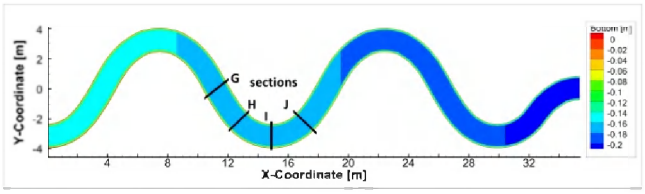

Figure 2. FCF flume: bathymetry and control sections G, H, I and J

The length of the sine-generated channel section was 35 m. The sinuosity, as a measure of meandering indicating the ratio of the length of the river section along its bends to the straight-line distance of the section, was 1.34. The wavelength was 14.96 m. The 45° trapezoidal main channel had a top-width of 1.6 m and a bed slope of 1.83 ‰. In the initial, bankfull state, the water depths in the main channel were about 0.15 m.

TABLE III. SEDIMENT CLASSES

Sediment Class	*Mean Grain Diameter*	*Percentage Fraction*
[-]	*[mm]*	*[%]*
Fraction 1	0.18	16
Fraction 2	0.48	16
Fraction 3	1.33	36
Fraction 4	3.19	32

The sediment entering at the inlet part of the model was returned from the model outlet. The bed load material was defined by a d_{16} of 0.35 mm, a d_{50} of 1.33 mm, and a d_{84} of 3.19 mm. In the absence of an accurate representation of the bed load material, the grading curve in the numerical models was linked to the characteristic data given by Wormleaton et al. [21] (see Table III). This particle size distribution allowed only partial transport, so that sorting effects occurred.

IV. HYDRAULIC FEATURES

The analysis of the main hydraulic features in the TELEMAC-3D or SSIIM models was based on steady flow conditions and fixed bed. Despite the different mesh strategies comparable cell sizes and cell distributions were chosen. The subsequent results were consistently evaluated and compared. In particular one of the objectives was to reproduce the occurring secondary flows in the curved channel sections. To estimate the secondary flow, the parts of the primary and secondary flow were separated and independently visualized within the observed cross sections.

A. *180 Degree Curved Channel*

While in the SSIIM model the standard k-ε model was used, the turbulence modeling of TELEMAC-3D was based on the smagorinsky model in horizontal direction and the mixing length model in the vertical direction.

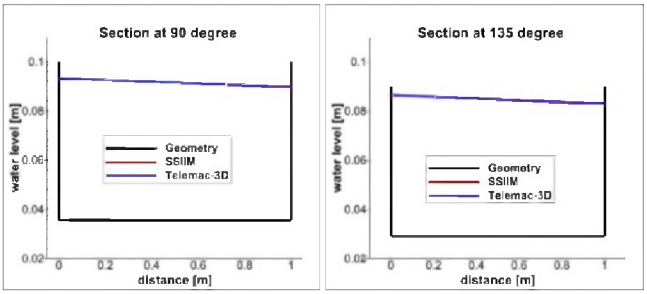

Figure 3. Simulated water level in cross sections at 90 and 135 degree

The simulated water levels along the curved channel sections are in a good agreement between the two models (Fig. 3). In both models a bed roughness of k_s=0.007 m was given. The maximum differences in water depth are below 1.0 percent.

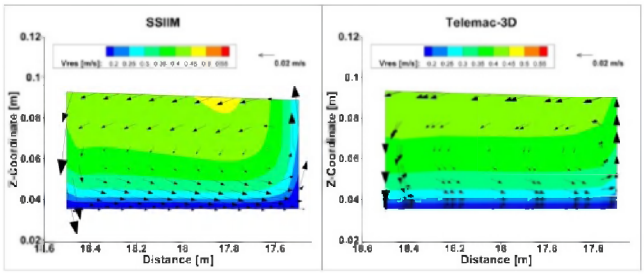

Figure 4. Comparison of secondary flow vectors and main velocity distribution at 90 degree

In both models the flow pattern as well as the intensity of the secondary flow closely match. The differences for the maxima of the secondary flow are lower than about 8 percent. Fig. 4 provides an example of the secondary flow vectors and the isosurfaces of the main velocity for the cross section at 90 degree.

B. *Meandering Channel*

For the simulations of the experiment of Wormleaton et al. [22] the turbulence modeling was arranged as described above (see sec. IV.A).

Again, a good agreement between the two models concerning the velocity distribution and the position of the maximum flow velocity could be observed (Fig. 5). This is further reflected in the formation and decay of the secondary flow along the channel and in the resulting secondary flow intensity and vortex structure. The characteristic of the secondary flow in the numerical models is close to the observations of Wormleaton et al. [22].

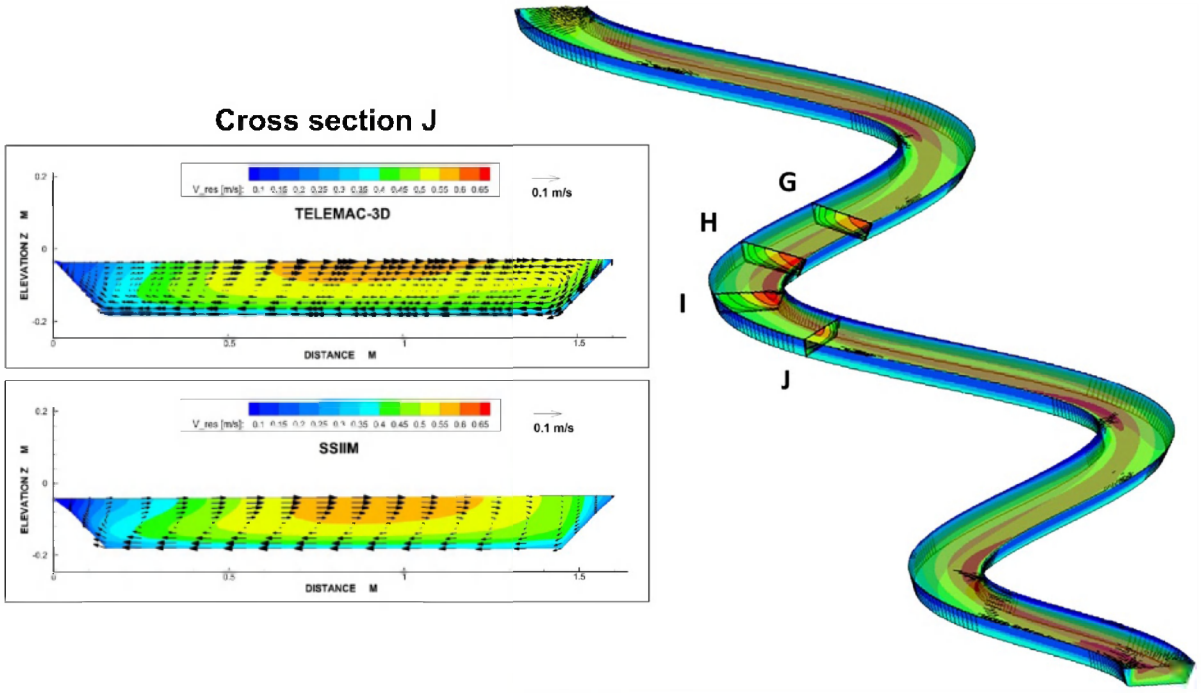

Figure 5. Evaluation of the determined secondary flow in cross section J

A direct comparison of the intensity and the frequency distribution of secondary flow computed at cross sections G, H, I and J shows good agreement among the models (Fig. 6). The range and the location of peak value of the secondary flow velocities within the sections secondary flow velocity match very well. The deviations of the maximum secondary flow velocities are lower than about 7 percent.

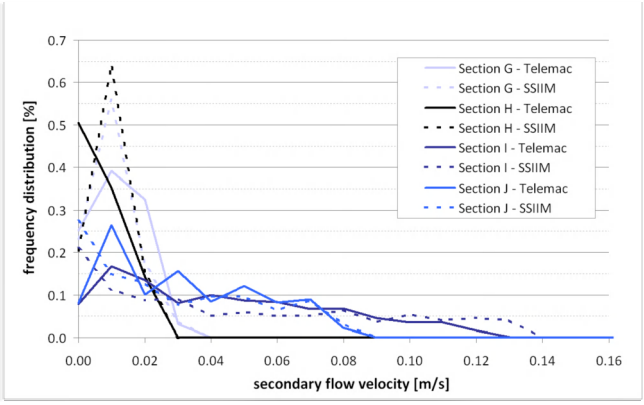

Figure 6. Analysis of the secondary flow dimensions and their frequency distribution based on cross-section

V. MORPHODYNAMIC MODELLING

For the morphodynamic modeling fractional sediment transport approaches have been used. The results of the best morphological parameter configuration (e.g. transport formula or hiding and exposure effects) are described below.

A. 180 Degree Cuved Channel

For the morphological comparison of the 180 degree bend experiment an already completed and calibrated SSIIM model of the University of Trondheim (Fischer-Antze et al. [11]) could be used. In this case, the fractional transport formula from Wu et al. [22] with a specific hiding and exposure approach was adopted. Whereas, the simulations with TELEMAC-3D/SISYPHE provided the best results with the sediment transport formula of van Rijn [20] and the hiding and exposure approach of Egiazaroff [6].

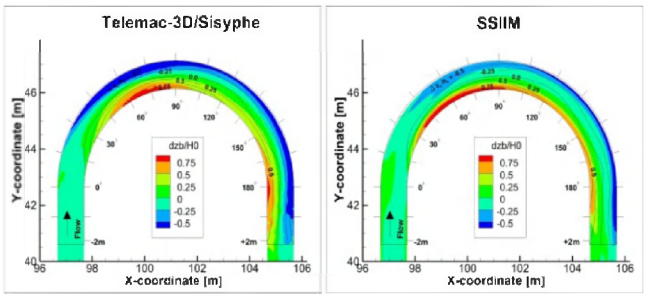

Figure 7. Contour plots of predicted bed evolution and experiment (lines)

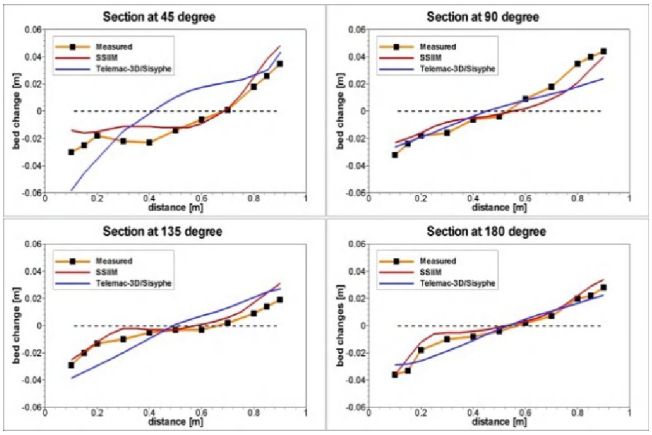

Figure 8. Comparison of calculated and measured bed evolution at different cross sections

The contour plots of the calculated bed evolution at the end of the hydrograph show a good qualitative agreement (Fig. 7). Both models reproduce the typical erosion outside and deposition inside of the channel bend. However, in the TELEMAC model increased erosion at the outer bank compared to SSIIM occurs. The cross sectional plots of bed evolution at 45, 90, 135 and 180 degrees of Fig. 8 confirm this observation. Compared to the experiments, the results of SSIIM generally show better agreement. Especially at the cross section of 45 degrees SSIIM reproduces the measured bed evolution superiorly.

B. Meandering Channel

For the test case of Wormleaton et al. [21] the sediment transport formula of Engelund & Hansen [9] was applied in the SSIIM model. For the consideration of hiding and exposure effects the approach of Egiazaroff [6] was used. In the TELEMAC-3D/SISYPHE model a fractional sediment transport version of the Meyer-Peter & Müller [16] formula was used in combination with the approach of Egiazaroff [6].

Fig. 9 shows contour plots of the predicted bed evolution. Again, both models predict the erosion and deposition along the bend well. The maximum values are in a comparable range but there are some deviations concerning the position of the erosion and deposition zones.

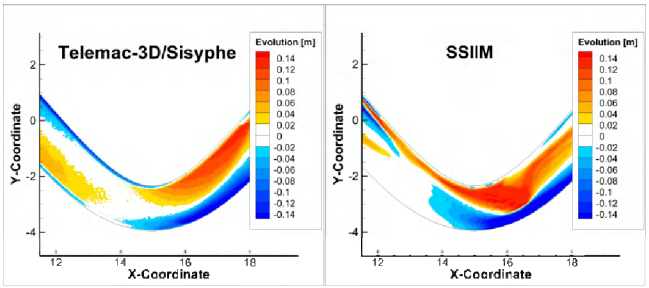

Figure 9. Comparison of predicted bed evolution

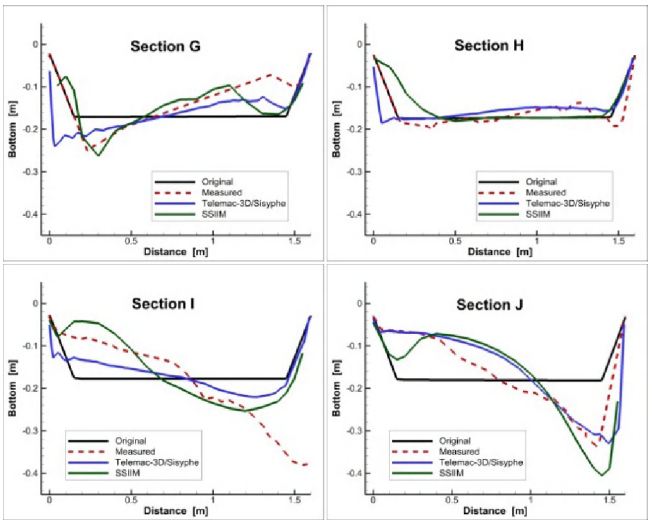

Figure 10. Comparison of the TELEMAC-3D/SISYPHE and SSIIM results with measured cross section data

The comparison of the results at cross sections G, H, I and J (Fig. 10) confirm these facts. In cross section G, the SSIIM results are slightly better compared to the measured bed levels, while in cross section H the bed evolution of the TELEMAC-3D/SISYPHE model are closer to the experiments. At the apex of the curve both models show obvious deviations from the measured bed levels, especially at the outer bank. This is probably due to the technical design of the flume, where vertical walls separate the main channel from the overbank parts. The experiments show erosion right up to these walls and so the local drop of resistance may have influenced the morphological processes. At the cross section J both models reproduce the measured bed levels in good agreement. However, the differences in maximum erosion between the prediction and the measurement are smaller in the TELEMAC-3D/SISYPHE model.

VI. CONCLUSION

With respect to the hydraulic results of the two different CFD codes TELEMAC-3D and SSIIM it could be shown that the water levels and velocity distributions are nearly similar for both model applications. In particular, the secondary flow, which has a significant influence on the sediment transport in curved channel sections, has been captured well of both codes. The secondary flow pattern as well as its intensity are comparably reproduced and show a good continuous agreement.

As one crucial result of the comparison between TELEMAC-3D/SISYPHE and SSIIM it can be stated that both models provide nearly similar hydraulic results in its applications on two laboratory experiments, despite the fact that different strategies were chosen for discretisation, flow solver and turbulence model.

In the Yen & Lee [23] experiment, some differences between the measured data and the results of the TELEMAC-3D/SISYPHE model, especially at the beginning of the bend, can be observed. The results of the SSIIM model generally show a slightly better agreement

with the measured data. Therefore, further investigations with TELEMAC-3D/SISYPHE, with the sediment transport formula of Wu et al. [22] are recommended.

The morphological features of the TELEMAC-3D/SISYPHE and the SSIIM model generally show good agreement with the flume experiment of Wormleaton et al. [21]. Although both models reproduce the measured data well, local deviations can be detected.

REFERENCES

[1] Ackers, P., White, R.W., "Sediment transport: a new approach and analysis", ASCE Jour. of Hydr. Division, Vol. 99, No. HY11, 1973

[2] Ashida, Mishiue, "Studies on bed load transport rate in alluvial streams", TransJSCE, Vol.4, 1973

[3] Brooks, H. N., discussion of "Boundary Shear Stresses in Curved Trapezoidal Channels", by A. T. Ippen and P. A. Drinker, ASCE Jour. of Hydr. Eng., Vol. 89, No. HY3, 1963

[4] Buffington, J. M., Montgomery D. R., "A systematic analysis of eight decades of incipient motion studies, with special reference to gravel-bedded rivers", Water Res. Research, 33(8), 1997

[5] Deleersnijder, E., "Upwelling and upsloping in three-dimensional marine models", Appl. Math. Modelling, 13: 462-467, 1989

[6] Egiazaroff, I.V., "Calculation of non-uniform sediment concentrations", Jour. of Hydr. Div. ASCE, Vol. 91, 1965

[7] Electricité de France, "3D hydrodynamics TELEMAC-3D Code - Release 5.8", Operating Manual, EDF R&D, 2007

[8] Electricité de France, "SISYPHE – Version 6.0", User Manual, EDF R&D, 2010

[9] Engelund, F., Hansen, E., "A monograph on sediment transport in alluvial streams", 3ième édition Techn. Univers. Of Denmark, 1967

[10] Einstein, H.A, "The bed load function for sediment trans-portation in open channel flow", US Dep. of Agriculture, Techn. Bull. No. 126, 1950

[11] Fischer-Antze, T., Ruether, N., Olsen, Gutknecht, D., "3D modeling of non-uniform sediment transport in a channel bend with unsteady flow", Jour. of Hydr. Res., Vol. 47, 2009

[12] Hervouet, J.-M., "Hydrodynamics of Free Surface Flows", John Wiley & Sons, West Sussex, England, 2007

[13] Jankowski, J.A., "A non-hydrostatic model for free surface flows", Institut für Strömungsmechanik und Elektron. Rechnen im Bauwesen, Universität Hannover, Bericht Nr. 56, 1999

[14] Karim, Kennedy, "A computer based flow and sediment routing", IIH Report N°250, Modelling for streams and its application to the Missouri River, University of Iowa, Iowa City, 1982

[15] Koch, Flokstra, "Bed level computations for curved alluvial channels", XIXth Congress of the International Association for Hydr. Res., New Delhi India, 1981

[16] Meyer-Peter, M., Muller, R., "Formulas for bed-load transport". Sect. Int. IARH Congress, Stockholm, Schweden, 1948

[17] Olsen, N.R.B., "A three-dimensional numerical model for simulation of sediment movements in water intakes", Dissertation, Univ. of Trondheim, Norwegian Inst. of Tech., 1991

[18] Olsen, N.R.B., "A three-dimensional numerical model for simulation of sediment movements in water intakes with multiblock option", User's Manual, 2013

[19] Soulsby, R., "Dynamics of marine sands", Thomas Thelford Edition, 1997

[20] Van Rijn, L.C., "Sediment transport - Part I: bed load - Part II: suspended load", Jour. of Hydr. Division, Proc. ASCE, 110, HY10, 1431-56, HY11, 1613-41, 1984

[21] Wormleaton, P. R., Hey, R. D., Sellin, R. H. J., Bryant, T., Loveless, J., Catmur, S. E., "Behavior of Meandering Overbank Channels with Graded Sand Beds", Jour. of Hydr. Eng., Vol. 131, No. 8, 2005

[22] Wu, W., Wang, S.S.Y., Jia, Y., "Nonuniform sediment transport in alluvial rivers", Jour. of Hydr. Res., Vol.38, No.6, 2000

[23] Yen, C., Lee, K., "Bed Topography and Sediment Sorting in Channel Bend with Unsteady Flow", Jour. of Hydr. Eng., Vol. 121, No. 8, 1995

TUC 2013, 16-18/10/2013, Karlsruhe - Kopmann, Goll (eds.) - © 2013 Bundesanstalt für Wasserbau ISBN 978-3-939230-07-6

Probabilistic Channel Infill Approach

M. A. F. Knaapen
Coasts and Estuaries
HR Wallingford
Wallingford, United Kingdom
m.knaapen@hrwallingford.com

C. Wertwijn
Civil Engineering and Management
University of Twente
Enschede, the Netherlands

***Abstract*—The design of access channels aims to achieve a balance between the requirements for navigation and the need for both capital and maintenance dredging; these are essentially the key factors on which decisions are based, whilst considering the constraints posed by the site-specific environmental settings and legislation. Within the constraints of navigation requirements, channel and trench design can be optimized to minimize capital dredge volumes and the expected sedimentation and related costs of maintenance dredging. However, the infill of channels and trenches is highly stochastic, due to the large number of uncertainties in flow and wave forcing, sediment characteristics and the well-known limitations in sediment transport models. This paper describes an approach taking these uncertainties into account.**

I. INTRODUCTION

The infill of channels and trenches in practice is difficult to estimate. There is considerable uncertainty in the calculation of sediment transport and infill rates that are difficult to capture. As the costs of dredging in general are high, it is important to get the best infill predictions possible, taking these uncertainties into account. This is impossible using a single model. An ensemble of model simulations, however, does allow engineers to quantify the uncertainties and determine the most likely infill rates.

Bakker et al. [1] proposed a stochastic approach based on a highly simplified model for sediment transport. Such a simplified approach does account for all parameter uncertainties. However, by missing the fundamental physical processes of sediment transport, it also introduces additional uncertainties. To make the stochastic approach more accurate, it needs to be combined with a proper model to calculate sediment transport and morphological change.

Here, the stochastic approach with ensemble simulations is extended using a more advanced numerical model for channel and trench infill based on the TELEMAC modeling system [2], [3]. This model has achieved good agreement with observed channel infill over time in flume experiments.

To avoid large computation times, this model is used as a numerical flume simulating relatively small sections of a trench or channel. Further reduction in the computation time is achieved using a morphological speed-up factor. The model is then run with a large number of different settings for e.g. grain sizes, roughness, slope effects for a range of forcing conditions, using Monte Carlo techniques.

The structure of the paper is the following: Section II summarises the specific settings of the sediment transport model. Previous results are given in section III, showing the best model prediction and a sensitivity analysis into the effect of the grain size on the trench development. Section IV describes the parameter variations in the ensemble simulations. And section V then gives the results of this ensemble. Conclusions are drawn and discussed in section VI.

II. THE MODEL

TELEMAC is run in depth averaged mode, fully coupled to SISYPHE for sediment transport and uses wave results from TOMAWAC for wave stirring. The depth averaged sediment concentration is derived from the Soulsby-van Rijn formula [4]:

$$C_S = q_s (hU)^{-1}, \tag{1}$$

where q_s is the suspended load transport rate, h the water depth and U the depth average velocity. The erosion-deposition term is based on Miles [4]:

$$W_s (C_S - C)_{z=0} = W_s \left((1+2\tau^2)\mathrm{E}(\tau) - 2\tau\pi^{-\frac{1}{2}} e^{-\tau^2} \right) (C_S - C_0)_{z=0}, \tag{2}$$

with W_s the settling velocity of the sediment and C_s the saturated concentration just above the bed and C_0 the actual concentration above the bed. Finally, τ is a non-dimensional time.

The model has shown to accurately reproduce suspended sediment transport in the Thames, and the morphodynamic development trenches in flume experiments [2].

III. PREVIOUS RESULTS

A. Best fit model

Previous work showed that the coupled TELEMAC-SISYPHE model using default settings reproduces the infill measured during flume experiments by van Rijn [6] very well (Fig. 1).

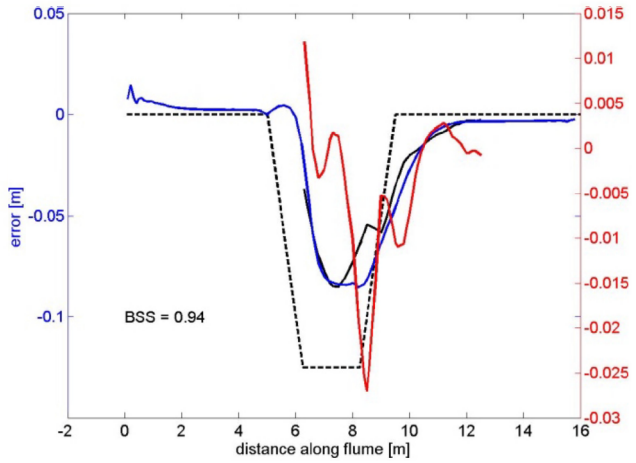

Figure 1. The morphodynamic model has an almost perfect fit with the flume experiments of van Rijn [5]. The black lines denote the initial (dashed) and final bathymetry measured in the experiments. The Blue line denotes the predicted bathymetry, while the red line (right axis) shows the difference between the measured and modelled levels.

The experiments were performed at Delft Hydraulics in a small flume with a length of 17 m, a width of 0.3 m and a depth of 0.5 m (Fig. 2). The channel had side slopes of 1 to 10 and a depth of 0.125 m. Sediment was used with D50 = 0.1 mm and D90 = 0.13 mm. To maintain equilibrium bed conditions away from the channel, 0.0167 kg/s/m sediment was fed into the flume at the inflow boundary. Regular waves with a period of 1.5 s and height of 0.08 m were generated and a steady current following the waves was imposed. The water depth was 0.255 m and the current velocity was 0.18 m/s.

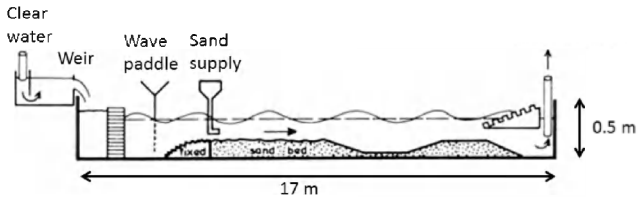

Figure 2. Cross profile of the measurement section of the flume (after [6]).

The difference between modelled and measured profiles is small. The maximum bed level error is still large, i.e. less than 25 mm on an observed bed change up to 50 mm, but this happens very locally. The Brier Skill score [7] is 0.94, where 1.0 denotes a perfect fit. The maximum error in the prediction is located at the upstream end of the trench, where some sediment appears to have slumped in the flume experiments. See [2] or [3] for more details.

B. Sensitivities to grain size

A sensitivity analysis showed that the dynamics of the trench change when varying the grains size. The analysis shows that the grain size has an influence on the infill rates. With a grain size of 0.3 mm, which would be the modelling grain size if the sediment scaled to best reproduce suspended load transport, the channel migrates a bit further, while the reduction in channel depth slightly increases as well (Fig. 3). However, with an even larger grain size (1 mm), the reduction in channel depth reduces compared to the best model (Fig. 4). The migration is about the same as with the 0.1 mm sediment, but the width of the channel is massively increased.

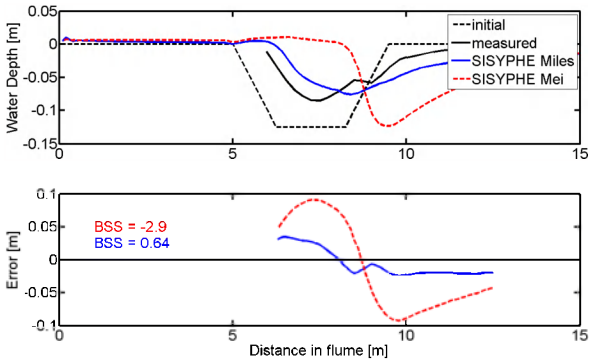

Figure 3. Prediction using 0.3mm sediment

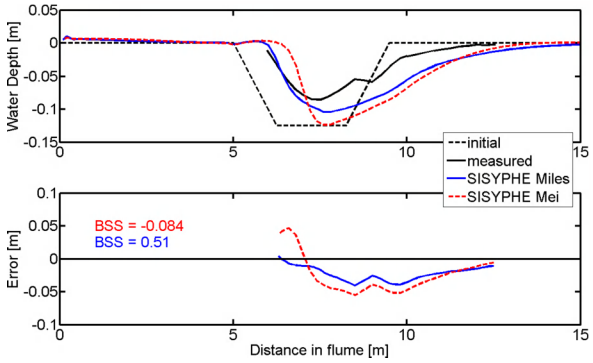

Figure 4. Prediction using 1mm sediment

IV. ENSEMBLE RUN

The findings of the sensitivity analysis show some non-linear behaviour as a function of the grain size used. To investigate further, an ensemble of simulations is derived. In principle, the same model is used as described above. However, as we are interested in practical applications, the model results are not scaled back to the flume scale. This results in a situation of a dredged trench with a depth of 1.25 m in a bottom below 2.5 m of water that flows at 0.56 m/s. Wave stirring is caused by 5 s waves 0.8 m high. The grain diameter is 0.1 mm.

The ensemble simulations introduce uncertainty around the default settings. The same model was run repeatedly with slightly different parameter setting. Assuming perfect hydrodynamics, sediment and bed characteristics are varied around the non-default parameters:

- Grain sizes (D50 and D90)
- Bed roughness
- Turbulent viscosity

All these parameter are varied assuming log normal distributions (see Fig. 5 to Fig. 8), a sensible choice for parameters with values close to zero. As a result, the right hand tails are larger than the left hand tails of the distribution. The peaks of the distributions coincide with the default settings used in the original model.

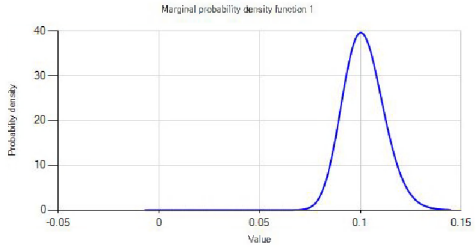

Figure 5. PDF of D_{50} in mm

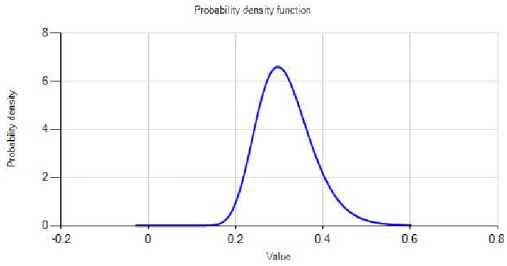

Figure 6. PDF of D_{90} in mm

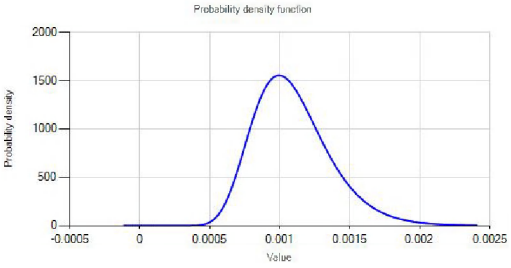

Figure 7. PDF of viscosity

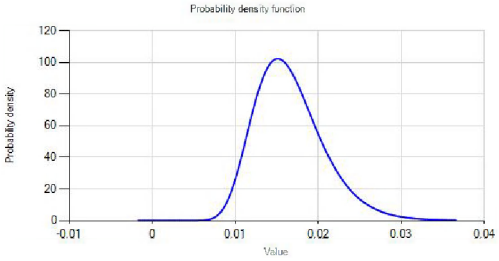

Figure 8. PDF of bed roughness length in m

An ensemble of 100 runs is created from these settings. These runs are compared to the reference run with the original model, with the default settings. To save time all runs were performed with a slightly larger time step, introducing additional model error, as the channel migrates further downstream. To compare the results, from the profiles the deepest point (referred to as depth) and the width of the area that is deeper than 0.75 m (referred to as width) are determined.

V. RESULTS

The results of the ensemble simulations are shown in Fig. 9. All simulations were stable and showed consistent dynamics of the bed. All predicted profiles are in a narrow margin around the profiles predicted using the default settings.

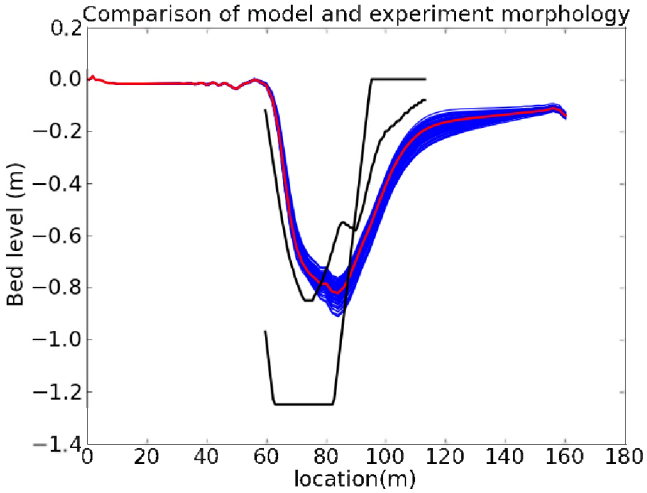

Figure 9. The ensemble of the resulting bed level profiles (blue) compared with the measured profile (initial and final) and the default prediction (red).

However, when looking at specific information the results are not all what they appear at first sight. In the case of a trench, the key elements in the channel profile are the maximum depth after a specific time and the width over which a specific depth is achieved. Fig. 10 and Fig. 11 show the histograms of the maximum depth and width with at least 0.75 m below the bed level.

The mean maximum depth in the trench is 0.82 m (Fig. 10), which is equal to the maximum depth below the surrounding bed predicted by the model with the default settings. The peak of the distribution is at 0.8 m, while the median value is 0.81 m.

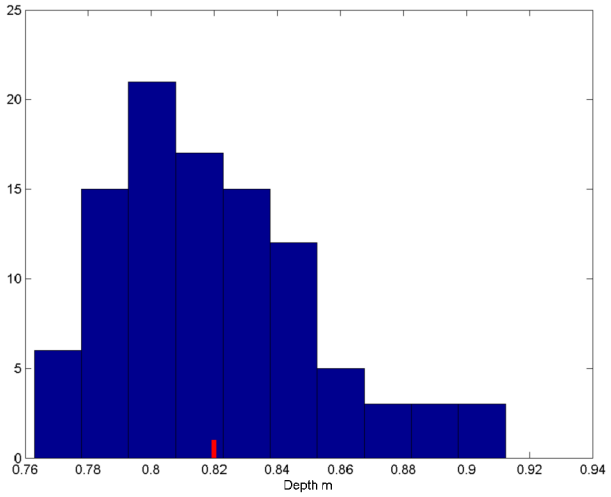

Figure 10. The histogram of the 100 resulting depth estimates at the end of the run shows that the most likely value does not coincide with the result of the default setting (red bar).

The distribution of the width over which a 0.75 m depth is achieved is given in Fig. 10. It shows a bimodal distribution, with peaks as 10 m and 12 m. Both the median and the mean are approximately 10m, which is also the peak of the distribution. All these values are 3 m less than the 13 m predicted by the model with the default settings.

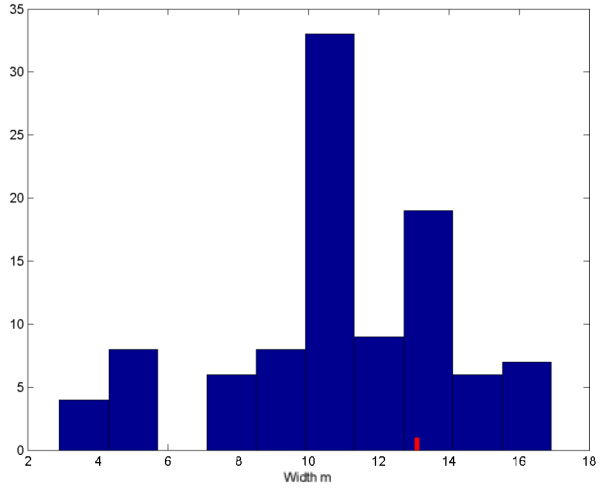

Figure 11. The histogram of the 100 resulting channel widths (defined as the width of the part that is deeper than 0.75 m). Again, this figure shows that the most likely value does not coincide with the result of the model with the default setting (red bar).

VI. Conclusions

A Monte Carlo approach is applied to quantify the uncertainties of infill in channels and trenches. The result is a statistical distribution that allows decision makers to take all natural uncertainties into account. The results using the most likely setting, which is using the default parameters for TELEMAC-SISYPHE, do neither match the mean expected change nor the most likely outcome. This is caused by the non-linearity of the distribution for the parameters and the nonlinearity of the equations. Therefore, the information regarding the uncertainties is likely to change the decisions regarding the dredging strategies.

In most practical applications there is less precise information on the sediment and bottom characteristics. In such a situation, the best settings will not necessarily produce the most likely result. Therefore, ensemble simulations will be necessary.

In this study, the focus has been on the impact of uncertainty in the sediment composition and bed structure. The uncertainty in flow, water levels and wave conditions has been ignored. However, in many cases these are the main uncertainties in the channel or trench infill. In the next phase of this research, the ensemble will be extended to include these factors.

Increasing the modelling time step to safe computation time, caused the channel to migrate further downstream, whereas the flow and initial sediment transport do not show any significant change with the larger time step.

VII. Funding

This work has been funded through HR Wallingford's Strategic Research Program.

References

[1] Bakker, S.A., Winterwerp, J.C., Zuidgeest, M. (2010). "Uncertainty analysis of the mud infill of the Olokola LNG approach channel". PIANC MMX Congress Liverpool UK, 2010, p. 286.

[2] Knaapen, M.A.F., Kelly, D.M.." Modelling sediment transport with hysteresis effects". Proceedings TELEMAC & MASCARET User Club. La Rochelle. Proc. XVIIIth TELEMAC & MASCARET User Club, EDF Corporate University, Chatou France, 2011, pp. 22-27.

[3] Knaapen, M.A.F., Kelly, D.M.. "Lag effects in morphodynamic modelling of engineering impacts", Proceedings ICCE, Santander, 2012.

[4] Soulsby, R. "Dynamics of Marine Sands," Thomas Telford. London, 1997.

[5] Miles, G. V. "Sediment transport models for estuaries", Hydraulics Research Station Wallingford, Wallingford, 1981.

[6] Van Rijn L. C. "Sedimentation of dredged channels by currents and waves", Journal of Waterway, Port, Coastal and Ocean Engineering, ASCE. Vol. 112, 5, 1986.

[7] J. Sutherland, D.J.R. Walstra, T.J. Chesher, L.C. van Rijn, and H.N. Southgate (2001). "Evaluation of coastal area modelling systems at an estuary mouth", Coastal Engineering", 2004, pp.119-142.

TUC 2013, 16-18/10/2013, Karlsruhe - Kopmann, Goll (eds.) - © 2013 Bundesanstalt für Wasserbau ISBN 978-3-939230-07-6

Implementation of an erosion law in TELEMAC-2D: a way to predict the characteristics of a breach?

C. Laroche, M. Alquier
CETE Méditerranée
Aix en Provence, France
christophe.laroche@developpement-durable.gouv.fr

***Abstract*—The feasibility of the implementation of an erosion law in TELEMAC-2D has been investigated to represent a dike failure by overtopping. This work is part of the french research project LEVEES.**
Results from this implementation were compared with results from the internal coupling between SISYPHE and TELEMAC-2D.

The first stage of the breach formation process is correctly represented with both methodologies. But it is not the case for the widening.

After listing the various phenomena responsible for the widening, we discuss the experiences and the opportunities to implement them in TELEMAC-2D.

I. INTRODUCTION

One goal of the LEVEES research project is to prove that fluvial dike failures by overflow can be correctly represented. This would mean that it is possible to predict the final width and depth of the breach, if a breach occurs.

To model the soil erosion process of earth-fill and homogeneous embankment dikes, we opted for the bi-dimensional model TELEMAC-2D (V6P1 version) coupled with an erosion law.

First, we present the methodology applied to implement the erosion law in TELEMAC-2D. Then we detail the case study and we compare our results with results obtained with SISYPHE. Finally, we discuss further developments and some limits of our implementation.

II. METHODOLOGY

A. Principle

TELEMAC-2D, a widely used open-source program in engineering, is used to simulate free-surface flows in two dimensions of a horizontal space. TELEMAC-2D solves the Saint-Venant equations using in our case the finite-element method and a computation mesh of triangular elements. At each point of the mesh, the program calculates the depth of water and the two velocity components.

An erosion law was implemented in TELEMAC-2D to estimate the new bottom elevation between two consecutive time steps.

We decided to use the erosion law defined by Partheniades [1], which gives the erosion rate as a function of effective shear stress ($\tau - \tau_c$) and a detachment rate coefficient (k_d).

$$\varepsilon = k_d \times (\tau - \tau_c) \quad (1)$$

- k_d is the detachment rate coefficient of the material (erodibility factor) ($m^3/N.s$)

- τ_c is the shear threshold (Pa)

This law gives information on the erosion of a cohesive material but not on deposits downstream.

The shear stress τ is calculated using the following formula:

$$\tau = \rho * g * h * I \quad (2)$$

The slope I of the water surface is approximated using the Manning-Strickler formula:

$$V = K_s * R_h^{2/3} * I^{1/2} \quad (3)$$

The Hydraulic radius R_h is considered to be equal to the water level (h) and the norm of the velocity (V) can be found easily using u and v.

Finally, the erosion law uses the characteristics of the flow given by TELEMAC, the Strickler coefficient (K_s) and the material's characteristics τ_c and k_d.

At each time step t, TELEMAC 2D determines h, u and v at every point of the mesh, using the bottom elevation. These data enable us to determine at every point of the mesh, if there is any erosion and, if it occurs, the value of the erosion ($\varepsilon \times dt$).

Using this value, we can determine the new bottom elevation of each point of the mesh, which is used by TELEMAC 2D to calculate h, u and v at the consecutive time step t+dt.

Furthermore only the wet points of the mesh (h > 0) are erodible. This implies that:

- On one hand, with this method we can represent simultaneously the breach and the scour hole which grows at the rear of the breach.
- On the other hand in this way, it is impossible to represent the widening of the breach. Indeed, assuming a constant flow, the erosion concentrates the overflow on one part of the dike and the lateral sides of the breach cannot be eroded because the effective shear stress is null.

B. Implementation

We focus on earth-fill and homogeneous embankment dikes, so the characteristics of the overbank and embankment materials are considered to be the same.

The characteristics of the embankment material depend on the humidity and compaction of the material [2], but in our implementation they are kept constant.

In this paper, the widening of the breach is not studied, because first tests are not conclusive. With our method, only the vertical erosion (of the breach and the overbank) is represented, so the concentration of the overflow on one part of the dike could create a very deep erosion channel. To limit this phenomenon, the minimum altitude of the points of the mesh was fixed at 2.5 meters, which is the altitude of the bottom of the riverbed close to the dike.

To reduce computational time the domain on which the erosion law is applied is smaller than the total mesh.

In this configuration, the results from our implementation could easily be compared with the results from SISYPHE. This comparison will be done at the end of this paper.

III. DESCRIPTION OF THE CASE STUDY

A. Geometric and hydraulic description

We considered a channel with a 0.1 % slope, a trapezoidal section 20 m wide at the bottom and 26 m at the surface.

The dike is 6 m wide at the crest and 14 m at the base. It is placed on the left bank, 4 m back (Fig.1).

The overbank has the same slope as the channel. It is 2 km long and 1 km wide.

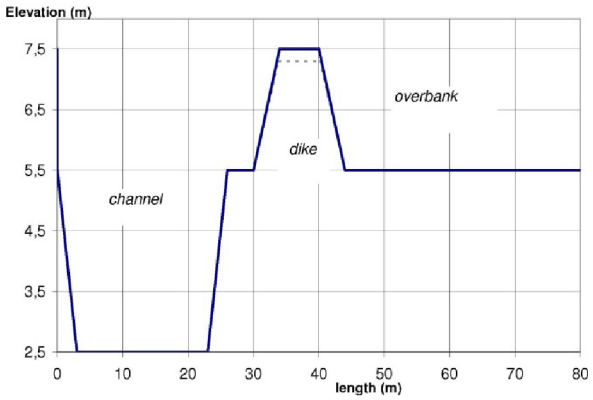

Figure 1. Profil of the dike and channel

To fix the position of the breach, we cut a notch, in the middle of the dike crest, 20 cm deep 18 m wide (Fig. 2).

The size of the mesh is 3 meters in the breach. Then, the size of the mesh increases gradually to reach 50 meters.

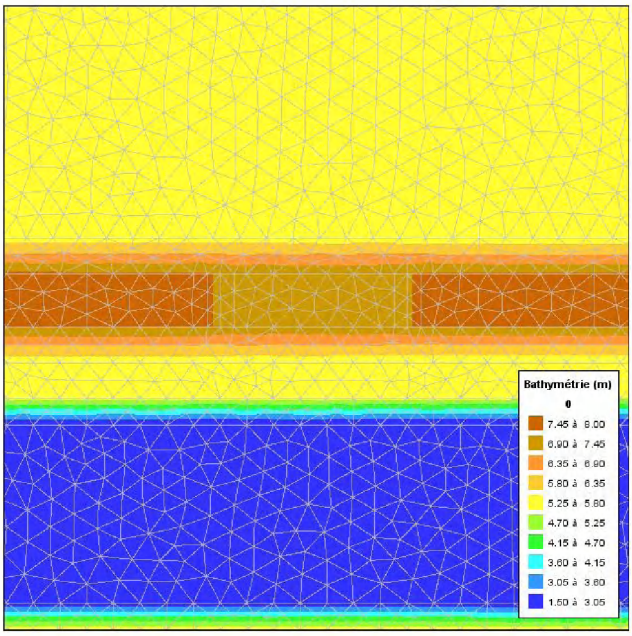

Figure 2. Mesh in the area close to the notch

The model of turbulence used is the one with a constant viscosity of 0.005 m/s^2.

The Strickler friction coefficient is fixed at 20 m$^{1/3}$s^{-1}.

The flood lasted, approximately, 78 hours. On this hydrograph, the overflow starts at t = 5400 s when the flow reaches 205 m^3/s (Fig. 3).

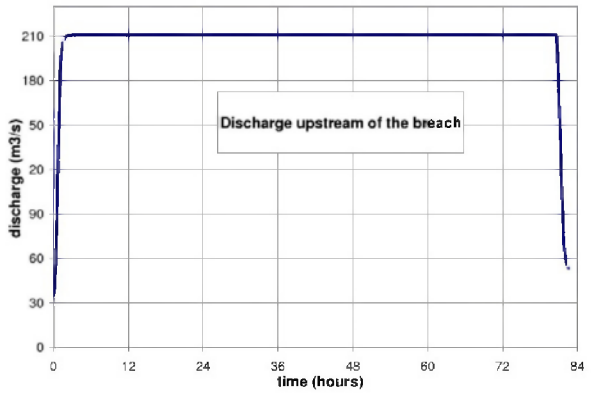

Figure 3. hydrograph upstream of the breach

B. Choice of the physical characteristics of the dike and the overbank material.

We tested three materials, an easily erodible one (Set 1), a moderately erodible one (Set 2) and a resistant one (Set 3):

- Set 1 : $K_d = 10^{-5}\ m^3/(N.s)$ and $\tau_c = 0.1\ Pa$
- Set 2 : $K_d = 10^{-7}\ m^3/(N.s)$ and $\tau_c = 10\ Pa$
- Set 3 : $K_d = 10^{-8}\ m^3/(N.s)$ and $\tau_c = 50\ Pa$

The erodibility of the materials is considered from Fig. 4.

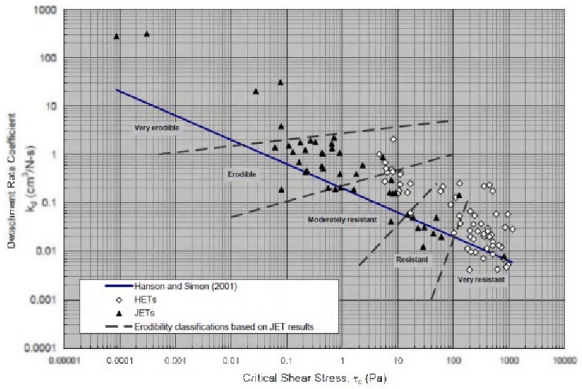

Figure 4. Erodibility of the materials based on k_d and τ_c parameters according to [3]

To represent the scour hole downstream of the breach, only the dike and the area of the overbank less than 750m away from the breach were included in the erodible domain. A 40m wide strip (centered on the breach) of the land between the river and the dike is considered erodible as well.

IV. RESULTS

A. Results with our implementation

The dike made out of the more erodible material is completely breached one hour after the start of the overflow (Fig. 5) whereas the dike made out of the moderately erodible material resisted several dozen hours (Fig.6).

The dike made out of the more resistant material is not breached despite an overflow for several dozen hours.

The resistance to breaching of the materials proposed by the model with our method is in accordance with the erodibility of the materials proposed in [3] and presented in Fig. 4.

For all sets, the development of the scour hole is consistent with the development of the breach.

The moderately erodible material (Set 2, Fig. 6) verifies the fact that the erosion begins at the same time at the base of the downstream face and at the downstream crest of the dike. Then it appears at the upstream crest. The average vertical erosion rate of the upstream crest is 0.5 cm/h whereas it is 1.5 cm/h for the downstream crest.

The erosion is much more rapid for set 1 since the average erosion rate is 1.9 m/h.

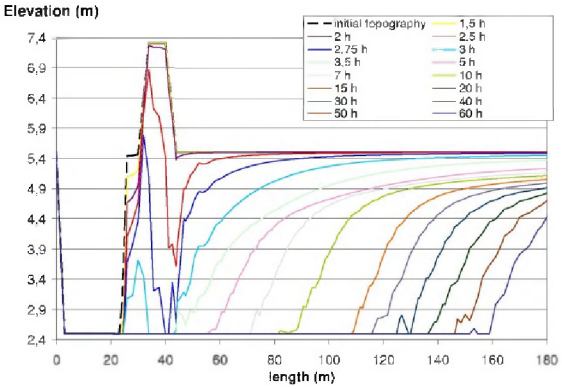

Figure 5. time evolution of the erosion (set 1)

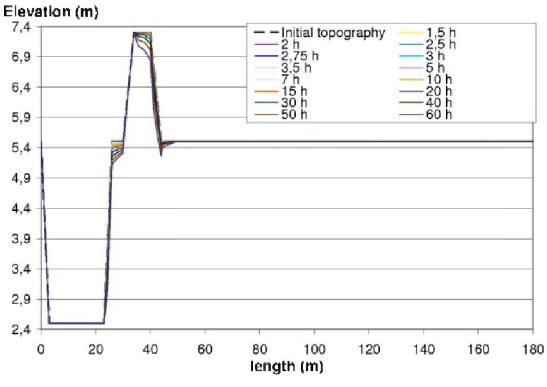

Figure 6. time evolution of the erosion (set 2)

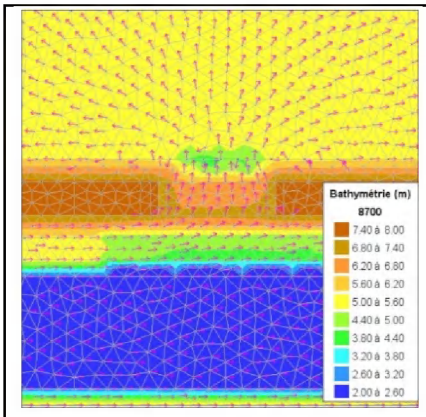	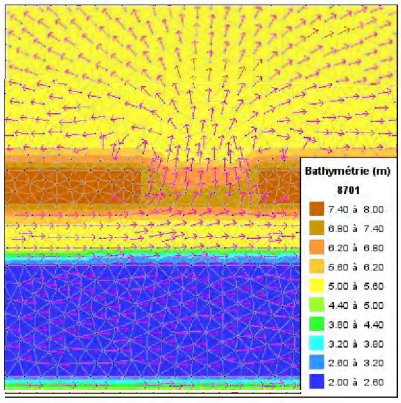	About 50 minutes after the beginning of the overflow *The velocity field in red is represented with constant magnitude*
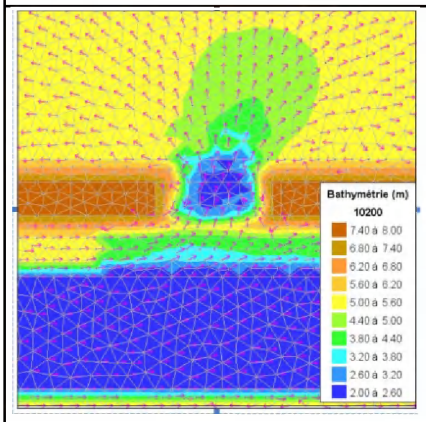	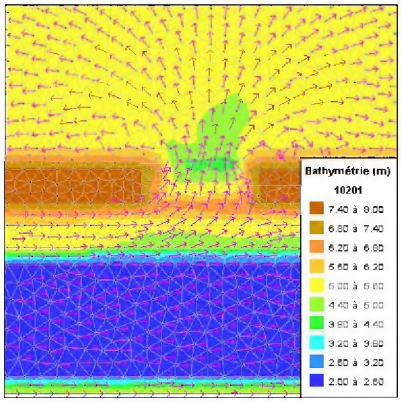	About 1 hour and 15 minutes after the beginning of the overflow
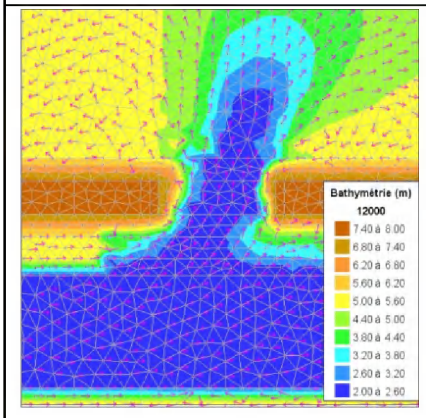	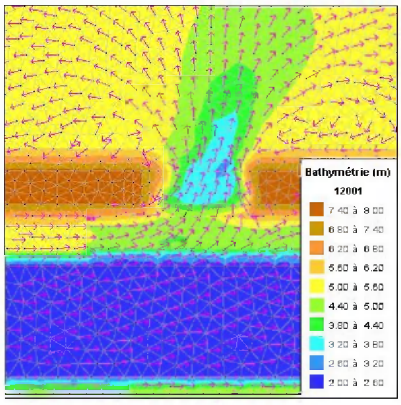	About 1 hour and 45 minutes after the beginning of the overflow
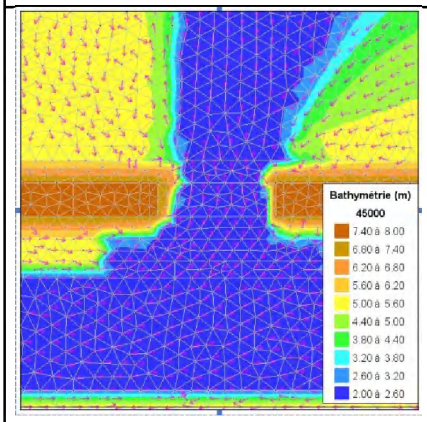	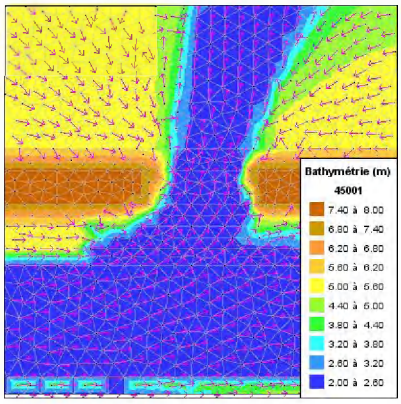	About 11 hours after the beginning of the overflow
Our implementation	SISYPHE	

Figure 7. Comparison between our implementation and SISYPHE – easily erodible material (set 1)

B. *Influence of the mesh size*

We used the model with a much finer mesh around the breach and the scour hole (1m); the erosion was very similar to the one previously obtained but the erosion rates were significantly higher: 3.3 m/s compared to 1.9 m/s (for set 1).

For the moderately erodible dike (set 2), the rates were almost doubled. Consequently half of the dike's height was therefore eroded.

The discharge through the breach (m^3/s) is mainly unaffected by the change of the mesh.

This test shows that our results depend on the mesh size.

C. *Comparison with SISYPHE*

In another test, we used the internal coupling between SISYPHE and TELEMAC-2D, the coupling period is equal to 1 and without slope effect. SISYPHE is used with a not erodible bed in the entire channel, the overbank upstream the dike isn't erodible and the dike neither, excepted close to the notch. Only the set 1 was used to compare results between SISYPHE and our method. This comparison shows that:

- The final breach width is about 15 meters with SISYPHE and 17.5 meters with our method. The difference concerns only one element length.
- In Fig. 8, the discharges through the breach are similar. The maximum discharge estimated by SISYPHE is about 120 m^3/s, with our method it is about 110 m^3/s (Fig. 8).

With our method, the dike is more rapidly eroded, as Fig. 7 shows.

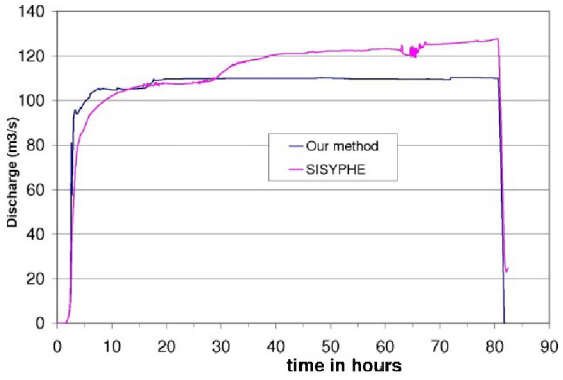

Figure 8. Comparison of discharges through the breach

V. DISCUSSION

Different methodologies could represent the first stage of the breaching process by overtopping, like our implementation and SISYPHE. They give similar results. In its current version, it appears that SISYPHE cannot represent the second stage, the widening of the breach. And we hope it will be possible to use our implementation to represent this widening.

This means, that we would be able to represent phenomena such as:

- The undercutting and the collapse of the breach sides (mass failure), which can be considered as continuous erosion process (undercutting) combined with discrete erosion process (mass failure).
- The sliding of the breach sides, which is a discrete erosion process.
- The headcut erosion, which can be observed on the outward face of the dike for cohesive material.

During the widening, more than one of these phenomena must be considered, as in [4] and [5]. We suppose that, in order to represent correctly the widening, the most important phenomena are the undercutting and the collapse of the breach sides. We didn't find any reference in the literature about the implementation of these phenomena in TELEMAC-2D. We just find some references about the implementation of the sliding of river banks [6] in TELEMAC-2D and in SISYPHE (subroutine maxslope). Thus, we will develop our own methodology to represent the undercutting and the collapse of the breach sides.

However, some questions remain:

- What is the mesh size to use to predict accurately the erosion rate of the dike?
- What is the influence of the turbulence model and which one must be used?
- Is the finite elements scheme relevant in this case?

ACKNOWLEDGEMENT

The authors would like to thank the Directorate for Research and Innovation of French Ministry of Ecology, Sustainable Development and Energy and CETMEF.

REFERENCES

[1] Parthéniades E. (1965). Erosion and deposition of cohesive soils.Journal of the Hydraulic Division, n°91, pp 105-139.

[2] Morris M.W.(2009). Breaching Processes: A state of the art review, In FLOODSite project, rep No T06-06-03, HR Wallingford UK.

[3] Wahl T. L., Hanson G. J., Reggazzoni P.L. (2009). Quantifying erodibility of embankment materials for the modelling of Dam breach processes. Proc. of the ASDSO Dam Safety, Hollywood, Florida, 2009, 24p.

[4] Mohamed M.A.A, Morris M.W. and Ghataora G.S. Improving the accuracy of prediction of breach formation through embankment dams and flood enbankments. Impact project, http://www.impact-project.net/publications/wp2_pub1.pdf

[5] Marche C., Mahdi T. and Quach T. ERODE : a reliable method for determining the potential failure hydrograph by overtopping of individual earth embankments. Commission internationale des grands barrages, Proc. of the 22 th congrès des grands barrages, Barcelone, juin 2006, 19p.

[6] Die Moran A. (2012). Physical and numerical modelling investigation of induced bank erosion as a sediment transport restoration strategy for trained rivers. The case of the old Rhine. PhD thesis University Paris Est

TUC 2013, 16-18/10/2013, Karlsruhe - Kopmann, Goll (eds.) - © 2013 Bundesanstalt für Wasserbau ISBN 978-3-939230-07-6

Prediction of the bed friction coefficient using either high resolution bathymetric data or granulometry samples

N. Huybrechts, H. Smaoui and A. Ouahsine
Roberval Laboratory of Numerical Hydraulic
(joint Research Unit CETMEF-UTC)
UMR CNRS 7337
Compiègne, France
nicolas.huybrechts@developpement-durable.gouv.fr

S. Le Bot, Y. Ferret, C. Michel and R. Lafite
M2C Morphodynamique Continentale et Côtière
UMR CNRS 6143 Université de Rouen,
Rouen France
Sophie.Lebot@univ-rouen.fr

***Abstract*—Two methods to predict the bed friction coefficient from information related to the bed texture, either bathymetric data or granulometric samples are tested and compared to in situ measurements in coastal environment. For the studied configuration, located near the Somme bay in the eastern English Channel, the method based on granulometry appears as the most efficient in term of accuracy and set up easiness.**

I. INTRODUCTION

The Somme estuary, located in France in the eastern English Channel (Fig. 1), endures a severe sedimentation with an increase of the mean bed level about 1.3 cm/year [1]. The sedimentation may result from the asymmetry of the tidal current and the associated residual sediment flux between the flood and the ebb. This phenomenon is probably increased by different hydraulic structures built during the last centuries to domesticate the tide or river dynamics and to gain farmland. More recently, new hydraulic works have been planned to limit the sedimentation, such as flush operation from the Somme channel or an experimental realignment project [2].

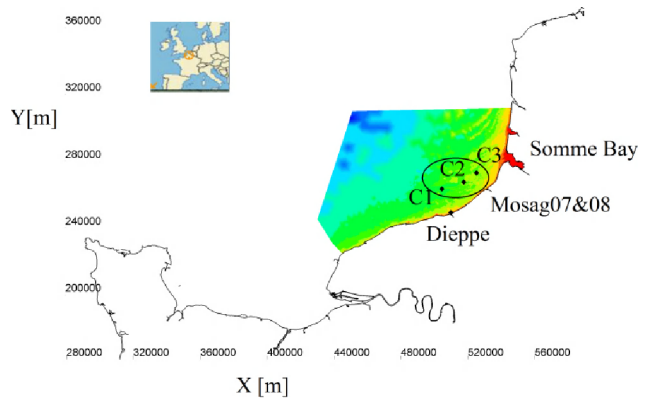

Figure 1. Location of the Somme Bay and extension of the numerical model

To predict the bed morphology evolution and the influence of these hydraulic works, it is necessary to estimate the sedimentation rate feeding the bay from offshore. Field surveys (Mosag07 and Mosag08 on Thalia vessel, Fig. 1), conducted offshore, about 30 km away from the mouth in South West direction [3] (Ferret *et al.*, 2010), lighten the presence of marine sandbanks and dunes ranging from 100 m to 1800 m in wavelength. The presence of bedform, such as dunes, strongly influences the hydrodynamic characteristics and the sediment transport rates. Their influence thus needs to be included into the methodology. The field surveys included high resolution bathymetric data, measurements of tidal currents, wave characteristics and bed material composition.

A 2D numerical model of the Somme estuary is developed. This model comprises a large coastal area (up to 60 km offshore and along shore, Fig. 1) in order to predict the sediment feeding from the sea. In coastal area, the grid can often reach a resolution about 500 to 1000 m. The bedforms are thus not physically represented. Using finer grid may allow to physically represent dunes but it will also require a 3D computation to deal with the 3D flow behaviour induced by dunes. In 2D numerical models, the dune influence is thus generally reckoned through empirical formulae. This kind of formula is generally built from datasets collected on river in equilibrium conditions. Their application to estuarine [4] or coastal environments is still challenging because of: the unsteady behavior of the flow induced by the tide and the waves, and the lack of *in situ* data to validate the predicted value of the roughness.

In the present contribution, different methodologies are tested to predict the bed friction coefficient induced by the dunes from information related to bed texture such as either bathymetric or granulometric data. Numerical results are compared to in situ measurements of tidal levels and flow velocities. Attention is currently paid on the area covered by the Mosag07&08 surveys (Fig. 1).

II. AVAILABLE DATA ON THE STUDIED AREA

A. Studied area

The Somme estuary covers an area about 70 km^2. Flow rate of the Somme River is about 30 m^3/s (yearly average) and is controlled through a lock at Saint Valery sur Somme. The tide is semidiurnal, dominated by M_2 component and its amplitude can reach more than 8 m during spring tide. The bay is covered by a high percentage of tidal flats and salt marshes.

B. Hydrodynamic Data

No tidal gauge is available in the Bay of Somme. The nearest gauge is located at Dieppe (Fig. 1) and data are made available by the "Service Hydrographique et Océanographique de la Marine" (SHOM). Field surveys occurred about 30 km South-West from the bay mouth (Fig. 1) in 2007 and 2008. During these surveys [3,5], tide levels, flow velocities, wave height and period were measured for a neap spring cycle (~15days). ADCP (Acoustic Doppler Current Profiler) measurements occurred at locations C1 - C2 in 2007 (Fig. 1 or zones SW and C respectively on Fig .2) and at C3 in 2008 (Fig. 1 or inside zone E Fig. 2). For each campaign, a neap and a spring event characterized by low wave activities have been selected to compare with the numerical results.

C. Bathymetry Data and Bedform Information

High resolution bathymetric data (1 sampling point/3m) were collected offshore during surveys MOSAG07& MOSAG08 (Fig. 1). In the intertidal part of the Bay of Somme, Light Detection and Ranging (LiDAR) data (1 sampling point/1m) have been acquired in February 2013 by the CLAREC operational team (M2C Lab, University of Caen). Elsewhere bathymetric data collected by the SHOM are used. The bathymetric data have been analysed to extract information about the bed form height and wavelength using ParamDunes software developed by the SHOM [5]. From the analysis of Moasag07&08 data, 4 different zones of bedforms are defined (North West NW, South West SW, Center C, and East E; [5]). Similarly, 2 additional zones are defined [6] from the LiDAR data (Small Dunes SD and Medium Dunes MD).

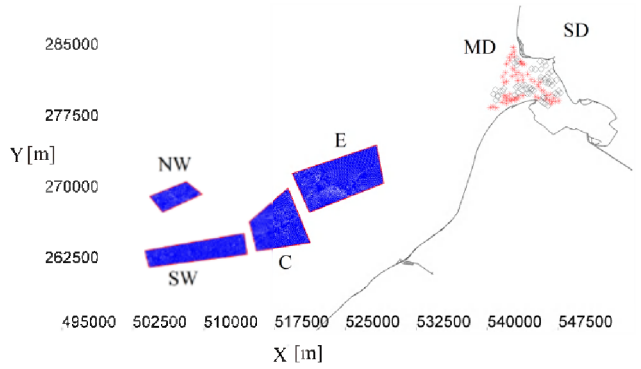

Figure 2. Bed form zones

For each zones, the averaged values of the bed form height and wavelength are summarized in Table I. Bed form height can reach up to 9 m in the NW zone and the values decrease down to 0.25 m in the tidal flat area at the mouth (SD).

TABLE I. BED FORM GEOMETRY [5,6]

Zones	*Dune height H (m)*	*Dune wavelength L (m)*	*Equivalent bed roughness k_s (m)*
NW	9.00	900	1.53
SW	6.50	530	1.32
C	4.25	375	0.80
E	6.00	425	1.37
SD	0.25	2.8	0.17
MD	0.6	7.5	0.40

D. Granulometric data

About 700 bed material samples are available in the area covered by the numerical model (Fig. 3). M2C Rouen collected 290 in the studied area (MOSAG07&08, Fig. 1) between 2005 - 2008 and 240 samples near the bay mouth between 2009 and 2013. Other samples come from the SHOM database.

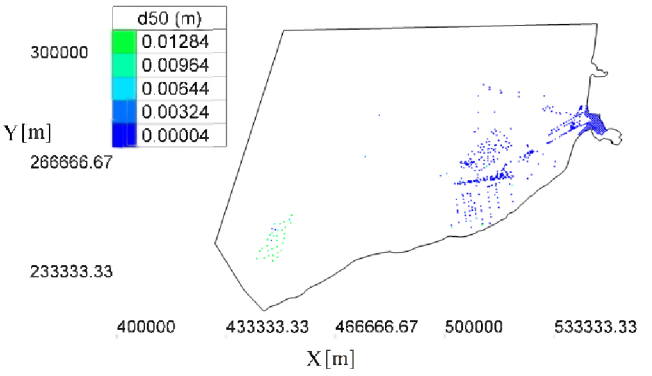

Figure 3. Location of the bed material samples

Moving from South West (SW, Fig. 2) to East (E, Fig. 2), the bed material becomes progressively finer: d_{50} about 1 mm around C1 (zone SW, Fig. 2), within 0.6 ~ 0.7 mm around C2 (zone C, Fig 2) and within 0.2 ~ 0.3 mm around C3 (zone E, Fig. 2).

III. MODEL SET UP

The unstructured grid is formed of 36349 nodes. Distance between nodes is ranging from 5 km (offshore) to 3 m in some channels inside the bay. The numerical domain is extending along the seaside from Etretat to Le Touquet and contains two bays: the Somme and the Authie estuaries (Figs 1&3).

The current release V6P2 of TELEMAC-2D is used to solve shallow water equations. Nikuradse formulation is chosen to impose the bed friction coefficient. Constant flow rates are imposed for the Somme and Authie rivers. The treatment of the offshore boundary condition is discussed in the next section.

IV. Sensitivity to the Tidal Model

In estuarine configuration, it is necessary to provide the tide level and velocities on offshore boundary. The imposed values are calculated from harmonic constants provided by global or regional tidal model. Influence of the harmonic constants on the accuracy of computed water levels has been pointed out by Huybrechts et al. [4] on the Gironde estuary in France. Simulations based on harmonic constants from Janin and Blanchard [7], SHOM and NEA atlases (North East Atlantic solution, [8]) have been compared. For the Gironde estuary, best results were obtained using NEA atlases. Similar comparison has also been performed by Pham and Lyard [9] on the Paimpol and Bréhal site (Brittany France). In their study, they have compared simulations based on harmonic constants from Janin and Blanchard [7], NEA atlases and regional tidal solution form Oregon State University (European Shelf database "ES"). NEA atlases allow to integrate 46 harmonic components whereas ES atlases give 11 harmonic constants (M2, S2, N2, K2, K1, O1, P1, Q1, M4, MS4, and MN4). For the Paimpol and Bréhal site, NEA and ES atlases provide similar accuracy for the water levels whereas less difference is observed between measured velocity and computed velocities based on the ES solution [9]. The comparison between the NEA and ES solutions is continued here and is currently based on a quantitative criterion: the Relative Mean Absolute Error "RMAE" [10]. The RMAE is given by (1):

$$RMAE = \frac{\langle |Y_c - X_c| \rangle}{\langle |X_c| \rangle} \quad (1)$$

where X_c (x_1, ..., x_N) is a set of observations and Y_c the model predictions. The mean value noted <> is defined by (2).

$$\langle |X| \rangle = \frac{1}{N} \sum_{i=1}^{N} |x_i| \quad (2)$$

The quality criteria associated with RMAE criteria is reminded in Table II [10]. The spring event of 2007 is selected to perform the comparison and two different values of the bed roughness are imposed k_s= 0.5 and 1 m. Scores of the different simulations are summed up in Table III.

TABLE II. Quality criterion

	RMAE
Excellent	<0.2
Good	0.2-0.4
Reasonable	0.4-0.7
Poor	0.7-1.0
Bad	>1.0

TABLE III. RMAE scores for ES and NEA solutions

	Velocity C1	*Velocity C2*	*Water level C2*	*Average*
ES k_s=0.5 m	0.16	0.22	0.07	0.15
ES k_s=1 m	0.16	0.24	0.07	0.16
NEA k_s=0.5 m	0.16	0.17	0.21	0.18
NEA k_s=1m	0.12	0.15	0.23	0.17

ES solution appears as the most accurate for the water level whereas NEA solutions provide better predictions for velocities. Results obtained with ES k_s=0.5 m and NEA k_s=1 m are illustrated on Figs 4 and 5.

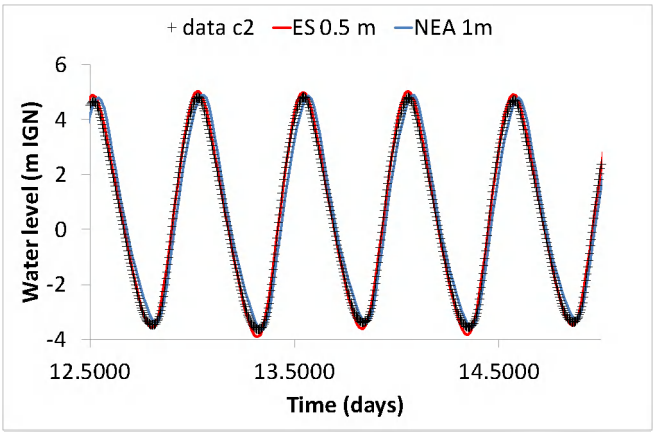

Figure 4. Sensitivity to the tidal model and bed friction coefficient. Influence on the water levels (T=0 correspond to July 20th at 0h TU)

In term of tidal amplitude (Fig. 4), both solutions are in good agreement with the measured data. NEA solution presents a slight delay in phase (10-15 min) compared to the measurements. NEA solution better captures the time evolutions of the velocity during the flood, low and high tides. However, peaks of ebb velocities (at C1 and C2, Fig. 5) are not in phase compared to the ADCP measurements and ES solution. A time lag is now observed

for the computed velocities based on ES solutions especially during low or high tides.

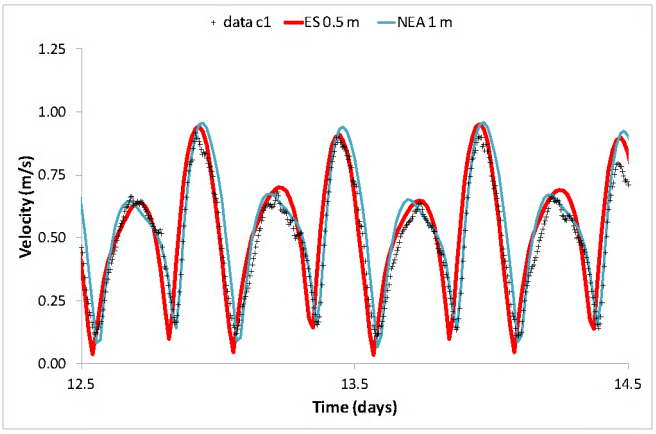

5A

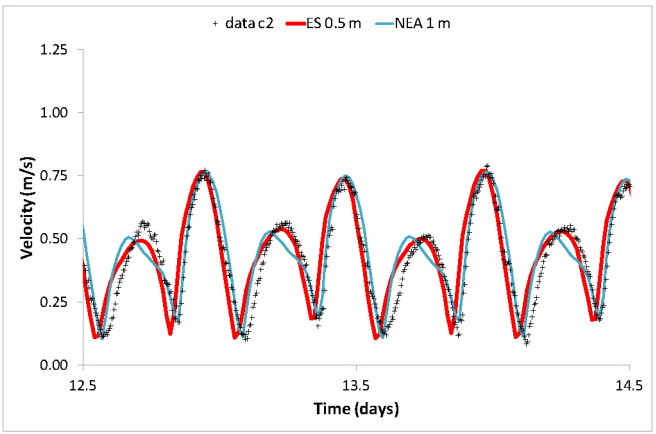

5B

Figure 5. Sensitivity to the tidal model and the bed friction coefficient. Influence on the velocity levels at C1 (5A) and C2 (5B) (T=0 corresponds to July 20th at 0h TU)

In average (Table III), ES solution reaches the lowest value of the RMAE and it is thus further kept in this contribution.

V. BED FRICTION PREDICTION USING BATYHMETRIC DATA

van Rijn formula [11] is used to predict the equivalent bed roughness k_s which is decomposed into grain roughness k'_s and roughness induced by bedforms k''_s (3).

$$k_s = k'_s + k''_s \quad (3)$$

In this section, it is assumed that the dunes are dominant and the roughness induced by bedforms k''_s is only evaluated from information related to the dune geometry (2, [11]).

$$k''_s = 1.1\gamma_d H\left(1 - e^{-25H/L}\right) \quad (4)$$

where H is the dune height, L the bedform wavelength and $\gamma_d = 0.7$ for field dune (= 1 for dune observed in flume).

For each zones of Fig. 2, a bed roughness can be computed from (2) (Table I). High resolution bathymetric data are available for some parts of the numerical domain. Data available for the whole domain have a lower space resolution and information on the bedform geometry cannot be extracted. An averaged bed roughness height (k_s = 1 m) is thus provided in the zones not covered by high resolution bathymetric data.

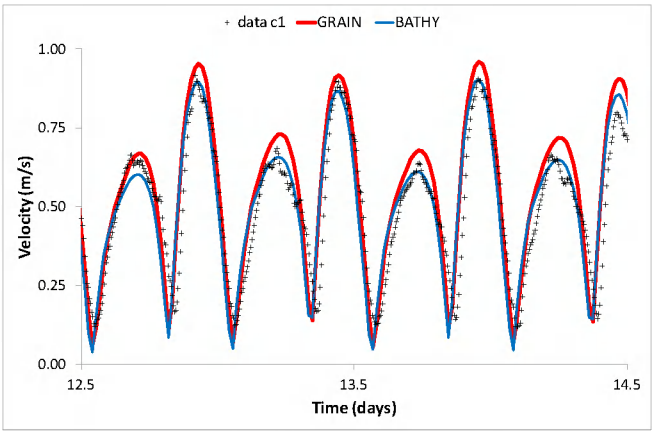

6A

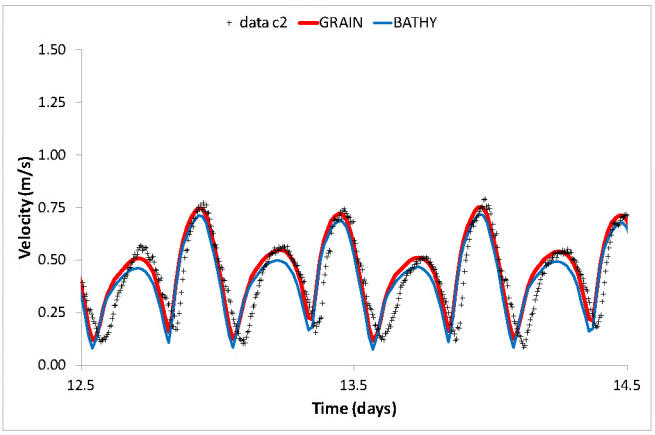

6B

Figure 6. Bed roughness predicted from bathymetrric data (BATHY) and granulometric samples (GRAIN). Comparison of velocity levels at C1 (6A) and C2 (6B) for the spring event of 2007 (T=0 corresponds to July 20th at 0h TU).

A map of bed roughness is generated for TELEMAC-2D. The bed friction coefficient is steady but variable in space. Fig. 6 A-B shows the time evolutions of the computed velocities (BATHY curves) for C1-C2 stations. For C2, the velocity signal has been too much damped by the friction coefficient whereas better agreement is observed for C1.

VI. BED FRICTION PREDICTION USING GRANULOMETRIC DATA

More recently, van Rijn [12] proposed a new version of its equation for the total equivalent bed roughness (3). The bedform roughness k"$_s$ is decomposed into roughness due to the ripples k_r, megaripples k_{mr} and dunes k_d (5)

$$k_s'' = \sqrt{k_r^2 + k_{mr}^2 + k_d^2} \quad (5)$$

The value of the roughness for each bedform component depends on the flow characteristics (depth h and flow velocity U) and the median diameter d_{50} (6).

$$k_s = fct\ (U, d_{50}, h) \quad (6)$$

From the granulometric data (Fig. 3), a map of the median diameter can be generated and a value of the d_{50} can be associated to each node. The map of the median diameter is entered as formatted data file into SISYPHE. TELEMAC is calling SISYPHE at each time step and SISYPHE is returning to TELEMAC the value of the bed roughness (neither bed load, suspension load or bed evolution are calculated by SISYPHE). The bed friction coefficient is now unsteady (tide variation) and variable in space. Computed ttime evolutions of the velocities for C1 and C2 (GRAIN curves) are plotted on Figs. 6 for the spring event of 2007. Velocity amplitudes are correctly reproduced for C2 whereas more differences are noticed during ebb peaks for C1.

VII. SYNTHESIS ON THE DIFFERENT METHODOLOGIES

Two methodologies to supply the values of the bed friction coefficient have been tested in this contribution: predicted space variable bed friction from bathymetric data (BATHY) and predicted time and space variable bed from granulometry data (GRAIN). The different values of the predicted roughness at the locations of C1 and C2 are summed up in Table IV.

TABLE IV. VALUES OF THE BED ROUGHNESS AT C1 AND C2

Bed roughness (m)	*C1*	*C2*
Constant value	0.5	0.5
BATHY	1.32	0.80
GRAIN	0.4	0.32

In Table IV, time averaged values are given for GRAIN method. Fig. 8 illustrates how the bed roughness is evolving according to the tide variation. Values are higher during the flood than the ebb and they are minima during low or high tides.

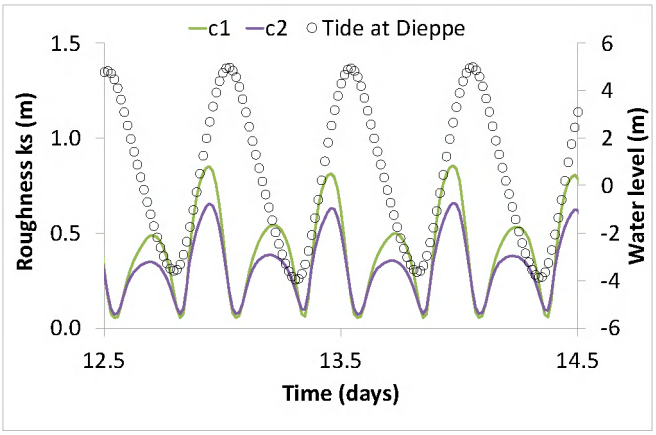

Figure 7. Time evolution of the bed roughness during tidal cycle (T=0 correspond to July 20th at 0h TU).

Between the different methodologies, the value of the roughness varies within 0.4 to 1.32 m at C1 and within 0.32 to 0.8 m at C2 whereas the median diameter varies respectively between 1 mm to 0.6 mm from C1 to C2. RMAE scores are given in Table V.

TABLE V. RMAE SCORES FOR BATHY AND GRAIN APPROACHES

RMAE	*Velocity C1*	*Velocity C2*	*Water level C2*	*Average*
BATHY	0.16	0.25	0.07	0.16
GRAIN	0.17	0.21	0.07	0.15

The accuracies of both approaches according to RMAE criteria are relatively similar. In practice, both these predicted values can serve as first set of friction value if a finer calibration is desired. However, both methods need to specify information relative to the bed texture (bed form geometry or sediment composition). The method based on high resolution bathymetric survey is more time- and money-consuming. It requires expensive sensors as well as a long treatment and analysis of the data (through ParamDune) especially for wide domain. The method based on granulometry is cheaper and easier to set up. When high resolution bathymetric data are missing, the BATHY becomes more difficult to apply whereas GRAIN can be applied even with a low resolution of bed material samples. In regards of the comparison with the measured data (Figs. 6 and Table V), GRAIN appears slightly more efficient (combination of accuracy and set-up easiness) and this method is thus currently recommended.

The efficiency of GRAIN approach can be further illustrated on the time series of the flow velocities at location C3 during neap and spring tides in 2008.

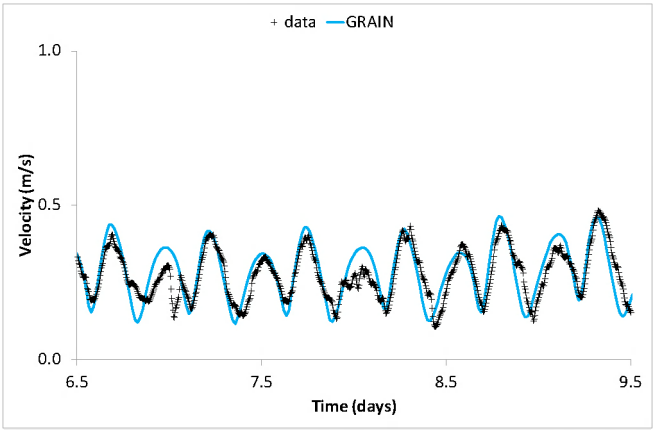

8A

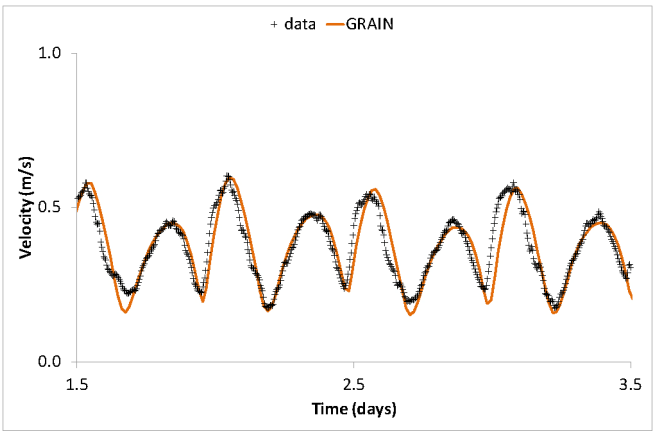

8B

Figure 8. Verification of the MT2 efficiency on the neap (9A) and spring tides (9C) in 2008. Comparison between measured data and computation "GRAIN" (T=0 correspond to July 21st 0h TU).

VIII. PERSPECTIVES

In this contribution, it has been implicitly assumed that the data relative to the bed texture are not evolving according to the tidal cycles. In a near future, it would be interesting to couple this methodology with graded sediment transport to analyse how the model can predict the sediment mixing during the tidal cycle and how this mixing can influence the bed roughness value. During the Mosag07&08 field surveys, higher wave activities have been noticed during a couple of days (waves up to 3 m high). A coupling with TOMAWAC to analyse the influence of the wave is forecast. New field surveys are also currently occurring near the bay mouth on tidal flat covered on small dunes (zones AD, SD, Fig 2). The present methodology will be also further tested on this new dataset.

ACKNOWLEDGEMENT

This study contributes to the "FORSOM" project funded by EC2CO INSU CNRS. Field measurements of Mosag 07&08 have been acquired in the framework of a study supported by the Hydrographic and Oceanographic Office of the French Navy (SHOM) and the Région Haute-Normandie. The authors want to thank the crew of the vessels 'Côte d'Aquitaine' (INSU/CNRS) and 'Thalia' (IFREMER). The SHOM is also thanked for providing complementary bathymetric and grain size data. The Région Picardy and the FEDER are thanked for founding the acquisition and processing of the LIDAR data.

REFERENCES

[1] F. Verger, Marais et estuaires du littoral français, Belin, Paris, 2005, p. 335.

[2] S. Ledoux, R. Waltherand and J. Rieu, "Projet de depoldérisation expérimentale de la Caroline- Baie de Somme". Congres SHF Morphodynamique et gestion des sédiments dans les estuaires, les baies et les deltas, p. 8, 2009

[3] Y. Ferret, S. Le Bot, B. Tessier, T. Garlan and R. Lafite, "Migration and internal architecture of marine dunes in the eastern English Channel over 14 and 56 year intervals: the influence of tides and decennial storms". Earth Surf. Process. Landforms, 35 (12), pp. 1480-1493. 2010

[4] N. Huybrechts, C. Villaret and F. Lyard, "Optimized predictive 2D hydrodynamic model of the Gironde estuary (France)", Journal of Waterway, Coast, Port and Ocean engineering , 138(4), pp. 312–322, 2012

[5] Y. Ferret, Morphodynamique de dunes sous-marines en contexte de plate-forme mégatidale (Manche Est). Approche multi-échelles spatio-temporelles. PhD Thesis, Université de Rouen, 2011, p. 305 + annexes.

[6] F. Druine, Transport sédimentaire résiduel en domaine intertidal estuarien. Exemple de la Baie de Somme. Master thesis, Master 1ère année SECC-ESE « Eaux, Sols, Environnement », Université de Rouen, 2013, p. 33.

[7] J-M. Janin and X. Blanchard, Simulation des courants de mare en Manche et proche atlantique", Rapport Interne HE-42/92.58, 1992, p. 158.

[8] I.L. Pairaud, F. Lyard, F. Auclair, T. Letellier and P. Marsaleix, "Dynamics of the semi-diurnal and quarter-diurnal tides in the Bay of Biscay", Continental Shelf Research, 28, pp. 1294-1315. 2008.

[9] C. T. Pham and F. Lyard "Use of tidal harmonic constants databases to force open boundary conditions in Telemac", TUC 2012, Oxford, UK, pp. 165-172, 2012.

[10] J. Sutherland, D.J.R Walstra, T.J. Chester, L.C. van Rijn, and H. N. Southgate "Evaluation of coastal area modelling systems at an estuary mouth". Coastal Engineering.. 51. pp 119-142, 2004

[11] L.C. van Rijn "Sediment transport, part III: bed forms and alluvial roughness" J. Hydraul. Eng.-Asce, 110(12), pp. 1733-1754,1984.

[12] L.C. van Rijn "Unified view of sediment transport by currents and waves. I: Initiation of motion, bed roughness, and bed-load transport", J. Hydraulic Eng. 133(6), pp. 649-667, 2007.

TUC 2013, 16-18/10/2013, Karlsruhe - Kopmann, Goll (eds.) - © 2013 Bundesanstalt für Wasserbau ISBN 978-3-939230-07-6

Hydro-sedimentological model of Mont Saint-Michel Implementation of ARTELIA model by CETMEF

A.-L. Tibéri-Wadier, P. Chassé
CETMEF
134 rue de Beauvais – CS 60039
60280 Margny-lès-Compiègne, France

R. Desguée
Syndicat Mixte du Mont Saint Michel
2 rue du Prieuré - BP29
50170 Ardevon, France

R. Walther, M. De Linares, A. Ledissez
ARTELIA
6 rue de Lorraine
38130 Echirolles, France

***Abstract*—This paper will present the model construction of Mont Saint-Michel by ARTELIA consultant and operating tests performed by CETMEF in the recent months. It is part of the project running since 1996 that aims to restore the maritime character of Mont Saint-Michel and to recover around it a natural environment regularly flooded by tides. A serie of tests has been operated by CETMEF and are presented in this paper. These tests concern the calculation of the volume of flushing, the study of the influence of the ground level of the Eastt channel and the hydro-sedimentory modeling from a recent bathymetry.**

I. INTRODUCTION

The Bay of Mont-Saint-Michel suffered an estimated 1 million m^3/year sedimentation which induces the gradual disappearance of sea landscape bay. The restoration of the maritime character of Mont Saint-Michel gave rise to a series of hydro-sedimentary studies conducted between 1997 and 1999 by ARTELIA consultant. The goal was to restore and maintain around Mont Saint-Michel an environment bathed by the sea and naturally maintained by the rivers. In this context, the Syndicat Mixte "Baie du Mont-Saint-Michel" wishes to have new tools to understand the consequences and to issue a technical opinion on the project which includes the construction of a new dam on the Couesnon river and the restructuring of the dike-road which provides access to the Mont Saint-Michel. It is through this project that the hydro-sedimentary numerical model was developed by ARTELIA consultant from 2008 to 2010. The model consists of around 30,000 nodes of calculation, includes large and small bay of the Mont Saint-Michel, the Couesnon river and dam, and is composed of sandy-mud mixture that lies around the Mont Saint-Michel. Since 2011 CETMEF uses and implements the model to answer questions of the Syndicat Mixte and the committee of experts that advises the owner of the works.

II. CONSTRUCTION OF THE MODEL BY ARTELIA

The project to restore the maritime character of Mont Saint-Michel aims to recover around it a natural environment regularly flooded by tides.

Several hydro-sedimentary studies were conducted between 1996 and 2001 to develop the project which is now in its final phase of construction. Since the beginning of the project, CETMEF provides technical assistance on hydro-sedimentary issues to the Mission of Mont Saint-Michel of the *"Direction Départementale de l'Equipement de la Manche"*.

In 2006, a protocol specified the terms of the partnership between the French government and *Syndicat Mixte "Baie du Mont-Saint-Michel"* on the basis of support to the Syndicat Mixte, owner of the project. In this context, CETMEF is responsible for leading a Scientific Committee.

During its first sessions, the Scientific Committee advised the Syndicat Mixte to develop a numerical model to optimize its choices in terms of hydro-sedimentary point of view.

ARTELIA consultant was selected for the development of the numerical model. This is based on the hydro-sedimentary chain calculations with TELEMAC coupled to the specific module of sediment transport and evolution SISYPHE. This hydro-sedimentary model was developed between 2008 and 2010.

The model was then transferred to the Syndicat Mixte, which now relies on CETMEF to implement the model at the request of the Scientific Committee for monitoring operating tests.

The project of restoration of the maritime character of Mont Saint-Michel consists of:

- The construction of a dam on the Couesnon with 8 gates that are operated with the aim of making flushing flow,
- Digging both channels to regulate the flow of the Couesnon: East and West channels of the Mont Saint-Michel,
- Construction of a sharing weir between these two channels to ensure that the flow is well shared. to the Mount,
- The removal of the dike-road that allows today the arrival at the foot of the Mont, and its replacement by a gateway on piles,
- The creation of an embankment at the foot of Mont Saint-Michel for the arrival of the gateway.

The hydro-sedimentary model that was built reproduces all these elements of the project.

The choice was made to model a relatively wide area; with a maritim border away from the edge of the small bay, which connects Cancale to Granville. Thus the relatively mobile seabed is far away from the place where the boundary conditions are applied.

The boundary conditions are:

- Maritime boundary: water levels and velocities deduced from a larger model of the Channel sea;
- Rivers Sée, Sélune and Couesnon: respective rivers flows;
- Couesnon dam: implementation of a law for conveyance, function of upstream and downstream water levels.

Fig. 1 shows the extent of the model with the location of the different boundary conditions.

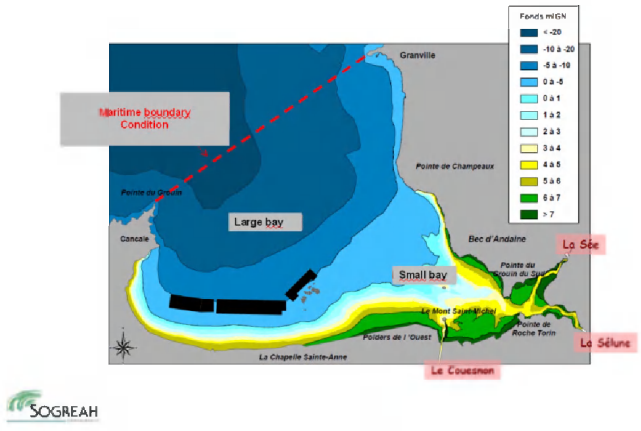

Figure 1. Extent of hydro-sedimentary model of Mont Saint-Michel

Bathymetric and topographic data are derived from different sources and dates. However, the strategy was to retain only two different bathymetric models, one from 1997 and the other from 2007, which only differ in area of the small bay.

Fig. 2 shows the different bathymetric data used to build the model.

This section presents the construction phase of the model produced by ARTELIA: topographic and hydrodynamic data, the choices that have underpinned the construction of the model and the results in terms of bathymetry and mesh.

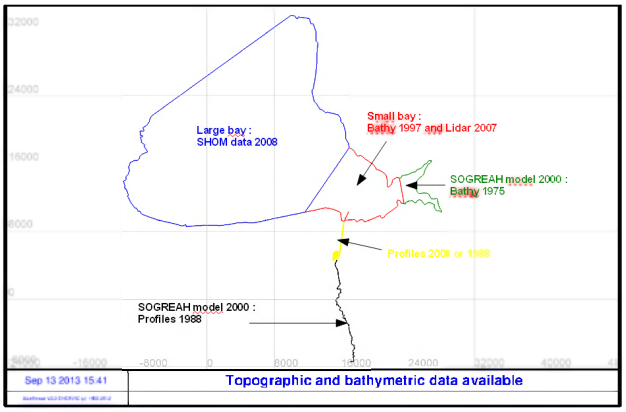

Figure 2. Topographic and bathymetric data available

A single mesh was applied to the bathymetry in 1997 and 2007, the latter providing the best possible results of hydrodynamic and morphodynamic timing of these two states.

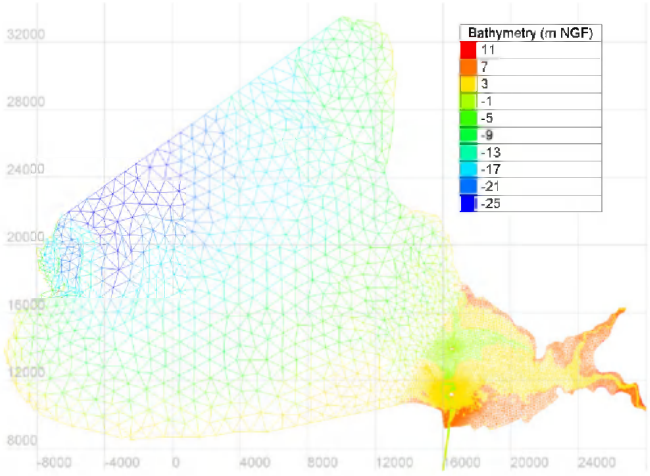

Figure 3. Overview of the mesh of Mont Saint-Michel model

Thereafter, a mesh less fitting to the existing bathymetry was done for the operational testing model.

The model mesh for operational testing has about 30,000 nodes.

Fig. 3 presents an overview of the mesh for the operating tests.

III. CALIBRATION OF THE HYDRODYNAMIC MODEL FOR HYDRO-SEDIMENTARY CALCULATIONS

The models based on bathymetric and topographic data from 1997 and 2007 have been calibrated first in hydrodynamics with current and water levels measured in the large bay, the small bay and the Couesnon river. The main calibration parameters are the friction coefficients and the conveyance of the "*caserne*" dam on the Couesnon river.

Hydraulic and sediment short-term calibration was then carried out on a series of topo-bathymetric and hydro-sedimentary measurements made during the summer of 2009.

Finally, a long-term hydro-sedimentary calibration was performed for the period of 1997-2007. The long-term calibration seeks to replicate the morphological changes at a larger spatial scale, small bay, giving still greater importance to the results in the vicinity of the Mont. The influence of the wave is taken into account for long-term simulations.

The main calibration parameters have focused on the particle size of the sand (which is variable in the bay), the concentration of mud in the bay and reducing erodibility on grassy banks. Analysis of the results focused on changes in the volume of sediment stored in the small bay, the raising of the banks and the progression of grassy banks, and general morphological changes.

The major failure of the model concerns the wandering of channels that cannot be reproduced by it. In the model the channels are fixed, while in reality, their wandering causes a distribution of erosions. It can be concluded that the overall measured indicators such as the overall flow of sediment into the bay or the overall trend of increasing grassy banks are well reproduced in the simulations.

IV. OPERATING MODEL BY ARTELIA : SENSIVITY TESTS AND OPERATING TESTS

After the calibration phase and model validation, ARTELIA operated the model for carrying out tests of sensitivity on several parameters on the one hand, and for the performance of tests of operation of the other hand.

Two types of sensitivity tests were performed:

- Calculations of short-term period timing July-August 2009, with tests on the influence of different calculation parameters (mesh roughness characteristics of the silty fraction, the average grain size of sand);
- Calculations of long-term representative of the period 1997-2007 with tests on the methodology used for the simulation of long periods (duration of forcing scenario, wave, flow of rivers).

Operating tests used the model with the hydro-sedimentary settings from the short-term timing. The operation of the Couesnon dam represents operating instructions programmed into the controller. The waves are not taken into account.

Hydraulic forcing of the tide and the Couesnon are:

- Initialization cycle of 15 days : average tide amplitudes and low flow of Couesnon 0.5 m3/s;
- First operating cycle of 15 days : Low Tide – High Tide – Low Tide and low flow of Couesnon 0.5 m3/s;
- Second operating cycle of 15 days: Low Tide – High Tide – Low Tide and average flow of Couesnon 12 m3/s.

Fig. 4 shows the tide imposed for operating tests.

The operating tests focused on the influence of the downstream and upstream of the dam bathymetry Couesnon, the influence of the management of the dam and the influence of the release of sediment.

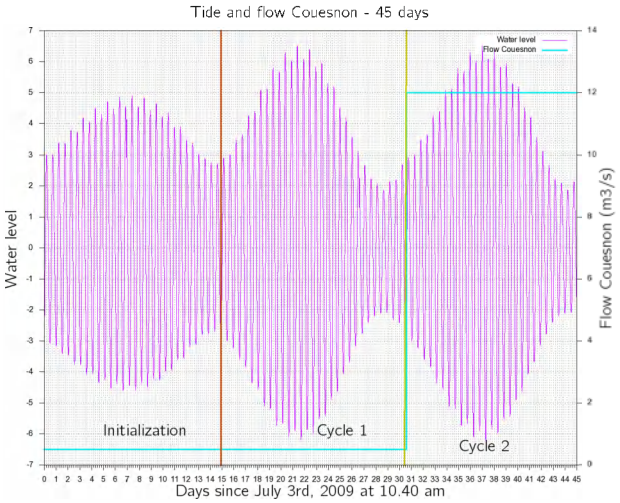

Figure 4. Viewing tidal and flows of the Couesnon imposed for operating tests

V. PROVISION OF THE MODEL TO THE SYNDICAT MIXTE AND CETMEF

The hydro-sedimentary model of Mont Saint-Michel has been available to the Syndicat Mixte and CETMEF in early 2011 and specific training in its implementation was provided by ARTELIA during one week in January 2011.

VI. RESULTS OF OPERATIONS OF THE MODEL

CETMEF began operating the hydro-sedimentary model of Mont Saint-Michel in 2011 and continues its operations at the request of the Monitoring Committee. A series of tests was conducted.

The following three tests are described below :

- calculation of the volume of flushing
- study of the influence of the ground level of the East channel
- hydro-sedimentary modeling from a recent bathymetry

Calculation of the volume of flushing

The first operations were focused on the calculation of the volume of flushing. The results were compared with previous calculations made by ARTELIA with the code 1D CARIMA. These calculations were carried out in pure hydrodynamic method and gave satisfactory results.

Influence of the ground level of the East channel

The aim of this calculation was to evaluate the influence of the ground level of the East channel on the flows and velocities in the two channels. Three calculation were performed, with the ground level respectively at 2,0 m, 2,5 m and 3,0 m.

Model constuction

These simulations were performed on the cycle of 45 days described above, represented on Fig. 4. The flow of the Couesnon is 0,5 m3/s during the whole simulation.

For example, Fig. 5 shows the bathymetry of the model with the ground level of the East channel at 2,5 m NGF.

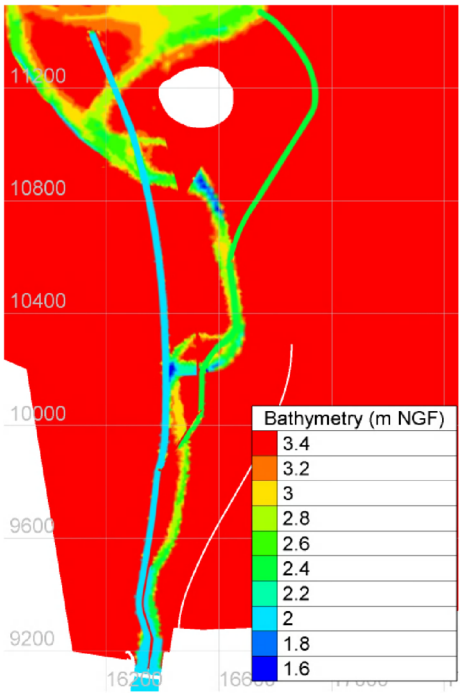

Figure 5. Bathymetry for the ground level of the East channel at 2,5 m NGF

Method of analysis of the results

The analysis of simulation results is made by plotting the flows in the East and West channels for some tides, this for the three ground levels of the Esat channel

Fig. 6 represents flushing flow down the dam and Fig. 7 represents the flow during the flood and ebb tide on a profile between the dam and the Mont.

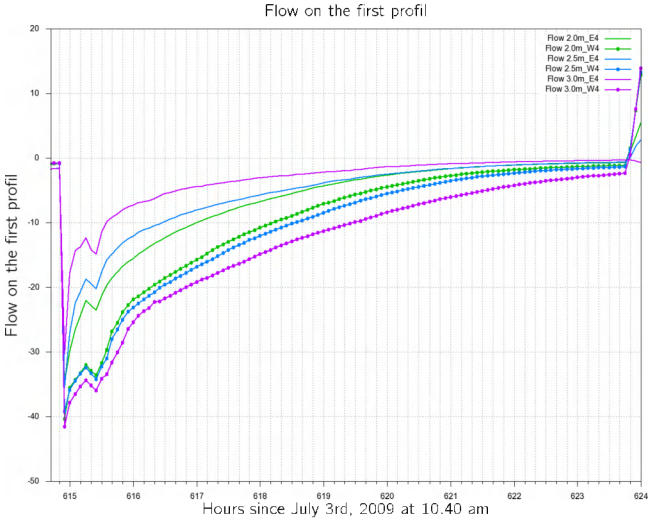

Figure 6. Flushing flow down the dam

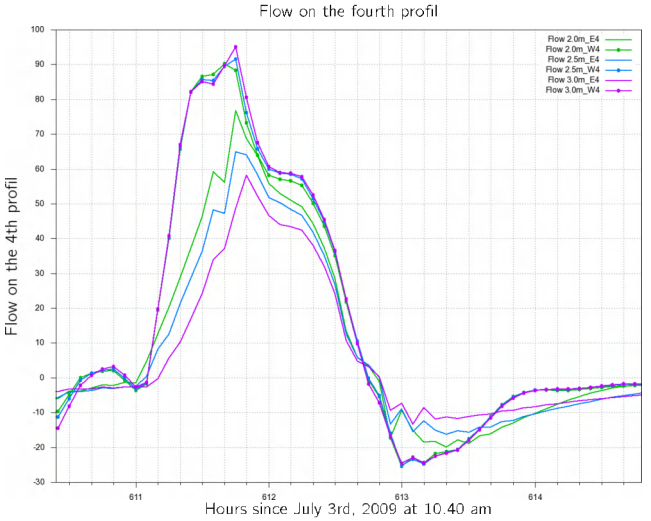

Figure 7. Flow during the flood and ebb tide

Consluions of the test

The main conclusions of this test are :

- The ground level of East channel has no influence on how the tide rises in the west channel
- The lower the ground level of the East channel is, the more the flows are important
- If the ground level of the East channel is lowered, flushing discharge in this channel increases. On the contrary, it decreases in the West channel.
- Flushing flow in the East channel is always lower than flushing flow in the West channel.

Hydro-sedimentary modeling from a recent bathymetry

Recently, the Scientific Committee wished to test the model with bathymetry closer to the current situation, including operating Lidar data that have been collected around Mont in May and October 2012.

Model constuction

The hydro-sedimentary model was modified to integrate these new bathymetric data. Two bathymetric models were made:

- the first one corresponds to the real ground in December 2012. In particular, the sharing weir is not completely built, so the East channel joins the West channel before the Mont. This bathymetry is visible on Fig. 9.
- the second one is a projection of the final bathymetry of the project: the ground levels are initially calibrated on the bathymetry of 2012, and we take into account the facilities provided at the end of the whole work: East channel dug rating the 3.0 mNGF, sharing weir calibrated to score 4.5 mNGF, embankment built to the South of the Mont, embankment South of Mont finished, dike-road removed. Fig. 10 shows this bathymetry.

The simulations were performed on the cycle of 45 days represented on Fig. 4. Three flows of the Couesnon were tested : constant at 0,5 m3/s low flow, constant at 12.0 m3/s average flow, actual flow rates observed during the winter 2012-2013, from December 10, 2012 to January 24, 2013. Fig. 10 shows the discharges of the Couesnon tested.

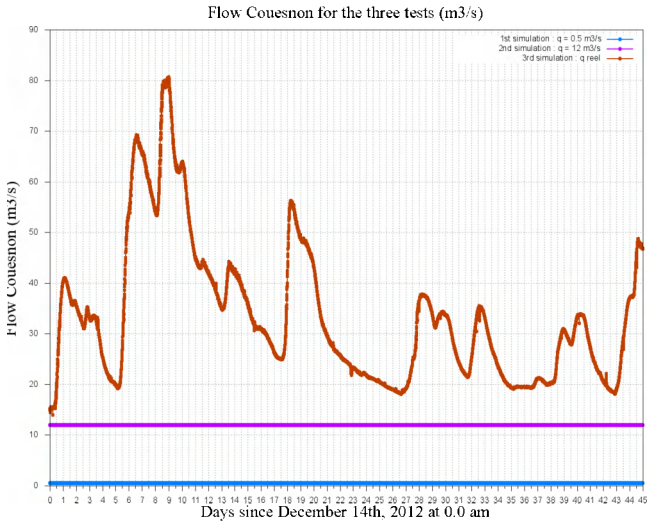

Figure 8. Three flows of the Couesnon tested

Method of analysis of the results

The results of the modeling are analyzed thanks to a series of five profils, through which sediment flows are calculated. These analysis profiles are shown on Fig. 9 and 10.

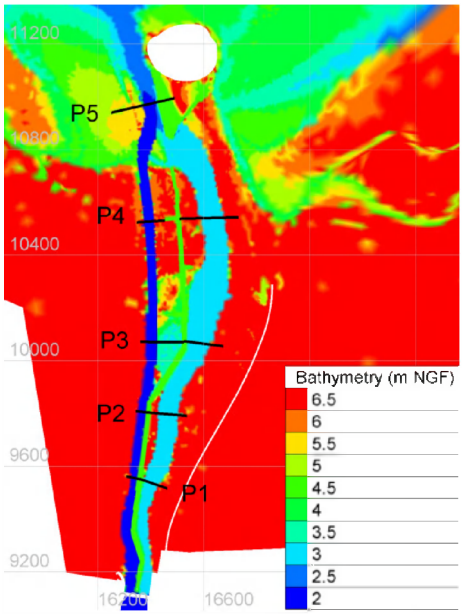

Figure 9. Bathymetry for model 'December. 2012' and analysis profiles

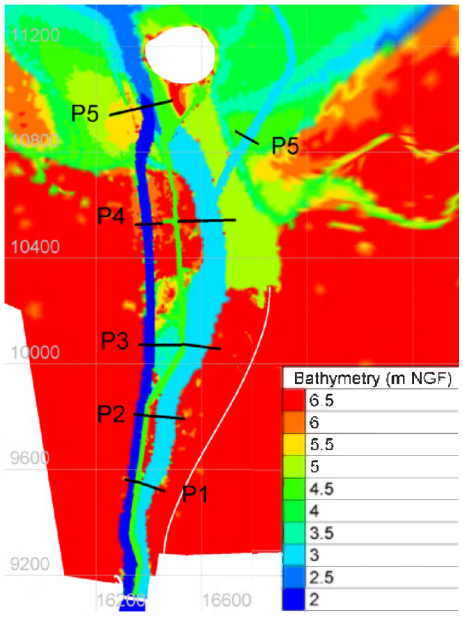

Figure 10. final bathymetry and analysis profiles

For a series of couples (tide, flow of the Couesnon), we calculate the amount of sediment which cross each profile. Fig. 11 shows for example, for a meduim tide (C=61) and for a flow of 0,5 m3/s, the sediment flow through the third profile.

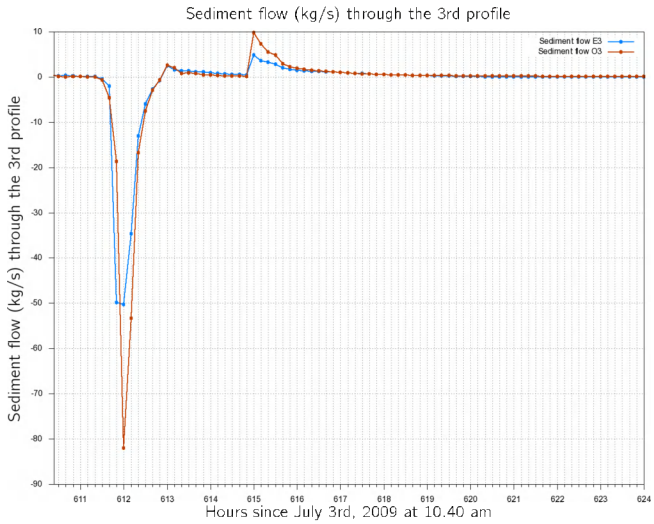

Figure 11. Sediment flow through the third profile

By integration, we estimate the amount of sediment which crosses the profile. The following table is given as an example. The tide and flow of the Couesnon are the same as before.

TABLE I. AMOUNT OF SEDIMENT WHICH CROSSES EACH PROFILE (MASS TONNES)

Profile	Sediment flow during flood and ebb tide Hours 611 to 614	Sediment flow during the flushing flow Hours 614 to 618	Balance on the whole tide
	Mass tonnes		
E1	-86	32	-54
O1	-69	36	-33
E2	-77	22	-55
O2	-79	33	-46
E3	-90	21	-69
O3	-107	29	-79
E4	-99	14	-86
O4	-101	21	-80
E5	-415	24	-391

Consluions of the test

The analysis of the whole results of the modeling shows that when the flow of Couesnon is low (0.5 m3/s), the simulation calculates an overall trend resulting in a rather fattening channels than erosion. This trend was also observed in the work of ARTELIA, achieved by operating tests.

The simulation with actual flows of Couesnon recorded between December 10, 2012 and January 24, 2013 led to a more moderate result. Channels tend to erode near the dam, where the influence of the flow is the most important. At the downstream end of the channels, depending on the terms of flows and waves, the sediment moved back or down the channels.

VII. CONCLUSION AND PERSPECTIVES

The conclusion of these tests is both forcings imposed in the model (tide and flow Couesnon) are both critical to the assessment of sediment transport in the channels between the dam and the Mont. Trends for fattening or erosion are determined by the relative importance of tide and flow Couesnon.

The hydrosedimentary model developed by ARTELIA between 2008 and 2011, on behalf of the Syndicat Mixte of Mont Saint-Michel, continues to be operated by CETMEF, at the request of the Scientific Committee and the Syndicat Mixte until the end of the project. It helps the Scientific Committee in its analyses and brings it any assistance in formulating its opinion.

REFERENCES

[1] SOGREAH – Conception et mise à disposition d'un outil de modélisation numérique hydrosédimentaire – Phase 1 : construction du modèle – Rapport final R1-V1 – Janvier 2009.

[2] SOGREAH – Conception et mise à disposition d'un outil de modélisation numérique hydrosédimentaire – Phase 2 : Tests de sensibilité – Rapport R2 – Septembre 2010.

[3] SOGREAH – Conception et mise à disposition d'un outil de modélisation numérique hydrosédimentaire – Phase 3 : calage hydro-sédimentaire long-terme – Rapport R3 – Octobre 2010.

[4] SOGREAH – Conception et mise à disposition d'un outil de modélisation numérique hydrosédimentaire – Phase 6 : calage hydro-sédimentaire court-terme – Rapport R6 – Septembre 2010.

[5] SOGREAH – Conception et mise à disposition d'un outil de modélisation numérique hydrosédimentaire – Phase 5 : analyse des mesures effectuées sur les chasses expérimentales – Rapport R5 – Janvier 2010.

[6] CETMEF – Mont Saint-Michel. Evolution de la bathymétrie du relevé Lidar 2012 par simulation hydrosédimentaire – Mars 2013.

TUC 2013, 16-18/10/2013, Karlsruhe - Kopmann, Goll (eds.) - © 2013 Bundesanstalt für Wasserbau ISBN 978-3-939230-07-6

Dispersion of suspended sediment from dredging operations in the St. Clair River

P. Prodanovic
Water Resources and Marine Engineer
Riggs Engineering Ltd.
London, Ontario, Canada
pprodanovic@riggsengineering.com

***Abstract*—Focus of this paper is on dispersion of suspended sediment resulting from maintenance dredging operations in the St. Clair River, located between the Province of Ontario (Canada) and the State of Michigan (United States). A portion of the dredging efforts are required near the river's outlet at Lake St. Clair, where combined effects of upstream river flows and lake circulation govern the sediment transport processes. Generally, as the distance of the navigation channel into the lake increases, the sediments become finer from the sudden drop of river velocity. Reduced river velocities and wind driven circulation and waves developing in Lake St. Clair are responsible for creating deposits of fine materials within the downstream navigation channels. Removal of these sediments is required through dredging operations. Coupling of TELEMAC-2D and TOMAWAC numerical models is used to capture hydrodynamics of both marine and riverine influences of the study area. The CDFATE model is used to quantify near-field mixing and dispersion, while the PSED particle tracking model is used to assess far-field suspended sediment concentration and its eventual deposition.**

I. INTRODUCTION AND BACKGROUND

The outlet of the St. Clair River, located between the borders of Canada and Unites States, serves as a key part of the shipping route for vessels sailing between the upper and lower Great Lakes. A portion of the eroded sediment carried by the St. Clair River is deposited within limits of the navigation channels near the outlet at Lake St. Clair. Dredge areas near the outlet and within the limits of the South Channel are the focus of this study (see Fig. 1). Sediment accumulating in these areas poses navigation hazards for commercial vessels that require grade depths of 8.6 m below chart datum for safe passage. Regular dredging operations are thus required to maintain navigation depths.

The dredge areas within the limits of the South Channel are referred to as Upstream Shoal area, and the Cut-off Channel. The Upstream Shoal area (located between Basset and Harsen islands) generally accumulates sediment from reduced currents as the flow in the South Channel separates in two directions causing fine and medium sand fractions to fall out of suspension. The Cut-off Channel is a man-made navigation channel 8.5 km long and 200 m wide that runs between Seaway and Basset islands and is entirely within Canadian waters. The target dredging area within the Cut-off Channel is the lower third reach where deposition of sediment and proportion of fines generally increase with channel distance towards the lake. Deposition within the Cut-off Channel results from reduced river velocities that make the sediments settle (or drop out of suspension). During wind events, lake circulation and wave effects can move lake sediments and deposit it within the limits of the navigation channel thus increasing sediment deposition.

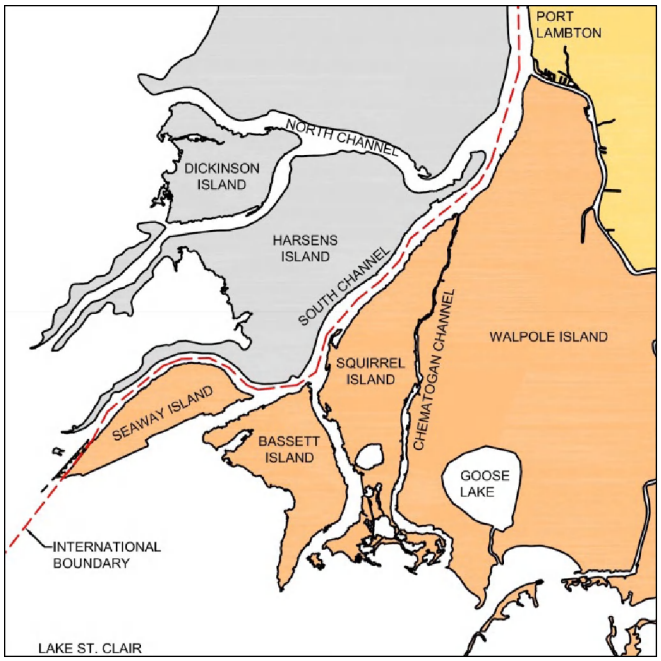

Figure 1. Study area

The focus of this paper relates to potential water quality impacts associated with dredging operations. Dredging operations have the potential to release sediments into the water column that could cause adverse water quality impacts on aquatic life within the waterway. Specifically, the main focus of this paper is to formulate a methodology that can quantify impacts from different dredging equipment and thus assess impacts in terms of total particulate matter or total suspended solids concentrations. Secondary objective is to assess the fate of the particulate matter released into the water column (i.e., where will be resuspended sediment eventually deposit). For water quality impacts, the Canadian

Water Quality Guideline for the Protection of Aquatic Life [1] for total particulate matter suggests that a maximum increase of 25 mg/L above background levels should not be exceeded for any short-term exposure. Similar guidelines are used elsewhere in the world.

Current government regulations require near- and far-field analyses associated with discharges of sediment laden waters to watercourses. Near-field mixing is defined as a region of the receiving water body where initial momentum, buoyancy and outfall geometry influence the process of mixing. The mixing in this zone occurs in the immediate vicinity of the discharge and is dependent solely on the characteristics of the effluent and its discharge mechanism (outfall pipe, overflow weir, etc.). The area where the momentum, buoyancy and the outfall geometry govern the shape and size of the plume is defined as the near-field. After the plume rises or falls (depending on its characteristics), the initial momentum and buoyancy effects are dissipated, and effects of the receiving water velocity, density and temperature become more pronounced. The plume may then bend and disperse due the hydrodynamic characteristics of the ambient waters. The region where the plume is dominated by receiving water characteristics is defined as the far-field zone.

Numerical modeling is used in this study to evaluate impact of dredging activities on water quality within a waterway. A hydrodynamic model is used to quantify velocity magnitudes and directions, which are then used as inputs to water quality and sediment transport modules. This paper will present a methodology that was applied to study water quality impacts of dredging operations within the lower reaches of St. Clair River.

The rest of this paper is organized as follows: Section II presents results of a literature review on previous numerical modeling efforts within St. Clair River and Lake St. Clair. The methodology developed to assess water quality impacts associated with dredging operations is presented in Section III, and provides a brief description of the models used. Application of the numerical modeling related to dispersion of suspended sediment is given in Section IV. Results are presented in a qualitative manner in Section V (since the project is currently ongoing). Concluding remarks are offered in Section VI along with recommendations for future work.

II. Literature Review

Hydraulics of the St. Clair River and hydrodynamics of Lake St. Clair have been extensively studied by Canadian and American researchers. In a study by Environment Canada [2], an RMA-2 hydrodynamic model was used to study encroachment effects on upstream water levels. Reference [3] also used RMA-2 to develop and calibrate a hydrodynamic model of St. Clair River, Lake St. Clair and Detroit Rivers as part of a source water assessment program for public water intakes in the State of Michigan. References [4] and [5] describe application of the FVCOM model to develop a real time Huron to Erie Connecting Waterways Forecasting System (HECWFS). The forecasting system provides real-time information on current and water levels for the entire St. Clair River, Lake St. Clair and Detroit River waterway.

Multiple independent studies were recently completed that focused on erosion, conveyance, and the ability of the St. Clair River to regulate water levels of the upper Great Lakes. Numerical models were developed and calibrated for use in assessments of water level impacts. As part of that study Canadian Hydraulics Centre [6] has developed a TELEMAC-2D model of the St. Clair River and Lake St. Clair. Since the study objectives were related to water levels of the upper reaches of the St. Clair River near Lake Huron, marine influences of Lake St. Clair were not necessary and therefore not included in their modelling work.

Hydrodynamics of Lake St. Clair are presented in reference [5], where mixing and relationship between hydraulic and wind-driven currents was studied. Their observations and simulations show that there exist distinct regions in the lake that are forced by either hydraulic flow from the river, or wind stress over the lake. During wind storms these regions can shift, and significantly influence currents. Measurements of sediment resuspension in Lake St. Clair have been studied in [7], which shows wave action as the major cause of sediment resuspension. Reference [8] investigates wave-current interaction in Lake St. Clair and show effects of wave propagation against strong current gradients.

III. Methodology

In order to study the impact of sediment released into the water column from dredging operations a number of different models were used and linked. Each of the models is briefly described below.

The TELEMAC numerical modelling system is used in this work to estimate hydrodynamic forcing of the study area. Specifically, the TELEMAC-2D model is used to capture hydraulic and wind-driven currents, while the TOMAWAC model is used to represent wave generation and propagation from open lake to the dredge areas. TELEMAC-2D solves numerically the non-linear Saint-Venant equations using the method of finite elements. TOMAWAC is a third generation phase-averaged wave model which captures the evolution of the two dimensional wave energy spectrum from winds, currents and bathymetry also using the finite element method. In this study, TELEMAC-2D and TOMAWAC were coupled such that each model influences, and is influenced by, the other. The coupling allows the process of wave-current interaction to be captured.

Near-field mixing calculations have been completed using the CDFATE mixing model, developed by the U.S. Army Corps of Engineers, Waterways Experiment Station, Vicksburg, Mississippi [9]. CDFATE was developed for the purpose assessing impact on receiving waters from continuous discharge of dredged material into the water column. The CDFATE model is based on the CORMIX model, which is used for evaluating near-field effects of municipal outfalls discharged into receiving waters.

Far-field TSS concentrations are simulated by using the PSED particle tracking model [10]. PSED model was

developed originally for the Canadian Hydraulics Centre. PSED is a sediment transport model that is designed to predict the fate of material suspended during dredging operations. Processes such as settling, deposition, re-suspension, and particle-bed interactions are considered to simulate movement of both fine and coarse sediment. The PSED model requires inputs of hydrodynamics (velocities and water surface elevations), bathymetry, and characterization of native sediments. Characteristics of sediments introduced to the water column via dredging activities are also required. Instead of modelling every grain of sand, the PSED particle tracking model uses discrete particles known as parcels to carry out sediment transport computations. Parcels are specified as having a mass with preset grain size distribution. A similar particle tracking model (known as PTM) is routinely used by US Army Corps of Engineers for impact assessment of dredging operations.

TELEMAC-2D and TOMAWAC were used to obtain hydraulics, wind and wave-driven currents for the study area. Currents generated were extracted and used in the near-field mixing calculations using CDFATE, and far-field particle tracking simulations using PSED. Near-field mixing calculations are able to identify the spread of the suspended sediment plume in the immediate zone of discharge (the first 100 m), while the far-field particle tracking calculations were used to simulate concentrations of total suspended solids further away (distances greater than 100 m).

IV. Application of Numerical Modeling

Numerical model developed in this work uses National Oceanic and Atmospheric Administration (NOAA) bathymetric survey from 2000 for the St. Clair Flats Channels (the lower portion of the St. Clair River where the main river splits into a number of channels) and Lake St. Clair. A bathymetric survey of the Cut-off Channel completed by the Canadian Hydrographic Service (CHS) in 2013 was merged with NOAA surveys to come up with the most representative bathymetric data set for study area. Bathymetric information was used to generate a Triangular Irregular Network (TIN), carefully constructing breaklines to properly delineate limits of the navigation channels in the study area. Bathymetry of the study area is shown in Fig. 2.

Hourly water level data from the Canadian gauge at Port Lambton (ID 11950, years 1962-2012) and United States gauge at Windmill Point (ID 9044049, years 2001-2012) were collected and analyzed. An inspection of the data suggested that a difference of 0.3 m in water level exists between Port Lambton (upstream gauge) and Windmill Point (downstream gauge) during periods of calm winds and thus could be used to drive the model. Hourly wind speed and direction data for Lake St. Clair was obtained from the NOAA's meteorological station at St. Clair Shore, Michigan (ID CLSM4, years 2001-2012) and was used to apply wind over the lake portion of the model. A wind rose for St. Clair Shore station suggests nearly uniform directional spread of wind speeds, with a slight emphasis of southwest winds.

The boundaries of the model were set at Port Lambton and Windmill Point gauges. To develop inflows at the upstream model boundary, water level differences between Port Lambton and Windmill Point were used for the initial run of the hydrodynamic model. The simulations produced an inflow of 5600 m^3/s at Port Lambton by using water level difference of 0.3 m, which is consistent with previous studies.

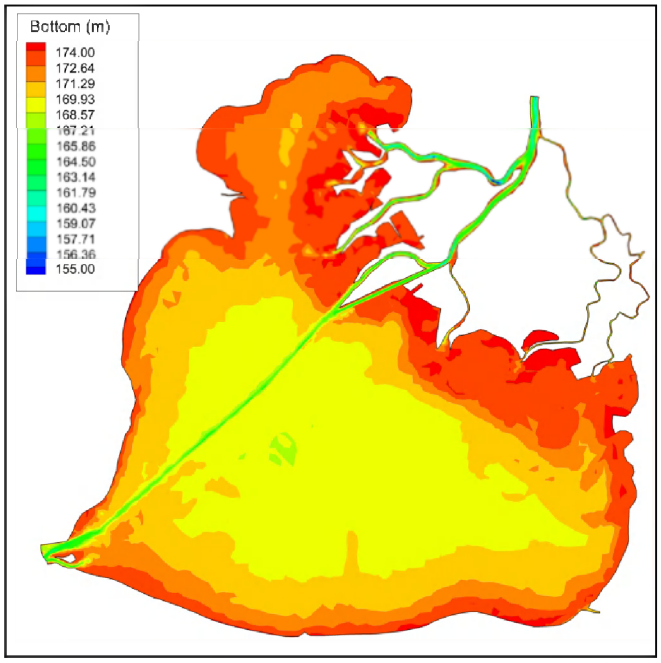

Figure 2. TELEMAC-2D model domain and bathymetry

This procedure of initializing the model with upstream and downstream water levels, and allowing the domain to slowly drain is also used in [4]. After initializing the model with appropriate flows, wind effects were added to the model to simulate marine influences (wave generation and wave induced currents). TELEMAC-2D and TOMAWAC models were coupled, and thus used to estimate currents in the dredge area for various scenarios.

A TELEMAC-2D hydrodynamic model was developed that includes the entire Lake St. Clair and the lower reaches of St. Clair River (only the reaches downstream of Port Lambton were included). The model domain contains 9,284 nodes and 16,600 triangular elements that are used to represent the waterway. The model mesh is refined within the Cut-off Channel with node spacing of approximately 50 m. Further upstream the mesh within the St. Clair River consists of elements approximately 200 m in length, while the offshore waters of Lake St. Clair have element lengths in the order of 600 m.

Application of the above methodology is illustrated by evaluating water quality and dispersion characteristics of the decant water discharged into the watercourse from a typical dredging operations using a Trailing Hopper Suction Dredge (TSHD). A THSD is a self propelled marine vessel that is capable of unassisted loading and unloading of dredged sediment. The vessel uses onboard installations to store into its hoppers (i.e., large onboard bins) the sediment/water mixture that are removed from the bed of the lake or river during dredging activities. A THSD uses large drag-heads

that are lowered to the bottom of the dredged area to loosen the bottom materials. The sediments along with water are suction lifted and placed onto onboard hoppers. The heavier sediment particles inside the hoppers settle out and remain on the bottom of the hoppers, while the finer fractions remain in suspension within the water column in the hopper. Once the capacity of the on board hoppers is reached water, along with finer material fractions, is discharged back into the watercourse. Decant water discharge is assumed to occur at a rate of 1 m^3/s (3600 m^3/hr), with assumed concentrations of 200, 400 and 1000 mg/L of total suspended solids.

Near-field dispersion and mixing analysis was evaluated for the dredge areas at Upstream Shoal and the Cut-off Channel. Velocities were extracted from the coupled TELEMAC-2D TOMAWAC simulations and used in the near-field calculations. Geometry of a typical THSD was used assuming that the overflow discharge takes place via single outlet pipe submerged 1 m below the water surface.

In order to assess far-field impact of the proposed THSD overflow discharges, the hydrodynamics generated by TELEMAC-2D and TOMAWAC models was used as input into the PSED particle tracking model. Characteristics of the native sediments within the dredge areas are obtained via grain size curves collected during the 2012 sampling program and are used to define properties of both bed and source sediments within the study area. (Source sediments are referred as those that are released into the water column during dredging operations). The PSED model is used to simulate the fate of sediments introduced into the water column, specifically focusing on total suspended solids concentrations away from dredging activities. PSED was also used to identify locations where the source sediment falls out of suspension (or settles on the bottom).

Discharges associated with the THSD overflow operations were simulated in PSED using the same parameters as in the near-field calculations. Far-field simulations were carried for Upstream Shoal and Cut-off Channel dredge area. A range of simulation scenarios were used to assess impact (no wind, light breeze, and storm conditions). Discrete particles were released for a typical 12 hrs dredging operation, while the simulations were carried out for a total of 36 hrs. Longer simulations were required to identify fate of the suspended sediments. For each scenario, averaged path of the plume were extracted, and concentrations at 100, 500, 1000, and 1500 m away from the dredge areas were computed. Depth-averaged total suspended solid concentrations were computed on a 25 m by 25 m grid by counting the number of particles in each cell and dividing it by the cell volume. (Mass of each particle in the simulations was set at 1 kg.) Total suspended solids concentrations at 100 m downstream predicted by the PSED far-field model have been compared with the CDFATE near-field model for consistency.

V. RESULTS

Since the project is currently in the stages of environmental approvals, only qualitative results shall be presented. Velocities and streamtraces established by carrying out the coupled TELEMAC-2D TOMAWAC simulations are shown in Fig. 3 and Fig. 4 for the cases of calm winds and light breeze conditions, respectively. It is evident that wind-induced circulation plays significant roles in establishing velocity for the dredge areas adjacent to the Cut-off Channel. A plot showing significant wave heights generated using light breeze southwest winds is shown in Fig. 5, where it is evident that wave propagation is heavily influenced by strong currents within the limits of the navigation channel.

Currents at the Upstream Shoal dredge area are not affected by wind-driven circulation and wave effects (as they are more than 8 km upstream from the lake), but can be affected by backwater influence. Backwater influence is particularly important during periods of strong winds when seiche effects generate standing waves in the lake. The dredge areas of the lower third of the Cut-off channel are however affected by lake influences, as evidenced by a gyre that is present just south of Seaway Island during southwest conditions. Capturing hydrodynamics of upstream river and downstream lake influences is absolutely necessary for water quality assessments.

Near-field simulations carried out using CDFATE were able to demonstrate that the Upstream Shoal dredge area has a significantly more dilution capacity then downstream dredge areas. Generally high rates of dilution at the Upstream Shoal area results from high river velocities and limited lake influence. The dredge areas in the Cut-off Channel, having lower flow velocities and being under marine influences of the lake have shown lower dilution rates of the released sediment.

Far-field calculations using the PSED particle tracking model were able to validate the near-field results when comparing concentrations of total suspended sediment at a distance 100 m away from the discharge. Having two completely different methods produce nearly identical results only adds to the confidence in the selected methodology. Simulations show that the Upstream Shoal dredge area has a high far-field dilution potential (and relatively low total suspended solids concentrations downstream) since it is located in a zone of relatively high river velocity. The downstream dredge areas are characterized by much lower channel velocities and finer sediment fractions. The interaction between lake circulation, wind generated waves and upstream river flows all play a role in determining suspended sediment concentrations before eventually settling out in the lake. Simulations have shown smaller far-field dilution potential and generally higher total suspended solids concentrations. Higher concentrations were encountered when the plume travels from initially deep waters within the navigation channel to shallower portions of the lake.

VI. CONCLUSIONS

The open source TELEMAC-2D hydrodynamic and TOMAWAC wave modules were applied in a study investigating water quality impacts associated with dredging operations in the lower St. Clair River. The TELEMAC system and its modules were able to seamlessly capture the interaction of both riverine (upstream flows) and marine (wind induced currents, wave generation and propagation)

influences of study area. Hydrodynamics generated by the TELEMAC system were used as input data for the near-field and far-field models to assess water quality impacts associated with dredging operations.

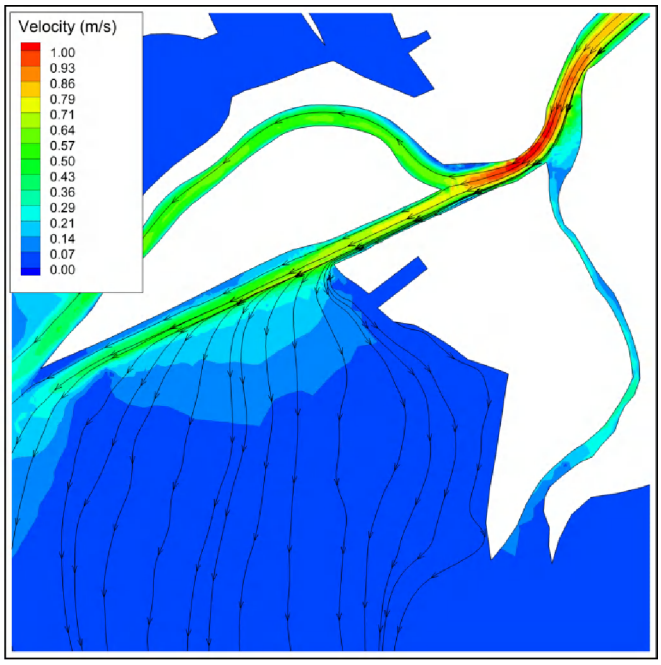

Figure 3. Velocity and streamtraces plot for calm wind conditions

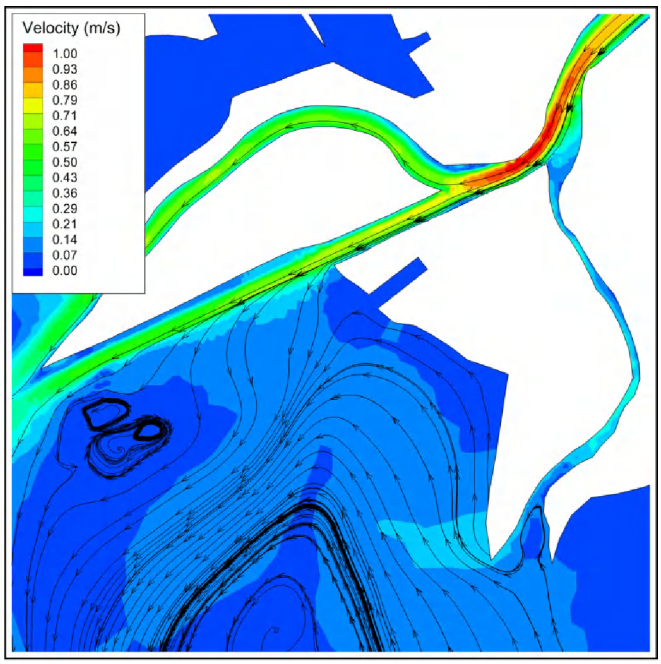

Figure 4. Velocity and streamtraces plot for southwest light breeze conditions

Future applications of the model developed in this work will investigate outcomes from a variety of discharges sources and dredging operations, and will provide valuable information to decision makers that will ultimately ensure the most appropriate dredging and disposal strategies are developed and implemented.

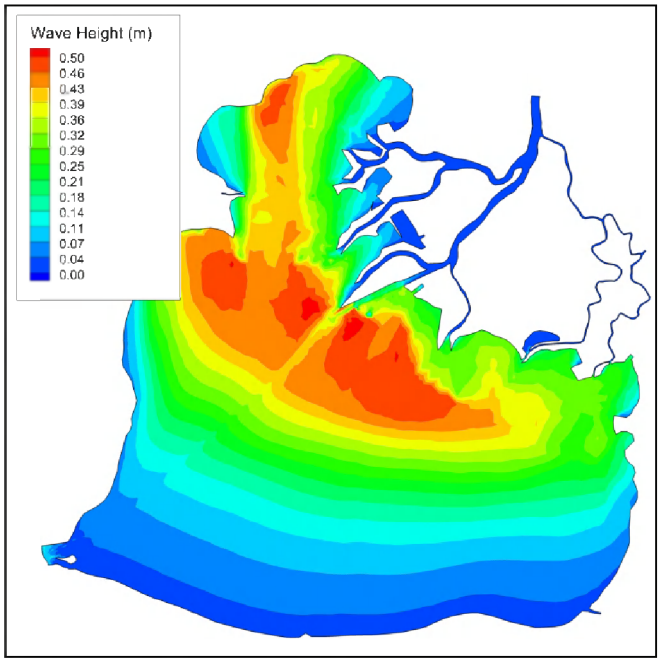

Figure 5. Waves over Lake St. Clair during southwest light breeze conditions

REFERENCES

[1] CCME. Canadian water quality guidelines for the protection of aquatic life: Total particulate matter. In: Canadian environmental quality guidelines, 1999, Canadian Council of Ministers of the Environment, Winnipeg, Manitoba, 2002.

[2] A. Thompson. "Comprehensive encroachment analysis of the Detroit and St. Clair rivers," Final Report, Environment Canada, Burlington, Ontario, July 2000.

[3] D. J. Holtschlag and J. A. Koschik. "A two-dimensional hydrodynamic model of the St. Clair-Detroit River Waterway in the Great Lakes Basin," Water-Resources Investigations Report 01-4236, U.S. Department of the Interior and U.S. Geological Survey, 2002.

[4] E. J. Anderson, D. J. Schwab, and G. A. Lang. "Real-time hydraulic and hydrodynamic model of the St. Clair River, Lake St. Clair, Detroit River System," Journal of Hydraulic Engineering, Vol 136(8), pp. 507-518, 2010.

[5] E. J. Anderson, and D. J. Schwab. "Relationship between wind-driven and hydraulic flow in Lake St. Clair and the St. Clair River delta,", Journal of Great Lakes Research, Vol 37, pp. 147-158, 2011.

[6] CHC. "Hydrodynamic model of the St. Clair River with TELEMAC-2D," Technical report CHC-CTR-084, Canadian Hydraulics Centre, National Research Council, Ottawa, Ontario, March 2009.

[7] N. Hawley and B. M. Lesht. "Sediment resuspension in Lake St. Clair," Limnology and Oceanography, Vol 37(8), pp. 1720-1737, 1992.

[8] F. P. Brissette, I.K. Tsanis and J. Wu. "Directional spectra and wave-current interaction in Lake St. Clair," Journal of Great Lakes Research, Vol 19(3), pp. 553-568, 1993.

[9] D. Chase. "CDFATE User's Manual," Report prepared for the U.S. Army Engineer Waterways Experiment Station, Vicksburg, Mississippi.

[10] Pacific International Engineering. "PSED4.3 A Lagrangian sediment transport model, technical documentation," prepared under contract to Canadian Hydraulics Centre, Ottawa, Ontario, pp. 89, 2006.

TUC 2013, 16-18/10/2013, Karlsruhe - Kopmann, Goll (eds.) - © 2013 Bundesanstalt für Wasserbau ISBN 978-3-939230-07-6

St Egrève reservoir – Multi-dimensional modelling of flushing and evolution of the channel bed

E. Valette[1], C.Villaret[2,3], P. Tassi[2,3], M. Jodeau[2]

[1]Centre d'Ingénierie Hydraulique
Electricité De France
Le Bourget du lac, France

[2]Laboratoire National d'Hydraulique et Environnement
Electricité De France
[3]Laboratory of Hydraulics Saint-Venant
Chatou, France

***Abstract*—Sediment transport and deposition in reservoirs are natural processes. In the French valleys, the filling of reservoirs depends on the production of sediment from the watersheds; it can be large and may be composed of gravel and/or silts. Hydroelectricity operators account for the influence of sediment transport when operating dams, as they need to evaluate the consequences of dam operations on the reservoir morphology.**

The Saint Egrève dam is located downstream of the city of Grenoble, on the Isere river in France. Over time, the reservoir has silted up. Frequent flushing operations allow the maintenance of a channel in the reservoir, but siltation bank formation on either side of the channel is irreversible. Due to the urban location of the reservoir, maintaining the freeboard of the upstream dike of the reservoir during the design flood is a major issue. Nowadays, the evolution of the filling is such that the channel erosion during the flood must be taken into account to estimate a realistic freeboard.

During a first part of the study, 1D morphodynamics simulations were performed by using the MASCARET/COURLIS module. The model was calibrated and validated with measured sediment fluxes corresponding to two flood scenarii and then applied to a project design situation. A second part of the study consisted on performing 2D and 3D numerical simulations using TELEMAC-2D and TELEMAC-3D coupled to SISYPHE, respectively, and comparing results with the 1D model.

I. INTRODUCTION

Sediment transport and deposition in reservoirs are natural processes. Recently, it has been estimated that the worldwide sedimentation in reservoirs corresponds to about one per cent of the whole capacity per year [5]. In specific areas, sedimentation rates can be significantly higher; it may reach more than 70% of reservoir initial capacity [1]. The filling of reservoirs depends on the production of sediment from the watersheds, the hydrology of the watershed, geometry and hydraulics of the reservoir and management of reservoir capacity [4]. The reservoir sedimentation impacts the river reach upstream the dam as much as the downstream reach: storage loss, delta deposition, blocking or clogging of intakes or bottom gates, downstream erosion, ecology, etc. Consequently, one has to take into account sediments when operating dams; therefore we need means to predict the consequences of dam operations on sediment transport and reservoir morphology.

Flushing operations aim at eroding sediments from reservoirs to maintain or to increase their storage capacity and/or prevent flooding upstream the dam. In such operations, the release of sediments to the downstream reach may be significant and should be controlled [2]. There are different ways of predicting the downstream impacts of such operations, often relying on the experience. Nevertheless, numerical modelling can be used as a tool for planification and operation activities. In this work, the flushing of Saint Egrève reservoir is simulated with different modules of the TELEMAC-MASCARET System and comparisons with experimental data are presented and discussed.

II. SITE DESCRIPTION

The St-Egrève reservoir (France) is located in the Grenoble urban area, as shown on Fig. 1, downstream the confluence of the Isère and Drac rivers (9270 km^2 catchment area). The St-Egrève dam is a run-of-river power station, with a maximum turbine discharge of 540 m^3/s. The dam comprises 5 identical openings with overflow flaps, and a 25-meter wide tainted gate with 6 meters of lifting height and a weir at elevation 196.50 m NGF. The normal reservoir level (FSL) during operation is 205.50 m NGF. The capacity of the reservoir in 1992 was 3.86 hm^3. For safety reasons, a security distance of 1 meter with respect to the crest of the reservoir embankment must be guaranteed for a flood of 3000 m^3/s.

Figure 1. Location of the St-Egrève reservoir

The Isère River is highly loaded with fine sediment, and in the St-Egrève reservoir this sediment is deposited. The St-Egrève reservoir shows a sediment accumulation on the left bank that continues to silt up (see Fig. 2). In 2010 its elevation was 204.5 m NGF on average, i.e. one meter below the FSL. If this bar continues to silt up, bank volume will reach 1.45 hm^3. The remaining channel has a variable topography in its cross sections: its minimum area in the absence of flushing can be estimated at 250 m^2, i.e. a volume of about 0.6 hm^3 along 2500 meters. The channel is deepened during floods, and the maximum volume that it can reach is estimated at 2.41 hm^3, as shown on Fig. 3.

Figure 2. St Egrève reservoir during a flushing event.

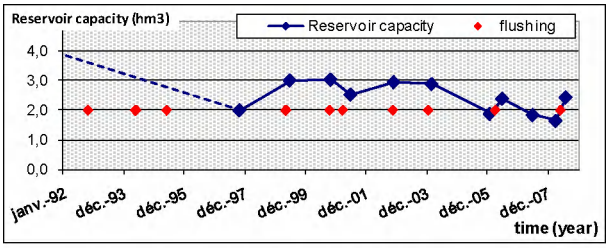

Figure 3. Evolution of the reservoir capacity

III. 1D MORPHODYNAMICS SIMULATIONS

A. *Aim of the study*

The COURLIS software (internally coupled to the 1D hydrodynamics model MASCARET) was used to determine the bottom evolution kinetics during floods. COURLIS computes the bottom evolutions in a channel section as a function of the bed shear distribution in the cross-wise direction of the flow [3]. The objective was to verify that when starting with a high degree of siltation, the erosion at the start of flushing is sufficient to guarantee the preservation of the 1-meter freeboard with respect to the crests of the dikes. In this work, only the calibration and validation of the model are presented.

B. *Available measurements*

Two events were used to calibrate and validate the numerical model: flushing operations performed in May 2008 and May-June 2010. Bathymetries of the reservoir were surveyed before and after each of these events. Turbidity meters placed upstream and downstream of the reservoir enable monitoring of the sediment concentration evolution during a flood and determination of the silt volumes having passed through between the bathymetric measurements and the flushing operations. In addition, sediment samples were taken from the reservoir in September 2010.

C. *Model calibration*

The calibration data corresponds to the May 2008 flushing operation. This flushing operation was preceded and followed by two bathymetric measurements, one in April and one in August 2008. The grid was based on cross-section profiles 100 meters apart derived from the bathymetric data. These profiles were pre-processed to achieve a calculation profile every 50 meters. The chosen Strickler coefficient is taken equal to 45 m$^{1/3}$ s^{-1}.

Model calibration revealed the necessity to model three distinct sediment layers, as shown in Fig. 4. The top layer represents the slightly consolidated sediment (easily remobilised), the second layer the recently deposited sediment (few years), and the third sediment layer the most consolidated. Sediment layers were constructed from the bathymetric data: (i) In 2008, the previous flushing operation dated from April 2006. The layer of old sediment was comprised between the non-erodable bottom measured in the topographic surveys prior to the impounding of the dam and the bathymetry of July 2006; (ii) The layer of recent sediment was represented by the sediment deposited between the bathymetries of July 2006 and April 2008; and (iii) The layer of slightly consolidated sediment was considered equal to the estimated volume of sediment deposited between the date of the bathymetry and the flushing episode, i.e. 150,000 tons. Assuming a dry matter concentration of 1000 g/l, this layer represents a deposit of roughly 70 cm at the bottom of the channel with respect to the April 2008 profile. Besides, the slope stability angle is considered constant and equal to 15°.

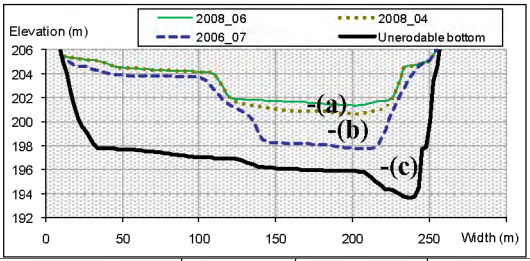

Sediment layers	C (kg/m^3)	τ_{ce} (Pa)	M (kg/s/m^2)
(a) Slightly consolidated	1000	1	0.005
(b) Recent	1100	6	0.06
(c) Old	1100	8	0.02

Figure 4. Sedimentary layer creation

The flushing parameters and the results are summarized on Fig. 5.

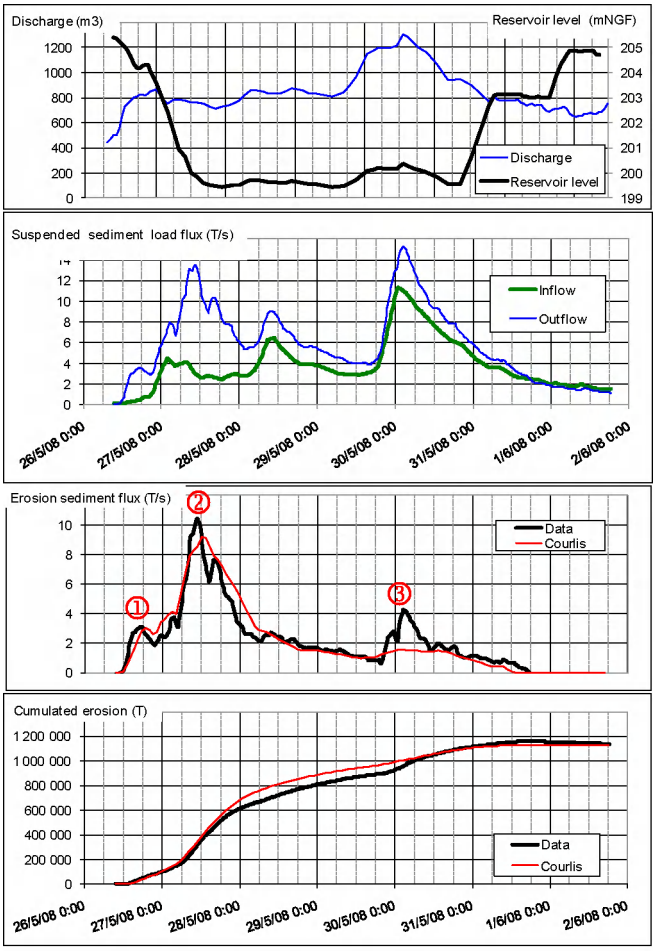

Figure 5. Simulation results of the calibration.

The following phases can be observed:

- During the lowering of the water level (phase 1), we observe an erosion peak due to the slightly consolidated silt①,
- The main erosion peak ② corresponds to the end of the phase 1, when the water level has reached its minimum level. It is well represented by the 1D model although the maximum peak value is slightly underestimated. The increased erosion ③ is due to the passage of the flood peak (phase 3). This third peak is also underestimated. ③

The calculated mass of eroded sediment (1.13 Mt) is in good agreement with the measured mass (1.14 Mt. The evolution of the eroded mass over time can also be well adapted. At the time of the flood peak on May 30 at 1 pm, over a million tons of sediment had already been eroded. A comparison of the profiles measured during August 2008 with the computed profiles yields to satisfactory results, Fig. 6. However, the COURLIS simulation results in the channel are deeper than those measured in bathymetry. This can be attributed to a considerable accumulation of sediment in the reservoir during the period between the end of flushing (end of COURLIS simulation) and the bathymetry date. Indeed, the high flow episode of June 2008 lasted after the flushing, causing solid matter inflows and significant settling in the reservoir of an order of magnitude of 300,000 tons (i.e. 1 meter of sediment deposited on average in the channel over three months).

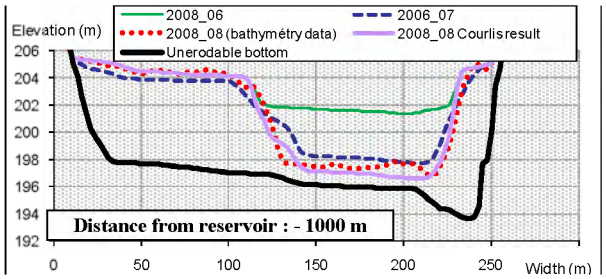

Figure 6. Evolution of the cross-section profiles

D. Model validation

The model was validated with data from the flushing operation of May-June 2010. Two bathymetric surveys preceded and followed this flushing, in April and August 2010, respectively.

The layer construction is based on the calibration values and results, Fig. 7:

- (c) An old sediment layer is comprised between the non-erodable bottom and the result of the 2008 COURLIS calculation.
- (b) A recent sediment layer is comprised between the bottoms produced by the 2008 COURLIS calculation and the bathymetric profiles of April 2010 translated by -30 cm.
- (a) A layer of slightly consolidated material is constructed from the bathymetric profiles of April 2010 and the same one translated by -30 cm in the channel.

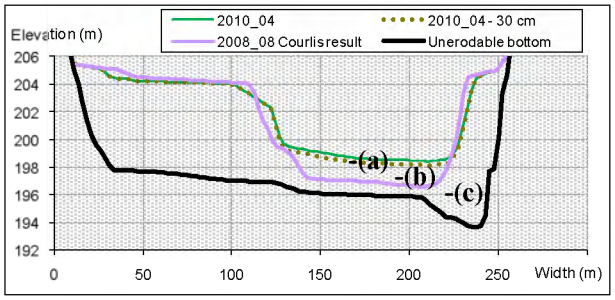

Figure 7. Sediment layer characteristics (see Fig. 4 for values)

The flushing parameters and the results are summarized in Fig. 8. The following points should be highlighted:

- During the phase of the lowering of the water level, we clearly see the erosion peak due to the slightly consolidated sediment.

- The main erosion peak, corresponding here to the passage of the flood peak during the lowering phase, is well represented.
- The flux at the end of the episode is underestimated in comparison with measurements.

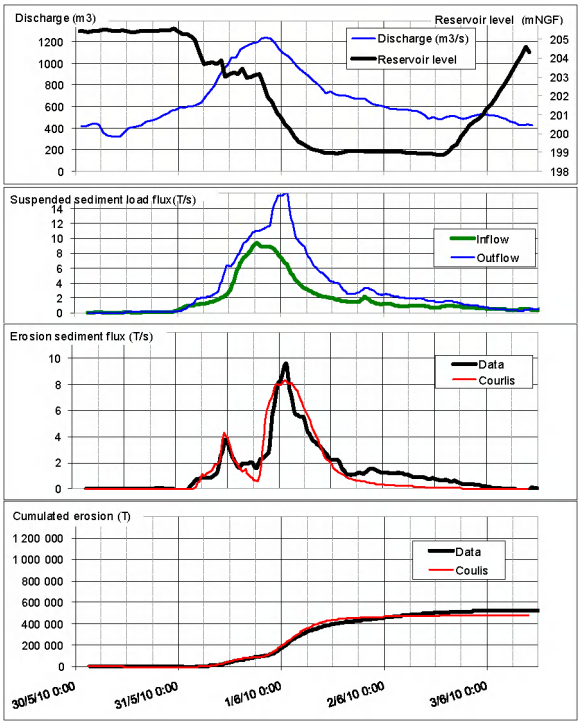

Figure 8. Validation calculation results

The correlation between the calculated mass of eroded sediment (0.48 Mt) and the measured one (0.52 Mt) is satisfactory. The evolution of the eroded mass over time is also well represented (the scale used on this graph during the calibration was maintained). The Analysis of cross-section profiles yields results similar to those presented for the calibration, Fig. 9. The deeper erosion depth obtained by COURLIS can be attributed to a considerable accumulation of sediment in the reservoir during the period between the end of flushing and the bathymetry date (non-simulated period). Indeed, the high flow episode of June 2010 lasted after the flushing, causing solid matter inflows and significant settling in the reservoir of an order of magnitude of 400,000 tons (i.e. 1 to 1.5 meter of sediment deposited on average in the channel over three months).

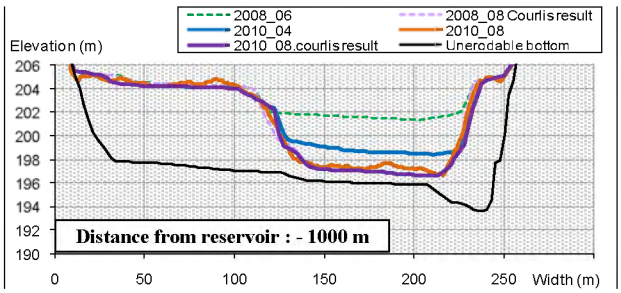

Figure 9. Evolution of the cross-section profiles

E. Influence of parameters: number of layers

The erosion stress, the surface erosion rate and the number of layers are the main parameters of the erosion module and have a strong influence on the results. An illustration of the influence of the number of layers is given in Fig. 10 and Fig. 11. Assuming only one single layer it is impossible to determine correctly the evolution of the erosion for the considered floods. The use of a single stress of 9 Pa, given acceptable results for the flood 2008, leads to an excessively low value for the 2010 flood.

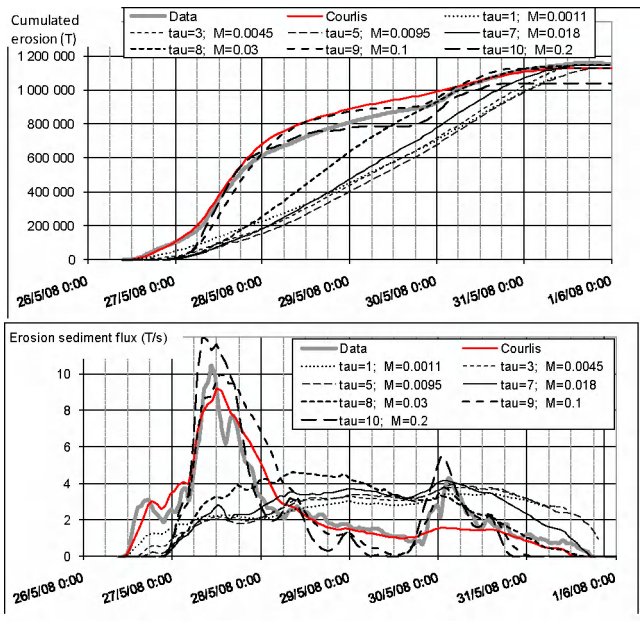

Figure 10. Calibration with a single constant layer of sediment

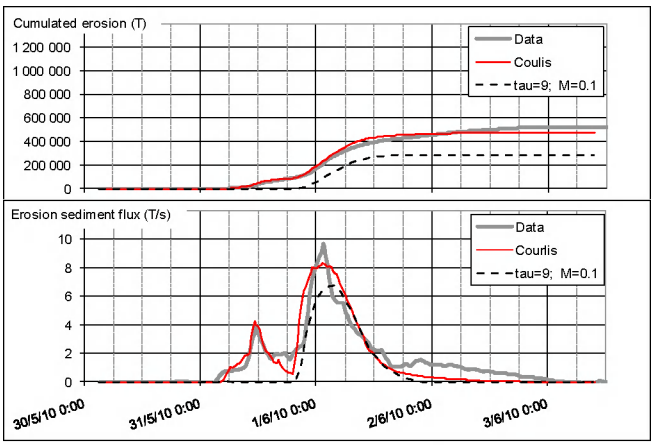

Figure 11. Results for the validation case

IV. 2D/3D MORPHODYNAMICS SIMULATIONS

In complement to 1D simulations, 2D and 3D numerical computations were also performed using (*i*) the 2D hydrodynamic module TELEMAC-2D, internally coupled to the two-dimensional sediment transport module SISYPHE, and (*ii*) the 3D hydrodynamics module TELEMAC-3D, internally coupled to SISYPHE.

Our objective was to compare the different modules of the TELEMAC-MASCARET System in this simple elongated geometrical configuration which is perfectly adapted for 1D simulation, even if the 2D and 3D simulations would give more insight in the detailed structure. In this section, the accuracy of the various models, their adaptability, and required CPU time are studied.

A. Multi-layer model development

In the 1D model (COURLIS), the sediment bed layers have been defined based on historical bathymetries.

In SISYPHE, for 2D and 3D simulations, the bed layers and properties are supposed to be uniform and determined according to the 1D model hypothesis, allowing for some slight variations: the different layers, their initial thicknesses and concentrations, are assumed to be uniformly distributed through the whole domain at the start of the flushing event. The erosion parameter M is also supposed to be constant, while the critical erosion shear stress increases as a function of bed density. SISYPHE model parameters are summarized in Table 1.

TABLE I. SEDIMENTARY LAYER SETUP

Sediment layers	**C (kg/m^3)**	**τ_{ce} (Pa)**	**M (kg/s/m^2)**	**Thickness (m)**
Slightly consolidated	600	2	0.03	0.3 (channel) 0 (bank)
Recent	1000	5	0.03	2.5 (channel) 0.5 (bank)
Old	1100	10	0.03	2->10 (2008) 3->10 (2010)

B. Comparison of model results for the 2008 flood

Both 2D and 3D hydrodynamic models use the same value of the Strickler friction coefficient (52 m$^{1/3}$s^{-1}). Both 2D and 3D models are therefore equivalent and give similar results regarding the main hydrodynamics parameter for sediment transport applications (the bed shear stress): The only difference comes from the directions: in 2D, the bed shear stress is supposed to be aligned with the mean flow direction, whereas in 3D, the bed shear stress is aligned with the near bed flow. Fig. 12 shows the comparison between all model results and the data for the net eroded sediment fluxes. All models give globally similar results and successfully reproduce the two first peaks (1, 2), but underestimate the third one corresponding to the flood peak.

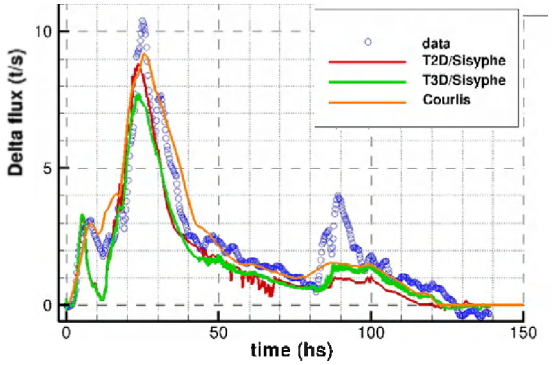

Figure 12. Total sediment flux (2008)

Fig. 13 shows a plan view of the bed elevation, at the end of the flushing event, in 2D (13.b) and 3D (13.c) which are compared with the differential bathymetry (Fig. 13.a). As can be observed, the bed erosion should be overestimated in both 2D and 3D simulations. Similar results were also obtained in the 1D model. However, this discrepancy could be attributed to an accumulation of sediment in the reservoir during the period between the end of flushing and the date of the bathymetry (non-simulated period): 1 meter of sediment deposited on average in the channel in 2008, 1 to 1.5 meter in 2010.

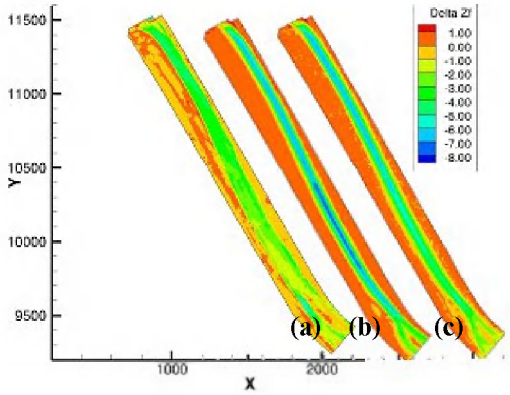

Figure 13. (a) Measurements – Δz 04/2008 – 08-2008; (b) 2D results; (c) 3D results

C. Comparison of model results for 2010

After the calibration step model parameters (bed friction, as well as the number of layers and their characteristics) are fixed for the validation step. All models are able to reproduce the observed net sediment fluxes, as shown in Fig. 14. Fig. 15 shows the bathymetric evolution, obtained by the 2D (Fig. 15b) and 3D models (Fig. 15c) in comparison with the data (left hand side). Despite the good agreement when comparing with observations, all models tend to overestimate the bed evolution (Cf. § III D).

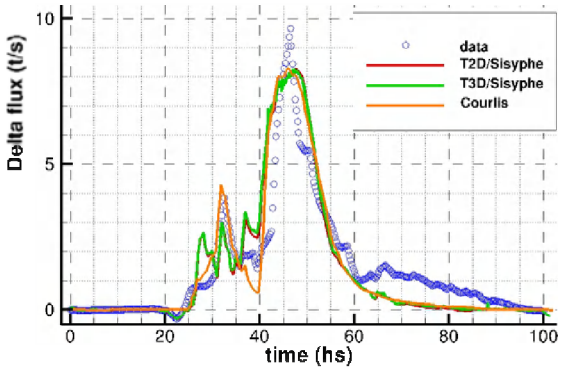

Figure 14. Total sediment flux (2010)

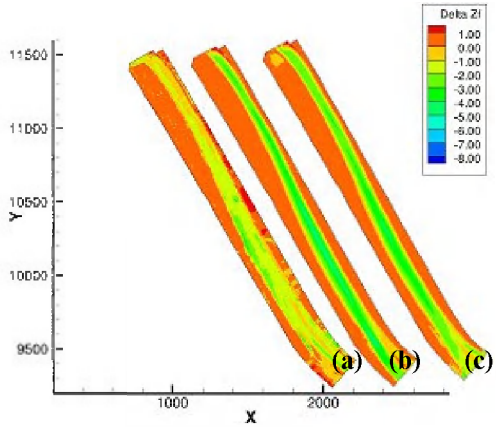

Figure 15. (a) Measurements – Δz 06/2010 – 08-2010; (b) 2D results; (c) 3D results

V. COMPARISON OF 1D, 2D AND 3D MODEL RESULTS

A. Discussion

After proper calibration to define the bed structure (number of bed layers and sediment characteristics), model results for the 2008 event as well as for the 2010 flushing event, show that all three modules (1D, 2D and 3D) were able to predict accurately the amount of sediment which is flushed out during a typical flushing event. All the modules may be used conveniently as operational tools to monitor the efficiency of flushing events.

This simple geometrical configuration does not necessitate the use of a complex 2D or 3D models, and the 1D model assumption is perfectly adapted to represent this type of event. In addition the 2D and 3D model give more insight in the flow structure and access to a detailed plan view of the model results (bed evolution, bed shear stress distribution…). On the other hand, the 1D tool can be viewed as a handier tool for the initialization of the bed layers based on historical bathymetry.

B. Comparison of CPU time

To compare CPU time, the number of processors, as well as compiler type, need to be specified. All 1D, 2D and 3D simulations have been run on Linux station Z600 (compiler intel 64b). Both 2D and 3D models were run in parallel using 8 processors. The use of parallel computing allows performing 2D simulations for a computational time comparable with the time required to run the 1D model, whereas the 3D model (5 vertical planes) showed to be more expensive.

TABLE II. COMPARISON OF CPU TIME

	1D (1 Proc)	**2D (8 Proc)**	**3D (8 Proc)**
Number of mesh Dx Dt	300 Variable	2-10 m 10s	5 layers 0.5 s
2008 Flushing 6 days 9 h	10 mn	12 mn	3 h 44 mn
2010 flushing 4 days 6 h	6 mn	7 mn	1.5 h

VI. CONCLUSION

Three hydrodynamic and sediment transport models of the TELEMAC-MASCARET System, namely COURLIS/ MASCARET (1D) and SISYPHE coupled to TELEMAC-2D and -3D, have been applied to simulate the effect of a flushing event. After proper calibration of the various sediment parameters and bed structure, all models could successfully reproduce the amount of sediment eroded and therefore could be used as operational tools to predict the efficiency of flushing event.

The computational domain presented an elongated, unidirectional geometrical configuration, which is particularly well adapted for a 1D application and, therefore, allowed a fair comparison with the 2D and 3D models. We emphasize that the choice of the spatial dimension to which apply the different models depends mainly on the scale of the problem (time and space) and the degree of detail of application. For more complex configurations than the one presented here, 1D models can be used to simulate the entire reach, providing then the boundary conditions for more detailed 2D or 3D analysis in important subreaches.

Future work will include the implementation, verification and validation of the fully 3D cohesive sediment transport processes within TELEMAC-3D.

REFERENCES

[1] Bouchard, J.-P. & Bertier, C. Morphological change in reservoirs in relation to hydraulic conditions. River Flow, 2008.

[2] Brandt, S. Classification of geomorphological effects downstream of dams. Catena, 2000, 40, 375-401.

[3] Marot D., Bouchard J.-P. and Alexis A. Reservoir bank deformation modeling: application to Grangent reservoir. J. Hydr. Eng., 2005, Vol. 131, (7).

[4] Morris, G. L. & Fan, J. Reservoir sedimentation handbook. McGraw-Hill, 1997.

[5] Mahmood, K. Reservoir sedimentation: impact, extent, and mitigation. Technical paper. International Bank for Reconstruction and Development, Washington DC, USA, 1987.

TUC 2013, 16-18/10/2013, Karlsruhe - Kopmann, Goll (eds.) - © 2013 Bundesanstalt für Wasserbau ISBN 978-3-939230-07-6

1D sediment transport modeling for a sustainable sediment management: Two Case Studies of Reservoir Flushing

P. Durand, M. Jodeau, A.-L. Besnier, E. Delahaye
EDF R&D – LNHE (National Laboratory for Hydraulics and Environment), Chatou, France
{pauline.durand; magali.jodeau; anne-laure.besnier; eve.delahaye}@edf.fr

***Abstract*—COURLIS [1] is a one dimensional sediment transport numerical code developed by EDF-R&D-LNHE in association with CETMEF. COURLIS is based on a coupling between the hydraulic open-source software MASCARET [2] (part of TELEMAC-MASCARET system) and a sediment module which handles sediment processes for sand and silt. This numerical tool is used to predict the effects of dam operations as emptying or flushing. In this work, the capability of the code is illustrated with two examples of reservoir flushing, which concern the Saint-Martin-La-Porte Reservoir in the Alps and the Plan d'Arem Reservoir in the Pyrenees.**

I. COURLIS NUMERICAL CODE

Among the different options for modeling flow and sediment transport in reservoir, one dimensional modeling is well adapted if one is not trying to explain and reproduce patterns in deep areas, or around confluences and bifurcations. One dimensional modeling is well suited if long term simulations are expected, and if cross section average values are looked for. Besides, in longitudinal configurations, one dimensional modeling performs as well as 2D modeling as shown by the example of St-Egrève Reservoir modeling [3].

COURLIS numerical code allows the calculation of the sediment transport of mud and sand in open channels under unsteady flow conditions. The outputs of the model are the sediment concentrations throughout the waterway and the changes in the river bed bathymetry due to sediment transport, erosion and deposition.

COURLIS numerical code has already been used to define efficient sediment management for various French reservoirs: the Genissiat Reservoir [1], the Grangent Reservoir [4], the flushing of Saint-Egreve Reservoir in the Alps [5], and the empying of Tolla Reservoir in Corsica [6]. When data were available [4] and [5], the comparison between calculations and measurement showed very good agreement.

A. Cross section view

Despite a one dimensional computation for the flow, the sediment bed is described by a bi-dimensional approach, that is to say sediment layers are defined transversally to the flow axis and bed elevation is computed in 2D, see Fig. 1.

Each sediment layer is characterized by its thickness, its concentration (C_{layer}), its percentages of sand and silt, sand grain size and cohesive sediment characteristics.

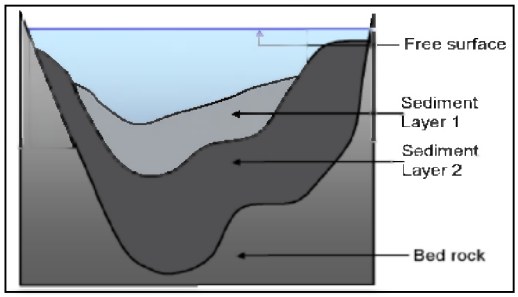

Figure 1. Sedimentary layers for modeling

B. Equations

COURLIS is based on an internal-coupling between the component MASCARET [2], part of the TELEMAC-MASCARET system, which solves the 1D shallow water equations and the sediment module which handles sediment processes. Both hydraulic and sediment components could be coupled at each time step, i.e. the hydraulic variables are calculated for a fixed bed, then the sediment transport and the bed evolution are calculated.

For both type of sediments, sand and silt, an advection-dispersion is solved:

$$\frac{\partial AC}{\partial t} + \frac{\partial QC}{\partial x} = \frac{\partial}{\partial x}\left(kA\frac{\partial C}{\partial x}\right) + E - D \qquad (1)$$

where A is the cross sectional flow area, C the suspended concentration, Q the flow rate, k the dispersion coefficient, E and D are respectively the Erosion and Deposition linear rates.

Erosion and deposition for sand and cohesive sediment are dealt separately:

- For cohesive sediments, Partheniades [7] and Krone [8] empirical formulae are used:

$$E = M\left(\frac{\tau}{\tau_{CE}} - 1\right) \quad (2)$$

$$D = w_s C\left(1 - \frac{\tau}{\tau_{CD}}\right) \quad (3)$$

where M is the erosion rate coefficient, w_s is the settling velocity, τ_{CD} and τ_{CE} are respectively the deposition and the erosion critical shear stresses.

The local shear stress is written:

$$\tau = \frac{\rho g h u^2}{K_s^2 R_h^{4/3}} \quad (4)$$

where g is the gravity, h the local water depth (variable in the section), u the mean velocity, K_s the Strickler coefficient, R_h the hydraulic radius, and ρ the fluid density.

- For sand, the transport capacity is calculated with the Engelund and Hansen [9] formula:

$$q_s = 0.05\sqrt{\frac{\delta d^3}{g}}\frac{K^2 R_h^{1/3}\tau_{eff}}{(\rho_s - \rho)gd} \text{ where } \tau_{eff} = \tau\left(\frac{K}{K_p}\right)^{3/2} \quad (5)$$

where K_p is the grain friction coefficient, ρ the fluid density and ρ_s the sediment density, d the particle median diameter, and $\delta = \frac{\rho_s - \rho}{\rho}$.

The equilibrium concentration, C_{eq}, is written:

$$C_{eq} = \frac{\rho_s q_s}{Q} \quad (6)$$

The erosion and deposition rates are calculated depending on:

$$\begin{cases} \text{if } C_{sand} \geq C_{eq} \text{ deposition} & D = w_s\left(C_{sand} - C_{eq}\right) \\ \text{if } C_{sand} \leq C_{eq} \text{ erosion} & E = w_s\left(C_{eq} - C_{sand}\right) \end{cases} \quad (7)$$

For both cohesive sediments and sand, the bed evolution is then expressed depending on the erosion and deposition rates:

$$\frac{\partial Zb}{\partial t} = \frac{D}{C_{deposition}} - \frac{E}{C_{layer}} \quad (8)$$

The bank failure is taken into account using a simple model, the bank slope is compared to a stability slope (submerged or emerged). If the critical slope is exceeded, sediment deposit is supposed to collapse immediately and is spread along the section. A more complex model based on soil mechanics is also implemented [4].

II. ST-MARTIN-LA-PORTE

A. Introduction

The Saint-Martin-la-Porte Reservoir, on the Arc River, with a storage capacity of 68 000 m^3, is one of the many reservoirs on the river. Besides, it limits the suspended particles entering the downstream Longefan, Flumet and Cheylas Reservoirs, all managed by EDF.

A long term study for a more sustainable management of the reservoir is on-going to optimize the flushing scenarios and frequency and to assess the optimal geometry of the reservoir for an adequate decantation rate.

A 1D model of the Saint-Martin-la Porte Reservoir was built to optimize the sediment management.

B. Modeling reservoir flushing

The structure of the 1D model is described by three sedimentary layers, which are depicted in Fig. 2.

The model was calibrated on the last flushing event of June 2012, with a lot of site measurements: bathymetries (before and after flushing event), sediment concentration (inflow and outflow) measured during the event, and a large scale scanner surveying of the water level during the event.

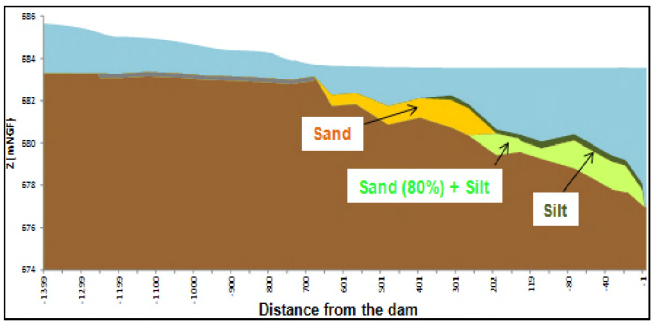

Figure 2. Sedimentary layers for modeling Saint-Martin-la-Porte Reservoir

Despite the few direct measurements of the sediment characteristics, and the torrential flow observed during the flushing event (high speed flow leading to high constraint on sand layer, which in turn results on fast changes of the bathymetry), the comparison of the model results with the measurements shows that the model reproduces well the erosive behaviours of the reservoir during flushing events. Indeed the suspended sediment concentrations calculated by the model downstream of the dam are closed to the measured concentrations, see Fig. 3.

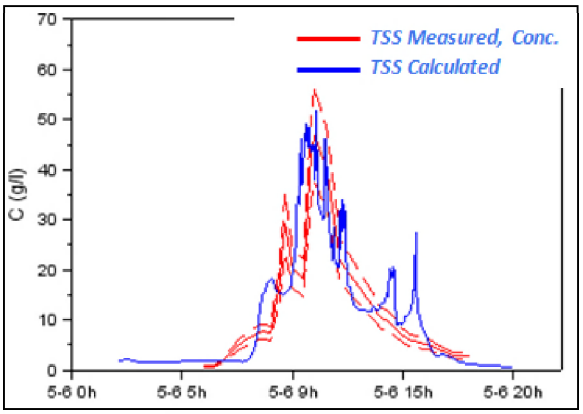

(a)

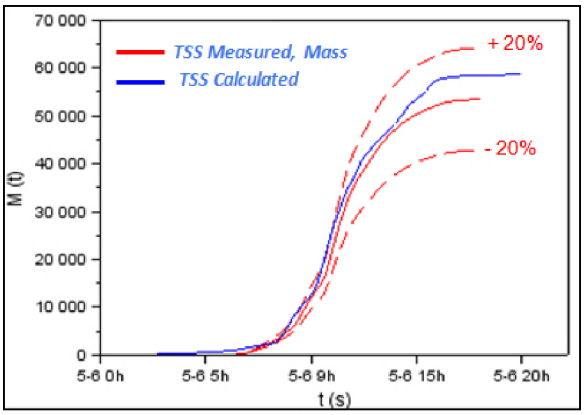

(b)

Figure 3. (a) concentrations, (b) cumulated mass transferred

Further work will include testing different flushing scenarii (intensity and duration) and studying the decantation processes.

III. PLAN D'AREM

A. Introduction

The Plan d'Arem Reservoir was completed in 1970 with a total storage capacity of 500 000 m^3. It is the first upstream dam located past the Spanish/French border on the Garonne River and managed by EDF. The Plan d'Arem Reservoir has high sedimentation rates which lead to continued capacity reduction.

A dredging project is planned for 2014. It would be followed by annual hydraulic flushing events to maintain the reservoir at the best operating capacity. Flushing operations have to be controlled to limit environmental impact, i.e. the release of sediments to the downstream reach.

The Plan d'Arem 1D model shows how numerical modeling can be used to assess the sediment release and to define an optimal flushing scenario.

B. Modeling reservoir flushing

The Plan d'Arem Reservoir is characterized by a sedimentation of both sand and mud. In the 1D model, based on field data, two sedimentary layers are therefore distinguished: one layer of sand in the upstream area, and one layer of silt in the downstream area, see Fig. 4.

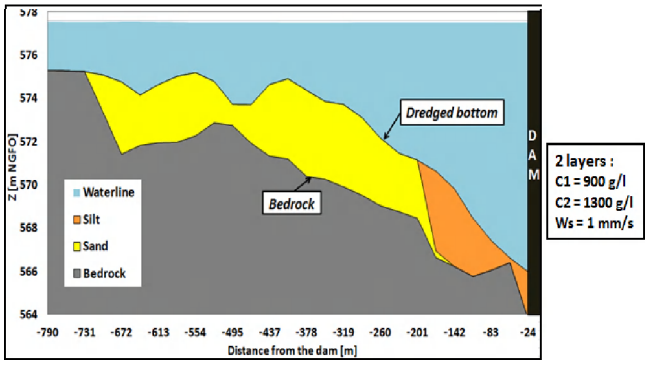

Figure 4. Sedimentary layers for modeling

C. Flushing scenario

Hydraulic flushing events have two goals: to maintain the dredged state, and to limit environmental impact.

Downstream impact is mainly about water quality degradation, and in our specific area, the impact on troutlet mortality, starting to be observed when the sediment concentration reaches 10 g/l, after 24 hours of exposure.

A reference scenario was defined by the dam operator during the establishment of the dredging project. We compare it to another scenario with a level lowering rate in the reservoir two times slower. The downstream maximum reached sediment concentration is then reduced from 6.6 g/l to 2.8 g/l, see Fig. 5.

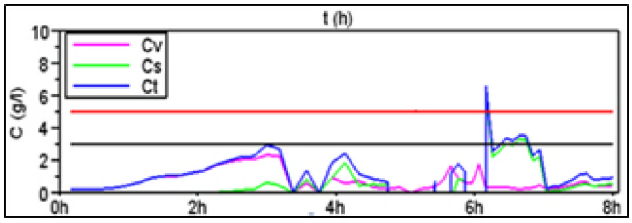

(a)

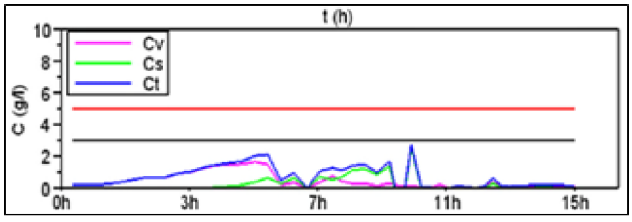

(b)

Figure 5. Output concentrations: (a) reference scenario, (b) with halving speed of level lowering.
Cv: silt concentration, Cs: sand concentration, Ct: total concentration

Future work will imply an inter-comparison between the 1D and 2D models of Plan d'Arem and the development of the bank erosion module to consolidate the results.

IV. CONCLUSION

Both cases show how COURLIS is a useful tool for reservoir management, as it reproduces well the erosive processes observed during a flushing event and is able to assess the sediment release to the downstream reach. COURLIS can therefore be used to define an optimal flushing scenario and to predict scenarios (by means of calibration) as illustrated in the second case.

REFERENCES

[1] C.Bertier, J.-P. Bouchard, & L. Dumond, "One dimensional model for reservoir sedimentation management". River Flow Conference, 2002.

[2] N. Goutal & F. Maurel, "A finite volume solver for 1D shallow-water equations applied to an actual river". Int. J. Numer. Meth. Fluids, 2002.

[3] E. Valette, C. Villaret, P Tassi & M. Jodeau, '' St Egrève reservoir – Multi-dimensional modelling of flushing and evolution of the channel bed" 2013 TELEMAC MASCARET User Club.

[4] D. Marot, J.-P. Bouchard & A. Alexis, "Reservoir bank deformation modeling: application to Grangent reservoir". Journal of Hydraulic Engineering, 2005.

[5] E. Valette, & M. Jodeau, "How to predict the sedimentological impacts of reservoir operations?" ICSE, 2012.

[6] M. Jodeau & S. Menu, "Sediment transport modeling of a reservoir drawdown, example of Tolla reservoir". River Flow Conference, 2012.

[7] Partheniades, E., 1965 - Erosion and Deposition of Cohesive Soils. Journal of the Hydraulics Division, Proceedings of the ASCE, vol 91, N°HY1, pp. 105-139.

[8] Krone, R. B., 1962 - Flume studies of the transport of sediment in estuarial shoaling processes, Technical Report, Hydraulic Engineering Laboratory, University of California, Berkeley.

[9] Engelund, F. and E. Hansen, 1967. A monograph on sediment transport in alluvial streams. Technical University of Denmark.

TUC 2013, 16-18/10/2013, Karlsruhe - Kopmann, Goll (eds.) - © 2013 Bundesanstalt für Wasserbau ISBN 978-3-939230-07-6

A 2Dh hydrodynamic model of the Scheldt estuary in 1955 to assess the ecological past of the estuary

S. Smolders, P. Meire, S. Temmerman
Ecosystem Management Research Group
University of Antwerp (UA)
Antwerp, Belgium
svensmolders@gmail.com

F. Cozzoli
Spatial Ecology
Netherlands Institute of Sea Research (NIOZ)
Yerseke, The Netherlands

S. Ides
Antwerp Port Authority
Antwerp, Belgium

Y. Plancke
Flanders Hydraulics Research (FHR)
Antwerp, Belgium

***Abstract*—The macrozoöbenthos model of Cozzoli et al. [1] uses maximum flow velocity, inundation time, daily averaged salinity and daily salinity range to assess habitat suitability. A 2Dh hydrodynamic TELEMAC model of the Scheldt Estuary with a bathymetry of 1955 was built and calibrated for water levels. The hydrodynamic parameters and the tracer values for salinity are used as input for the macrozoöbenthos model to assess the ecological situation of the estuary in 1955. This paper discusses mainly the difficulties of retrieving the right boundary conditions and parameter settings for this model. The mesh resolution influences model parameters like tracer diffusivity and velocity diffusivity so they can't be taken from a different calibrated model.**

I. INTRODUCTION

Estuaries worldwide form the transition zone between sea/ocean and the inland rivers; between fresh and salt water. This transition zone knows a unique ecological richness typical for estuaries [2]. Due to human pressure: expanding economical activities, cities and ports, this unique ecological niche has to be protected. Most parts of the Scheldt Estuary in the Netherlands and Belgium are protected as Natura 2000 area. Structural changes to these areas can only be done if the ecology is not harmed or is even benefitting. It is however very difficult to assess the impact of future changes on the ecology. Ecotope maps and habitat maps are made for the ecological evaluation of the system. The creation of such maps is a time consuming task, since a lot of parameters are necessary to create them: depth maps, soil composition, wave action, current velocity, geomorphology, salt and possibly nutrients. For some of these data field samples have to be taken. This method of evaluation has proven its value, but is not useful for scenario analysis, where quick results are needed for the assessment of different possible future scenarios.

Cozzoli et al. [1] developed a model to predict the habitat suitability for macrozoöbenthos. This model uses only four parameters: maximum flow velocity, inundation time, daily averaged salinity and daily salinity range. These parameters are easily available from a hydrodynamic model. This benthos model is an ideal tool for the assessment of ecological changes caused by morphological changes. The macrozoöbenthos fauna is the trophic level between basic nutrients, algae and higher trophic levels like birds and fish. Different morphological scenarios can be simulated using only a 2Dh hydrodynamic model to generate the four parameters necessary for the benthos model. For every point in a models mesh the habitat suitability for macrozoöbenthos species can be predicted and this for different scenarios. In this way maps can be created which can be compared with a reference map. With the help of some guidelines from an ecologist, for example that the total biomass needs to increase in a certain area or a specific species is needed more in another area; a modeler can apply and assess the changes in benthos habitat suitability within minutes.

In the same way that we can assess the changes in benthic habitat suitability for future scenarios, we can assess the changes for a model with the bathymetry and boundary conditions of some past period. Comparing it with the current situation will give new insight in the ecological development of the estuary. In this paper we discuss the building of a model of the Scheldt Estuary with the bathymetry of 1955 and the problems encountered doing this: model boundary conditions and the value for the tracer diffusivity (no measurements available). Model simulation results will be used as input for the macrozoöbenthos model.

II. 2DH TELEMAC MODEL OF SCHELDT ESTUARY IN 1955

A. Scheldt Estuary

The Scheldt Estuary extends from Vlissingen, The Netherlands (km 0) to Ghent, Belgium (km 160). At Merelbeke and Gentbrugge (Ghent area) weirs prevent the tide from penetrating more upstream. The tidal influence reaches to major tributaries (they are included in the model, Fig. 1). Discharges of the Scheldt and tributaries are negligible compared to the tidal volume. The estuary is well

mixed, which means that vertical salinity gradients are small or negligible [3]. Tide gauge measurement stations are numerous but only the ones used for calibration of water level data are given in Fig. 1: Cadzand, Westkapelle, Vlissingen, Terneuzen, Hansweert, Antwerpen, Hemiksem, Temse, Sint-Amands, Dendermonde, Boom, Walem, Duffel. In 1955 the average tidal range at the mouth was 3.82 m NAP (Normaal Amsterdams Peil ~ mean sea level) and at Antwerpen it was 4.86 m NAP.

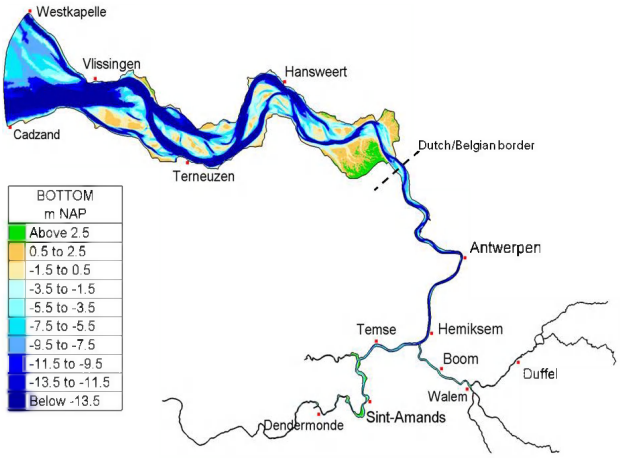

Figure 1. Area and bathymetry of Scheldt Estuary model in 1955. Red dots indicate tide gauge measurement stations used for calibration of the model.

B. Mesh

A new mesh was built for this model using Blue Kenue. The outline was taken from another TELEMAC model of the Scheldt Estuary. It was adapted to use for the 1955 model based on the bathymetry data sets that were available. Upstream Hemiksem (Fig. 1) the mesh of the 2009 model was reused. This area is of less interest for the research and was created with the channel mesher, as the flow direction is pseudo 1D and to save on calculation nodes. Downstream Hemiksem a mesh resolution of 40m was used to have a very high resolution for the benthos model. In the mouth area a mesh resolution of 300m was used quickly decreasing (Edge growth ratio 1.08) towards the 40m resolution just downstream from Vlissingen (Fig. 1).

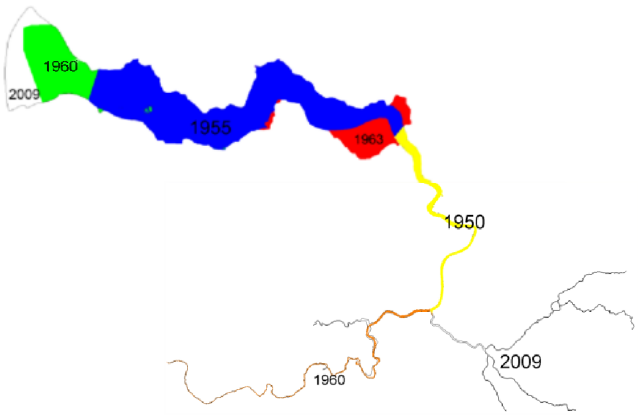

Figure 2. Indication of which bathymetry data of which year is used in what part of the model.

C. Bathymetry

Fig. 2 shows a map of the model with different colours. Each colour represents a different year of which the bathymetry data was used for the model. The mouth area consists of bathymetry of 1960. The main part of the Western Scheldt (Fig. 2, blue colour) consists of bathymetrical data from 1955; it is the area of interest for our research. For the larger marsh areas (Fig. 2, red colour) data from 1963 were used. The Sea Scheldt, downstream Hemiksem, (Fig. 2, yellow colour) consists of a bathymetry from 1950. The Sea Scheldt, upstream Hemiksem, (Fig. 2, brown colour) consists of a bathymetry from 1960. The bathymetry data of the tributaries (Fig. 2, grey colour) was kept the same as in the 2009 model. The resolution of the grid in this part of the model is too large for an accurate bathymetrical representation. Water movement in this upstream part of the model was adjusted using the bottom friction coefficient.

D. Boundary conditions

The downstream boundary condition is a free surface boundary with the water level time series that was recreated for this model. The upstream boundaries are discharges. There are six upstream discharge boundaries.

1) Water level at estuary mouth

No continuous water level measurements of 1955 are available. For the model we need a time series of water levels for 1955 or close to this date with a ten minute interval for Cadzand to implement as boundary on the model. A three hour interval time series of water levels for Vlissingen for 1954 was available together with all low and high water levels. With this information a boundary condition time series with a 10 minute interval could be made following the next steps:

a) Harmonic analysis of the three hour interval time series of Vlissingen for 1954 was executed in Matlab using t_tide [4]. Only the tidal constituents that had a sound to noise ratio higher than 5 were used in the following steps. An offset of -0.056m compared to the 0m NAP level was found in the harmonic analysis.

b) With the found harmonic components a new complete, ten minute interval, time series of the water level of Vlissingen was created using t_predict in Matlab [4], i.e. an astronomical time series.

c) A correction for the offset was made to the astronomical time series by adding +0.056m.

d) For the whole of 1954 the difference between high water level measured and the high water level calculated, i.e. the astronomical tide, was taken. The same was done for the low water levels. These differences were averaged over a 14 day period, i.e. a neap spring tidal cycle, with calculation of the RMSE. We want to find a 14 day period in 1954 were the difference between measured and reconstructed tide is the smallest. The calculation time window was moved with an interval of one week. For one year 49 average differences were calculated. The period from 26th of October till the 8th of November (week 42) showed the smallest average difference

(0,28m). The RMSE values per week of 1954 are given in Fig. 3.

e) The difference between the astronomical tide time series and the measured high and low water levels is caused by meteorological influences. The astronomical time series is corrected based on the measured values and this is done per high or low water separately. For a certain high water (HW) all points in the time series of that tide, higher than 0m NAP, are multiplied with the following factor: (HW measured/HW astronomical). This is done for every single high and low water in the selected spring neap tidal cycle.

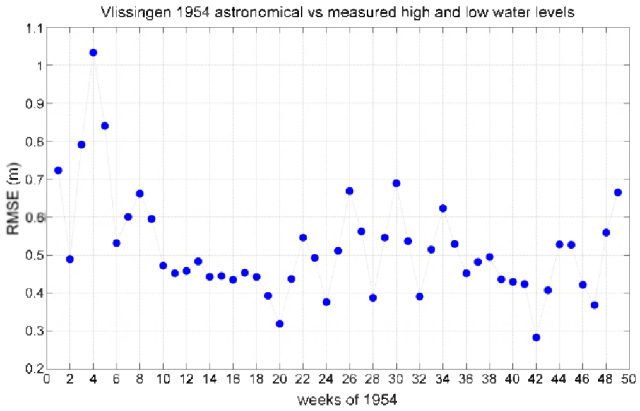

Figure 3. RMSE values for 2 week interval average differences between measured and reconstructed astronomical tide of 1954.

f) If the difference in phase of high or low water between measured and astronomical tide is larger than 10 minutes, the phase is corrected for the particulate high or low water. The time interval will stay at 10 minutes, so if a correction is made, one or more points are removed or added to the same tide. All points (water level every 10 minutes) in between the high and low water, that have the phase difference, need to be corrected and were resampled. The result is a perfectly reconstructed time series of the water levels in Vlissingen in 1954 (Fig. 4).

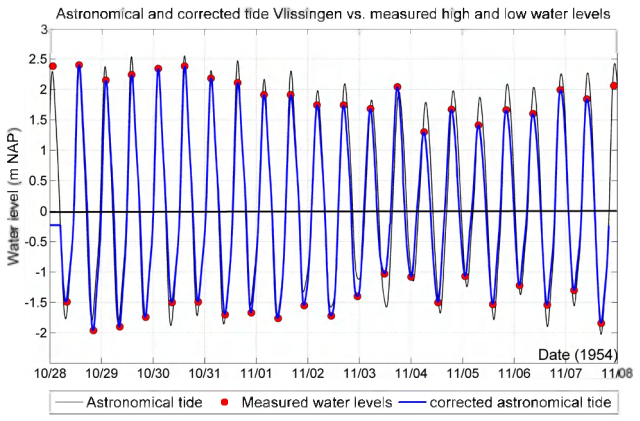

Figure 4. Astronomical tide compared with measured high and low water levels and the corrected tide for water level and phase.

g) For the model boundary we need this time series for Cadzand and not for Vlissingen. So an extra correction has to be made for the water level and phase. A QQplot was made for the water levels at Vlissingen and Cadzand. For 1954 the water level of Cadzand is on average 0.03m higher than the water level of Vlissingen. Applied only on the used spring neap tidal cycle the difference was only 0.005m. So 0.005m was added to the time series of Vlissingen. The same was done for the phase and high water occurred 34 minutes earlier in Cadzand compared to Vlissingen in 1954. The same was done for Westkapelle. The final boundary condition time series was found by taking the average of the Cadzand and Westkapelle time series and add 0.04m to it.

2) Discharges upstream boundaries

The discharges in the Scheldt Estuary didn't change much over the last 60 years. There is a seasonal variation and big influence of individual rain events. No daily averaged discharge data were available for the simulation period October-November 1954, therefore an average discharge per boundary was calculated taking the daily averaged discharges of October and November of the last ten years into account. These values were used as fixed continuous discharge values for the upstream freshwater discharge boundary conditions. For the Scheldt River, Dender, Zenne, Dijle, Grote Nete and Kleine Nete these values are respectively 28m³/s, 8m³/s, 10m³/s, 18m³/s, 4m³/s and 5m³/s.

III. CALIBRATION

The model was calibrated using a Manning bottom friction coefficient for areas in between tide gauge measurement stations. No measurements of flow velocities or discharges were available for 1954. High and low water levels and their time of occurrence were available for Vlissingen, Terneuzen, Hansweert, Antwerpen, Hemiksem, Temse, Sint-Amands, Dendermonde, Boom, Walem and Duffel (Fig. 1). Per station measured high and low water levels are compared with the simulated ones. Changing the bottom friction coefficient between two stations will affect the water levels. A cost function is used to evaluate the calibration effort of a simulation. Since only the part of the model downstream Antwerpen is of major interest, these stations are given a higher weight factor (δ) then the ones upstream Antwerpen. The total sum of all weight factors should be equal to one, as shown in (1). The stations Vlissingen, Terneuzen, Hansweert and Antwerp were given four times the weight of the station more upstream and Hemiksem was given twice the weight of the stations upstream. For the calibration 16 high and 16 low water levels were compared. An average difference (D_{avg}) in water level (WL) was calculated per station for these high and low water levels (n = # high or low water levels used for calibration) separately as shown in (2).

$$\sum_{i=1}^{m} \delta_i = 1 \qquad (1)$$

$$D_{avg}(WL) = \frac{\sum_{j=1}^{n}(WL_{meas.}(j) - WL_{model}(j))}{n} \qquad (2)$$

Finally the cost function summarizes all stations with their own weight factor, as shown in (3). The cost function gives a value for high and low water separately and for their phase

$$Cost = \sum_{i=1}^{m} \delta_i * D_{avg}(WL)_i \quad (3)$$

To start the first calibration simulation the Manning coefficients of a 2009 model were used in a simplified form. In total five calibration steps were simulated of which the fourth one gave the best results. The cost function for high and low water levels together gave a weighted average difference of 0.05m for the first simulation. The cost function for the Root-Mean-Square-Error (RMSE) on these water level differences gave 0.14m. For the phase the cost functions weighted average delay was 18 minutes with RMSE of 21 minutes. These results improved and the fourth simulation gave a cost function weighted average on the water levels of 0.05m, the same result as the first simulation, but the RMSE dropped to 0.08m. The cost function value for the phase improved to 11 minutes with a RMSE of 14 minutes. The final Manning coefficient values used in the fourth simulation are shown in Fig. 5.

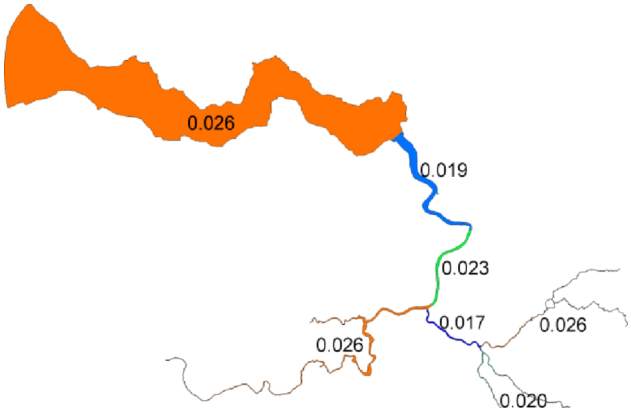

Figure 5. Manning coefficients for the best calibration result.

Although several tide gauge measurement stations are present in the downstream part of the estuary (orange part in Fig. 5), one general Manning coefficient of 0.026 gave the best results for this part. Only results from the calibration period will be used further, so we did not validate it further.

IV. SALINITY

A. Salinity as passive tracer in 1954 model

Salinity was added to the model as a passive tracer. There are no salinity data available for 1954, so the tracer could not be calibrated for this model. Salinity as a passive tracer was already successfully calibrated in another Scheldt Estuary TELEMAC model representing the bathymetry of 2009 [to be added]. The parameter value for the tracer diffusivity, i.e. 0.8m²/s, was taken from this model and applied in the 1955 model. Where we expected the same salinity intrusion or less, because of a smaller tidal range, the simulation results gave a much higher salt intrusion (Fig. 7). Because there were no data to compare the results with, further test were done to confirm or refuse the models salinity results.

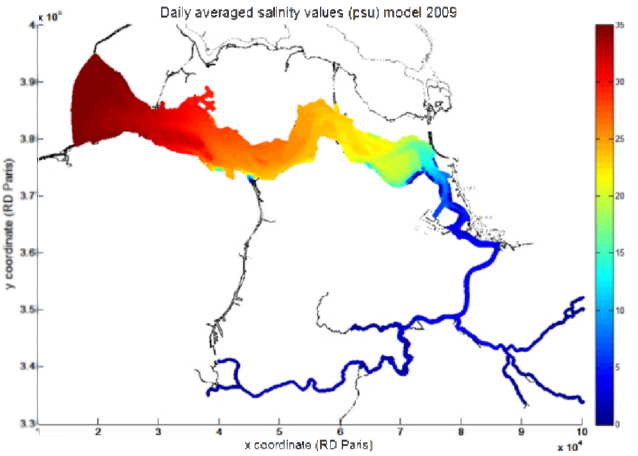

Figure 6. Daily average salinity values (PSU) in model of 2009.

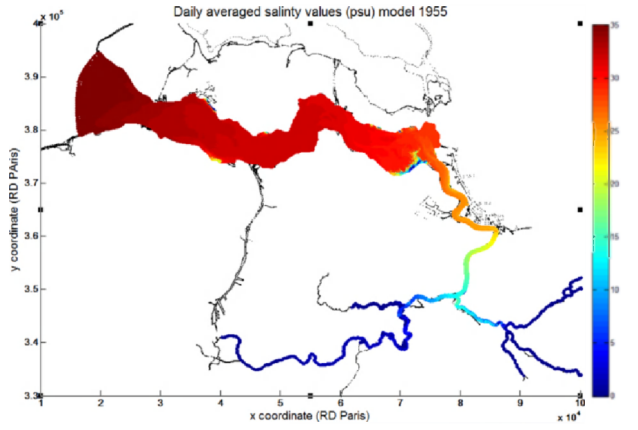

Figure 7. Daily averaged salinity values (PSU) for model of 1955 using the same tracer diffusivity value as the model of 2009.

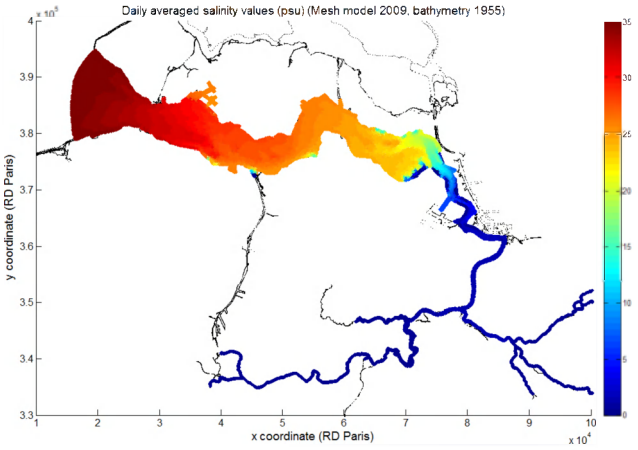

Figure 8. Daily averaged salinity values (PSU) for model with mesh of 2009 model and bathymetry and boundary conditions of 1955.

The total diffusion in the model is always the sum of the natural diffusion, i.e. the tracer diffusivity value given by the user, and the artificial or numerical diffusion in the model. This artificial diffusion is influenced by model parameters like the mesh size and the time step. By changing the mesh resolution, one changes the total diffusion in the model. Since the mesh resolution in the model of 1955 is much finer (40m) than that of the model of 2009 (150m), the diffusion and the salinity results in the model of 2009 (Fig. 6) will not be comparable with the diffusion and results of the 1955 model (Fig. 7). In fact the finer mesh resolution of the 1955 model increased the total diffusion in the simulation, giving a wrong salinity distribution in the estuary. With no calibration data and a different mesh than the 2009 model it was impossible to get the salinity value right in this model.

The solution for the salinity calibration problem was to apply the 1955 models bathymetry on the mesh of the 2009 model, for which the salinity influencing model parameter values were calibrated and known. Using also the 1954 boundary conditions gave salinity results that were in the line of expectations (Fig. 8). Salinity results of this simulation were mapped on to the finer mesh of the 1954 model using Blue Kenue in order to have salinity values for every node of the 1954 model mesh.

This method of using another calibrated and validated model of the same area to simulate tracer values for a period for which no data were available, can also be turned around: the bathymetry and boundary conditions data of 2009 could be used on the 1954 model mesh and then the salinity could be calibrated for this mesh and time step. This way demands a new round of calibrating the salinity data, which is time consuming, and therefore it was chosen to do it the other way. It might still be a good solution if it was absolutely necessary to have the salinity diffusivity parameter value for the 1954 model mesh.

B. Tracer sensitivity

1) Mesh size

Every physical term in the TELEMAC model will have a different reaction to mesh size because of the numerical or artificial diffusion. The fact that mesh resolution plays an important role in the artificial diffusion of advection schemes is shown in the following example: the artificial diffusion of a simple 1D upwind scheme in finite differences is given by (U*dx)/2, where U is the velocity and dx the mesh size. The artificial diffusion may completely mask the values given by turbulence models, especially in free surface flows where the mesh size may be several kilometres [5].

To have an idea of the influence of the mesh size on the salinity distribution in both the 2009 and the 1954 model, all parameters were kept the same in two simulations where only the mesh resolution was altered. The initial tracer value was set to zero. The result for a certain point (the same location in both meshes) is given in Fig. 9. The higher mesh resolution clearly speeds up the diffusion of the tracer. This example shows that an increasing mesh resolution increases the artificial diffusion in the model.

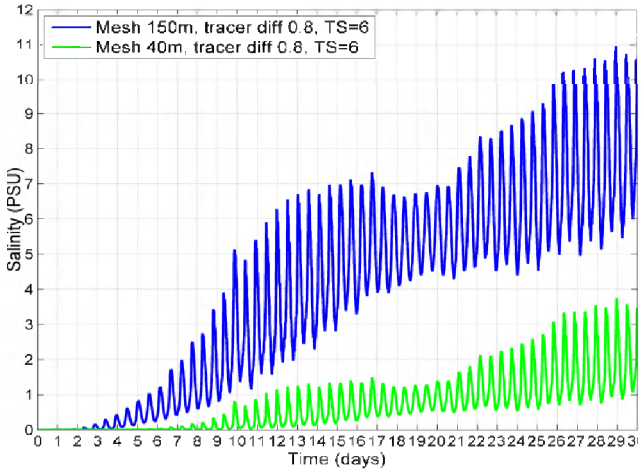

Figure 9. Influence of mesh resolution on tracer (salinity) values while all other parameters were kept constant.

Since all physical parameters are affected by artificial diffusion the result seen in Fig. 9 is thus not only the result of a changed tracer diffusion. It is a result of the influence of a changing mesh resolution on artificial diffusion and thus on all physical parameters in the model. This must explain why the salinity diffusion in the 1955 model, although the mesh resolution had decreased and thus decreasing the numerical diffusion, is higher than in the 2009 model with its coarser mesh.

2) Time step

To meet the Courant criterion the time step will be reduced with reducing mesh size. With a different time step the advection schemes may behave differently. For example the method of characteristics is less diffusive in one step than in two half steps. [5].

The salinity diffusion in the 2009 model was tested for two different time steps, i.e. 6 and 60 seconds. A smaller time step will result in larger salinity diffusion. The effect of the time step on the salinity diffusion in our model was small, i.e. less than half a PSU unit.

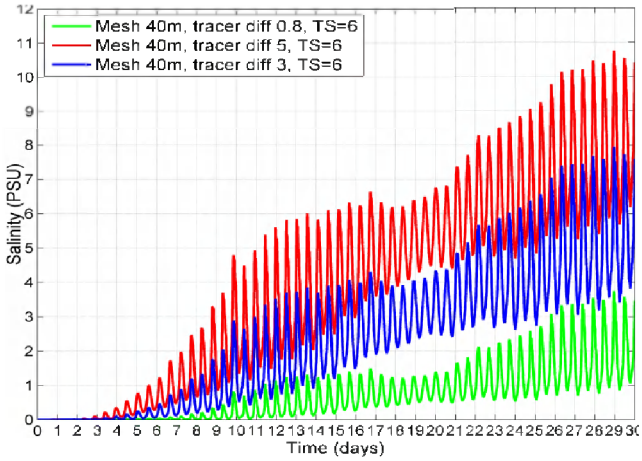

Figure 10. Effect of the tracer diffusivity value on tracer diffusion, while all other parameters were kept constant.

3) Tracer diffusivity

Finally, the effect of different values for the tracer diffusivity parameter was tested to compare their impact on tracer diffusion with the effect of especially mesh resolution. All other parameters were kept constant while the tracer diffusivity parameter values altered from 0.8 to 3 to 5m²/s. The results are shown in Fig. 10. In increase in tracer diffusivity from 0.8 to 5m²/s shows the same effect on the salinity distribution as a mesh resolution increase from 40m to 150m.

V. Application of Benthos Model

For every node in the mesh of the model the maximum flow velocity, the inundation time, the average salinity and the salinity range are calculated over a single spring tide. These are the input parameters for the macrozoöbenthos model of Cozzoli et al. [1,6]. Without going further into detail about this model, an example is shown in Fig. 11, where two maps of the Western Scheldt are shown, i.e. the situation in 1955 and the one in 2010, giving the bivalve, Macoma baltica, expressed in g/m². The figure also shows the difference in total tons of ash-free dry weight (AFDW) of M. baltica for the entire estuary between 1955 and 2010. Regarding the numbers given in the figure it is important to realize that the output of the benthos model is expressed in potential of biomass (0.95 percentile) because this gives a better estimation of the habitat suitability [7, 8]. More information about the difference in Macrozoöbenthos between 1955 and 2010 and the difference between Eastern and Western Scheldt can be found in [6].

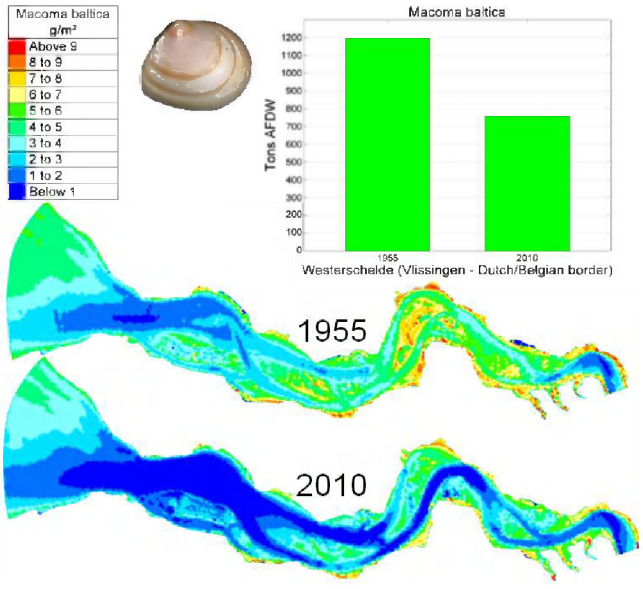

Figure 11. Maps of the Western Scheldt showing the bivalve, M. baltica, expressed in g per m² in 1955 and 2010. The total ash-free dry weight difference for the estuary between 1955 and 2010 is given in the bar chart.

VI. Conclusions

With the knowledge and help of a Scheldt Estuary model of 2009 a new model was calibrated for 1955. A seaward water level boundary time series was re-created using harmonic analysis. Calibration was done with measured high and low water values. Salinity was modeled as a passive tracer on the mesh of the 2009 model using boundary conditions and bathymetry of the 1955 model, because the 2009 model was calibrated for salinity. The tracer diffusivity is the sum of the parameter value and the numerical diffusivity. The mesh size, time step, velocity diffusivity and tracer diffusivity value determine the total diffusion of the salinity in the model.

A reliable calibrated 2Dh hydrodynamic model of 1955 with a complete salinity gradient provides all the information (maximum flow velocities, inundation time, average salinity and salinity range) for the application of a macrozoöbenthos model to compare the present (2009) and past (1955) ecological state of the Scheldt Estuary.

Acknowledgement

This research was financially supported by the Port of Antwerp and the Dehousse scholarship of Antwerp University. The authors like to thank Flanders Hydraulics Research for the cooperation and the Canadian Hydraulics Centre for the Blue Kenue software. Finally our gratitude goes to the TELEMAC consortium for making the TELEMAC software freely available and the great support they offer via the website!

References

[1] F. Cozzoli, M. Eelkema, T. Bouma, T. Ysebaert, V. Escaravage, P.M.J. Herman, 2013. A mixed modeling approach to predict the effect of environmental modification on species distributions. “unpublished”.

[2] R. Costanza, R. d’Arge, R. de Groot, S. Farber, M. Grasso, B. Hannon, K. Limburg, S. Naeem, R. O’Neill, J. Paruelo, R. Raskin, P. Sutton, M. van den Belt, 1997. The value of the world’s ecosystem services and natural capital. *Nature* 387, 253–260.

[3] W. Baeyens, B. van Eck, C. Lambert, R. Wollast, L. Goeyens, 1998 General description of the Scheldt estuary. *Hydrobiologia* 34, 83-107.

[4] R. Pawlowicz, B. Beardsley, and S. Lentz, 2002. "Classical Tidal Harmonic Analysis Including Error Estimates in MATLAB using T_TIDE", Computers and Geosciences, 28, 929-937.

[5] Jean-Michel Hervouet, personal communication on TELEMAC forum (www.openTELEMAC.org) June, 2013.

[6] F. Cozzoli, S. Smolders, M. Eelkema, T. Bouma, T. Ysebaert, V. Escaravage, P. Meire, S. Temmerman, P.M.J. Herman, 2014. Antropocene in estuaries: effects on macrozoobenthos. “unpublished”.

[7] M.J. Anderson, 2008. Animal-sediment relationship re-visited: Characterising species’ distributions along an environmental gradient using canonical analysis and quantile regression splines. Journal of Experimental Marine Biology and Ecology, 366 (2008) 16-27.

[8] F. Cozzoli, T. Bouma, T. Ysebaert, P.M.J. Herman, 2013. Application of non-linear quantile regression to macrozoobenthic species distribution modelling: comparing two contrasting basins. Marine Ecology Progress Series 475 (2013) 119-133.

TUC 2013, 16-18/10/2013, Karlsruhe - Kopmann, Goll (eds.) - © 2013 Bundesanstalt für Wasserbau ISBN 978-3-939230-07-6

Interactive coupling of TELEMAC with the open source water quality model DELWAQ

M. Jeuken, J. Mooiman
Deltares Software Center (DSC)
Deltares
Delft, The Netherlands
michel.jeuken@deltares.nl, jan.mooiman@deltares.nl

Y. Audouin
National Hydraulic and Environment Laboratory (LNHE)
EDF R&D
Chatou, France
yoann.audouin@edf.fr

***Abstract*—A static, file based coupling between TELEMAC and DELWAQ was first established in 2004, and has since been improved by various developers. DELWAQ is the computational water quality engine of the D-Water Quality and D-Ecology programmes of the Delft3D suite. DELWAQ was only available by a paid license, but since March 2013 the code of DELWAQ is available under a GPL license, and thus has become more generally available. In this paper Deltares and EDF introduce a Fortran-function based coupling of TELEMAC and DELWAQ that makes it possible to run TELEMAC and DELWAQ interactively per calculation time step. The interactive coupling facilitates the possibility to introduce feedback mechanisms from DELWAQ to TELEMAC, or influence substances modelled in DELWAQ from TELEMAC. The interactive coupling can be used, for example, to model the effect of sediments or water plants on the hydraulic flow in TELEMAC, or real time control of structures based on water quality.**

I. INTRODUCTION

At the beginning of this century National Hydraulics and Environment Laboratory (LNHE; now part of EDF R&D) became interested in coupling their hydraulic models TELEMAC2D and TELEMAC3D (from here on referred to as TELEMAC) [1] from the TELEMAC-MASCARAT modelling suite to the water quality engine DELWAQ [2] from WL|Delft Hydraulics (currently merged into Deltares). Before the coupling could be established it was necessary to define a procedure that allows the consistent and mass conserving coupling of the finite element TELEMAC model for two- and three-dimensional flow with the finite volume Delft3D-WAQ model for water quality. A first version of the static, file based coupling of TELEMAC with DELWAQ was established in 2004 and published in 2007 [3], and has since been improved by various developers. This work has been carried out as part of a joint development by LNHE and WL|Delft Hydraulics to explore the mutual interaction of their software, and is still continued by EDF and Deltares.

Recently the wish emerged to establish a time step based interactive coupling between TELEMAC and DELWAQ. This would facilitate the introduction of feedback mechanisms from DELWAQ to TELEMAC, or influence substances modelled in DELWAQ from TELEMAC at run time. The interactive coupling can be used, for example, to model the effect of sediments or water plants on the hydraulic flow in TELEMAC, or real time control of structures based on water quality.

The interactive coupling was implemented by making DELWAQ available as a dynamic library to TELEMAC. Fortran-functions in the dynamic library of DELWAQ allow TELEMAC to initialise a DELWAQ calculation, control the progress of the calculation in DELWAQ time step by time step and to make it possible to send the data currently send to DELWAQ through files directly into DELWAQ memory, and tell DELWAQ to finalise its calculation. The functionality could be extended to creating TELEMAC output files containing DELWAQ results, have DELWAQ results directly influence the hydraulic calculations or directly interfere in the DELWAQ calculation from TELEMAC.

When running TELEMAC and DELWAQ interactively, both models still use their own input and output files. TELEMAC only needs to know from its input that it has to run interactively, and DELWAQ must know it doesn't need to read the static coupling files any more, although they can still be produced by TELEMAC. Since both TELEMAC (July 2010) and recently DELWAQ (March 2013) are available in open source, these developments are generally available. At the time of writing, the coupling is only tested on Microsoft Windows using Microsoft Visual Studio 2010 with Intel Visual Fortran Composer XE2011.

II. WATER QUALITY MODELLING WITH DELWAQ

DELWAQ is the computational engine of the D-Water Quality and D-Ecology programmes of the Delft3D suite. It is based on a rich library from which users and developers can pick relevant substances and processes to quickly put water and sediment quality models together.

A. Extensive library & state of the art solvers

The processes library covers many aspects of water quality and ecology, from basic tracers, dissolved oxygen, nutrients, organic matter, inorganic suspended matter, heavy metals, bacteria and organic micro-pollutants, to complex algae and macrophyte dynamics (see an overview in Fig. 1). It is also possible to program your own processes using the Open Processes Library Configuration Tool (OpenPLCT).

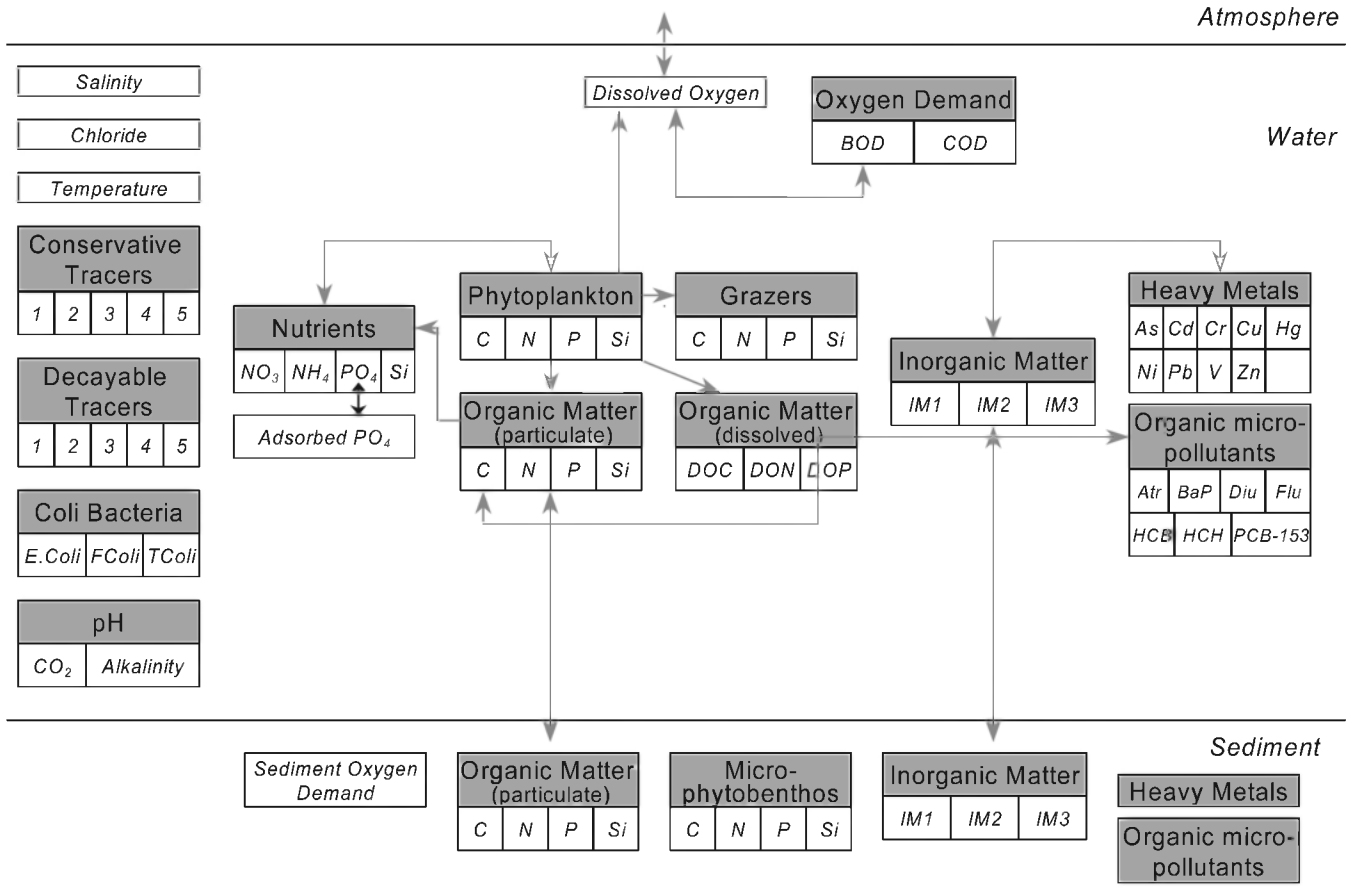

Figure 1. General overview of the processes available in DELWAQ

Since DELWAQ is open-source, it is also possible to modify the existing processes directly (at your own responsibility). High performance solvers, for example with local adaption by switching between explicit and implicit schemes [4], enable the simulation of long periods, often required to capture the full cycles of the processes being modelled. DELWAQ incorporates over 30 years of experiences in water quality and ecology modelling and is constantly updated and extended.

B. Easy coupling to hydraulic models

The finite volume approach underlying DELWAQ allows it to be coupled to the 1D flow of SOBEK, the structured grid hydrodynamics of Delft3D-FLOW and the upcoming D-Flow Flexible Mesh engine (1D-2D-3D) of the Delft3D suite [5] or other models such as TELEMAC. Any description of the motion of water would be suitable if available in the right format. Advanced features allow for increased flexibility in model configuration: hydrodynamics can be aggregated in space and time, water and sediment layers may have a different resolution and coarser sub-grids can be used to improve performance or facilitate input specification.

C. DELWAQ available as open source

After gaining experience with the open source release of Delft3D-FLOW in January 2011 the source code of DELWAQ was added to the open source repository of Delft3D in March 2013 under a GPL license. It has been presented in two webinars that are still viewable on the Deltares website [6]. By putting DELWAQ in open source Deltares invites all experts to collaborate in further development and research in the field of water quality, ecology and morphology using DELWAQ.

III. IMPLEMENTATION OF THE INTERACTIVE COUPLING

To implement the interactive coupling both TELEMAC and DELWAQ were modified. The dynamic library of DELWAQ has been improved, and calls to DELWAQ functions have been added to TELEMAC. Both models still read their own input files. TELEMAC only needs to know that it has to start the interactive coupling with DELWAQ, and the DELWAQ input needs to be modified a little so it doesn't read the files from the file based coupling anymore.

A. TELEMAC

The file based coupling of TELEMAC with DELWAQ is mainly implemented in the TEL4DEL subroutine. It can handle both 2D and 3D results, and is thus available to both TELEMAC2D and TELEMAC3D. The interactive coupling doesn't make the file based coupling obsolete because it has its own advantages when interaction between TELEMAC and DELWAQ is not relevant. Reading the results from files when only the DELWAQ input has changed is more efficient than running TELMAC again. With hydraulic simulations of a repetitive nature, it is also possible for DELWAQ to extent

the calculation period of a TELEMAC run by repeating a specific period from the files multiple times. This is useful to model longer tide cycles from a short TELEMAC run, a feature currently not possible with the interactive coupling. Because the calls to functions in DELWAQ require the DELWAQ dynamic libraries to be available at all time, pre-processor statements were added to allow ease compilation of a standard TELEMAC version that doesn't require the DELWAQ libraries. After a call has been made to DELWAQ, the TEL4DEL routine always checks whether the operation was successful.

B. DELWAQ

On the DELWAQ side a lot of work had already been done in other projects. It was already possible to run DELWAQ in separate steps. A run could be initialised, run time step by time step, and then finalised. There was however still room for improvement in the sending and receiving of data. Also the pre-processing step from the program DELWAQ1, that previously had to be run as a separate executable, has been made available as a dynamic library. To run the interactive coupling some modification is necessary to the input files. Normally DELWAQ will read the hydraulic data from files, but it is possible to suppress this by setting up the input with constant values. Via calls to the dynamic library functions of DELWAQ the hydrodynamic data from TELEMAC can then be put in.

C. Steps in calculation

The most direct coupling is to perform a DELWAQ time step after every TELEMAC time step. In most applications however, water quality modelling allows for larger time steps than hydraulic modelling. Therefore the file based coupling already facilitated aggregation of TELEMAC results in time, and this can also be used with the interactive coupling. The following steps can be seen in Fig. 2:

1. An initialisation call tells DELWAQ to read the name of the DELWAQ project file from a file named "runid.waq", and read other options from "delwaq.options". TELEMAC doesn't need to know the name of this project. The time frame and time step in DELWAQ are retrieved, and checked for the current limitations to timings of the calculation. Then the initial volumes are sent to DELWAQ to calculate the initial masses in the system.
2. One or more TELEMAC time steps are performed, depending on the aggregation period.
3. At the end of an aggregation period the hydraulic data is sent to DELWAQ. The volumes at the end of the (aggregated) TELEMAC time step, and the average areas and flow over the (aggregated) time step. Optionally average salinity, temperature, vertical dispersion and/or velocity is sent, when available.
4. A DELWAQ time step is performed.
5. Return to TELEMAC for a next time step, and repetition of steps 2-5.
6. Let DELWAQ finalise its calculation, close its files and finish all of its processes.

D. Variations in the time steps and calculation periods

There are limitations to the time steps that can be chosen in DELWAQ. The current implementation allows the DELWAQ calculation to start at any point in the simulation after the start of the TELEMAC calculation (to allow for a spin-up period in TELEMAC). It is also possible to have DELWAQ perform multiple time steps within a (aggregated) TELEMAC time step, and to let DELWAQ stop its calculation before the TELEMAC calculation stops. These timings have to be chosen with some care, because the communication moments need to be aligned. The determining factor in this is the (aggregated) TELEMAC time step. The start and stop time of DELWAQ need to be a multiple of the (aggregated) TELEMAC time step, and the DELWAQ time step needs to be a divisor of the (aggregated) TELEMAC time step.

In the situation that DELWAQ performs multiple time steps per (aggregated) TELEMAC time step, multiple calls to DELWAQ are necessary (Fig.3). All of the data provided by TELEMAC stays constant over the (aggregation) TELEMAC time step, except for the volume data. Because for the interactive coupling the input file of DELWAQ was modified in such a way that DELWAQ assumes the volumes to be constant, it does not interpolate volumes by itself any more. Therefore interpolated volume data at the end of the DELWAQ time step is calculated by TELEMAC, and sent to DELWAQ (step 3a). After each DELWAQ time step performed (step 4a), the next interpolated volume data is sent (step 3b) for the next DELWAQ time step (4b), and this is repeated until the end of the (aggregated) TELEMAC time step is reached.

IV. APPLICATION OF THE INTERACTIVE COUPLING

For the interactive coupling some manipulation of the DELWAQ input file is necessary. The interactive coupling is shown to work in a set of test cases.

A. Setting up the coupling

A good way to set up an interactive calculation between TELEMAC and DELWAQ is to start with a file based run first. Using the DELWAQ GUI you can set up a model easily when importing the steering file from TELEMAC (T2DD11, which has to be renamed to T2DD11.hyd), and a substance file created by the OpenPLCT. Using the GUI you can also define horizontal dispersion, the use of vertical dispersion as calculated by TELEMAC , the timeframe, initial conditions, boundary conditions, process parameters (including linking salinity, temperature and velocity as modelled by TELEMAC), set the numerical options, add discharges, add observation points and set the output options. It is of course also possible to work directly from a DELWAQ input file. It is handy to use identical reference times in both models.

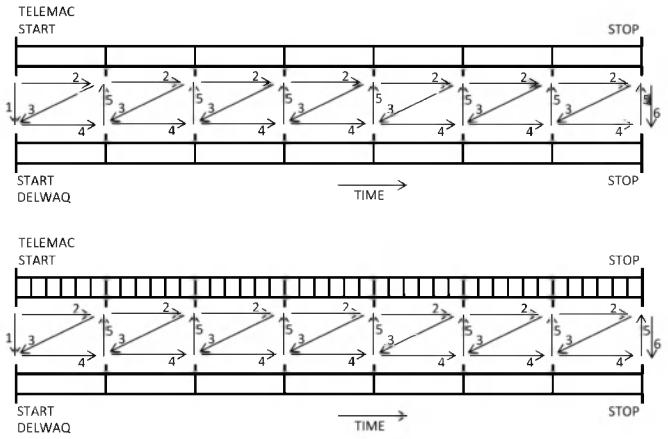

Figure 2. Calculation steps with equal TELEMAC, aggregation and DELWAQ time step (top) or with aggregation to a bigger DELWAQ time step. Each block represents a calcualtion time step in model.

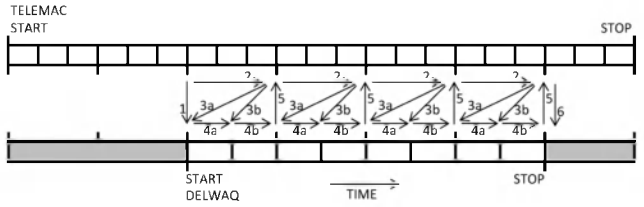

Figure 3. An example of possible variations with different start and stop time, TELEMAC aggregation time step and multiple DELWAQ time steps.

The interactive coupling is not yet supported directly by the DELWAQ GUI, so after making the initial setup, you have to modify the DELWAQ input file yourself using a text editor, and then you cannot use the GUI any more. You can still use the GUI to generate new parts of the input file, and merge them into your edited input file. The references in the input file to the files that contain the time series information (T2DDL1 (volume), T2DDL2 (area) and T2DDL3 (flow), and optionally T2DDL4 (salinity), T2DDL8 (temperature), T2DDL9 (velocity) and T2DD10 (vertical dispersion) have to be replaced by dummy static information (an overview of the file based coupling can be found in Table I). These values will be replaced by the interactive coupling.

B. Test cases and results

We tested the coupling in two 2D and two 3D test runs with different time step settings and compared the results of the interactive coupling with the file based coupling. We also tested an extended interactive coupling that manipulates the concentrations in DELWAQ directly as an example of the potential of the interactive coupling. The test cases are based on the "RIVIERE AVEC DEUX PILES DE PONT" case. We only show results for case 2D B that runs TELEMAC for 400 time steps of 2 seconds and ends after 13 minutes and 20 seconds. The hydrodynamics are aggregated to steps of 20 seconds. The DELWAQ calculation starts after 1 minute and 20 seconds with a time step of 5 seconds, and stops after 12 minutes. The location of the monitoring point used in the time series can be seen in Fig. 8.

In DELWAQ we model three substances. The substance "Continuity" to check the water balance, and two tracers named cTR1 and cTR2. Continuity has an initial concentration of 1.0, 1.0 on all boundary conditions, and should result in concentrations of 1.0 during the whole run. cTR1 is initially set to 25 mg/L, with an inflow boundary concentration of 100 mg/L this will gradually turn into 100 mg/L. cTR2 is initially set to 75 mg/L, with an inflow boundary concentration of 0.0 mg/L this will gradually turn into 0.0 mg/L. In the test cases the sum of cTR1 and cTR2 should always be 100 mg/L. A screenshot showing mixed up screen messages during the run can be seen in Fig. 4. The results for file based coupling and interactive coupling turn out to be identical, show 1.0 for continuity (Fig. 5), and the concentrations of cTR1 and cTR2 add up to 100 mg/L (Fig. 6).

With the interactive coupling it is possible to influence the DELWAQ calculation from TELEMAC. To illustrate this we let TELEMAC place a 'watermark' at 100 seconds after the DELWAQ calculation start time. The concentrations of the tracers in the examples are changed in a selection of cells. The concentrations of cTR1 are set to 100 mg/L, and the concentrations of cTR2 are set to 0.0 mg/L, thus the sum of cTR1 and cTR2 still remains 100 mg/L. The result of the 'watermark' can be seen in Fig. 7 and Fig. 8.

V. CONCLUSION AND DISCUSSION

It is shown that it is possible to run DELWAQ from TELEMAC interactively on a time step by time step basis providing hydraulic data through memory to DELWAQ using function calls to the DELWAQ dynamic library. This produces exactly the same results as using the file based coupling. It is also shown that it is possible to manipulate the substances in DELWAQ from TELEMAC. The file based coupling is not obsolete, because if interaction between TELEMAC and DELWAQ is not necessary, it is often more efficient.

At the time of writing the interactive coupling has been developed and tested on Windows using Microsoft Visual Studio 2010 with Intel Visual Fortran Composer XE2011. We have not yet managed to get the interactive coupling working on Linux, but we hope to fix this as soon as possible. Further developments would include applying the interactive coupling to more complex TELEMAC-DELWAQ models and introduce more interaction between TELEMAC and DELWAQ. It is also considered to add the possibility of spatial aggregation to the interactive coupling.

ACKNOWLEDGEMENT

We would like to thank Arjen Markus for last minute proofreading of the text.

TABLE I. OVERVIEW OF FILES CREATED IN THE FILE BASED COUPLING BETWEEN TELEMAC AND DELWAQ

Standard fil©ename	*Logical unit*	*T/S*[a]	*Unit*	*Content*	*N*[b]	*D3D ext.*[c]
T2DDL1	NSOU	T	m^3	Volume	S	vol
T2DDL2	NMAB	T	m^2	Area	E	are
T2DDL3	NCOU	T	m^3/s	Flow	E	flo
T2DDL4	NSAL	T	g/m^3	Salinity	S	sal
T2DDL5	NINI	S	m^2	Hor. surface	N	srf
T2DDL6	NVEB	S	-	Exchanges	E	poi
T2DDL7	NMAF	S	m	Node dist.	E	len
T2DDL8	NTEM	T	°C	Temperature	S	tem
T2DDL9	NVEL	T	m/s	Velocity	N	vel
T2DD10	NVIS	T	m^2/s	Vert. disp.	S	vdf
T2DD11	NCOB	S	-	Steering file	-	hyd

a. *The file contains T: time series information or S: static information*

b. *The file contains information per S: segment, E: exchange or N: node*

c. *The common extension used in Delft3D*

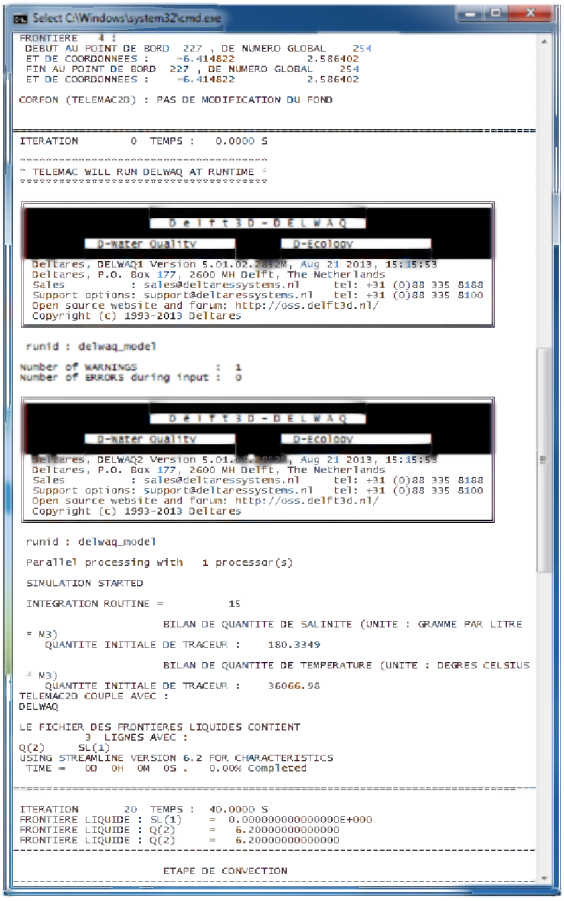

Figure 4. Screenshot showing interactive run of TELEMAC and DELWAQ, with messages from TELEMAC in French and DELWAQ in English

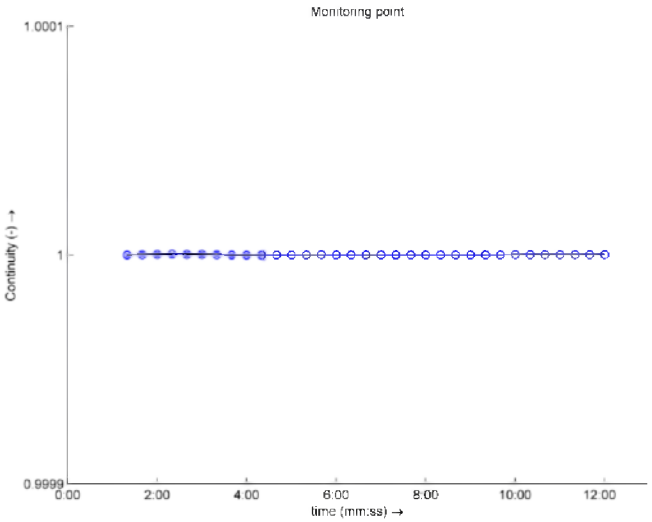

Figure 5. Continuity file based (blue O) and interactive coupling (black line)

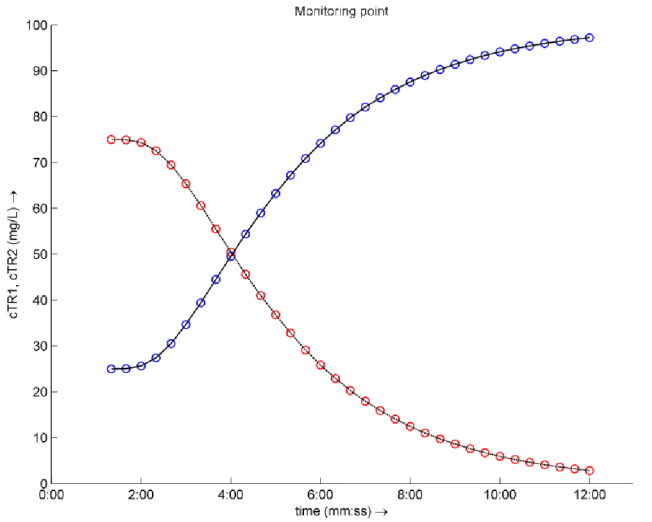

Figure 6. cTR1 (blue O), cTR2 (red O) in file based coupling and cTR1 (black solid line), cTR2 (black dashed line) in interactive coupling (mg/L).

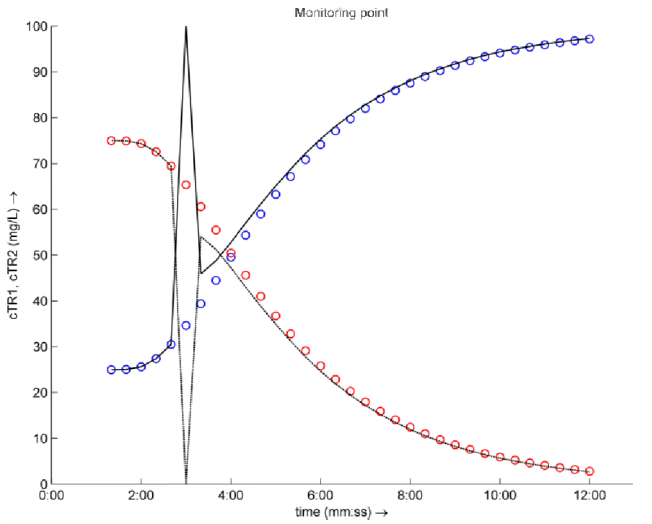

Figure 7. Same as Fig.6 but with interactive 'watermark' event at 3:00.

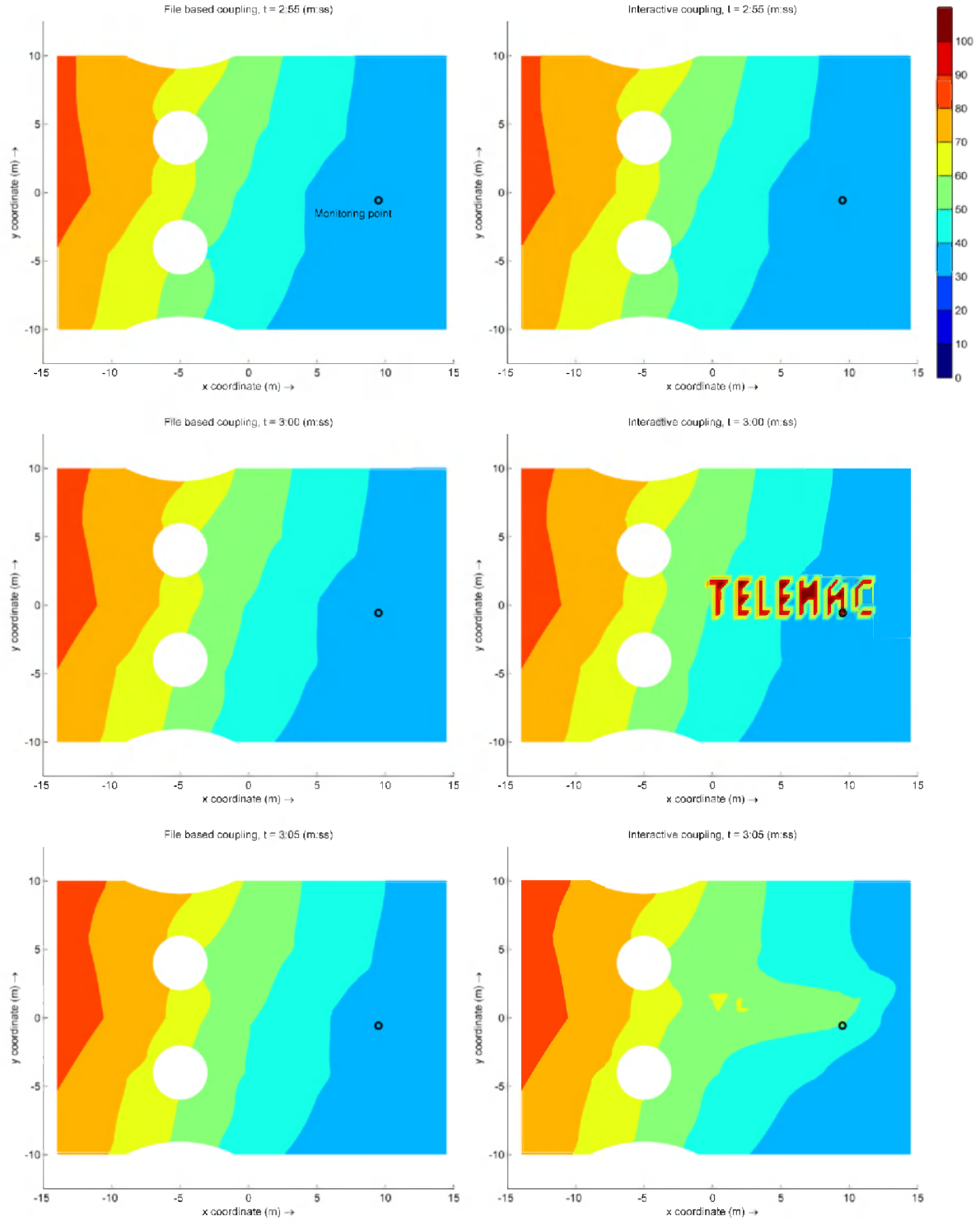

Figure 8. Example of TELEMAC influencing DELWAQ the concentration of tracer 1 (cTR1; mg/L). On the left three time steps from the file based coupling and the interactive coupling of case 2D B. On the right the interactive coupling leaving a 'watermark' at 0:03:00. The O indicates the monitoring point.

REFERENCES

[1] TELEMAC-MASCARET: http://www.opentelemac.org

[2] DELWAQ: part of Delft3D: http://oss.deltares.nl/web/delft3d

[3] L. Postma and J.-M. Hervouet, "Compatibility between finite volumes and finite elements using solutions of shallow water equations for substance transport," Int. J. Numer. Meth. Fluids, Volume 53, Issue 9, pages 1495–1507, 30 March 2007.

[4] Slingerland, v. P., M. Borsboom and C. Vuik, 2009. A local theta scheme for advection problems with strongly varying meshes and velocity profiles. Tech. Rep. 08-17, Delft University of Technology.

[5] Manuals to SOBEK , Delft3D and D-Flow Flexible Mesh: http://publicwiki.deltares.nl/display/DSM.

[6] http://oss.deltares.nl/web/delft3d/webinars

TUC 2013, 16-18/10/2013, Karlsruhe - Kopmann, Goll (eds.) - © 2013 Bundesanstalt für Wasserbau ISBN 978-3-939230-07-6

Application of TELEMAC System at the Southern Brazilian Shelf: Case Study of Tramandaí Beach Oil Spill

C. Eadi Stringari, M. I. Corrêa da Silva Machado, E. de Paula Kirinus
Instituto de Oceanografía
Universidade Federal do Rio Grande
Rio Grande, Brazil
caio.stringari@gmail.com

W. Correa Marques
Instituto de Matemática Estatística e Física
Universidade Federal do Rio Grande
Rio Grande, Brazil

Abstract—**This work presents the results of simulation of an oil spill occurred in 26th January 2012 on Tramandai beach, located at Northern portion of the Southern Brazilian Shelf (SBS). This work was carried out through the coupling between two numerical models: the hydrodynamic three-dimensional model TELEMAC-3D which is part of the TELEMAC-MASCARET suite and the ECOS (Easy Coupling Oil System) which is being developed at Universidade Federal do Rio Grande (FURG). Both models are forced by synoptic winds data and daily ocean data. This work presents the hydrodynamic pattern modelled for the region, the superficial drift of oil slick, the oil weathering and a "risk map". Hydrodynamic results show a classical wind driven pattern due the action of the winds and the oil drift results indicate that the spilled oil reaches the coastline after 10 hours over a sand dune field (region with high oil sensibility). The oil weathering indicates an evaporation of approximately 18% and an emulsification of 70%. Therefore, these effects increase the oil density in 4.6% intensifying its vertical dispersion.**

I. INTRODUCTION

As fossil fuel based society, oil spills have been inherent to the oceans. There are daily reports of spills due to harbour, platforms (FSPOs) and ship operations. In addition, oil compositions consist of several long chain and/or polycyclic aromatic hydro carbonates which once in contact with the environment become toxic compounds, causing a series of processes ranging different timescales and also causing chronic and irreversible effects [1].

The Southern Brazilian Shelf (SBS) is an environment with specific characteristics. It is characterized by a large continental shelf, located between 28°S and 35°S and is influenced by the presence of two western boundary currents, the Brazil and Malvinas currents, respectively. In fact, the region marks the transition between tropical, subtropical and sub-polar waters with the presence of several different water masses. The influence of the two major freshwater sources, the Patos Lagoon and the La Plata River, is also important for the region dynamics due to the buoyancy driven circulation caused by their freshwater plumes. Finally, near-shore there are the influence of modulated tides, winds and waves interacting with manmade structures and the biggest Southern Brazilian harbour, the Rio Grande harbour complex. This area is ideal for application of numerical models since a number of processes can be evaluated providing good contributions to the knowledge of the dynamics of the region. Moreover, due to the harbour activity, the region is prone to have accidents with oil and other chemical spills. Oil spills in marine ecosystems could generate a series of effects in different temporal and spatial scales and some of them could be irreversible. Numerical modelling of these processes is a powerful tool with low computational cost to investigate the path and behaviour of spilled oil.

The Southern Brazilian Littoral (Fig. 1 A and Fig. 1 B) is a continuous sand line with Southwest-Northwest (SW-NW) orientation, which could be geographically divided in tree major sections: (1) the South Littoral, (2) the Middle Littoral and (3) the North Littoral [2]. Tramandaí beach is located at the North Littoral portion, where the major biodiversity of whole littoral is found due to the more complex local geomorphologic factors [3].

The North Littoral has susceptibility to oil spills due to the presence of oil capture buoys. These buoys are located in the coastal area capturing the oil from tanker ships and transmitting to the Osório oil plant. There are two buoys in this region; however, this work is focused on the nearest buoy from the coastline, located at 30◦01'36" S 50◦05'12"W. This buoy is located at the 25 m isobath and is connected with the Osório plant by a 6 km oil-duct and further to the Alberto Pasqualini refinery (REFAP), in Porto Alegre, by a 90 km long oil-duct. Fig. 1 C shows the location of the buoy with the "+" signal.

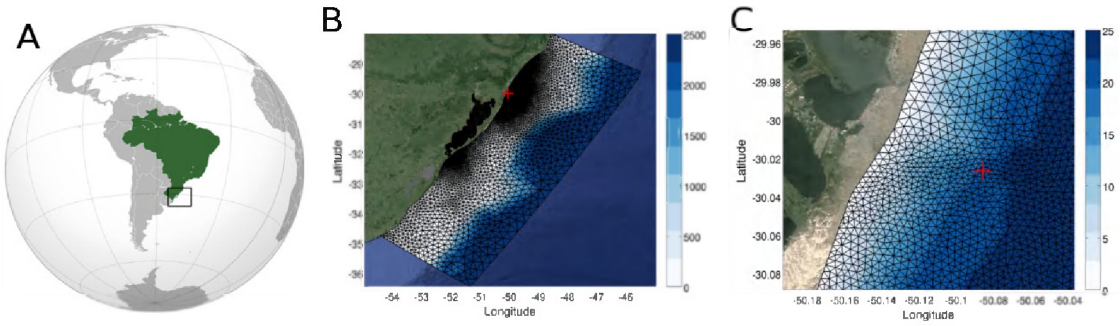

Figure 1. a) Overview of the Study Region. b) Numerical domain and discretization of SBS. c) Detail of Tramandaí coastline. The red Cross signal indicates the location of the spill.

In accordance with the Brazilian legislation, numerical simulations regarding oil spills may be used to define the area which could be influenced by the activities involving oil. These studies are used to support the environmental diagnostic, such as: the elaboration of risk maps, oil sensitivity charts and contingency plans used by oil companies and environmental agencies [4].

In this way, the oil spill numerical modelling is a comprehensive tool that might provide support to the environmental agencies and companies. Nevertheless, a powerful hydrodynamic model must be used to represent the ocean conditions near-shore; otherwise the oil spill model cannot work. Therefore, the objective of this work is to present the application of TELEMAC-3D for providing the ocean state variables to an oil spill model in such a way that is possible to have the high resolution conditions needed to evaluate the oil spill event which occurred in 26th January 2012 within the Tramandaí Coast.

II. METHODOLOGY

A. *Hydrodynamic Model*

The hydrodynamic simulation of process was carried out using the three-dimensional finite-element open-source model TELEMAC-3D (http://www.opentelemac.org). This model solves the Navier-Stokes equations considering the local variation of the free surface, ignoring the density variation on the mass conservation equation and considering the Boussinesq approximation to solve the momentum equations [10].

The finite element techniques is used to spatially discretize the hydrodynamic equations considering the sigma levels for the vertical discretization and the Multidimensional Upwind Residual Distribution (MURD) for the advection of three-dimensional variables. A time step of 90s and the Coriolis coefficient of -7.72 10-5 s^{-1} (latitude 30◦ S) were used in the hydrodynamic simulation. Following the methodology of [11] the horizontal turbulence process was modelled using an adapted Smagorinsky and a mixing length model for coastal areas in order to estimate the horizontal and vertical turbulent processes, respectively.

The vertical discretization consists of fifteen sigma levels distributed in such way that the top and the bottom most layers of the water column have more sigma levels than the middle of water column. This type of distribution allows to better represent the superficial and bottom layers which is ideal for oil spills since the processes involved in oil spills are very often restricted either to the first centimetres of the water or, in case of sedimentation, to the bottom.

B. *Oil Spill Model*

The behaviour and fate of the spilled oil were investigated using the ECOS (Easy Coupling Oil System) model, registered at the Instituto Nacional da Propriedade Industrial - INPI under contract: BR 51 2013 00013. ECOS is a lagrangian and weathering oil spill model developed at the Universidade Federal do Rio Grande – FURG. This model's major feature is the easiness of the process of coupling it with hydrodynamic models already written.

Based and developed within the state change paradigm and written in object-oriented FORTAN 95 language, the ECOS model is subdivided into several modules. Each module is responsible for computing an oil property and some modules have a linkage function.

The ECOS model characterizes the main features acting in an oil spill, isolating the processes according to their influence and intra-cooperation. There are several modules and subroutines responsible to evaluate the phenomena in which the oil is exposed. In order to have a better organization and an optimum usage of the structures, the object-oriented programming technique has been used to follow the interrelationships between the physical properties of the spilled oil.

ECOS handles the oil like discrete particles using lagrangian approximation to evaluate the tracer (particles) proprieties during time. The tracer trajectories are evaluated considering the oil as a large number of particles which move independently in water. The tracer velocities are interpolated at each node of the hydrodynamic numerical domain (Fig. 1 B). The final tracer position depends on four different factors: (1) current velocity, (2) wind velocity, (4) spreading effect and (4) turbulent diffusion.

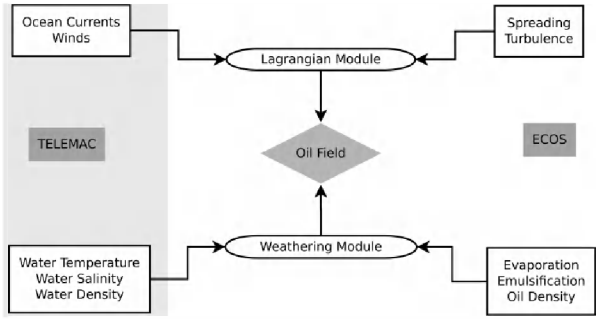

Figure 2. ECOS-TELEMAC-3D Coupling.

The module called *Environment* has the function to gather the environmental variables. The hydrological parameters used by this module are the velocity fields, water temperature, water salinity, water levels, water density and winds. This is the most important module of ECOS since it acts like a data source for the whole rest of the model. It is also the starting point for coupling with hydrodynamic models. Oil weathering is evaluated in a module called *Weathering*, which receives the information from the *Environment* module after parameterization. Here the phenomena of evaporation and emulsification are evaluated and the oil density is estimated. The oil slick transport is evaluated by the module called *Lagrangian* which receives information of the velocity fields from the *Environment* module and evaluates the phenomena of spreading and turbulent diffusion.

C. *Coupling between TELEMAC-3D and ECOS*

The ECOS code was directly coupled to the TELEMAC-3D source code. Hydrodynamics and the wind information from TELEMAC-3D are transferred to ECOS' *Lagrangian* module for the evaluation of the tracer positions at each time step. After all the properties have been evaluated, the final position of each tracer is integrated in time using a second order Runge-Kutta method. Salinity, temperature, and the water density are transferred to ECOS' weathering module, which evaluates the oil evaporation, emulsification and density. Fig. 2 shows the coupling between these models. For more details regarding the coupling procedure see [4].

III. NUMERICAL DOMAIN, BOUNDARY AND INITIAL CONDITIONS

The numerical domain (presented at Fig. 1 B, 1 C and 3) consists of a triangular mesh produced with the pre-processor MATISSE. There are 426210 nodes and 771694 elements within the three-dimensional mesh implying a resolution of 100 meters on the coastal region of Tramandaí and around 0.25 degree at the coarser portions of the mesh at the open ocean.

In order to evaluate the hydrodynamics of the SBS, the oceanographic parameters from HYCOM (HYbrid Coordinate Ocean Model, http://hycom.org) were used in this work as boundary conditions. These data sets present moderate temporal and spatial resolution and also have been used worldwide. Fig. 3 shows the boundary conditions implemented in TELEMAC-3D in which the red line indicates temperature and salinity values, the yellow line indicates the oceanic currents which are prescribed at Northern and Southern boundaries, the blue line indicates tides and low frequency ocean levels which are prescribed only at the Eastern boundary and finally the arrows indicate the air temperature and winds which are prescribed for the whole numerical domain.

The three major river discharges of this region were considered as liquid boundary conditions of the Patos Lagoon through the usage of climatologic data provided by the Brazilian National Water Agency (ANA, http://www.ana.gov.br). Ocean currents, low frequency water levels, temperature and salinity with a temporal resolution of 24 hours and a spatial resolution of 0.25 degree were interpolated to each boundary node of the numerical domain. The five major components of the astronomical tides (K1, M2, N2, O1 and S2) were extracted from the Grenoble Model (FES95.2, Finite Element Solution v.95.2) and also interpolated to the boundary nodes of the numerical domain. The outer boundary was forced with winds and air temperature from NOAA reanalysis (www.cdc.noaa.gov/cdc/reanalysis) with a temporal resolution of 6 hours and spatial resolution of 0.5 degree. These data were interpolated through the whole numerical domain.

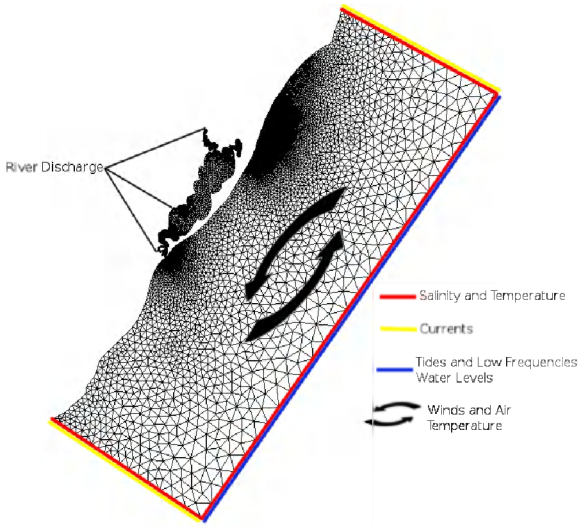

Figure 3. TELEMAC-3D boundary conditions.

TELEMAC-3D was initialized with temperature, salinity and velocity varying spatially. A "hot-start" procedure was used: A simulation was carried out between 1st and 31st December of 2011, then the last time-step of this simulation was considered as the initial condition for the simulation used in this work, starting at 1st January of 2012.

ECOS uses the Fay formulation [11] to simulate the initial condition for an accidental punctual spill with circular shape. This formulation takes in account the differences between oil and water density and the oil volume to estimate the initial area of the slick based on the different superficial tensions and diffusion coefficients. The initial oil density was 912 kg/m^3; the standard water density was 1025 kg/m^3

and the spilled oil volume was 13.42 m³. The information regarding the spill was cordially given by the Brazilian Environmental protection Agencies and the Brazilian Navy.

IV. Results and Discussion

A. Hydrodynamic

Because the major influences on the oil path in this region are the winds and currents [12], the hydrodynamic results of this work are focused on the behaviour of the costal wind-driven currents and the sea surface height (SSH).

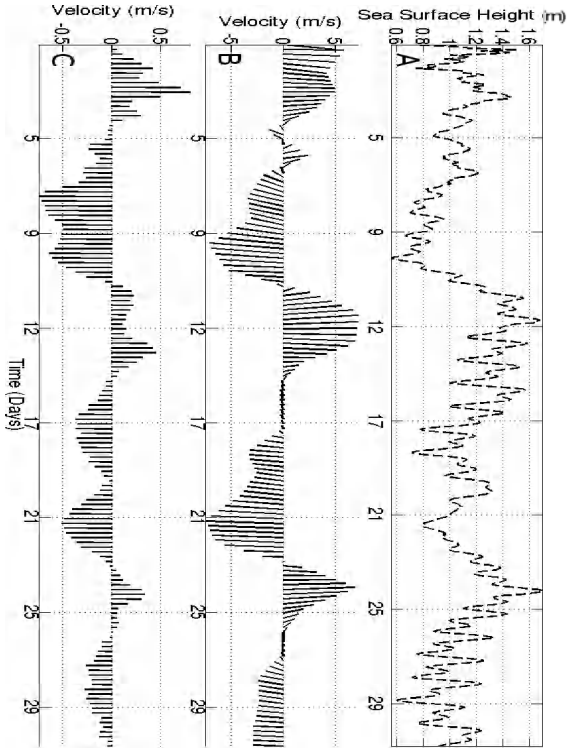

Figure 4. Temporal variability of: A) Sea surface height; B) Wind speed and direction; C) Surface currents speed and direction.

Fig. 4 shows temporal series of SSH, winds and surface currents. These time series were obtained at the buoy region shown in Fig. 1 C and indicated by the "+" marker. The SSH is in the expected theoretical range for this region with values around 1.0 m. Throughout the simulation a bidirectional behaviour of coastal currents is observed. This pattern relies on the interchange of wind direction due to the passage of frontal meteorological system in this region. This pattern of the wind circulation was identified before for the SBS [5, 6, and 13] and the bidirectional behaviour of the coastal currents was presented at Tramandaí coast by [14, 15].

Fig. 5 to 10 show the variability of the coastal currents and SSH in intervals of ten days. Colour gradients and vectors indicate the intensity and direction of the currents whereas white contours indicate values for SSH.

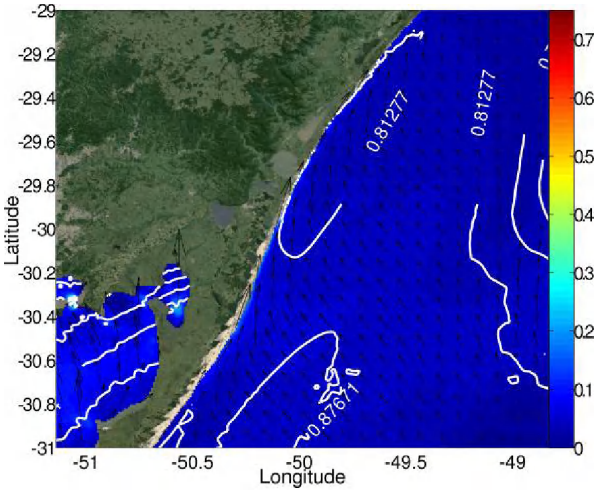

Figure 5. Spatial variably of surface currents and SSH for 1st of January.

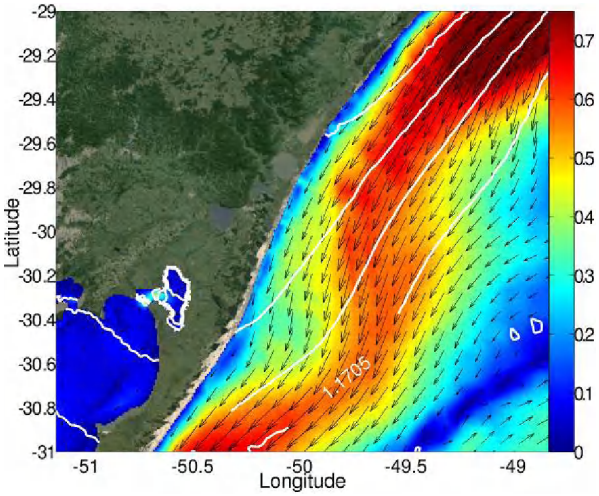

Figure 6. Spatial variably of surface currents and SSH for 10th of January.

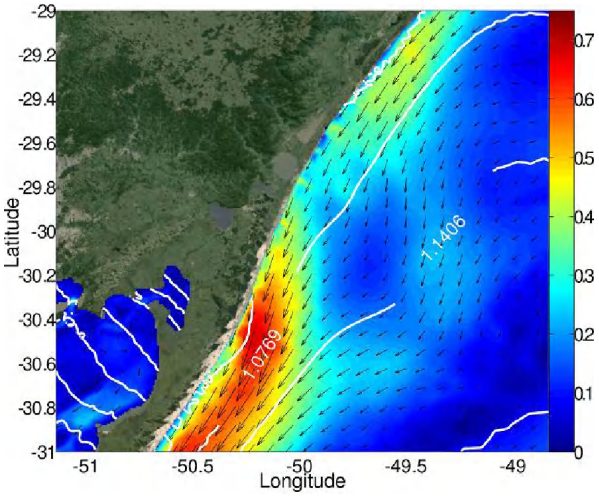

Figure 7. Spatial variably of surface currents and SSH for 20th of January.

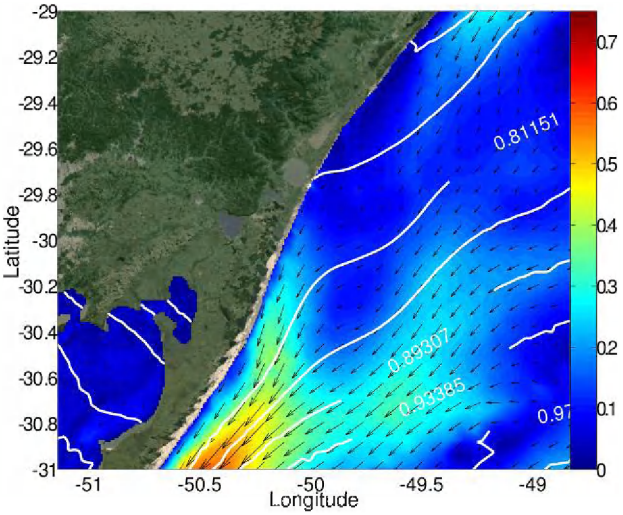

Figure 8. Spatial variably of surface currents and SSH for 30th of January.

While whether looking at Fig. 5 and 6 it is possible to see a change in current directions, all other Fig. (6-8) show a pattern with orientation Northeast-Southwest. Where the variations of SSH are more abrupt and the values are lower, the intensity of currents are higher due to the mass conservation and the barotropic transport. Having a look at Fig. 6 it is possible to see meanders, probably caused by the bottom influence. Moreover, the southern portion of the region has strong currents which is probably also related to the bottom topography. The influence of the bottom topography modulating the coastal circulation is discussed for the region by [15]. Unfortunately, there was no hydrodynamic data available for the region for a comparison; however, the values found for the currents intensity and direction are compatible with the literature [13, 14, and 15] and also the major qualitative features of the austral summer conditions are well represented for the model. In addition, TELEMAC-3D was calibrated and validated for the investigation of the hydrodynamic, morphodynamic and wave processes along the SBS in previous studies [5, 6, 7 and 8].

B. Oil drift and Weathering

ECOS was started for the 26th of January at 12:00 (Brazilian time) and computed tracer positions and oil weathering over the entire spill event. Fig. 9 shows the evolution of oil drift for intervals of 1 hour (grey scale). The oil spill follows the direction of mean surface currents and winds, reaching the shore after 10 hours. The extension of the coastal region affected is dislocated circa 5 km more to the south than reported by the Brazilian environmental authorities, even though the final position of the tracers are dislocated the dimensions of the spill are very much similar to the reported.

The oil field clearly follows the resulting direction between the wind field and the current field according to the influence of momentum transfer coefficient which was set to 35% to winds and 100 % for currents. It is also possible to infer that the tracer velocities reduce near the coastline because of the reduction of the current velocities caused by the increase of the bottom stress.

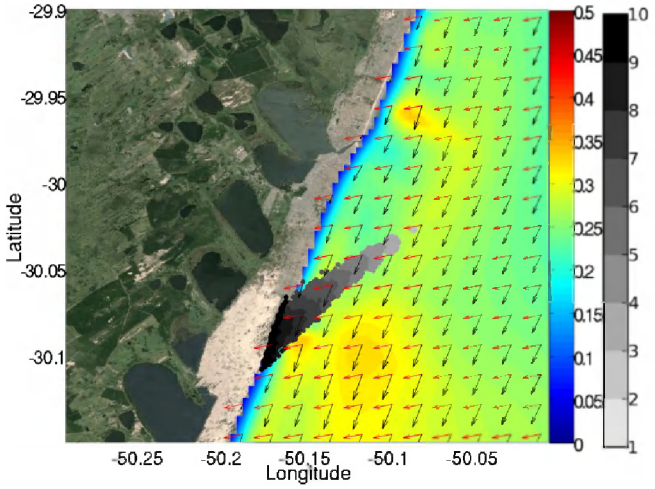

Figure 9. Oil drift evolution. Grey scale shows the oil spill duration in hours while colour scale shows the intensity of the currents. Black vectors currents intensity. Red vectors represent the wind direction and intensity.

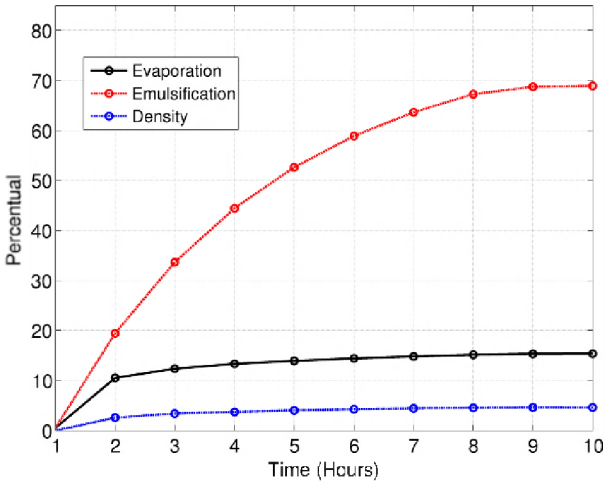

Figure 10. Temporal evolution of oil weathering properties. Red line: emulsification, blue line: increase in density and black line: evaporation. All values are expressed in percentage.

The oil weathering is represented by the evaporation, emulsification and density shown in Fig. 10. The emulsification rapidly increases from the initial state to approximately 80% while the evaporation slightly increases to approximately 10 % within 10 hours. The changes of the oil properties affect directly the oil density which increases 4.6% within 10 hours resulting in a final value of 1016.5 kg/m^{-3}. This could lead to a sinking process since this value is closer to the salt water density.

Finally, an initial development of a "risk map" was carried out. The map shown in Fig. 11 evaluates the risk (probability) of the oil slick reaching the coast line. The method is based on the volume spilled, the number of particles and geographic location of the coastline and the tracers [16]. The result shows that the region with the highest risk is a sand dune field near Cidreira city.

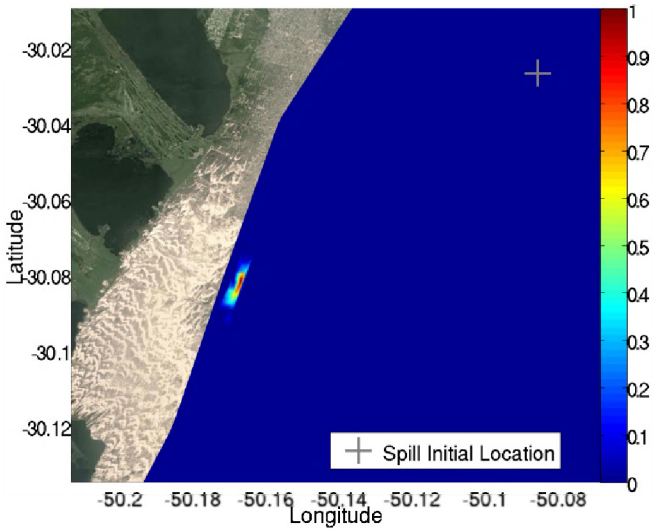

Figure 11. Risk (or probability) map for the oil spill event reaching the coastline.

V. FINAL CONSIDERATIONS

The conclusions of this work are:

- The hydrodynamic behaviour is regulated by the winds and bottom topography showing a bidirectional pattern throughout the simulation;
- The major features of the coastal circulation were well represented by TELEMAC-3D, such as the alternation of the current directions due to the wind field, the coastal meanders and the bottom induced topography.
- The oil slick reaches the coast line after 10 hours induced by the averaged currents and wind field;
- The oil weathering is responsible to an increase of 4% in oil density leading the vertical circulation processes of the oil spilled;
- The main endangered area is a sand dune field near Cidreira city.

ACKNOWLEDGEMENT

The authors thank to the Conselho Nacional de Desenvolvimento Científico e Tecnológico - CNPQ and the Petrobras' Programa de Recursos Humanos (PRH-27) for the fellowships provided which helped the development of this work. The authors also thank to the Fundação de Amparo à Pesquisa do Estado do Rio Grande do Sul - FAPERGS for partially support this work (Process: 11/1767-4, Process: 1018144 and Process: 179912-3). Further acknowledgements go to the Brazilian Navy and Brazilian environmental agency (IBAMA) for the information regarding the oil spill, to the Brazilian National Water Agency (ANA) for the water discharge data, the National Oceanic & Atmospheric Administration (NOAA) for the atmospheric data sets, to the HYCOM consortium for the oceanic data sets and finally to TELEMAC-MASCARET consortium for providing TELEMAC modelling system to accomplish this research.

REFERENCES

[1] Burns, K. A., Garrity, S., Jorissen, D., Macpherson, J., Stoelting, M., Tierney, J., and Simmons, L. Y. (1994). The galeta oil spill ii.unexpected persistence of oil trapped in mangrove sediments morlaix twenty years after the Amoco-Cadiz oil spill. Estuarine, Coastal and Shelf Research, 38:349–364.

[2] Calliari, L. J., Toldo Jr, E. E., and Nicolodi, J. a. L. (2006). Rio grande do sul 437. In Erosão e Progradação do Litoral Brasileiro, pages 437–445. Ministério do Meio Ambiente - MMA.

[3] Weschenfleder, J. and Zouain, R. N. A. (2002). Variabilidade Morfodinâmica das Praias Oceânicas entre Imbé e Arroio do Sal , RS , Brasil. Pesquisas em Geociências, 29(1):3–13.

[4] Mello, L. F., Stringari, C. E., Eidt, R. T., and Marques, W. C. (2012). Desenvolvimento de Modelo Lagrangiano de Transporte de Óleo: Estruturação e Acoplamento ao Modelo Hidrodinâmico TELEMAC3D. In Pesquisas Aplicadas em Modelagem Matemática, volume I, pages 1–21. Unijui, Ijuí, 1 edition.

[5] Marques, W. C., Fernandes, E. H. L., and Moller, O. O. 2010. Straining and advection contributions to the mixing process of the Patos Lagoon coastal plume, Brazil. Journal of Geophysical Research, 115(C6).

[6] Marques, W. C., Fernandes, E. H. L., Monteiro, I. O., and Möller, O. O. 2009. Numerical modeling of the Patos Lagoon coastal plume, Brazil. Continental Shelf Research, 29:556–571.

[7] Marques, W. C., Fernandes, E. H., Möller Jr, O. O., Moraes, B. C., and Malcherek, A. 2010. Dynamics of the Patos Lagoon coastal plume and its contribution to the deposition pattern of the southern Brazilian inner shelf. Journal of Geophysical Research, 115.

[8] Marques, W. C.; Fernandes, E. H. L. ; Rocha, Luiz A. O. ; Malcherek, Andreas . Energy converting structures in the Southern Brazilian Shelf: Energy conversion and its influence on the hydrodynamic and morphodynamic processes. Journal of Earth Sciences and Geotechnical Engineering, v. 1, p. 61-85, 2012.

[9] Silva, P. D. 2011. Interação onda-corrente na Plataforma Continental Interna do Sul do Brasil. Master Degree Thesis. Instituto de Oceanografia. Universidade Federal de Rio Grande.

[10] Hervouet, J. M. (2007). Free surface flows: Modelling with finite element methods. John Wiley & Sons, England.

[11] Fay, J. A. (1969). The spread of oil slicks on a calm sea. Oil on the Sea, Plenum Press, pages 53–63.

[12] Stringari, C. E. (2013). The influence of winds and coastal currents on the oil spill event : Case study of Tramandaí Beach , 26 th January 2012. In II Conferência Internacional em Tecnologias Naval e Offshore: Energia e Sustentabilidade - NAVTEC 2013. Rio Grande, Brazil.

[13] Costa, R. L. and Möller, O. O. (2011). Estudo da estrutura e da variabilidade das correntes na área da plataforma interna ao largo de Rio Grande (RS, Brasil), no sudoeste do Atlântico Sul, durante a primavera-verão de 2006-2007. Revista de Gestão Costeira Integrada, 11(3):273–281.

[14] Jung, G. B. (2010). Estrutura e Propagação de Correntes Longitudinais na Praia de Tramandaí - RS. Dissertação de mestrado, Universidade Federal do Rio Grande do Sul.

[15] Toldo Jr., E. E., Almeida, L. E. S., Dillenburg, S. R., Tabajara, L. L., and Borghetti, C. (1993). Parâmetros Morfodinamicos e Deriva Litoranea da Praia de Tramandaí - RS. GEOSUL, 15(1):75–88.

[16] Wojtaszek, K. (2003). Application of transport model for building contingency maps of oil spills on the North Sea. Mater of Science Thesis.

Author Index

XXth TELEMAC-MASCARET User Conference 2013

TELEMAC-MASCARET is an integrated program simulating free surface flow, developed for civil and environmental hydraulics engineers, researchers and students.

Initially developed at Electricité de France R&D, TELEMAC-MASCARET is now open source and managed by a consortium of six European core users: Artelia, BAW, CETMEF, Daresbury Laboratory, EDF and HR Wallingford.

TELEMAC-MASCARET User Conference brings together users and developers for interaction and networking. 2013 was the 20th in a highly successful series of conferences. The contributions accepted by the Scientific Committee of the TELEMAC-MASCARET Consortium cover the following topics:

- *River and urban floods, and coastal surges and tsunami waves*
- *River, estuaries, maritime and coastal sediment processes*
- *Waterworks and coastal structures design and sustainability*
- *Waves and tidal renewable and hydro power energy assessment*
- *Water quality, ecology and environmental impact*
- *Numerical methods, code coupling and high performance computing*
- *Data assimilation, optimisation, risks and uncertainties*

ISBN 978-3-939230-07-6
Printed in Germany

BAW Bundesanstalt für Wasserbau
Kompetenz für die Wasserstraßen